UNIVERSIDAD DE GRANADA

DOCTORAL THESIS

Modeling and Simulation of Semiconductor Nanowires for Future Technology Nodes

Author:
Enrique González Marín

Supervisors:
Dr. Andrés Godoy Medina
Dr. Francisco Javier García Ruiz

A thesis submitted in fulfillment of the requirements
to obtain the International Doctor degree as part of the
Programa de Doctorado en Física y Ciencias del Espacio
in the

Nanoelectronics Research Group
Departamento de Electrónica y Tecnología de los Computadores

Granada, 14th May, 2014

Editor: Editorial de la Universidad de Granada
Autor: Enrique González Marín
D.L.: 2133-2014
ISBN: 978-84-9083-153-3

Declaration of authorship

Mr. Enrique González Marín, as Ph.D Candidate, and Dr. Francisco Javier García Ruiz and Dr. Andrés Godoy Medina, as Ph.D Supervisors and Professors of Electronics at the Departamento de Electrónica y Tecnología de los Computadores of the Universidad de Granada in Spain,

Guarantee by signing this thesis:

that the research work contained in the present report, entitled ***Modeling and Simulation of Semiconductor Nanowires for Future Technology Nodes***, has been performed under the full guidance of the Ph.D Supervisors and, as far as our knowledge reaches, during the work, it has been respected the right of others authors to be cited, when their publications or their results have been used.

Granada, 14th May, 2014.

Dr. Andrés Godoy Medina
Full Professor of Electronics

Enrique González Marín
Ph.D Candidate

Dr. Francisco Javier García Ruiz
Tenured Professor of Electronics

To Laura

Why is there something rather than nothing?

The Principles of Nature and Grace, Based on Reason

Gottfried Wilhelm Leibniz (1646-1716)

Acknowledgements

I would like to acknowledge in these few lines a number of people who helped me during my PhD work, and to whom I am indebted.

Foremost, I would like to express my most sincere gratitude to my advisors Prof. Francisco J. García Ruiz and Prof. Andrés Godoy Medina for giving me the opportunity to start this exciting experience a little over three years ago. They have been a constant source of good advice and encouragement, patience and knowledge. We have spent many hours carrying out stimulating scientific discussion and I hope we will be able to continue this into the future. Without their help this Thesis would not have been possible

I wish to thank the directors of the Departamento de Electrónica y Tecnología de los Computadores: Prof. Juan E. Carceller Beltrán and Prof. Juan Antonio López Villanueva. Their classes during my degrees in Telecommunications and Electronics Engineering were tremendously motivating and awoke my sincere interest in electronics.

I am indebted to Prof. Fracisco Gámiz Pérez, manager of the Nanoelectonics Research Group to which I belong. Shortly after starting my PhD work, the Nanoelectronics Group was awarded by the Universidad de Granada, due to its outstanding contributions, the best research group of the year. After this time, I fully understand why it was so. Prof. Gámiz's passion for research and his ability to convey it set an example for me.

It is difficult to overstate my appreciation to Prof. Heike Riel for giving me the occasion to visit the IBM Research Lab in Zurich during the three months of spring 2013. My internship in the Nanoscale Electronics Group, that she manages, was both a thrilling professional and personal experience. I would also express my gratitude to Prof. Volker Schmidt who guided my research there and made me feel like a true friend. I take the opportunity to thank all the members of the Nanoscale Electronic Team for their treatment and their hospitality. I felt like I was at home during the working time

of these months.

I am thankful to all the members of the Departamento de Electrónica y Tecnología de los Computadores for their enthusiasm during these years. I wish to specially apologise to Prof. Isabel María Tienda Luna and Prof. Blanca Biel for frequently invading their offices to fill the board with formulas. Prof. Tienda Luna was an essential part of that work and I want to thank her for all her help. I could not forget to acknowledge Prof. Pablo Sánchez Moreno from the Departamento de Matemática Aplicada and his enthusiastic mathematical talks. During this time I shared the office with Prof. Diego P. Morales Santos. It is priceless that your officemate is always in a good mood, ready to encourage you and to aid you always but also to detach when you need it. I wish to not forget Prof. Carlos Sampedro Matarín who facilitated my Lab classes, providing me all the material and knowledge needed, and Prof. Encaranación Castillo Morales who gave me very thorough Lab tutorials. I am also indebted to Prof. Luca Donneti who showed how to use the cluster for the simulations. I would also like to convey my public gratitude to the rest of PhD students in the department. It was heartwarming to share the PhD candidate typical anxieties as a group.

I wish to remember my friends, some of whom are now quite far. I feel fortunate that they are part of my life. Thanks for all the unforgettable shared moments. Since I am an only child, you are the siblings I choose.

I could not forget my family: my grandfather, my aunt and cousins, and Laura's parents and siblings. This is also thanks to them. My parents, María Amalia and Cristóbal, put the right amount of love and demand in my education. They make me feel like the happiest child in the world, and I intend to make them proud of everything I do in life.

Finally, I could not finish without writing a few words to Laura. Now that a period is finishing in our lives and the future seems uncertain, there is only one sure thing. Wherever and however it will be, it will find us together.

Contents

Part I

Prologue

Abstract

Nanoelectronics Research Group
Departamento de Electrónica y Tecnología de los Computadores

Modeling and Simulation of Semiconductor Nanowires for Future Technology Nodes

by Enrique González Marín

The main purpose of this PhD Thesis is the analytical and numerical study of Multiple Gate (MuG) architectures and III-V compound semiconductors as technological alternatives to continue the downscaling process of the MOSFET beyond the 22nm node.

To do so, electrostatic and transport simulators, able to solve the Schrödinger, Poisson and Boltzmann equations for a 1D electron gas, have been implemented. The electrostatic solver is based on a non-parabolic effective mass approximation being able to deal with arbitrary geometries, materials and orientations, to achieve the charge and potential distribution in the 2D cross-section of a MuG structure. The transport solver linearizes the 1D Boltzmann equation using the momentum relaxation time approximation (MRT), solving it by a rigorous implicit approach not common in the literature. It includes novel models for surface roughness, coulomb dispersion, bulk phonons, polar optical phonons and alloy disorder scattering mechanisms, including static dielectric screening, constituting a state-of-the-art mobility simulator.

In addition, a fully analytical model able to accurately describe the electrostatic behavior of III-V cylindrical NWs is developed. It is, to the best of our knowledge, the most complete analytical description of the charge and potential distributions in III-V NWs presented in the literature up-to-date. The model provides analytical expressions for the calculation of the subband energies and the wavefunctions of the Γ-valley, taking into account the wavefunction penetration into the gate insulator and the effective

mass discontinuity in the semiconductor-insulator interface, Fermi-Dirac statistics, two-dimensional confinement of the carriers and non-parabolic effects. It also allows the inclusion of arbitrary analytical profiles of interfacial states.

Using the numerical and analytical approaches, several relevant electrostatic and transport studies of Trigates and NWs are accomplished. These two structures are specially significant as they constitute the most consolidated architectures among MuG transistor devices. Trigate FET introduces the fewest changes to conventional planar transistor processing, enhancing the electrostatic control of the channel. NWs are the ultimate evolution of the MuG architectures providing the best suppression of short channel effects. Thus, our analytical approach allows to study the influence of the device size and material type on the inversion charge, the drain current, the gate capacitance and the threshold voltage of III-V NWs. To complete the analytical study, the numerical solvers are used to elucidate the role of the L-valley on the electrostatic and transport properties, concluding in a non-negligible influence as the NW diameter is reduced. The numerical approach is also used to compare the performance of Si and III-V Trigate structures. The impact of the fin width and the back gate bias is analyzed, showing that a) the mobility enhance observed for III-V Trigates is degraded when the width is reduced; b) the back gate bias control of the threshold voltage directly affects to the mobility. Finally the surface roughness is revealed as the main scattering mechanism limiting the mobility for the big majority of the sizes and materials at high inversion charges, being the mobility behavior at low inversion charges more complex and very dependent on size and materials.

Resumen

Nanoelectronics Research Group
Departamento de Electrónica y Tecnología de los Computadores

Modeling and Simulation of Semiconductor Nanowires for Future Technology Nodes

by Enrique González Marín

El principal objetivo de esta Tesis de Doctorado es el estudio analítico y numérico de arquitecturas multipuerta, MuG del inglés *Multiple Gate*, y compuestos semiconductores III-V, como alternativas tecnológicas para continuar el proceso de escalado del transistor MOSFET más allá del nodo tecnológico de 22nm.

Con este objetivo, se han implementado simuladores electrostáticos y de transporte capaces de resolver las ecuaciones de Schrödinger, Poisson y Boltzmann en un gas de electrones unidimensional. El simulador electrostático está basado en la aproximación de masa efectiva no parábolica, siendo capaz de tratar con geometrías, materiales y orientaciones arbitrarias para obtener las distribuciones de carga y potencial en la sección transversal bidimensional de la estructura MuG. El simulador de transporte linealiza la ecuación de transporte unidimensional de Boltzmann, usando la aproximación de tiempo de relajación del momento, MRT del inglés *Momentum Relaxation Time*, resolviendo el sistema resultante de manera implícta. Además incluye modelos novedosos de dispersión debida a rugosidad superficial, cargas coulombianas, fonones *bulk*, fonones ópticos polares y desorden por aleación.

Adicionalmente, se ha desarrollado un modelo completamente analítico que describe el comportamiento electrostático de nanohilos, NW del inglés *nanowire*. Es, hasta donde alcanza nuestro conociemiento, la descripción analítica más completa de la distribución de la carga y el potencial en NWs cilíndricos de materiales III-V presentada en la literatura hasta la fecha. El modelo proporciona expresiones analíticas

para calcular la energía de las subbandas y las funciones de onda del valle Γ, teniendo en cuenta la penetración de la función de onda en el aislante y la discontinuidad en la masa efectiva en la interfaz entre el aislante y el semiconductor, así como estadística de Fermi-Dirac, confinamiento bidimensional de los portadores y efectos no parabólicos. También permite incluir un perfil arbitrario de estados en la interfaz.

Haciendo uso de las aproximaciones numérica y analítica, se realizan varios estudios relevantes de carácter electrostático y del transporte en Trigates y NWs. Estas dos estructuras son especialmente siginificativas puesto que constituyen las arquitecturas MuG más consolidadas. Los Trigate introducen pocos cambios en el proceso de fabricación planar tradicional, al mismo tiempo que incrementan el control electrostático del canal. Los NWs son la evolución última de las arquitecturas MuG, proveyendo de la mejor supresión de los efectos de canal corto. De esta manera, usando el enfoque analítico se estudia la influencia del tamaño del dispositivo y el tipo de material en la carga en inversión, la corriente de dreandor, la capacidad de puerta y la tensión umbral en NWs III-V. Para completar el estudio analítico, los simuladores numéricos desarrollados se usan para comprender el papel del valle L en las propiedades electrostáticas y de transporte, concluyendo que tiene un influencia no despreciable a medida que el tamaño del dispositivo se reduce. El enfoque numérico se usa también para comparar el desempeño de estructuras Trigate de Si y materiales III-V. El impacto de la anchura del Trigate y de la puerta trasera es analizada, mostrando que: a) el incremento de la movilidad observado para Trigates III-V se degrada cuando la anchura se reduce y b) el control de la puerta trasera sobre la tensión umbral afecta directamente a la movilidad. Finalmente, la rugosidad superficial se revela como el principal mecanismo de dispersión limitador de la movilidad para la gran mayoría de tamaños y materiales a alto campo, siendo su comportamiento a bajo campo más complicado y muy dependiente del tamaño y material.

Chapter 1

Introduction

1.1 A success story

The story of the Metal Oxide Semiconductor Field Effect Transistor (MOSFET) and the integrated circuits (IC), is probably the most successful example of the curiosity, passion and effort characteristics of the human being nature. There is not such a comparable level of progress in a such short period of time in any other human activity during the history. In the brief lapse of time which goes from the appearance of the first implementation of the MOSFET by D. Kahng and M. Atalla [1] to nowadays, MOS technology has augmented its performance by a factor 10^6 [2]. If we look a little bit further in the past, to the precursors of the MOSFET, the vacuum tubes, or the Bipolar Juntion Transistor invented by J. Bardeen, W. Brattain and W. Shockley [3, 4], the evolution is even more astonishing. No other human development holds the comparison.

The workhorse for the increase of the MOSFET performance has been the down-scaling of the transistor dimensions. Guided by the Dennard rules [5], the size of the MOSFET has been reduced from 20μm to 22nm in the last 45 years. That scaling of the transistor dimensions had one main objective: the reduction of the capacitances associated to the MOSFET, and consequently the increase of its switching time and of the IC speed [6]. In addition, the reduction of the transistor area had two aside consequences: the reduction of the switching energy and the increase in the number of transistors per chip (which also contribute to increase the IC performance).

The continuous progress in the transistor scaling was fed by the sustained economic progress of the last quarter of the twenty century. In the context of the capitalism

market economy, the electronic revolution offered novel goods to be consumed, which rapidly became *first order* necessities. In the last decade of the past century the explosion of the information technology (IT), Internet and the global society continued pushing the revolution. In a kind of virtuous circle, we can state that the aforementioned factors are as much causes as consequences of the revolution. Now, the IT market is perfectly consolidated, and the electronic devices occupy every place in our life.

Figure 1.1: The market demand is secured by: a) the diversity of applications, b) the creation of new necessities, c) the voracity of IT consumers.

1.2 Hurdles in the way

While the market demand is secured by: 1) the diversity of applications, 2) the creation of new necessities, and 3) the voracity of IT consumers, the downscaling of the MOSFET is reaching the end of the road [7]. It is not the first time that we face this challenge, although previous statements on the downscaling halt were technological: in the seventies the spatial resolution of the IC was thought to be determined by the lithography wavelength [8], [9]; while in the early eighties direct tunneling through the SiO_2 gate insulator was asserted to lead to a disastrous leakage [10], [11]. Nevertheless,

the present scenario points out that we are approaching to unavoidable physical limits. The smallest of these limits is the Si interatomic distance ($\sim$ 0.3nm) [12]. Probably before that, at transistor channel lengths around 3nm, the direct drain to source tunnel will distort the MOSFET operation [13]. Whether the limit is 3nm or 0.3nm, the end is not far as the 22nm technology node is now in production.

An evidence of the proximity of the end is the continuous relentless of the scaling process. The shrink rate of the gate length, till the last technological nodes, was 0.7 per 3 years in average, according to Moore's law [14]. For the future nodes it is predicted to move to 0.85 per 3 years [6]. This deceleration has been reflected by the International Technology Roadmad for Semiconductor (ITRS) [15] which has successively relaxed their predictions for the future technology nodes, delaying their appearance. According to Prof. Iwai, that deceleration gives us 4 or 5 generations (in the most optimistic case up to 7 more generations) and around 20-25 years of continued scaling [16]. What will be the substitute once the end of the road is reached is an open question. 2D materials: as graphene and molybdenum disulfide [17, 18]; Carbon Nanotubes (CNT) [19], molecular electronics [20] or single-atom transistors [21] are good positioned alternatives. But there is still a lot of work to do to reach the limit and this manuscript works out on some of the most promising alternatives.

To be able to continue the MOSFET scaling beyond the 22nm technology node, it is worth to know why has the scaling process slowed down. Actually, it is a multiple answer question. Some main reasons are [22–30]:

(a) The increase in the power density of the IC, which leads to critical situations related to both the heat evacuation and the energy consumption.

(b) The short channel effects (SCEs) which result in an increased drain control of the channel in detriment of the gate control.

(c) The extreme reduction of the ON current, I_{on} and of the ON/OFF current ratio $I_{\text{on}}/I_{\text{off}}$.

(d) Technological issues concerning the fabrication process which lead to non-viable device variabilities.

The aforementioned reasons are actually quite interrelated. Thus, the increase of the IC power density is the result of the necessity of keeping a reasonable $I_{\text{on}}/I_{\text{off}}$ ratio, which imply the non-observance of the Dennard's scaling rules. According to these

scaling rules, if the device dimensions are reduced in a factor, K, then so must be the IC supply voltage. That ensures a constant IC power density at the same time that guarantees a K factor increment in the IC speed [5].

However, the reduction of the supply voltage has the side effect of strongly degrading the I_{on}/I_{off} ratio. Thus, the reduction of the supply voltage by a factor $1/K$ implies an equal reduction of I_{on}. That would not affect the I_{on}/I_{off} ratio as long as I_{off} was reduced in the same amount. But, instead of decreasing with reducing supply voltage, I_{off} increases exponentially (assuming that the threshold voltage, V_T, is also decreased to keep some symmetry in the switch operation) [13, 31].

The rate of increase in I_{off} with reducing V_T is controlled by the sub-treshold swing, SS, which at room temperature under ideal conditions cannot be lower than 60mV/dec. Best MOSFET implementations cannot bring $SS < 70 - 80$mV/dec which makes the scenario even worse [32, 33]. One consequence of the trade-off between IC power density and I_{on}/I_{off} ratio was the alteration of the main contributions to the IC consumed power, becoming the passive power density dominant in the last nodes[7].

The detention of the supply voltage reduction has not avoided anyway the degradation of the I_{on} current with the MOSFET scaling. The higher vertical electric field which results from the size reduction and constant supply voltage has leaded to a strong degradation of the mobility. This is pointed out as the main reason for the low current of small MOSFET implemented up to now [34, 35].

The increase of the IC power density is not the unique consequence of the supply voltage scaling halt as SCEs are also powered. Among them, Drain Induced Barrier Lowering (DIBL) becomes dominant [36]. For the ON state, DIBL reduces the gate control of the channel and affects to the circuit performance, reducing severely the IC speed. For the OFF state, DIBL can yield a punch-trough between the source and the drain, increasing the leakage current and therefore the passive power density. One classical way to reinforce the gate control over the channel was scaling the gate insulator thickness [5, 37, 38]. The main difficulty with the insulator scaling is the increase of the gate leakage current which increases the dissipated power density. The limit for the scaling in the SiO_2 thickness is around 1nm, which correspond to 3 atomic layers.

The technological issues related to the fabrication processes are not a minor question. As the devices get smaller, the fabrication process becomes more complex. The development of the technology requires more time and inversion, reducing the number of companies available to compete in the process. A good example of that is the Ex-

treme Ultraviolet Lithography [39]. Furthermore, the tiny size of the devices makes them sensitive to problems almost obliterated in the past. Thus, lithography and etch patterning-induced fluctuations can modify the device dimensions non-negligibly [40–42], compromising its reproducibility. Oxide recess or metal gate granularity are two additional problems [41, 42]. In bulk MOSFETs random dopants fluctuations has revealed as the major source of variability [43].

1.3 Present and future boosters

Once the main problems have been exposed, it is worth to focus on the possible solutions to keep the miniaturization process in the future generations. As the problems did not appear all of a sudden, it is interesting to have a brief look on the solutions that have moved us to the present node.

Till three or four generations ago there was no necessity to introduce really strong innovations in the MOSFETs design. Of course, the miniaturization process was laborious, but the rate of novelties introduced in the last decade exceeds a lot those needed in the former thirty years. For that reason, we will focus on the innovations introduced on the three nodes previous to the present [44].

The first novelty was the strain technology. The strain was adopted in the 90nm technology node to increase the Si mobility and therefore I_{on} [45]. This technology consists on stressing the Si lattice, by stretching or compressing it, resulting in a deformation of the Si band-structure. Under the proper conditions this deformation increases electron and hole mobilities [46, 47] The strain can be applied in the plane of current flow or perpendicular to it. It can be local or global and uniaxial or biaxial (with equal or distinct characteristics in each axis). The orientation also plays a role. Hence, there is a big amount of possible combinations to apply the strain, although not all of them result in higher mobilities [48].

The second novelty was the inclusion of high-κ oxides as the gate insulator. They were adopted to improve the gate control of the channel while keeping reasonable insulator thicks and reduced gate leakage currents [49, 50]. High-κ oxides were introduced in the 45nm technology node firstly as a stack of HfO_2-SiO_2[51, 52]. There, SiO_2 was used to guarantee a good interface with Si. The lack of a good interface is one of the main drawbacks of high-k materials, and it results in a high density of traps. Extensive research is still being done to improve the interface, allowing a direct contact of the

high-κ and Si, with interesting results when La_2O_3 is used achieving equivalent oxide thickness (EOT) of 0.48nm [53].

The third novelty was the Silicon-On-Insulator technology (SOI) [54]. SOI is based on the introduction of a buried insulator layer in the Si substrate. The insulator reduces the degradation due to DIBL and punch-through. In addition, SOI reduces the effect of ionizing radiations and the parasitic capacitance with respect to bulk technology [55]. Depending on the thickness of the Si layer which stands on the insulator, the semiconductor is partially or fully depleted, resulting in PD-SOI and FD-SOI technologies. The SOI compatibility with the traditional fabrication processes resulted in a rapid consolidation being extensively used in industry [56] as well as in research [57]. The main drawback of SOI is the poor heat evacuation of the insulator layer [58], which could discourage its adoption in the most aggressive phases of the downscaling process. Other problem is the higher price of the SOI wafer compared with the bulk Silicon counterpart [59].

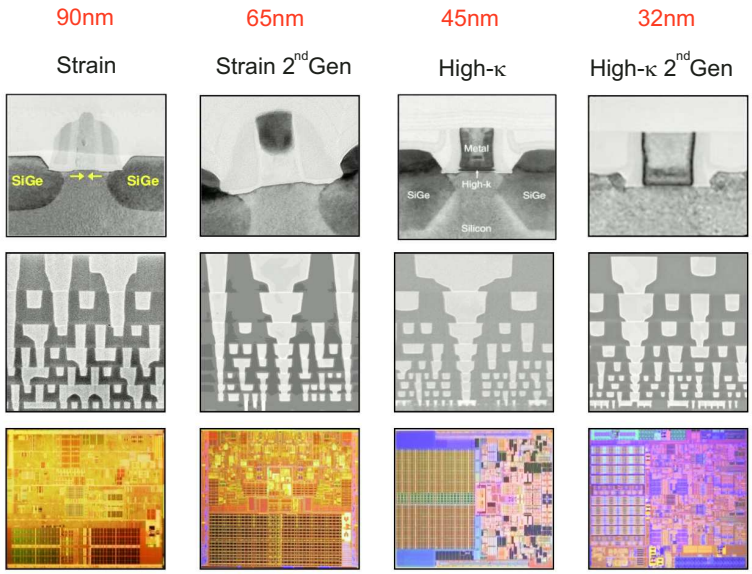

Figure 1.2: Main innovations introduced on the four nodes previous to the present. After [60].

For the sake of brevity, we have mentioned here just the three more relevant novelties. Nevertheless many others have been developed: elevated source and drain, superhalo doping profiles, integration of new silicides and metal materials to form the contacts, shallow trench isolation, work-function engineering, etc.

In spite of the outstanding nature of these innovations, the gravity of the problems makes them not enough to keep the downscaling process. For that reason some new alternatives must be found. This does not mean that the aforementioned solutions are not going to be used in the future, but they should be combined with other innovations. The main question is: what will be these new innovations? The answer to that question is not simple. There are several technological alternatives which have being presented as potential solutions. Two of the most promising are III-V compound semiconductors and Multiple Gate (MuG) architectures [6, 61]. The study of the combination of both of them is the main goal of this work.

III-V materials are a well known player in the microelectronics industry. Their properties make them specially appropriate for optical applications, being used in the implementation of lasers, light-emitting diodes or light detectors. In addition, they are supported by a well consolidated manufacturing industry, which provides big volumes of electronic circuits for a demanding and diverse market, going from smartphones and domestic entertainment to fiber-optics and satellite communications [61].

What makes III-V materials a promising alternative to Si is their potentiality to increase I_{on}. That would allow to reduce the supply voltage (and therefore the IC power density consumption) keeping the $I_{\text{on}}/I_{\text{off}}$ ratio, or increase the IC performance without augmenting the supply voltage. Moreover, this property is not altered by the downscaling of the channel. The increase of I_{on} is explained attending to the higher velocity, v, of the carriers in III-V materials. As the channel length is downscaled, the physical processes which limit v vary. Thus, for not too short channel lengths ($\gtrsim$ 10nm according to Ref. [62]), the carrier transport is diffusive, due to the carrier scattering, while for ultrashort channel lengths the transport is expected to be ballistic [63–65]. For the first case, $v \propto \mu$, where μ is the mobility, while for the second case $v = v_{\text{inj}}$, being v_{inj} the injection velocity of the electron at the source. In between the two regimes the transport is called quasi-ballistic and $v = v_{\text{inj}}(1 - r)/(1 + r)$ being $r \propto \mu$ a back scattering rate near to the source edge [64, 65]. Therefore, high μ and v_{inj} must be guaranteed to keep high I_{on} regardless of the channel length. III-V materials fulfill the requirement at least for electrons.

The cause of the main advantage of III-V materials (their lower effective mass in the Γ-valley) is also one of their possible limitations, as I_{on} is proportional to the carrier concentration, N_{i}, which is degraded due to the density of states bottleneck [66]. A reasonable trade-off between carrier concentration and carrier velocity is the sought solution. There are other challenges concerning III-V materials which should not be

obliterated: 1) The outstanding electron transport properties of these materials have not been observed for holes. Consequently, the implementation of CMOS technology would imply the use of different materials for NMOS and PMOS [**?**]. 2) Their high permittivity is detrimental for SCEs. 3) Technological issues such as the use of an appropriate gate insulator, or the co-integration on the Si fabrication process are not minor issues [61]. In spite of the aforementioned matters, III-V materials are addressed as one of the best positioned future technology booster by the ITRS [15].

As for MuG architectures, they are the most consolidated alternative proposed by academy and industry to continue the downscaling process [67, 68]. In their first 40 years of existence, the MOSFET design did not change very much [60]. The difficulties which arose with the downscaling process were faced under different approaches, but the MOSFET architecture for market oriented devices remained invariant. Of course, there were extensive research on the idea of augmenting the gate area, and devices with two or more gates were proposed [69]. That era was over in the 22nm technology node with the inclusion of MuG architectures in front-end products [60].

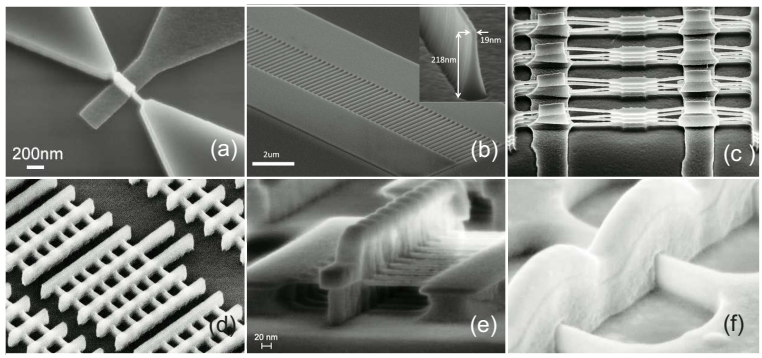

Figure 1.3: TEM images of different MuG architectures from academia: (a) FinFET from the University of California Berkeley [70], (b) Array of 100 fin structures from the Massachusetts Institute of Technology [71] (c) Inverter structure composed of four parallel stacks each with 4 Si NWs from the École Polytechnique Fédérale de Lausanne [72]; and from industry (d) Si Trigates from Intel®, [60] (e) Ring oscillator made of Si NWs from IBM®, [73] (f) FinFET from TSMC® [74]

The main idea behind the MuG architecture is increasing the gate electrostatic control. To do it, the MOSFET design is changed from planar, with the channel forming a 2D layer located below the gate, to 3D, with a vertical channel and the

gate, partially or completely, surrounding it. Depending on the region of the channel surrounded by the gate, the MOSFET is renamed as FinFET, in which two opposite faces of the channel are covered by the gate [75, 76], Trigate when three faces of the channel are covered by the gate [77, 78], and gate all around (GAA) or nanowires (NW) [79, 80] when the gate completely surrounds the channel. Other geometries such as the Ω FET [81] or the Π FET [82] are intermediate structures between Trigate and GAA, with some penetration of the gate into the buried insulator. We have intentionally omitted in the previous enumeration the planar double gate (DG) MOSFET, in which a back gate is introduced under the channel. Strictly speaking it is a MuG structure, but it does not share with the rest of the MuG structures a vertical channel and can be interpreted as a derivative of the SOI technology [83, 84]. Since the gate control on the channel is increased, several beneficial effect appears such as: 1) DIBL is reduced, 2) SS is decreased, being possible to achieve almost ideal values of 60mV/dec [36] and 3) punch-through and leakage current are almost suppressed [85].

Moreover, the fabrication process of MuG devices is CMOS compatible, and the same boosters proposed for the CMOS technology can be applied here: high-κ oxides, strain, SOI, epitaxial grew or metal silicide for the source and drain contacts.

1.4 Objectives

As the dimensions of the transistor have entered in the sub-50nm regime the downscaling process has slowed down. The aggressive reduction of the device size without a proper supply voltage scaling has enhanced the short channel effects and the power consumption, seriously compromising its performance. The solutions to that problems need to be assertive and new paradigms in the MOSFET structure and material composition are being addressed.

This PhD Thesis is devoted to the study of two of the most promising alternatives to continue the MOSFET downscaling process beyond the 22nm technology node: Multiple Gate architectures and III-V compounds semiconductors. Multiple Gate architectures increase the gate control on the channel resulting in reduced short channel effects. III-V materials have the potentiality to increase the ON current, allowing to reduce the supply voltage and the power consumption while keeping the device performance. This work aims areS:

- The analytical and numerical study of the behavior of III-V nanowires, focused

on the influence of the device size and material type on the inversion charge, the gate capacitance and the threshold voltage and the I-V characteristic.

- The numerical study of Trigate geometries made of III-V semiconductors and their comparison with their Silicon counterparts.
- The study of the electron mobility in III-V and Si NWs and Trigates in the diffusive regime including the most relevant scattering mechanisms which influence the mobility.

1.5 Methodology

Once the objectives have been established, a brief description of the methodology followed in this work is presented. The study of MuG architectures and III-V compound semiconductors is divided in two parts. The first one is consigned to the electrostatics of these devices while the second comprises the transport issues. Both parts have been worked out according to the following scheme:

- First the theoretical background necessary for the numerical and analytical resolution of the 2D Schrödinger and Poisson equations is summarized in Chapter 2.
- In Chapter 3, the 2D electrostatic simulator is described and its main characteristics (arbitrary geometries, orientation effects, non-parabolic bands, inclusion of interface charges, etc.) are highlighted. Later, in Chapter 4 the numerical solver is validated using experimental data, and used to study several relevant electrostatic magnitudes of Trigates and NWs such as: a) the population of satellite valleys of different III-V semiconductor NWs, b) the performance of III-V and SOI Trigates c) the effect of back gate bias on the threshold voltage of SOI Trigates.
- The analytical model for the potential, inversion charge and drain current of III-V cylindrical NWs is proposed in Chapter 5. To develop the model, the cylindrical symmetry of the device and the isotropic effective mass of Γ valley is taken into consideration to solve the Poisson and Schrödinger equations in polar coordinates. The results of this model are used to elaborate physically based analytical models for the gate capacitance and the threshold voltage in Chapter 6. Comparisons

with numerical simulations are accomplished for different materials, sizes and applied gate voltages.

- In Chapter 7 the necessary background on the Boltzmann Transport Equation (BTE) in a 1D electron gas is set, spotlighting those issues which need clear understanding. Later the linearization of the BTE, which is used for its solution, is presented, showing the implicit approach of the resulting equation system. The diffusive transport paradigm is completed in Chapter 8 with the calculation of the matrix elements in a 1D electron gas due to five different scattering processes: surface roughness, coulomb dispersion, bulk phonons (optical and acoustic), polar optical phonons and alloy disorder.

- Making use of the transport solver, in Chapter **??** the electron mobility of Si and III-V Trigates and NWs is studied. Specifically, the electron mobility of InAs NWs, and its dependence on the NW diameter, carrier density and population of the Γ, L and X valleys is analyzed. The mobility behavior of Si and InGaAs Trigate's architectures of different widths is compared; and the influence of the back gate bias on the transport properties of SOI Trigates is discussed.

- The mathematical details are included in the Appendixes A-E-

- Finally, the main conclusions of the work are present in Chapter 10.

Part II

Electrostatics

Chapter 2

Electrostatics of nanowires: background

2.1 Introduction

The rest of the Chapter is organized as follows. In Section 2.2 we present the independent particle Schrödinger equation, and we summarize the main assumptions needed to apply equivalent Hamiltonian approximation. Section 2.3 goes on the simplification of the Schrödinger equation presenting the effective mass approximation particularized for parabolic bands. In Section, 2.4 the Poisson equation is introduced. Both, Schrödinger and Poisson equations compose the physical background for the solution of the electrostatic problems studied in this part of the manuscript. In Section 2.5 we particularize both equations for 2D confined structures. In Section 2.6 we present a non-parabolic correction of the parabolic Schrödinger equation introduced in Section 2.3. Section 2.7 remind the density of states concept in a 1D electron gas, bringing the expression for the quantum electron concentration. Finally, Section **??** sums up the main conclusions of this Chapter.

2.2 Independent particle Schrödinger equation

The electron behavior in a semiconductor nano-device is governed by the laws of quantum mechanics. Its position, energy and momentum are probabilistic functions deter-

mined by the independent particle Schrödinger equation [86]:

$$\imath\hbar\frac{\partial}{\partial t}\Xi(\mathbf{r},t) = -\frac{\hbar^2}{2m_0}\nabla^2\Xi(\mathbf{r},t) + \Phi(\mathbf{r},t)\Xi(\mathbf{r},t) \tag{2.1}$$

where $\imath$ is the imaginary unit, $\hbar = h/2\pi$, h is the Planck constant, $\mathbf{r}$ is the position vector, t is the time, $\Xi(\mathbf{r},t)$ is the electron wavefunction, m_0 is the electron mass and $\Phi(\mathbf{r},t)$ is the electron potential energy due to the average force exerted by the rest of the electrons and atoms nuclei as well as by the external forces.

Equation (2.1) can be analytically solved only for simple idealized problems which is not case of our interest. Nevertheless, there are several approaches that may simplify Eq. (2.1).

In this manuscript we make use of the equivalent Hamiltonian and the effective mass (EMA) approximations, which have been proven as a accurate and efficient approaches [**?**]. A rigorous and detailed derivation of equivalent Hamiltonian approximation and EMA can be found in several textbooks [86], [87], [88]. Here we just spotlight the main assumptions of these approaches, presenting the necessary background for the numerical and analytical solution of EMA performed in Chapters 3 and 5.

First, let us consider Eq. (2.1) in absence of external forces. Then, $\Phi(\mathbf{r},t) = \phi_{\mathrm{c}}(\mathbf{r})$ where $\phi_{\mathrm{c}}(\mathbf{r})$ is the electron potential energy due to the semiconductor crystal lattice (comprised by other electrons and atoms nuclei). $\phi_{\mathrm{c}}(\mathbf{r})$ is assumed to be static and periodic following the spatial periodicity of the crystal.

For a static potential energy, Eq. (2.1) can be simplified by writing the electron wavefunction as:

$$\Xi(\mathbf{r},t) = \Xi(\mathbf{r})\zeta(t) \tag{2.2}$$

Substituting Eq. (2.2) into Eq. (2.1) and multiplying it by $1/\Xi(\mathbf{r})\zeta(t)$:

$$\imath\hbar\frac{1}{\zeta(t)}\frac{\partial}{\partial t}\zeta(t) = -\frac{\hbar^2}{2m_0}\frac{1}{\Xi(\mathbf{r})}\nabla^2\Xi(\mathbf{r}) + \phi_{\mathrm{c}}(\mathbf{r}) \tag{2.3}$$

So after applying separation of variables we get

$$\imath\hbar\frac{1}{\zeta(t)}\frac{\partial}{\partial t}\zeta(t) = E \longrightarrow \imath\hbar\frac{\partial}{\partial t}\zeta(t) = E\zeta(t) \tag{2.4}$$

$$-\frac{\hbar^2}{2m_0}\frac{1}{\Xi(\mathbf{r})}\nabla^2\Xi(\mathbf{r}) + \phi_{\mathrm{c}}(\mathbf{r}) = E \longrightarrow \left[-\frac{\hbar^2}{2m_o}\nabla^2 + \phi_{\mathrm{c}}(\mathbf{r})\right]\Xi(\mathbf{r}) = E\Xi(\mathbf{r}) \tag{2.5}$$

where the separation constant, E, is actually the electron energy [**?**]. Equation (2.4) results into:

$$\zeta(t) = \zeta(0)e^{-\imath\frac{E}{\hbar}t} \tag{2.6}$$

Equation (2.5) is an eigenvalue problem where E and Ξ are the eigenvalues and eigenfunctions of the Hamiltonian (H_c). Therefore, they can be renamed as E_i and Ξ_i, where i is the solution index.

The Bloch theorem imposes the periodicity of the electron wavefunction which is given by [86]:

$$\Xi_i(\mathbf{r},\mathbf{k}) = \frac{1}{\sqrt{\Omega}}e^{\imath\mathbf{kr}}u_i(\mathbf{r},\mathbf{r}) \tag{2.7}$$

where $u_i(\mathbf{r},\mathbf{k})$ is the so-called Bloch function and is directly related to the lattice potential $\phi_c(\mathbf{r})$ []; Ω is the volume of the semiconductor unit cell and $\mathbf{k}$ is the electron wavevector.

The periodicity of the crystal lattice and the electron wavefunction leads to a discretization of the reciprocal wavevector space. Therefore, there is a solution of Eq. (2.5) for each $\mathbf{k}$ value, but if the crystal is large enough $\mathbf{k}$ can be assumed as continuous and $E_i = E_i(\mathbf{k})$ is a band structure. Moreover $E_i(\mathbf{k})$ can be demonstrated to be periodic and therefore it study can be restricted to primitive cell of the wave-vector space.

The determination of the energy band structure has been accomplished in the literature for most semiconductors by approaches such as the pseudo-potential method [89], the $k\cdot p$ method [], the tight binding [**?**] method or ab-initio approaches [90]. For example, Fig. 2.1(a) shows the GaAs band structure as a function of the wave-vector, obtained by the pseudo-potential method by Chelikowsky *et al.* in Ref [91]. The wave-vector space can be reduced, using the crystal symmetry, to the irreducible wedge of the Brillouin zone showed for the zinc-blende structure in Fig. 2.1(b).

When the crystal lattice potential is perturbed by the lattice vibrations, impurities or external forces, the Hamiltonian of the Schrödinger equation can be written as perturbation of the crystal lattice Hamiltonian: $H_c + \phi(\mathbf{r})$, where $\phi(\mathbf{r})$ is the electron potential energy due to the external forces. If $\phi(\mathbf{r})$ is slowly varying function of the position and the branches of the band structure are enough separated (as it is the case for the first branch of the conduction band in Fig. 2.1), the Schrödinger equation can be written for the i-th branch of the dispersion relation as:

$$\imath\hbar\frac{\partial}{\partial t}\Xi(\mathbf{r}) = [E_i(-\imath\nabla) + \phi(\mathbf{r},t)]\Xi(\mathbf{r},t) \tag{2.8}$$

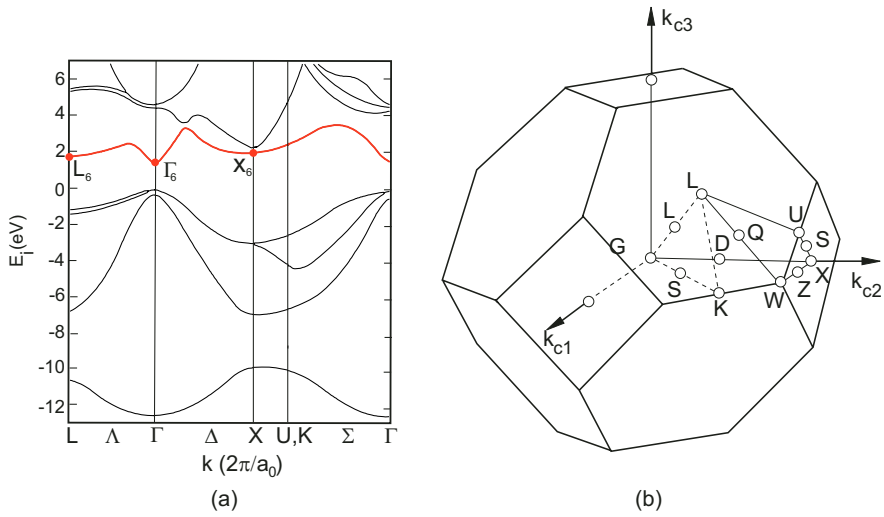

Figure 2.1: (a) GaAs energy band structure after Ref. [92]. The conduction band minimum energy points are labeled by Γ_6, X_6 and L_6. (b) Brillouin zone, irreducible wedge and high symmetry points of zinc-blende structure.

where $\phi(\mathbf{r})$ accounts only for the potential energy due to the external forces and E_i is the energy in the i-th branch obtained in the unperturbed problem. The wavefunctions solution of Eq. (2.8) are obviously different from those obtained for Eq. (2.1). Equation (2.8) is known as the independent particle equivalent Hamiltonian Schrödinger equation [**?**].

2.3 Effective Mass approximation

In most practical cases, just the lower $E_i(\mathbf{k})$ states of the conduction band are occupied by electrons. Thus we can focus on the minimum on the minimum of the $E_i(\mathbf{k})$ branches (labeled as Γ_6, X_6 and L_6 in Fig. 2.1). Near to the minimum the Bloch function dependence on $\mathbf{k}$ can be neglected [**?**] and Eq. (2.8) can be further simplified, resulting (using the separation of variables from the previous Section) into:

$$[E_i(-\imath\nabla) + \phi(\mathbf{r})]e^{\imath k_o \mathbf{r}}\Psi(\mathbf{r}) = E_n e^{\imath k_o \mathbf{r}}\Psi(\mathbf{r}) \tag{2.9}$$

where k_o is the wavevector corresponding to the minimum, E_n is the eigenvalue of the left hand side Hamiltonian, and Ψ is an envelope function which is related to the

wavefunction Ξ of Eq. (2.1) as [86]:

$$\Xi(\mathbf{r},t) = u(\mathbf{r},k_o)e^{-\imath\frac{E_n t}{\hbar}}e^{\imath k_o \mathbf{r}}\Psi(\mathbf{r}) \tag{2.10}$$

In other words the envelope function Ψ is a softy approximation of the electron wavefunction Ξ where the potential due to the crystal lattice is somehow averaged [**?**], [**?**]. Anyway, Ψ is accurate enough to describe the electron behavior in a vast majority of nanodevices studies (including those contained in this manuscript).

In Eq. (2.9), the potential due to the crystal lattice ϕ_c is not explicitly present. Its influence is modeled through the energy branch $E_i(\mathbf{k})$ which can be expanded into Taylor series (up to second order) around, $k_o = (k_{o1}, k_{o2}, k_{o3})$ as:

$$E_i(\mathbf{k}) = E_i(k_o) + \sum_j \left.\frac{\partial E}{\partial k_j}\right|_{k_o}(k_j - k_{jo}) + \frac{1}{2}\sum_{j,\,m}\left.\frac{\partial^2 E}{\partial k_j \partial k_m}\right|_{k_o}(k_j - k_{mo})(k_m - k_{mo}) \tag{2.11}$$

with $j,\ m = 1,\ 2,\ 3$. As $E_i(k_o)$ is a minimum of $E_i(\mathbf{k})$, the first derivatives evaluated at that point are null and $E_i(\mathbf{k})$ can be formulated, in matrix notation, as:

$$E_i(\mathbf{k}) = E_i(k_o) + [\mathbf{k} - k_o]\begin{bmatrix} \frac{1}{2}\left.\frac{\partial^2 E_i}{\partial k_1^2}\right|_{k_o} & \cdots & \frac{1}{2}\left.\frac{\partial^2 E_i}{\partial k_1 \partial k_3}\right|_{k_o} \\ \vdots & \ddots & \vdots \\ \frac{1}{2}\left.\frac{\partial^2 E_i}{\partial k_3 \partial k_1}\right|_{k_o} & \cdots & \frac{1}{2}\left.\frac{\partial^2 E_i}{\partial k_3^2}\right|_{k_o} \end{bmatrix}[\mathbf{k} - k_o]^T \tag{2.12}$$

It is possible to define an electron effective mass as:

$$m_{ij}^{-1} = \left.\frac{\partial^2 E}{\partial k_i \partial k_j}\right|_{k_o} \tag{2.13}$$

which characterizes the dispersion relation around the energy minimum. Then:

$$E_i(\mathbf{k}) = E(k_o) + \frac{\hbar^2}{2}[\mathbf{k} - k_o]\, W\, [\mathbf{k} - k_o]^T \tag{2.14}$$

where;

$$W = \begin{bmatrix} \frac{1}{m_{11}} & \frac{1}{m_{12}} & \frac{1}{m_{13}} \\ \frac{1}{m_{21}} & \frac{1}{m_{22}} & \frac{1}{m_{23}} \\ \frac{1}{m_{31}} & \frac{1}{m_{32}} & \frac{1}{m_{33}} \end{bmatrix} \tag{2.15}$$

W is a symmetric matrix and therefore can be diagonalized. The dispersion relation,

$E-k$, can the be written as:

$$E_i(\mathbf{k}) = E_i(k_o) + \frac{\hbar^2(k_{\mathrm{x}} - k_{xo})^2}{2m_{\mathrm{x}}} + \frac{\hbar^2(k_{\mathrm{y}} - k_{yo})^2}{2m_{\mathrm{y}}} + \frac{\hbar^2(k_{\mathrm{z}} - k_{zo})^2}{2m_{\mathrm{z}}} \tag{2.16}$$

If the point k_o is selected as the origin of the wavevector space, Eq. (2.16) can be further simplified:

$$E_i(\mathbf{k}) = E_i(k_o) + \frac{\hbar^2 k_{\mathrm{x}}^2}{2m_{\mathrm{x}}} + \frac{\hbar^2 k_{\mathrm{y}}^2}{2m_{\mathrm{y}}} + \frac{\hbar^2 k_{\mathrm{z}}^2}{2m_{\mathrm{z}}} \tag{2.17}$$

Using the parabolic dispersion relation of Eq. (2.17) into Eq. (2.9) results into the parabolic EMA Schrödiger equation:

$$\frac{\hbar^2}{2}\nabla W \nabla^T + \phi(\mathbf{r})\Psi(\mathbf{r}) = E_n'\Psi(\mathbf{r}) \tag{2.18}$$

where $E_n' = E_n - E_i(k_o)$ is the eigenvalue referred to the minimum of the branch and represents an energy subband being n the subband index. The truncation of the Taylor series in the second derivative term allows to reach a simple parabolic expression for the dispersion relation, but it can lead to a non-negligible error when $E_i(\mathbf{k})$ is not a parabolic function, as it is the case for III-V materials.

2.4 Poisson equation

In order to solve Eq. (2.18) we need to know the electron potential energy, $\phi(\mathbf{r})$, due to the external forces. It can be determined from the Poisson equation which relates the electrostatic potential, ψ, and the charge distribution in the device, ρ. The Poisson equation together with the Schrödinger equation presented in Section 2.2 completes the physical background necessary for the resolution of the electrostatic problems studied in this part of the manuscript and it is formulated as:

$$\nabla[\epsilon(\mathbf{r})\nabla\psi(\mathbf{r})] = -\rho(\mathbf{r}) \tag{2.19}$$

where $\epsilon(\mathbf{r})$ is the dielectric constant. The electrostatic potential, $\psi(\mathbf{r})$, and the electron potential energy, $\phi(\mathbf{r})$, are related as $\phi(\mathbf{r}) = -q\psi(\mathbf{r})$ where q is the electron charge. The charge distribution, $\rho(\mathbf{r})$ is given by:

$$\rho(\mathbf{r}) = q\left[p(\mathbf{r}) - n(\mathbf{r}) + N_{\mathrm{d}}^+ - N_{\mathrm{a}}^-\right] \tag{2.20}$$

where $p(\mathbf{r})$ and $n(\mathbf{r})$ are the electron and hole concentrations, and N_{d}^{+} and N_{a}^{+} are the donors and acceptor ionized impurities concentrations.

2.5 Particularization for 2D structures

In this manuscript we are interested structures that confine the electrons in two dimension, giving rise to 1D electron gases. In that case the wavefunction can be described as a plane wave in the non-confined direction. Then:

$$\Psi_i(\mathbf{r}) = \xi_i(\mathbf{s})\frac{e^{\imath k_{\mathrm{z}} z}}{\sqrt{L}} \tag{2.21}$$

where $\mathbf{s}$ is the vector position in the 2D confinement plane. Thus, introducing Eq. (2.21) into Eq. (2.18) we get:

$$\left[\frac{\hbar^2}{2}\nabla W \nabla^T + \phi(\mathbf{s})\right]\xi_i(\mathbf{s})\frac{e^{\imath k_{\mathrm{z}} z}}{\sqrt{L}} = E'_n\xi_i(\mathbf{s})\frac{e^{\imath k_{\mathrm{z}} z}}{\sqrt{L}} \tag{2.22}$$

which decomposing the ∇ operator into the confined and non-confined variables results into:

$$\left[\frac{\hbar^2}{2}\nabla_s w \nabla_s^T + \nabla_z \frac{1}{m_{\mathrm{z}}}\nabla_z^T + \phi(\mathbf{s})\right]\xi_i(\mathbf{s})\frac{e^{\imath k_{\mathrm{z}} z}}{\sqrt{L}} = E'_n\xi_i(\mathbf{s})\frac{e^{\imath k_{\mathrm{z}} z}}{\sqrt{L}} \tag{2.23}$$

where w is the 2×2 first submatrix of the diagonal matrix W given in Eq. (2.15). Thus:

$$\frac{e^{\imath k_{\mathrm{z}} z}}{\sqrt{L}}\left[\frac{\hbar^2}{2}\nabla_s w \nabla_s^T \xi_i(\mathbf{s}) + \xi(\mathbf{s})\frac{\hbar^2}{2m_{\mathrm{z}}}\imath^2 k_{\mathrm{z}} + \phi(\mathbf{s})\xi_i(\mathbf{s})\right] = E'_n\xi_i(\mathbf{s})\frac{e^{\imath k_{\mathrm{z}} z}}{\sqrt{L}} \tag{2.24}$$

canceling terms and rearranging we get:

$$\nabla_s w \nabla_s^T \xi_i(\mathbf{s}) + \phi(\mathbf{s})\xi_i(\mathbf{s}) = \varepsilon_n \xi_i(\mathbf{s}) \tag{2.25}$$

where $\varepsilon_n = E'_n - \frac{\hbar^2 k_{\mathrm{z}}}{2m_{\mathrm{z}}}$. This is the 2D Schrödinger equation which will be numerically and analytically solved in Chapters 3 and 5, respectively.

Regarding the Poisson equation, the particularization for a 1D electron gas can be readily accomplished. As the potential is assumed to vary slowly along non-confined direction, also is the charge density ρ. Then, the z component of the ∇ operator is

canceled out and the Poisson equation reduces to:

$$\nabla_s[\epsilon(\mathbf{s})\nabla_s\psi(\mathbf{s})] = -\rho(\mathbf{s}) \tag{2.26}$$

2.6 Non-parabolic corrections to the parabolic Schrödinger equation

Up to this point, we have approximated $E_i(\mathbf{k})$ as a parabolic function. However, at can be seen in Fig. 2.1(a), near to the conduction band minimums the dispersion relation is not always parabolic (see points X_6 and L_6). When the parabolic approximation is not accurate, the most common solution in the literature consists on introducing a non linear correction term $\beta_v E_i(\mathbf{k})^2$, where β_v is called the non-parabolicity factor of the v-th valley. Thus, the dispersion relation is expressed as [93], [66],:

$$E_i(\mathbf{k})(1+\beta_v E_i(\mathbf{k})) = \frac{\hbar^2 k_{\mathrm{x}}^2}{2m_{\mathrm{x}}} + \frac{\hbar^2 k_{\mathrm{y}}^2}{2m_{\mathrm{y}}} + \frac{\hbar^2 k_{\mathrm{z}}^2}{2m_{\mathrm{z}}} \tag{2.27}$$

Solving for $E_i(\mathbf{k})$:

$$E_i(\mathbf{k}) = \frac{-1+\sqrt{1+4\beta_v\gamma_{\mathbf{k}}}}{2\beta_v} \tag{2.28}$$

where we have defined:

$$\gamma_{\mathbf{k}} = \frac{\hbar^2 k_{\mathrm{x}}^2}{2m_{\mathrm{x}}} + \frac{\hbar^2 k_{\mathrm{y}}^2}{2m_{\mathrm{y}}} + \frac{\hbar^2 k_{\mathrm{z}}^2}{2m_{\mathrm{z}}} \tag{2.29}$$

Eq. (2.28) makes difficult the resolution of the Schrödinger equation since $E_i(\mathbf{k})$ can not be decomposed into confined and non-confined components [94]. In this work we follow the approach developed by Jin *et al.* [95], which proposed a non-parabolic dispersion relation written as:

$$E_i(\mathbf{k}) \simeq \phi_i + \frac{-1+\sqrt{1+4\beta_v(\gamma_{\mathbf{k},\mathrm{nc}}+E_i-\phi_i)}}{2\beta_V} \tag{2.30}$$

where E_i is i-th energy subband achieved from the parabolic Schrödinger equation and ϕ_i is the expectation value of the potential energy with respect to the wavefunction of the i-subband, defined as:

$$\phi_= \int_{\mathcal{A}} \xi_i^*(\mathbf{s})\phi(\mathbf{s})\xi_i(\mathbf{s})\, dA \tag{2.31}$$

where the integral is carried out in the 2D cross-section of the device. In Eq. (2.30) $\gamma_{\mathbf{k},\mathrm{nc}} = \hbar^2 k_\mathrm{z}^2/2m_\mathrm{z}$ is the non-confined component of $\gamma_\mathbf{k}$. This non-parabolic approximation does not require the solution of the non-parabolic Schrödinger equation as it uses the result from the parabolic EMA approximation, resulting in a simpler procedure.

2.7 Quantum electron concentration

To determine the quantum electron concentration, it is necessary to characterize the electron density in both the real and wave-vector space. In the real space, the electron distribution is fully determined by the square modulus of the electron wavefunction. In the wave-vector space, it is necessary to count the number of available electron states and their occupancy. In this Section we briefly remind the concept of density of states particularizing it to a 1D electron gas with a non-parabolic dispersion relation.

The wave-vector density of states, $g(\mathbf{k})$, is just the number of $\mathbf{k}$ states divided by the semiconductor volume. As previously mentioned, the periodicity of the crystal lattice involves a discretization of the wave-vector space. Each $\mathbf{k}$ state occupies a volume in the wave-vector space given by Ω_B/N where Ω_B is the volume of the Brillouin zone and N is the number of unit cells in the real space for the given volume, $\mathcal{V}$, of semiconductor: $N = \mathcal{V}/\Omega_\mathrm{C}$, being Ω_C the unit cell volume. Then, the wave-vector density of states is given by:

$$g(\mathbf{k}) = 2\frac{\Omega_\mathrm{B}/N}{\mathcal{V}} = \frac{(\mathcal{V}/\Omega_\mathrm{C})/\Omega_\mathrm{B}}{\mathcal{V}} = \frac{2}{(2\pi)^3} \tag{2.32}$$

where $\Omega_\mathrm{B}\Omega_\mathrm{C} = (2\pi)^3$ where the factor 2 accounts for the electron spin degeneracy. When a 1D electron as is considered, two of the three space direction are confined. Consequently Ω_B and Ω_C do not represent volumes but lengths and $\Omega_\mathrm{B}\Omega_\mathrm{C} = 2\pi$. The wave-vector density of states is given by:

$$g(k_\mathrm{z}) = 2\frac{\Omega_\mathrm{B}/N}{\mathcal{L}} = \frac{(\mathcal{L}/\Omega_\mathrm{C})\Omega_\mathrm{B}}{\mathcal{L}} = \frac{2}{2\pi} \tag{2.33}$$

The energy density of states, $g(E)$, can be determined changing the variable from $\mathbf{k}$ to E and using $E_i(\mathbf{k})$:

$$g(k_\mathrm{z})dk_\mathrm{z} = g(E)dE \rightarrow g(E) = g(k)\frac{dk}{dE} \tag{2.34}$$

Using the non-parabolic dispersion relation of Eq. (2.30) and rearranging terms we get:

$$g(E) = \frac{1 + 2\beta_v(E - \phi_i)}{\sqrt{2m^* \left[E - E_i + \beta_v(E - \phi_i)^2\right]}} \tag{2.35}$$

The states occupancy is determined by the Fermi-Dirac function:

$$f(E) = \frac{1}{1 + e^{\frac{E - E_{\mathrm{F}}}{k_{\mathrm{B}}T}}} \tag{2.36}$$

being k_{B} the Boltzmann constant and E_{F} the Fermi level. Therefore the electron density in the i-th branch in both real and energy spaces is given by:

$$n(\mathbf{s}, E) = \left| \xi_i(\mathbf{s}) \frac{e^{\imath k_z z}}{\sqrt{L}} \right|^2 \frac{1 + 2\beta_v(E - \phi_i)}{\sqrt{2m^* \left[E - E_i + \beta_v(E - \phi_i)^2\right]}} \frac{1}{1 + e^{\frac{E - E_{\mathrm{F}}}{k_{\mathrm{B}}T}}} \tag{2.37}$$

Integrating along the device total volume and the energy space gives the electron concentration under non-parabolic dispersion relation:

$$n = \int dE \frac{1 + 2\beta_v(E - \phi_i)}{\sqrt{2m^* \left[E - E_i + \beta_v(E - \phi_i)^2\right]}} \frac{1}{1 + e^{\frac{E - E_{\mathrm{F}}}{k_{\mathrm{B}}T}}} \tag{2.38}$$

where we have used the normalization of the wavefunction:

$$\int_{\mathcal{V}} |\xi_i(\mathbf{s}) \frac{e^{\imath k_z z}}{\sqrt{L}}|^2 dV = 1 \tag{2.39}$$

Equation (2.38) is the expression used along this manuscript to determine the quantum electron concentration. As for holes, and ionized impurities due to dopants, classical expressions are considered.

$$p = 2 \left(\frac{2\pi m_{\mathrm{h}} k_{\mathrm{B}} T}{\hbar^2} \right)^{3/2} e^{-\frac{E_{\mathrm{F}} - E_{\mathrm{v}}}{k_{\mathrm{B}}T}} \tag{2.40}$$

$$N_{\mathrm{a}}^- = N_{\mathrm{a}}\, f(E_{\mathrm{a}}) = \frac{N_{\mathrm{a}}}{1 + \frac{1}{g_{\mathrm{a}}} e^{\frac{E_{\mathrm{a}} - E_F}{k_{\mathrm{B}}T}}} \tag{2.41}$$

$$N_{\mathrm{d}}^+ = N_{\mathrm{d}}[1 - \ f(E_{\mathrm{d}})] = \frac{N_{\mathrm{d}}}{1 + g_{\mathrm{d}} e^{-\frac{E_{\mathrm{d}} - E_F}{k_{\mathrm{B}}T}}} \tag{2.42}$$

where m_{h} is the hole effective mass, E_{v} is the valence band energy, N_{a} (N_{d}), g_{a} (g_{d})

and E_a (E_d) are the acceptor (donor) concentration, level degeneracy and energy, respectively.

Chapter 3

2D Schrödinger-Poisson simulator for MuG structures

3.1 Introduction

The analytical calculus of the integral and differential equations which govern the electrostatic behavior of a Multiple Gate device (MuG) is not straightforward. Only in a few cases, and considering some approximations, these equations can be analytically solved, obtaining expressions for the involved physical quantities [96],[97],[98]. One of that cases is included in this manuscript in Chapter 5.

However, even assuming that analytical expressions are helpful to understand the device behavior, they are limited by the approximations made to solve the initial equations. The simplicity required for the analytical treatment is confronted to the complexity needed to properly describe the device's underlying physics.

Moreover, the study of technologically realistic devices involve among others: 1) not idealized geometries [99],[100],[101],[79], which complicate the analysis; 2) experimental inputs to the equations [102],[103] that cannot be reduced to analytical expressions; 3) fabrication dependent issues that cannot be treated from an analytical point of view [104][105].

For these reasons, the development of numerical tools able to study the device physics have played a main role in the nanoelectronics field from the very beginning [106], [107], [**?**]. In response to this requirement, several commercial simulators have been developed, allowing the study of 3D structures, such as Sentaurus^{TM} from

Synopsis®[108] or Atlas™ from Silvaco® [109], as well as 2D quantized devices, such as VPS from TU Wien [110]. The assessment of variability and fabrication processes has also been accomplished, for example by Gold Semiconductors Std. [111] and Athena™ from Silvaco® [112].

In this Chapter, we describe the main characteristics of a two dimensional simulator fully implemented within our group at UGR from scratch. Taking into consideration the extensive collection of commercial simulators, it can be questioned why to develop our own simulator. There are several reasons, among them

- Code control: most commercial simulators are black boxes which just allow an user-end control of the code.
- Versatility and extensibility: opposite to commercial simulators having our own code allows us to easily modify and extend it.
- Complete knowledge of the resolution process and its limitations: we know exactly how the equations are solved, what is included in the resolution and what it is neglected.
- Economic saving: usually commercial simulator licenses are expensive.

Of course there are also some disadvantages when developing our own simulator:

- Time consuming: putting down all the equations, testing and verifying the code requires much more time than just studying and configuring a commercial simulator.
- Not-optimized programming: it can affect to the simulation time.

The rest of the Chapter is organized as follows. Section 3.2 describes the main characteristics of the two dimensional Schrödinger-Poisson (SP2D) simulator. Section 3.3 outlines the development environment: MATLAB® and PDE toolbox™. Sections 3.4, 3.5, 3.6, 3.7 3.8, 3.9 and 3.10 detail the implementation of the main characteristics of SP2D and present a flux diagram. Finally, Section 3.11 sums up some conclusions.

3.2 Simulator description

In this Section, we outline the main characteristics of SP2D code which solves self-consistently the Schrödinger and Poisson equations for a 2D cross-section of the channel

of a multiple gate (MuG) device. Fig. 3.1 shows a 3D schematic view of a long channel Trigate device. The semiconductor and insulator media are plotted as orange and gray, while the gate contact (pinned with the label G) is plotted as red. The source and drain contacts (pinned with the labels S and D) are plotted as green. A cross-section of the 3D Trigate channel is marked with dashed lines and presented in a front view.

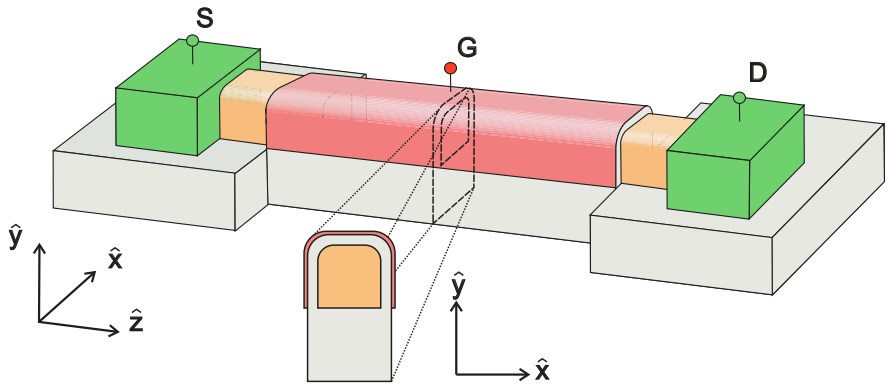

Figure 3.1: 3D schematic view of a Trigate device. The semiconductor and insulator media are plotted as orange and gray, while the gate contact is plotted as red. The source and drain contacts are plotted as green. A 2D cross-section cut along the channel is also plotted in a front view.

In Fig. 3.1 we have defined a Cartesian coordinate system where:

- $\hat{x}$ e $\hat{y}$ are the unit vectors corresponding to the directions which contain the plane where the 2D structure is placed (confinement plane) and
- $\hat{z}$ is the unit vector corresponding to the transport direction perpendicular to the 2D structure.

The expressions for the Schrödinger and Poisson equations were presented in Chapter 2. Here we recall and particularize them for 2D geometries. Thus, the 2D Schrödinger equation under EMA is given by:

$$E_n(-\imath\nabla)\xi(x,y) + \phi(x,y)\xi(x,y) = E\xi(x,y) \tag{3.1}$$

where E_n is the electron energy in the n-th band (fully determined by the semiconductor properties), $\xi(x,y)$ is the 2D wavefunction, $\phi(x,y)$ is the electron potential energy due to an external perturbing potential $\psi(x,y)$, and E is the total electron energy.

The numerical solution of the Schrödinger equation accomplished by SP2D assumes parabolic bands. This dispersion relation is later corrected using the method proposed by Jin *et al.* in Ref. [95] and presented in Chapter 2 (see Section 3.7 for details on the implementation of non-parabolicity). Under parabolic bands approximation we can write Eq. (3.1) in the semiconductor as:

$$-\frac{\hbar^2}{2}\begin{bmatrix} \frac{\partial}{\partial x} & \frac{\partial}{\partial y} \end{bmatrix}\begin{bmatrix} \frac{1}{m_{xx}} & \frac{1}{m_{xy}} \\ \frac{1}{m_{yx}} & \frac{1}{m_{yy}} \end{bmatrix}\begin{bmatrix} \frac{\partial}{\partial x} \\ \frac{\partial}{\partial y} \end{bmatrix}\xi^{\mathrm{s}}(x,y)+\phi^{\mathrm{s}}(x,y)\xi^{\mathrm{s}}(x,y)=E\xi^{\mathrm{s}}(x,y) \quad (3.2)$$

where the matrix element $1/m_{ij}$, with $i,j=[x,y]$, is related to the electron energy ellipsoid in the way explained in Section 3.6. For the insulator, we assume an isotropic electron effective mass, m_{ins}, and the Schrödinger equation is simplified to:

$$-\frac{\hbar^2}{2m_{\mathrm{ins}}}\left[\frac{\partial^2}{\partial x^2}+\frac{\partial^2}{\partial y^2}\right]\xi^{\mathrm{ins}}(x,y)+\phi^{\mathrm{ins}}(x,y)\xi^{\mathrm{ins}}(x,y)=E\xi^{\mathrm{ins}}(x,y) \quad (3.3)$$

where the electron potential energy in the insulator ϕ^{ins} takes into consideration the band offset ($\Delta\phi$) between the insulator and the semiconductor. The procedure followed to determine it is summarized in Section 3.4. In Eqs. (3.2) and (3.3) we have used the superscripts $^{\mathrm{s}}$ and $^{\mathrm{ins}}$ to distinguish the electron wavefunctions and potential energies in the semiconductor and insulator, respectively. Hereinafter in this Chapter, $^{\mathrm{s}}$ and $^{\mathrm{ins}}$ will be used to indicate that a variable is circumscribed to the semiconductor or the insulator media, respectively.

We do not solve the Schrödinger equation on the metal as the electron wavefunction is assumed to vanish at the metal-insulator interface.

For the solution of Eqs. (3.2) and (3.3) we impose boundary conditions which guarantee the continuity of the flux density through the semiconductor-insulator interface [1] [115]. They enforce:

(a) The electron wavefunction continuity at the semiconductor-insulator interface

$$\xi^{\mathrm{s}}(x,y)\Big|_{x,y\in\mathcal{C}_{\text{s-i}}}=\xi^{\mathrm{ins}}(x,y)\Big|_{x,y\in\mathcal{C}_{\text{s-i}}} \quad (3.4)$$

where $\mathcal{C}_{\text{s-i}}$ is the semiconductor-insulator interface path.

[1] An interesting discussion on the generalization of these boundary conditions can be found in Refs. [113] and [114].

(b) The continuity of the wavefunction derivative in the direction perpendicular to the semiconductor-insulator interface

$$\hat{n}\cdot\left[\frac{\partial}{\partial x}\hat{x},\frac{\partial}{\partial y}\hat{y}\right]\begin{bmatrix}\frac{1}{m_{xx}} & \frac{1}{m_{xy}}\\ \frac{1}{m_{yx}} & \frac{1}{m_{yy}}\end{bmatrix}\xi^{\mathrm{s}}(x,y)\Big|_{x,y\,\in\,\mathcal{C}_{\text{s-i}}}=\hat{n}\cdot\left[\frac{\partial}{\partial x}\hat{x},\frac{\partial}{\partial y}\hat{y}\right]\frac{1}{m_{\mathrm{ins}}}\xi^{\mathrm{ins}}(x,y)\Big|_{x,y\,\in\,\mathcal{C}_{\text{s-i}}} \tag{3.5}$$

being $\hat{n}$ the unit vector perpendicular to the interface at each point $(x,y)\in\mathcal{C}_{\text{s-i}}$.

The 2D Poisson equation is given by:

$$\nabla\cdot\epsilon\nabla\psi(x,y)=-\rho(x,y) \tag{3.6}$$

where ϵ is the dielectric constant and $\rho(x,y)$ is the charge density. We have considered homogeneous isotropic dielectric constants in each media. This way, Eq. (3.6) can be particularized for the semiconductor as:

$$\epsilon_{\mathrm{s}}\left(\frac{\partial^2}{\partial x^2}+\frac{\partial^2}{\partial y^2}\right)\psi^{\mathrm{s}}(x,y)=-q\left[-n(x,y)+p(x,y)-N_{\mathrm{d}}^{+}(x,y)+N_{\mathrm{a}}^{-}(x,y)\right] \tag{3.7}$$

where n, p, are the electron and holes concentrations and N_{d}^{+} and N_{a}^{-} are donor and acceptor ionized impurities concentrations, respectively. Equivalently for the insulator the Poisson equation is:

$$\epsilon_{\mathrm{ins}}\left(\frac{\partial^2}{\partial x^2}+\frac{\partial^2}{\partial y^2}\right)\psi^{\mathrm{ins}}(x,y)=-q\left[-n(x,y)+N_{\mathrm{ins}}(x,y)\right] \tag{3.8}$$

where N_{ins} refers to the insulator charge concentration, also including interface states (see Section 3.8 for a complete description). Note that the charge density in the insulator considers n. This is due to the electron wavefunction penetration into this media.

As already mentioned, SP2D assumes an ideal metal gate. Therefore, the Poisson equation is not solved on it and ψ in the metal is determined by the applied gate voltage, V_{g}. The metal properties are introduced through a boundary condition which determines the bias of the structure:

$$\psi^{\mathrm{ins}}(x,y)\Big|_{x,y\,\in\,\mathcal{C}_{\text{m-i}}}=V_{\mathrm{g}}-(\Phi_{\mathrm{m}}-\chi_{\mathrm{s}}) \tag{3.9}$$

where $\mathcal{C}_{\text{m-i}}$ is the path along the metal-insulator interface, Φ_{m} is the metal work function

and χ_s is the semiconductor electron affinity. The other boundary conditions considered for the Poisson equation are:

(a) The continuity of the potential and the electric flux density [2] at the semiconductor-insulator interface:

$$\psi^{s}(x,y)\Big|_{x,y\,\in\,\mathcal{C}_{\text{s-i}}} = \psi^{\text{ins}}(x,y)\Big|_{x,y\,\in\,\mathcal{C}_{\text{s-i}}} \tag{3.10}$$

$$\hat{n}\cdot\epsilon_{s}\left[\frac{\partial}{\partial x}\hat{x},\frac{\partial}{\partial y}\hat{y}\right]\psi^{s}(x,y)\Big|_{x,y\,\in\,\mathcal{C}_{\text{s-i}}} = \hat{n}\cdot\epsilon_{\text{ins}}\left[\frac{\partial}{\partial x}\hat{x},\frac{\partial}{\partial y}\hat{y}\right]\psi^{\text{ins}}(x,y)\Big|_{x,y\,\in\,\mathcal{C}_{\text{s-i}}} \tag{3.11}$$

(b) The nullity of the electric field in the direction of $\hat{n}$ at the outer boundaries of the structure

$$\hat{n}\cdot\left[\frac{\partial}{\partial x}\hat{x},\frac{\partial}{\partial y}\hat{y}\right]\psi^{\text{ins}}(x,y)\Big|_{x,y\,\in\,\mathcal{C}_{\text{i-e}}} = 0 \tag{3.12}$$

where $\mathcal{C}_{\text{i-e}}$ is the path between the insulator (usually a buried oxide for not SGT structures) and the external region. This condition is imposed from the charge neutrality of the whole structure.

Fig. 3.2 shows the front view of a 2D Trigate specifying the different contours paths between media: $\mathcal{C}_{\text{s-i}}$, $\mathcal{C}_{\text{m-i}}$ and $\mathcal{C}_{\text{i-e}}$. Although they are particularized for a Trigate structure, the extrapolation to any other kind of MuG structure is straightforward.

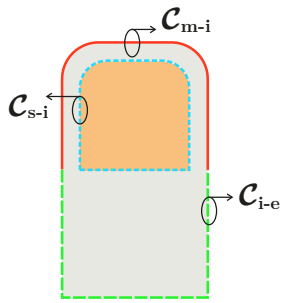

Figure 3.2: Contour paths in the boundaries between media for a 2D Trigate.

For the numerical implementation of Eqs. (3.2), (3.3), (3.7) and (3.8) SP2D uses MATLAB® programming language [116] and the Partial Differential Equation toolbox™ (PDE toolbox™) [117]. A brief description of PDE toolbox™ is given in Section 3.3.

[2] This boundary condition imposes null interface states. The way in which SP2D introduce interfaces states is discussed in Section 3.8

3.3 Finite Element Method

The PDE toolbox™ is a set of functions provided by MATLAB® which helps in the definition and resolution of 2D partial differential problems of several kinds: elliptic, parabolic, hyperbolic, eigenvalue and nonlinear elliptic.

The key feature of PDE toolbox™ regards the discretization method. Instead of using the Finite Differences Method (FDM) [118] for a regular discretization of the equations, PDE toolbox™ is based on Finite Element Method (FEM) [119]. The main advantages of FEM over FDM can be summarized in the following three [120]:

- More flexibility in terms of dealing with complex geometries and thin sections.
- Better treatment of inhomogeneous media.
- Reduced requirements on the regularity or smoothness of the solution.

The PDE toolbox™ implementation of FEM discretize the equations using a non regular grid composed of triangles which allows a better adaptation to curved complex geometries. Fig. 3.3 shows an example of a Trigate structure and a detail of the FEM grid near a rounded corner. As can be seen the non-regular grid is nicely adapted to the corner.

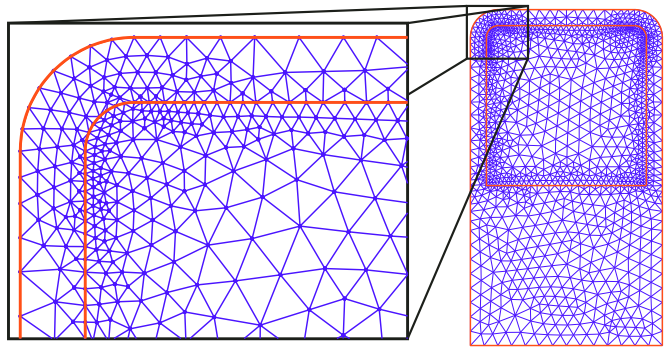

Figure 3.3: FEM grid for a 2D Trigate with rounded corners. Detail of the grid around a corner

Other remarkable characteristics of PDE toolbox™ are [121]:

- Versatile boundary condition specification.

- Flexible non-linear solvers
- Visualization tools for solutions, mesh and geometries.

The definition of equations and boundary conditions in PDE toolbox^{TM} is easy. It is not the aim of this Chapter to describe them. Extensive information can be found in Refs. [117] and [121]. In the next Sections, we detail the key features of the developed SP2D simulator.

3.4 Energy and potential reference system

In Section 3.2, we proposed a Cartesian coordinate system to spatially describe the 2D MuG geometry and particularized Schrödinger and Poisson equations for that system. We defined the paths which limit each media in the MuG device and imposed conditions to relate ξ and ψ in adjacent medias. However, the resolution of Schrödinger and Poisson equations requires an extra consideration: the definition of a reference system for the energies and the potential. This is the aim of this Section.

Two main issues constrain the specification of the energy reference system: (a) the origin, which, to allow an easy referencing, must be constant along the whole structure; and (b) the relation between the potential, ψ, the potential energy, ϕ, and the energy band diagram of the metal-insulator-semiconductor (MIS) structure.

Regarding the origin, no charge is expected to flow along the MuG 2D cross-section. Therefore, the Fermi level can be assumed constant ($E_{\mathrm{F}}(x,y) = E_{\mathrm{F}}$). For this reason, we choose it as the origin of the energy reference system.

Concerning the band diagram-potential relation, since SP2D is thought to study N-type devices, we have opted to identify the conduction band and the potential: $-q\psi(x,y) = \phi(x,y) = E_{\mathrm{c}}(x,y)$.

These definitions have three consequences: (a) the eigenvalues, E, of the Schrödinger equation and $\phi(x,y)$ are referred to E_{F} (b) the band offset between ϕ^{s} and ϕ^{ins} is given by the conduction band offset (CBO) of the MIS heterostructure; and (c) the gate applied voltage, imposed as a boundary condition to the Poisson equation must be referred to the potential origin, E_{F} (see Section 3.2).

The CBO determination is not a straightforward question. While the Schottky barrier model [122] has given very good results for Si-SiO_2 structures, it has been revised when other heterostructures are considered [123], [124], [125], [126]. The limitation

of the Schottky barrier model regards the lack of consideration of the heterostructure surface properties, which have revealed to play an important role on the CBO formation. Some discussion still remains on the underlying physical process which determine the band alignment of the heterostructure. The two main explanations refer to: (a) extrinsic defects: unsatisfied atomic bonds at the interface, [127], [128], [129], (b) intrinsic defects: metal induced gap states (MIGS),[130], [131], [132], [133], due to the penetration of the metal wavefunctions into the semiconductor gap. Although both theories suggest different physical origins, both conclude in the appearance of energetic states in the gap which lead to a pinning of the Fermi level in the semiconductor. The gap states distribution is then characterized, in both theories, by a charge neutrality level (CNL) which indicates a change in the polarity of those states. In both theories the band alignment expressions are equivalent.

Even if these theories are not fully correct, there is an agreement in their ability to explain experimental results [134], [135], [136]. Based on this experimental support we have considered the expression resulting from those models as appropriate to determine the CBO. Then, $\Delta\phi$ is given by:

$$\Delta\phi = (\chi_{\mathrm{s}} - \phi_{\mathrm{CNL,s}}) - (\chi_{\mathrm{ins}} - \phi_{\mathrm{CNL,ins}}) + S(\phi_{\mathrm{CNL,s}} - \phi_{\mathrm{CNL,ins}}) \tag{3.13}$$

where χ_{s} and χ_{ins} are the electron affinities of the semiconductor and the insulator, $\phi_{\mathrm{CNL,s}}$ and $\phi_{\mathrm{CNL,ins}}$ are the CNL of the semiconductor and the insulator, the values of which are obtained from Refs. [134], [135] and summarized (for the materials used thorough this manuscript) in Appendix F. S is the so-called pinning factor and determines how strong the Fermi level pinning is for a given heterostructure: $S = 1$, means no pinning, while for $S = 0$, E_{F} is fully pinned. It is worth to note that for $S = 1$ Eq. (3.13) results into the difference of electron affinities which is the Schottky barrier model applied to a semiconductor insulator interface. S was found to empirically depend on the dielectric constant of the wider gap material as given by [133]:

$$S = \frac{1}{1 + 0.1(\epsilon_{\mathrm{ins},\infty}/\epsilon_0 - 1)^2} \tag{3.14}$$

where $\epsilon_{\mathrm{ins},\infty}$ is the dielectric constant of the insulator at high frequency and ϵ_0 is the vacuum absolute permittivity.

3.5 Arbitrary geometry

As explained in Section 3.3, one of the main advantages of FEM is the versatility to adapt the grid to complex geometries. The aim of this Section is to briefly show the possibilities of SP2D to simulate complex MuG geometries. First, Fig. 3.4 shows four geometries generated by SP2D which reproduce the 2D cross-sections of real devices fabricated by (a) Intel® [99], (b) the University of California Berkeley [100], (c) the École Polytechnique Fédérale de Lausanne [137], and (d) the Tokyo Institute of Technology [102]. The TEM images of the devices are reproduced for comparison. Some of these geometries have been used in electrostatic studies obtaining very good agreement with experimental results (see Chapter 4 for details). We have kept the color code (including the blue color for the additional insulator) introduced in Section 3.2 for the different materials and for the boundaries between them.

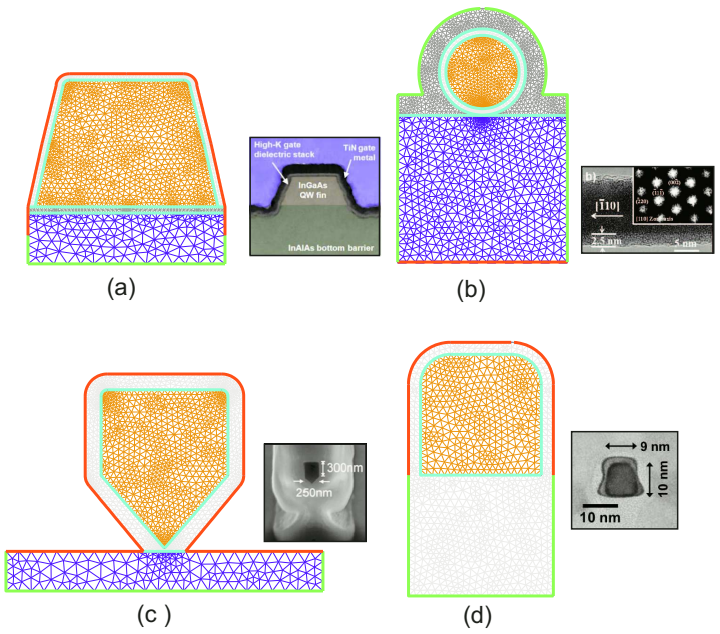

Figure 3.4: SP2D geometries reproducing real devices (TEM images are also reproduced) for: (a) a Trigate with tilted lateral walls from Intel® [99], (b) a NW from the University of California Berkeley [100], (c) a Triangular wire from the École Polytechnique Fédérale de Lausanne [137], and (d) a Trigate from the Tokyo Institute of Technology [102].

Other features of SP2D which deserve to be remarked are the simulation of (a) several insulator layers made of different materials, (b) non uniform insulator thicknesses, (c) buried gates, (d) several independently biased gates. Fig 3.5 shows two examples of device geometries generated by SP2D with some of these characteristics

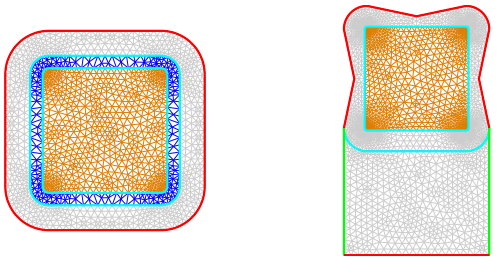

Figure 3.5: (a) SP2D NW with rounded corner and two insulator layers (b) SP2D Trigate geometry with non-uniform insulator thickness and two independently biased gates.

3.6 Arbitrary orientation

In Section 3.2 we employed the Schrödinger equation under the EMA for the 2D cross-section geometry and for an arbitraryly oriented device. There, we wrote the mass tensor in its general form. In this Section, we describe how SP2D relates each matrix element m_{ij} with $i,\ j = x,\ y$ in Eq. (3.2) with the ellipsoid effective mass. To do it we follow the work done in Refs. [138] and [139]. As discussed in Chapter 2 under the EMA the conduction band dispersion relation can be written as [3]:

$$E_{\mathrm{c}}(k) = E_{\mathrm{c,o}} + \frac{\hbar^2}{2}\, k_{\mathrm{e}}\, W_{\mathrm{e}}\, k_{\mathrm{e}}^T \tag{3.15}$$

where k_{e} is the wavevector in the ellipsoid coordinate system and W_{e} is the inverse effective mass tensor, also in the ellipsoid coordinate system. W_{e} can be written as:

$$W_{\mathrm{e}} = \begin{bmatrix} \frac{1}{m_{\mathrm{l}}} & 0 & 0 \\ 0 & \frac{1}{m_{\mathrm{t}}} & 0 \\ 0 & 0 & \frac{1}{m_{\mathrm{t}}} \end{bmatrix} \tag{3.16}$$

[3] As it was proposed in Chapter 2 it is assumed here that k_{e} is referred to k_{o} which is the wavevector corresponding to the minimum of the conduction band $E_{c,\mathrm{o}}$

being m_l and m_t the effective masses associated to the principal axes of the ellipsoid. Fig. 3.6(a) illustrates the coordinate system of the ellipsoid and the relationship between the ellipsoid axes and m_l and m_t, being $k_{\mathrm{e}1}$, $k_{\mathrm{e},2}$ and $k_{\mathrm{e},3}$ the ellipsoid coordinate system basis vectors.

The aim here is to rewrite k_e in the device reference system defined in Section 3.2 to be able to do the substitution $k = \imath\nabla$, where ∇ is expressed in the device reference system. First, we must reformulate k_e in the crystal coordinate system changing the basis through a rotation. We define the crystal basis coincident with the principal axis of a cubic system (see Fig. 3.6b). Thus, we can write:

$$k_\mathrm{e} = k_\mathrm{c} R_{\mathrm{e}\leftarrow\mathrm{c}} \tag{3.17}$$

where $R_{\mathrm{e}\leftarrow\mathrm{c}}$ is the matrix containing as columns the basis vectors of the ellipsoid coordinate system expressed in the basis of the crystal coordinate system. It obviously depends on kind of valley and ellipsoid. Fig. 3.6 shows an example of the construction of the $R_{\mathrm{e}\leftarrow\mathrm{c}}$ matrix for a L-valley ellipsoid.

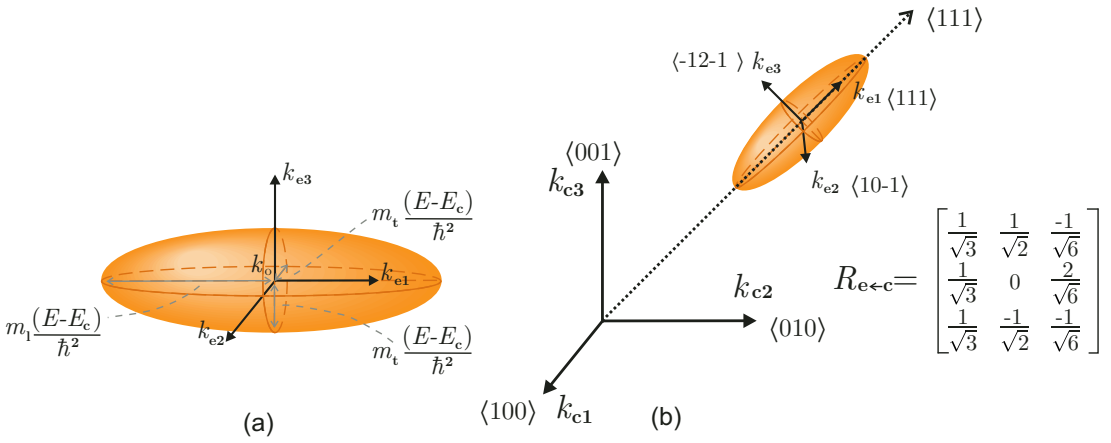

Figure 3.6: (a) Ellipsoid coordinate system $(k_{\mathrm{e}1}, k_{\mathrm{e}2}, k_{\mathrm{e}3})$ and effective masses. (b) Translation from ellipsoid coordinate system to crystal coordinate system $(k_{\mathrm{c}1}, k_{\mathrm{c}2}, k_{\mathrm{c}3})$ for a L-valley oriented in the $\langle 111\rangle$ direction.

Finally, we need to change from the crystal coordinate system to the device coor-

dinate system. To do so, we write

$$k_{\mathrm{c}} = kR_{\mathrm{c}\leftarrow\mathrm{d}} \tag{3.18}$$

where $R_{\mathrm{c}\leftarrow\mathrm{d}}$ is the matrix containing as columns the basis vector of the crystal coordinate system expressed in the basis of the device coordinate system. Usually, for comparison with technological results, what is given is the wafer orientation and/or the transport direction of the device referenced to the crystal cubic system. Then, the device coordinate system basis directions can be identified with the wafer orientation and the transport direction. To determine $R_{\mathrm{c}\leftarrow\mathrm{d}}$ we write the device basis vectors in columns (they are already expressed in the crystal coordinate system), and we do the inverse. But as the device basis vectors form an orthonormal basis, the inverse is just the transpose of the matrix. So $R_{\mathrm{c}\leftarrow\mathrm{d}}$ just contains the device basis vectors written in rows. Using Eqs. (3.17) and (3.18) we can write:

$$E_c(k) = E_{\mathrm{c},0} + \frac{\hbar^2}{2}\, k\, W_{\mathrm{d}}\, k^T \tag{3.19}$$

where $W_{\mathrm{d}} = R_{\mathrm{e}\leftarrow\mathrm{c}}\, R_{\mathrm{c}\leftarrow\mathrm{d}}\, W_{\mathrm{e}}\, (R_{\mathrm{e}\leftarrow\mathrm{c}}\, R_{\mathrm{c}\leftarrow\mathrm{d}})^T$ corresponds to the matrix tensor in the device coordinate system:

$$W_{\mathrm{d}} = \begin{bmatrix} \frac{1}{m_{xx}} & \frac{1}{m_{xy}} & \frac{1}{m_{xz}} \\ \frac{1}{m_{yx}} & \frac{1}{m_{yy}} & \frac{1}{m_{yz}} \\ \frac{1}{m_{zx}} & \frac{1}{m_{xy}} & \frac{1}{m_{zz}} \end{bmatrix} \tag{3.20}$$

As SP2D solves the Schrödinger equation in the 2D cross-section of the device, just the projection of W_{d} into the $x-y$ plane was considered in Section 3.2. There is another effective mass related parameter taken into consideration by SP2D and obtained from W_{d}: the conduction effective mass, m_v^*, which determines the effective mass in the transport direction, $\hat{z}$; where v stands for the valley index. m_v^* is used in the determination of $n(x,y)$, as it is shown in Section 3.7, and is calculated as the $(3,3)$ element of the W_{d} inverse matrix.

3.7 Non-parabolicity of the conduction band

The expression of the Schrödinger equation proposed in Section 3.2 assumes a parabolic dispersion relationship for the conduction band. However, as pointed out in Chapter 2, when III-V semiconductors are considered this approximation would result in an non-negligible error in the electron concentration, and must be corrected. SP2D follows the approximation proposed by Jin *et al.* in Ref. [95] and summarized in Section 2.6 to introduce the non-parabolicity of the conduction band. We recall here the expression for the electron concentration under the non-parabolic dispersion relationship introduced in Eq. (2.37), particularizing it for the 2D Cartesian coordinate system defined in Section 3.2 and the energy reference system described in Section 3.4.

$$n(x,y) = \frac{2}{\hbar}\sum_i |\xi_i(x,y)|^2 \int_{E_i^{\mathrm{NP}}}^{\infty} \frac{1+2\beta_v(E-\phi_i)}{\sqrt{2m^*\left[E-E_i+\beta_v(E-\phi_i)^2\right]}} \frac{1}{1+e^{\frac{E-E_{\mathrm{F}}}{k_{\mathrm{B}}T}}} dE \tag{3.21}$$

where we have kept the nomenclature introduced in Section 2.6, that is, E_i^{NP} is the non-parabolic energy minimum given by:

$$E_i^{\mathrm{NP}} = \phi_i + \frac{-1+\sqrt{1+4\beta_v\left(E_i-\phi_i\right)^2}}{2\beta_v} \tag{3.22}$$

β_v and m_v^* are the non-parabolicity factor and the conduction effective mass of the v valley, respectively; and ϕ_i is the expectation value of the potential energy with respect to the wavefunction of the i subband, defined as:

$$\phi_= \iint_{\mathcal{A}} \xi_i^*(x,y)\phi(x,y)\xi_i(x,y)\, dx\, dy \tag{3.23}$$

being $\mathcal{A}$ the device area.

Contrary to what can be done for 1D confinement [93], the integral in Eq. (3.21) cannot be easily split into a sum of two Fermi integrals and therefore it needs to be numerically integrated. However, the numerical integration of Eq. (3.21) diverges, since the integrand fraction has a pole for $E = E_i^{\mathrm{NP}}$.

Then, to determine the electron concentration we change the variable of integration

from energy, E, to wavevector, k, and $n(x,y)$ can be obtained as:

$$n(x,y) = \sum_i |\xi_i(x,y)|^2 \sum_k g(k) f_i(k) \tag{3.24}$$

where $g(k) = \frac{2}{\pi} dk$ is the density of states in the k space for 2D confinement and $f_i(k)$ is the occupation probability of the state with k wavevector in the i-th subband, that is the Fermi function evaluated at $E_i^{\mathrm{NP}}(k)$

$$f_i(k) = \frac{1}{1 + e^{\frac{E_i^{\mathrm{NP}}(k) - E_{\mathrm{F}}}{k_{\mathrm{B}} T}}} \tag{3.25}$$

Therefore:

$$n(x,y) = \frac{2}{\pi} \sum_i |\xi_i(x,y)|^2 \int_{-\infty}^{\infty} \frac{1}{1 + e^{\frac{E_i^{\mathrm{NP}}(k) - E_{\mathrm{F}}}{k_{\mathrm{B}} T}}} dk \tag{3.26}$$

where $E_i^{\mathrm{NP}}(k)$ is given by:

$$E_i^{\mathrm{NP}}(k) = \phi_i + \frac{-1 + \sqrt{1 + 4\beta_v \left(\frac{\hbar^2 k^2}{2 m_v^*} + E_i - \phi_i \right)^2}}{2\beta_v} \tag{3.27}$$

Eq. (3.26) does not diverge but it is computationally expensive. It should be done for each energy level and each point of the FEM grid (due to the accelerator convergence algorithm, see Section 3.9 for details). For a not very demanding simulation with 50 levels and a 1500 grid points it means 75000 integrals. But SP2D needs several iterations to achieve convergence in the solutions. Let us consider 5 iterations, which is a very favorable case. Then the number of integrations would be 375.000 for just one bias point. To reduce the computational cost of Eq. (3.26), SP2D tabulates the integral at the beginning of the simulation as a function of two parameters a and b. The tabulated integral is

$$\frac{2}{\pi} \int_{-\infty}^{\infty} \left(1 + e^{\frac{a}{k_{\mathrm{B}} T} + \frac{-1 + \sqrt{1 + 4\beta_v \left(\frac{\hbar^2 k^2}{2 m_v^*} + b \right)}}{2 k_{\mathrm{B}} T \beta_v}} \right) - 1 dk \tag{3.28}$$

which is valley dependent. Therefore, SP2D tabulates as many integrals as valleys are considered in the simulation. The range of variation of the parameters a and b depends on the size of the structure and the bias, but the integral is actually saturated for a small range of a. Fig. 3.7 shows the integral as a function of a and b for $m_v^* = 0.0453$

and $\beta_v = 1$ which are the values corresponding to the Γ valley of $InGa_{0.53}As_{0.47}$. Similar trends are found for different m_v^* and β_v values. The result for different m_v^* and β_v does not significantly vary.

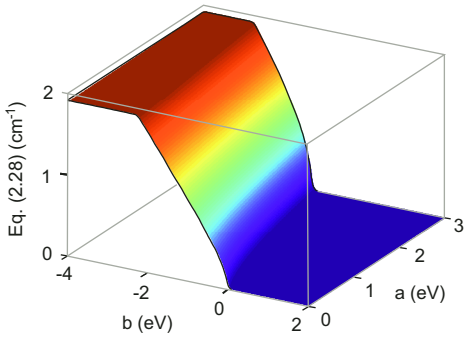

Figure 3.7: Integral of Eq. (3.28) as a function of a and b for $m_v^* = 0.0453$ and $\beta_v = 1$.

3.8 Insulator and interface charges

SP2D considers the presence of fixed insulator charges as well as interface traps. The implementation of fixed charges is straightforward. It merely implies the introduction of a constant (not dependent on ψ) in the insulator Poisson equation. For this reason, in this Section, we will focus just on the implementation of interface traps in the SP2D simulator. If we assume an amphoteric nature for the interface traps, Q_{it} can be related to the density of interface states, D_{it}, as given by [140]:

$$Q_{\text{it}}(x,y) = q \int_{E_v(x,y)}^{E_i(x,y)} D_{\text{it}}^{\text{d}}(E)[1 - f(E)]dE - q \int_{E_i(x,y)}^{E_c(x,y)} D_{\text{it}}^{\text{a}}(E) f(E) dE \tag{3.29}$$

where $x, y \in \mathcal{C}_{\text{s-i}}$, and the superscript a (d) refers to acceptor (donor) kind of traps. In Eq. (3.29) we have explicitly assumed that the energies associated to the interface traps are present only in the band gap of the semiconductor. Nevertheless, SP2D allows an arbitrary range of energies for the traps as well as arbitrary D_{it} profiles, including both: experimental profiles, such as [102], [141] or [142], and analytical profiles.

Using the energy reference system proposed in Section 3.4, Eq (3.29) can be rewrit-

ten as:

$$Q_{\mathrm{it}}(x,y) = q \int_{-q\psi(x,y)-E_{\mathbf{g}}}^{-q\psi(x,y)-E_{\mathrm{g}}/2} D_{\mathrm{it}}^{\mathrm{d}}(E)[1-f(E)]dE - q \int_{-q\psi(x,y)-E_{\mathrm{g}/2}}^{-q\psi(x,y)} D_{\mathrm{it}}^{\mathrm{a}}(E)f(E)dE \tag{3.30}$$

where it should be kept in mind that $x, y \in \mathcal{C}_{\text{s-i}}$.

Mathematically the interface traps have been commonly treated as a boundary condition to the Poisson equation (affecting to the continuity of the dielectric flux). This mathematical treatment implies that Q_{it} is located at a sheet of infinitesimal thickness at the insulator-semiconductor interface. However, Q_{it} is actually distributed in a thin region of the insulator near to the semiconductor interface. For micrometric devices, t_{ins} was several order of magnitude thicker than the Q_{it} distribution region, and the infinitesimal sheet approximation was appropriate. Nevertheless, the device scaling has leaded to thinner t_{ins} (actually of the order of the Q_{it} distribution region) questioning the infinitesimal sheet approximation. Indeed, the vision of Q_{it} as a spatially distributed charge (for nanometric devices) has been assessed by several studies in the literature [143][144].

In agreement with this point of view, SP2D deals with Q_{it} as a volumetric charge distributed along the insulator. Although some studies have provided experimental spatial distribution profiles for Q_{it} [144], there is still not conclusive knowledge about it. For this reason, we have considered in SP2D to four different kinds of spatial distributions: constant, linear, exponential and Gaussian.

The implementation of Q_{it} as a volumetric charge has one drawback: most of the literature published studies provide just D_{it} energy profiles [102], [141], [145], [142]. From D_{it} it is easy to determine the corresponding surface Q_{it} as in Eq. (3.29). However, we need to establish a correspondence between the surface Q_{it} and the volumetric Q_{it}. To do it, the Gauss law is used, so that we can write:

$$\psi|_{\text{i-m}} - \psi|_{\text{i-s}} = \frac{Q_{\mathrm{it,sf}}}{C_{\mathrm{ins,sf}}} \tag{3.31}$$

where $\psi|_{\text{i-m}} = \psi(x,y)|_{x,y\,\in\,\mathcal{C}_{\text{m-i}}}$ and $\psi|_{\text{i-s}} = \psi(x,y)|_{x,y\,\in\,\mathcal{C}_{\text{i-s}}}$ denote potentials at the metal-insulator interface, and at the semiconductor-insulator interface respectively, and we have used the subscript $_{\mathrm{sf}}$ to denote Q_{it} and C_{ins} per unit surface. In Eq. (3.31) one assumption is implicit: $\mathcal{C}_{\text{m-i}}$ and $\mathcal{C}_{\text{s-i}}$ are equipotential paths. This assumption,

which can be appropriate for rotationally symmetric devices, is not valid for $\mathcal{C}_{\text{s-i}}$ when complex MuG geometries are considered. A division of the insulator geometry into several regions $\mathcal{R}_i$, such as $\psi(x,y)|_{x,y\,\in\,\mathcal{C}_{\text{m-i}}\cap\mathcal{R}_i}$ and $\psi(x,y)|_{x,y\,\in\,\mathcal{C}_{\text{s-i}}\cap\mathcal{R}_i}$ (and thus $Q_{\text{it,sf}}$) can be assumed as constants, is required to apply Eq. (3.31). Fig. 3.8 shows a detail of the gate insulator of a Trigate device (with rounded corners) divided into several regions $\mathcal{R}_i$. A detail of two arbitrary regions is also plotted.

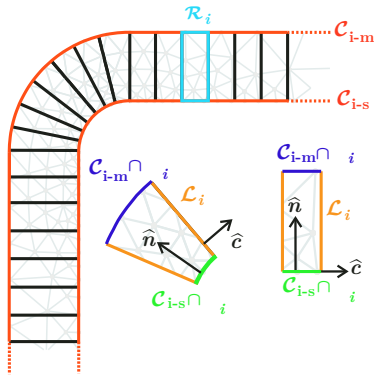

Figure 3.8: Detail of the gate insulator of a Trigate geometry (with rounded corners) divided into several regions $\mathcal{R}_i$. Curved and straight regions are also plotted specifying the region's contours and the vectors $\hat{n}$ perpendicular to $\mathcal{C}_{\text{s-i}}$ and $\hat{c}$ perpendicular to $\mathcal{L}_i$

The use of Eq. (3.31) for each $\mathcal{R}_i$ implies an extra condition: the electric flux trough $\mathcal{R}_i$ lateral boundaries, labeled as $\mathcal{L}_i$ in Fig. 3.8, must be negligible. Otherwise, Gauss law will not result into Eq. (3.31). This condition can be expressed mathematically as:

$$\hat{n}\cdot\nabla\psi|_{\mathcal{R}_i\cap[\mathcal{C}_{\text{s-i}}\cup\mathcal{C}_{\text{m-i}}]} \gg \hat{c}\cdot\nabla\psi|_{\mathcal{L}_i} \tag{3.32}$$

being $\hat{n}$ the unit vector normal to the interface path and $\hat{c}$ the unit vector normal to $\mathcal{L}_i$.

In the limit of region thicknesses approaching to zero, each region $\mathcal{R}_i$ can be reduced to a line perpendicular to the semiconductor-insulator interface, and both assumptions:

(a) $\psi(x,y)|_{x,y\,\in\,\mathcal{C}_{\text{m-i}}\cap\mathcal{R}_i}$ and $\psi(x,y)|_{x,y\,\in\,\mathcal{C}_{\text{s-i}}\cap\mathcal{R}_i}$ are constants, and

(b) that given by Eq. (3.32)

will be satisfied, as:

(a) $\mathcal{C}_{\text{m-i}} \cap \mathcal{R}_i$ and $\mathcal{C}_{\text{s-i}} \cap \mathcal{R}_i$ are reduced to points and ψ is a single-valued function, and

(b) ψ is only defined for the coordinate in the $\hat{n}$ direction, and its derivative in the $\hat{c}$ direction must be zero.

However, for a numerical solution using FEM the regions cannot be infinitesimally thin and finite thickness regions must be defined as SP2D does. Finally, it is worth to note that $C_{\text{ins,sf}}$ in Eq. (3.31) comes from the path integral of the electric field and, therefore, depends on the region considered.

After discussing the conditions of validity of Eq. (3.31), we now use the Poisson equation to determine the difference $\psi|_{\text{i-m}} - \psi|_{\text{i-s}}$ at each $\mathcal{R}_i$ as a function of the volumetric interface charge, $Q_{\text{it,vl}}$. But to be able to get this relationship, we make first the following premise for a given $\mathcal{R}_i$:

$$\nabla_{\parallel}\psi = 0 \tag{3.33}$$

where $\nabla_{\parallel} = \hat{c} \cdot \nabla$. In other words, ψ just varies (in each region) in the $\hat{n}$ direction. This premise is coherent and actually stronger than the one imposed in Eq. (3.32) and it forces (through Poisson equation):

$$\nabla_{\parallel}Q_{\text{it,vl}} = 0 \tag{3.34}$$

Thus, the differential form of Gauss law for a certain region $\mathcal{R}_i$ leads to:

$$\nabla_{\perp}\epsilon_{\text{ins}}\nabla_{\perp}\psi = -Q_{\text{it,vl}} \tag{3.35}$$

being $\nabla_{\perp} = \hat{n} \cdot \nabla$. It is worth to note that $\nabla_{\perp}$ and $\nabla_{\parallel}$ have been defined as scalar operators. Moreover, as shown in Fig. 3.8, $\hat{n}$ cannot be equally treated in regions where $\mathcal{C}_{\text{s-i}} \cap \mathcal{R}_i$ is a straight segment and those where it is a curved segment. In the first case it is not position dependent while in the second case it is. The mathematical procedure to integrate Eq. (3.35) is detailed in Appendix A. The results are:

$$\psi|_{\text{i-m}} - \psi|_{\text{i-s}} = \frac{1}{\epsilon_{\text{ins}}} \int_0^{t_{\text{ins}}} d\vartheta \int_{\vartheta}^{t_{\text{ins}}} Q_{\text{it,vl}}(\hat{\vartheta}) d\hat{\vartheta} \tag{3.36}$$

for straight segments and

$$\psi|_{\text{i-m}} - \psi|_{\text{i-s}} = \frac{1}{\epsilon_{\text{ins}}} \int_{\varsigma_c}^{\varsigma_c + t_{\text{ins}}} \frac{1}{\varsigma} d\varsigma \int_{\varsigma}^{\varsigma_c + t_{\text{ins}}} \hat{\varsigma} Q_{\text{it,vl}}(\hat{\varsigma}) d\hat{\varsigma} \tag{3.37}$$

for curved segments, where ς_c is the radius of the curved segment (SP2D actually implements curved segments as sections of circumference). Then, using Eq. (3.31), the relationship between $Q_{\text{it,sf}}$ and $Q_{\text{it,vl}}$ is given by:

$$Q_{\text{it,sf}} \frac{t_{\text{ins}}}{\epsilon_{\text{ins}}} = \frac{1}{\epsilon_{\text{ins}}} \int_{0}^{t_{\text{ins}}} d\vartheta \int_{\vartheta}^{t_{\text{ins}}} Q_{\text{it,vl}}(\hat{\vartheta}) d\hat{\vartheta} \tag{3.38}$$

and:

$$Q_{\text{it,sf}} \frac{\varsigma_c \ln(1 + t_{\text{ins}}/\varsigma_c)}{\epsilon_{\text{ins}}} = \frac{1}{\epsilon_{\text{ins}}} \int_{\varsigma_c}^{\varsigma_c + t_{\text{ins}}} \frac{1}{\varsigma} d\varsigma \int_{\varsigma}^{\varsigma_c + t_{\text{ins}}} \hat{\varsigma} Q_{\text{it,vl}}(\hat{\varsigma}) d\hat{\varsigma} \tag{3.39}$$

for straight and curved segments, respectively. These integral equations are underdetermined: there is not a unique expression of $Q_{\text{it,vl}}$ for a given value of $Q_{\text{it,sf}}$.

As aforementioned, SP2D implements four different $Q_{\text{it,vl}}$ profiles: constant, linear, exponential and Gaussian. The four profiles are defined in a region of thickness t_o, being $t_o \leq t_{\text{ins}}$, and their amplitude is determined by $Q_{\text{it,sf}}$. The expressions for the $Q_{\text{it,vl}}$ profiles, corresponding to linear and curved segment regions are summarized in Table 3.1.

Profile	Straight	Curved
Constant	$Q_{\text{it,vl}}(\vartheta) = A_{\text{cte}} U_{\text{st}}(\vartheta)$	$Q_{\text{it,vl}}(\varsigma) = A_{\text{cte}} U_{\text{cv}}(\varsigma)$
Linear	$Q_{\text{it,vl}}(\vartheta) = A_{\text{lin}} \left(1 - \frac{\vartheta}{t_o}\right) U_{\text{st}}(\vartheta)$	$Q_{\text{it,vl}}(\varsigma) = A_{\text{lin}} \left(1 - \frac{\varsigma - \varsigma_c}{t_o}\right) U_{\text{cv}}(\varsigma)$
Exponential	$Q_{\text{it,vl}}(\vartheta) = A_{\text{exp}} e^{-\frac{\vartheta}{\sigma_e}} U_{\text{st}}(\vartheta)$	$Q_{\text{it,vl}}(\varsigma) = A_{\text{exp}} e^{-\frac{\varsigma - R_c}{\sigma_e}} U_{\text{cv}}(\varsigma)$
Gaussian	$Q_{\text{it,vl}}(\vartheta) = A_{\text{gau}} e^{-\frac{\vartheta^2}{2\sigma_g^2}} U_{\text{st}}(\vartheta)$	$Q_{\text{it,vl}}(\varsigma) = A_{\text{gau}} e^{-\frac{(\varsigma - \varsigma_c)^2}{2\sigma_g^2}} U_{\text{cv}}(\varsigma)$

Table 3.1: $Q_{\text{it,vl}}$ profiles implemented by SP2D.

where $U_{\rm st}(\vartheta) = [U(\vartheta) - U(\vartheta - t_{\rm o})]$ and $U_{\rm cv}(\varsigma) = [U(\varsigma - \varsigma_{\rm c}) - U(\varsigma - (\varsigma_{\rm c} + t_{\rm o}))]$ and U is the step function. The values of $\sigma_{\rm e}$ and $\sigma_{\rm g}$ for straight segment regions are calculated to yield $Q_{\rm it,vl}(\sigma_{\rm e}) = 10^{-4} Q_{\rm it,vl}(0)$ and $Q_{\rm it,vl}(\sigma_{\rm g}) = 10^{-4} Q_{\rm it,vl}(0)$, respectively. Equivalently for curved segments regions, $\sigma_{\rm e}$ and $\sigma_{\rm g}$ are obtained imposing $Q_{\rm it,vl}(\sigma_{\rm e}) = 10^{-4} Q_{\rm it,vl}(\varsigma_{\rm c})$ and $Q_{\rm it,vl}(\sigma_{\rm g}) = 10^{-4} Q_{\rm it,vl}(\varsigma_{\rm c})$, respectively. Finally, the values of $A_{\rm cte}$, $A_{\rm lin}$, $A_{\rm exp}$, and $A_{\rm gau}$ are determined substituting the corresponding expression of $Q_{\rm it,vl}$ in Eqs. (3.38) and (3.39). The integration procedure is, in most cases, straightforward and the results are summarized in Tables A.1 and A.2 in Appendix A for straight and curved segments.

Fig. 3.9 shows the different $Q_{\rm it,vl}$ profiles implemented by SP2D: (a) constant, (b) linear (c) exponential and (d) Gaussian.

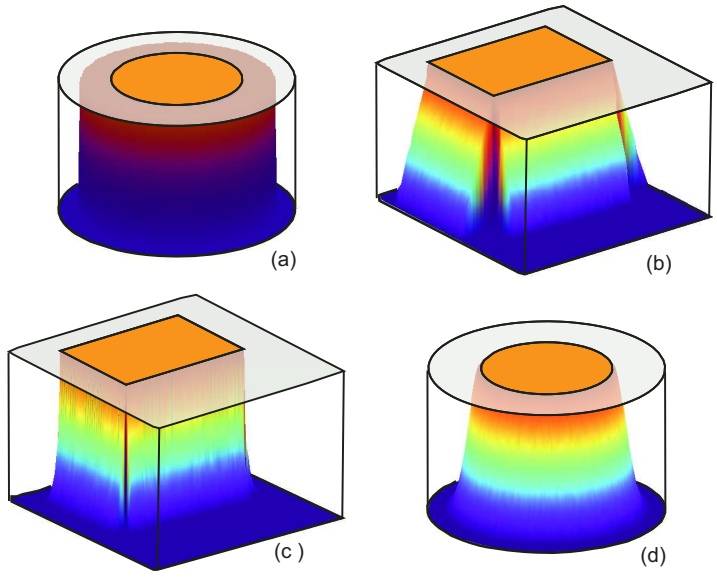

Figure 3.9: $Q_{\rm it,vl}$ profiles implemented by SP2D: (a) constant, (b) linear (c) exponential and (d) Gaussian. An schematic depiction of the device geometries is superimposed to the $Q_{\rm it,vl}$ profiles, where the semiconductor is plotted as orange and the insulator is plotted as semitransparent gray

To illustrate the versatility of the implementation, different geometries corresponding to a NW (a) and (d), and a Trigate device (b) and (c), are considered in Fig 3.9. A schematic depiction of the geometries is superimposed to the $Q_{\rm it,vl}$ profiles, where the semiconductor is plotted as orange and the insulator is plotted as semitransparent gray. In Fig. 3.9(a) $t_{\rm o} = t_{\rm ins}/2$ was assumed, while for 3.9(b), (c) and (d) $t_{\rm o} = t_{\rm ins}$

was set. To keep the figure simple, we have assumed a constant potential along the insulator-semiconductor interface and the same D_{it} energy profile for all regions.

3.9 Convergence algorithm

The wavefunctions, ξ_i, and energy levels, E_i obtained from Schrödinger equation determine the electron concentration, n. But n enters in the Poisson equation. Then, the Poisson solution for the potential, ψ, is translated into potential energy $\phi = -q\psi$ (where the potential barrier $\Delta\phi$ must be added in the insulator). ϕ is part of the Hamiltonian of the Schrödinger equation and affects the resulting eigenfunctions, ξ_i, and eigenvalues, E_i.

Thus, the equation system must be solved self-consistently. However, a simple iteration rarely converges. One common alternative scheme is underrelaxing the solution for the electron concentration. Then, for each iteration n is expressed as $n^{(j)} = \upsilon^{(j)} n^{(j)} + (1 - \upsilon^{(j)}) n^{(j-1)}$, where $^{(j)}$ is the iteration index and υ is an adaptive relaxation parameter [107]. However, the election of υ, which is iteration dependent, is not easy. A large $\upsilon^{(j)}$ results in oscillations while small $\upsilon^{(j)}$ slows the convergence [146]. This problem was solved in a very elegant and illustrative way by Trellakis *et al.* in Refs. [147],[148]. They used perturbation theory to determine the electron concentration when a perturbing potential energy was introduced in the Hamiltonian. Using a suitable approximation for a ratio of Fermi integrals, they found that the electron concentration in the j-th iteration could be expressed as:

$$n(x,y) = \frac{-qN_{\mathrm{c}}}{k_{\mathrm{B}}T} \sum_i |\xi_i(x,y)|^2 \mathcal{F}_{-\frac{1}{2}} \left(\frac{E_i - E_{\mathrm{F}} + \phi^{(j)-\phi^{(j-1)}}}{k_{\mathrm{B}}T} \right) \tag{3.40}$$

where N_{c} is the density of states of the conduction band:

$$N_{\mathrm{c}} = \sqrt{\frac{2m_v^* k_{\mathrm{B}} T}{\pi\hbar^2}} \tag{3.41}$$

and $\mathcal{F}_{-\frac{1}{2}}$ is the complete Fermi-Dirac integral [149], [150]. Eq. (3.40) assumes a parabolic dispersion relation for the conduction band.

We need to adapt this algorithm for the non-parabolic dispersion relation of Eq (3.21). Trellakis' approach to the problem defines a perturbation to the potential $\delta\psi$ such that $\psi \to \psi + \delta\psi$. The Hamiltonian became $H \to H - q\delta\psi$ while the energy

levels and wavefunctions change to $E_i \rightarrow E_i + \delta E_i$ and $\xi \rightarrow \xi + \delta\xi$, respectively; where $\delta E_i = -q\langle \xi_i | \delta\psi | \xi_i \rangle$.

For the non-parabolic case we have:

$$E_i^{\mathrm{NP}} = \phi_i + \delta\phi_i + \frac{-1 + \sqrt{1 + 4\beta_v \left(\frac{\hbar^2 k^2}{2m_v^*} + E_i + \delta E_i - \phi_i - \delta\phi_i \right)^2}}{2\beta_v} \tag{3.42}$$

where using Eq. (3.23) it is straightforward to see that $\delta\phi_i = -q\langle \xi_i | \delta\psi | \xi_i \rangle$ canceling out with δE_i as defined previously. Then, comparing Eqs. (3.21) and (3.42), we can conclude that the non-parabolic dispersion relation is transformed by the perturbation as:

$$E_i^{\mathrm{NP}} \rightarrow E_i^{\mathrm{NP}} + \delta\phi_i \rightarrow E_i^{\mathrm{NP}} + \delta E_i \tag{3.43}$$

The determination of the variation in the electron concentration, δn, due to the perturbation potential $\delta\phi$ is equivalent to that proposed in Ref. [147]. We replicate here only the first step from Trellakis mathematical elaboration to show the equivalence:

$$n \rightarrow n + \delta n \tag{3.44}$$

where δn is obtained as:

$$\delta n = \frac{\partial n}{\partial \psi}\delta\psi = \frac{2}{\pi}\frac{\partial}{\partial \psi}\sum_i |\xi_i(x,y)|^2 \int_{-\infty}^{\infty} \frac{1}{1 + e^{\frac{E_i(k) - E_{\mathrm{F}}}{k_{\mathrm{B}}T}}} dk \delta\psi = \tag{3.45}$$

$$\frac{2}{\pi}\sum_i |\xi_i(x,y)|^2 \frac{\partial}{\partial E_i(k)} \int_{-\infty}^{\infty} \frac{1}{1 + e^{\frac{E_i(k) - E_{\mathrm{F}}}{k_{\mathrm{B}}T}}} dk \frac{\partial E_i(k)}{\partial \psi}\delta\psi \tag{3.46}$$

$$+\frac{2}{\pi}2\sum_i |\xi_i(x,y)| \frac{\partial \xi_i}{\partial \psi}\delta\psi \int_{-\infty}^{\infty} \frac{1}{1 + e^{\frac{E_i(k) - E_{\mathrm{F}}}{k_{\mathrm{B}}T}}} dk \tag{3.47}$$

where $\frac{\partial E_i(k)}{\partial \psi}\delta\psi$ and $\frac{\partial \xi_i}{\partial \psi}\delta\psi$ are the perturbation in the non-parabolic dispersion relation and the wavefunction due to the perturbation in the potential $\delta\psi$, respectively. We can rename them as δE_i^{NP} and $\delta\xi_i$. But δE_i^{NP} was determined in Eq. (3.43) as equal to the

perturbation of the parabolic energy level δE_i. Then:

$$\delta n = \frac{2}{\pi}\sum_i |\xi_i(x,y)|^2 \int_{-\infty}^{\infty} \frac{-1}{k_\mathrm{B}T} \frac{e^{\frac{E_i(k)-E_\mathrm{F}}{k_\mathrm{B}T}}}{\left(1+e^{\frac{E_i(k)-E_\mathrm{F}}{k_\mathrm{B}T}}\right)^2} dk\ \delta E_i + \tag{3.48}$$

$$\frac{2}{\pi} 2 \sum_i |\xi_i(x,y)| \delta\xi_i \int_{-\infty}^{\infty} \frac{1}{1+e^{\frac{E_i(k)-E_\mathrm{F}}{k_\mathrm{B}T}}} dk \tag{3.49}$$

In addition, it is easy to get the equivalence of the derivative given by:

$$\frac{\partial}{\partial E_i(k)} \int_{-\infty}^{\infty} \frac{1}{1+e^{\frac{E_i(k)-E_\mathrm{F}}{k_\mathrm{B}T}}} dk = \int_{-\infty}^{\infty} \frac{-}{1} k_\mathrm{B}T \frac{e^{\frac{E_i(k)-E_\mathrm{F}}{k_\mathrm{B}T}}}{\left(1+e^{\frac{E_i(k)-E_\mathrm{F}}{k_\mathrm{B}T}}\right)^2} dk \tag{3.50}$$

and the derivative of the Fermi Dirac integral particularized for order 0.

$$\frac{\partial}{\partial x} \int_0^{\infty} \frac{1}{1+e^{\epsilon-x}} dx = \int_0^{\infty} \frac{-e^{\epsilon-x}}{(1+e^{\epsilon-x})^2} dx \tag{3.51}$$

If we assume that the approximation made by Trellakis *et al.* for the quotient of Fermi integrals of order $-\frac{1}{2}$ and $-\frac{3}{2}$ is also valid for orders 0 and 1, the procedure to determine δn with a non-parabolic dispersion relation is equivalent to that for parabolic bands. Then, we can reformulate the electron density under non-parabolic approximation using the Trellakis algorithm as:

$$n(x,y) = \frac{2}{\pi}\sum_i |\xi_i(x,y)|^2 \int_{-\infty}^{\infty} \left(1+e^{\frac{E_i(k)+\phi^{(j)}-\phi^{(j-1)}-E_\mathrm{F}}{k_\mathrm{B}T}}\right)^{-1} dk \tag{3.52}$$

In the next Section we depict the flow diagram of SP2D including the adapted Trellakis algorithm.

3.10 SP2D flow diagram

In this Section, we briefly describe the SP2D flow diagram. Fig. 3.10 shows the flow diagram of a common run of SP2D.

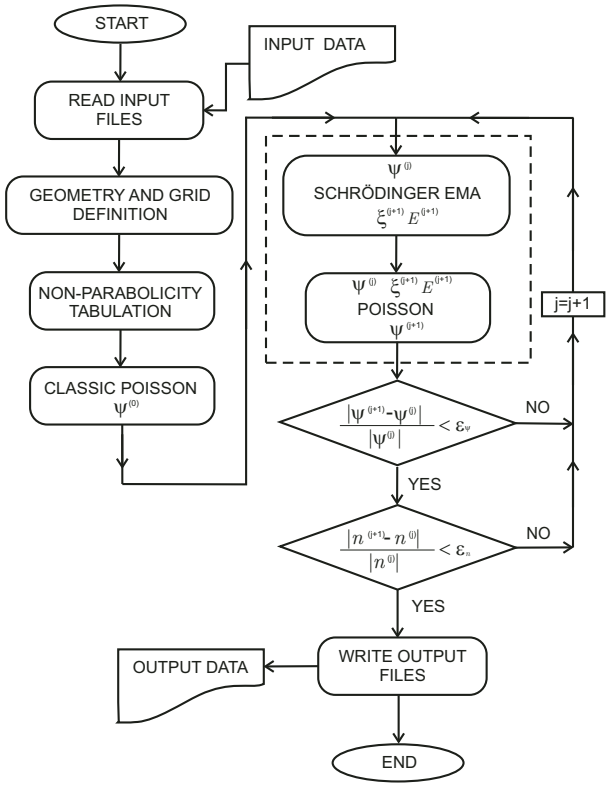

Figure 3.10: Flow diagram of SP2D. The predictor-corrector scheme adapted from Ref. [147] is framed in a dashed line rectangle.

The simulation starts reading several input files which detail: (a) the geometry (device width and height, insulator(s) thickness(es), rounded/squared corners, and all other parameters concerning the geometry description), (b) the materials involved (semiconductor, insulator(s), metal(s)),(c) configuration parameters (kind of device, grid size, range of biasing, device orientation, etc). Using several distinct input files allows us to clearly structure the input information.

From the kind of device and the geometry information, SP2D defines the structure to be simulated, generates the FEM grid, and determines the boundary conditions. Using the material information, the semiconductor and insulator(s) parameters are loaded and the non-parabolic integral is tabulated. Then, the orientation is used to determine the effective mass matrix and expressions for the semiconductor and insulator charge are formulated.

Next step is the self-consistent solutions of the Schrödinger and Poisson equations. A first solution for the potential is obtained using a classical approximation. After that, SP2D enters in the predictor-corrector scheme adapted from Trellakis which for the iteration $^{(j+1)}$ can be summarized as:

(a) Solve the Schrödinger equation using the solution for $\psi^{(j)}$ obtained from previous Poisson iteration ($\psi^{(0)}$ is obtained from a classical simulation). That provides $\xi_i^{(j+1)}$ and $E_i^{(j+1)}$.

(b) Solve the non-linear Poisson equation using $\xi_i^{(j+1)}$, $E_i^{(j+1)}$, $\psi^{(j)}$ into the electron concentration expression given by Eq. (3.52). That gives $\psi^{(j+1)}$.

(c) Check the convergence criteria and come back to step (a) or continua.

Fig. 3.10 frames the predictor-corrector algorithm in dashed line. We use a double convergence criteria: for the potential and the electron concentration. As they are spatial dependent magnitudes we look for the worst case:

$$\frac{\max\left|\psi^{(j)}-\psi^{(j+1)}\right|}{\max\left|\psi^{(j)}\right|}<\varepsilon_{\psi} \tag{3.53}$$

$$\frac{\max\left|n^{(j)}-n^{(j+1)}\right|}{\max\left|n^{(j)}\right|}<\varepsilon_{n} \tag{3.54}$$

where ϵ_ψ and ϵ_n are convergence thresholds set to 10^{-4}. Once the convergence has been achieved, SP2D save all the results calculated in an output file and the run is ended.

3.11 Conclusions

In this Chapter, a self-consistent Schrödinger-Poisson solver was developed, which is able to deal with arbitrary geometries, materials and orientations to achieve the charge and potential distribution in the cross-section of a MuG structure. A non-parabolic effective mass approach was employed for the Schrödinger equation, and the contribution of Γ, X (Δ for Silicon) and L valleys was included. In addition, the developed simulator allowed the inclusion of arbitrary profile of interface states.

Chapter 4

Electrostatic analysis of MuG devices using SP2D

4.1 Introduction

In this chapter we apply SP2D to the study of several relevant electrostatic magnitudes in MuG architectures. Specifically, here we focus on two structures, Trigates and NWs due to their technological performance. The Trigate architecture introduces the fewest changes to conventional planar transistor processing, while allowing a very good control of the channel [151]. Indeed, as aforementioned Intel® has recently taken to production microprocessors based on the Trigate architecture on bulk wafers [60]. Meanwhile, NW FETs, first experimentally achieved by IBM® [79], have demonstrated superior electrostatic control of the channel thanks to their surrounding gate.

In addition to the geometrical versatility of SP2D, we make use of its non-parabolic dispersion relation description to study, besides SOI substrates, III-V materials. Other characteristics of SP2D such as arbitrary orientation and the inclusion of interface states are also exploited in the five electrostatic studies performed in this Chapter.

The rest of this Chapter is organized as follows. In Section 4.2 we compare SP2D results with those obtained from a two-bands $k \cdot p$ simulator and we validate SP2D using experimental data taken from a Trigate architecture. In Section 4.3 we focus on the study of III-V NWs. In particular we analyze the population of satellite valleys of different III-V semiconductors and we briefly discuss their implications on the conduction effective mass and the gate capacitance. In Sections 4.4 and 4.5 a comparative

study of III-V and Si MuG architectures is performed. Thus, Section 4.4 is focused on the performance of III-V and SOI Trigates as a function of the device width while Section 4.5 compares DG and Trigate architectures, emphasizing the need of 2D studies to achieve a proper understanding of Trigate behavior. Sections 4.6 and 4.7 pay attention to SOI Trigate architectures. Section 4.6 deals with the effect of back gate bias on V_{T} and analyze the body effect. In Section 4.7 we analyze the influence of D_{it} on the threshold voltage, V_{T}, and subthreshold swing, SS, of MuG structures. Finally, Section 4.8 sums up some conclusions.

4.2 Validation of SP2D, non-parabolic EMA and semiconductor parameters

In this Section we validate the SP2D simulator presented in Chapter 3 justifying its use in the electrostatic studies proposed in subsequent Sections.

First we check the EMA for the electrons. To do so, the results from SP2D are compared to those obtained from a two-band $k \cdot p$ simulator also implemented in the Nanoelectronics Research Group [152]. Fig 4.1 shows the linear electron concentration, N_{i}, as a function of the applied gate voltage, V_{g}, for several Si-SiO_2 cylindrical NWs (see Fig. 4.2 for a schematic depiction) with sizes ranging from 3nm to 10nm and $t_{\mathrm{ins}} = 1$nm. Two transport orientations have been considered (a) < [111] and (b) [110]. EMA non-parabolic results are plotted as dashed lines while $k \cdot p$ results are plotted as solid lines.

As can be seen in Fig. 4.1, the non-parabolic SP2D accurately reproduces the results for all NWs sizes in both orientations. Only for the smallest size there is slight difference in the results between EMA and $k \cdot p$. This result is in good correspondence with other validations of EMA pointed out in the literature [153]. The non-parabolicity parameter of Si is small, $\beta_{\Delta} = 0.5\mathrm{eV}^{-1}$, and therefore Si does not imply a very disadvantageous scenario for parabolic EMA. For this reason, and in order to keep it clear, we have not plotted parabolic EMA results on Fig. 4.1.

In contrast if III-V semiconductors are considered, the non-parabolic factor is higher and the differences between parabolic and non-parabolic dispersion relation results are larger. Fig. 4.3 presents N_{i} versus V_{g} for (a) InAs and (b) GaAs cylindrical NWs with $R_{\mathrm{s}} = 5$nm (circles) and $R_{\mathrm{s}} = 15$nm (squares) considering parabolic (dashed) and non-parabolic dispersion relations (solid). Al_2O_3 with $t_{\mathrm{ins}} = 2$nm was employed as insulator

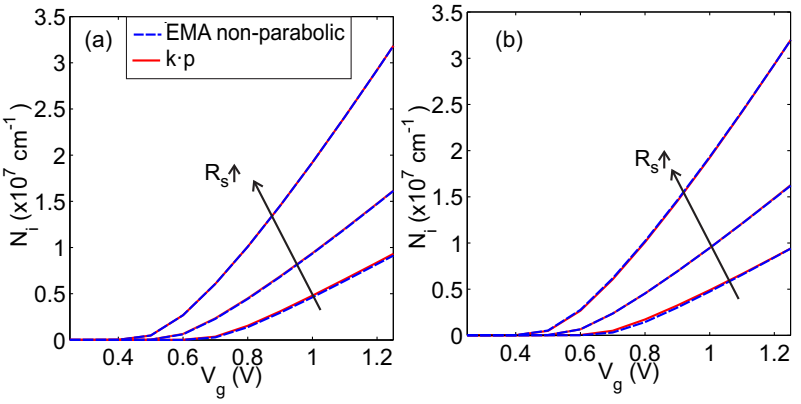

Figure 4.1: Electron concentration, N_{i}, as a function of the gate voltage, V_{g}, for several Si-SiO_2 cylindrical NWs with sizes ranging from 3nm to 10nm and t_{ins} = 1nm, calculated using EMA non-parabolic (dashed) and $k \cdot p$ six band simulations (solid) for (a) [111] and (b) [110] transport orientations.

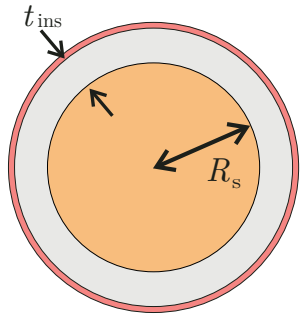

Figure 4.2: Cylindrical NW geometry: R_{s} is the semiconductor radius and t_{ins} is the insulator thickness.

and [100] transport orientation is assumed.

The non-parabolic factors of InAs and GaAs for the different valleys are summarized in Appendix F. As can be observed, the parabolic approach underestimates the electron concentration for both materials. However, the error is larger for InAs than for GaAs, since β_{Γ} for InAs more than doubles its value for GaAs. An extensive comparison between parabolic and non-parabolic electrostatic results of III-V NWs can be found in Ref. [154].

One non-negligible question regarding simulation concerns the selection of an appropriate set of material parameters. There are several references in the literature which have compiled extensive information about III-V semiconductors parameters [92], [155],

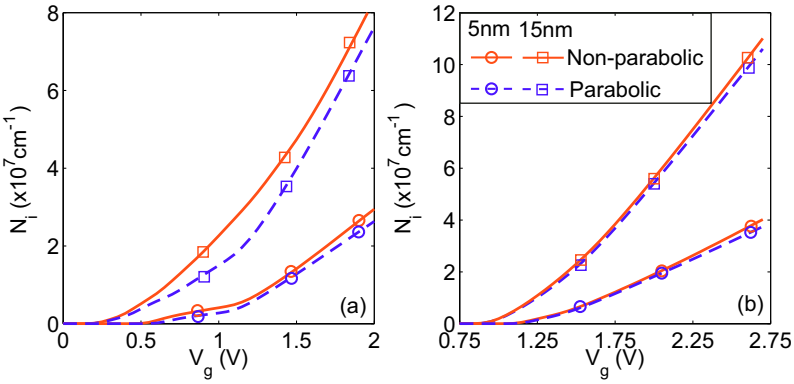

Figure 4.3: N_i, as a function of V_g, for (a) InAs and (b) GaAs NWs with $R_\mathrm{s} = 5$nm (circles) and $R_\mathrm{s} = 15$nm (squares) considering parabolic dispersion relation (dashed) and non-parabolic dispersion relation (solid).

[89], [90]. A brief discussion on their influence on the simulation results becomes necessary. To do it, we have selected, due to their completeness and clarity, two studies by Kim *et al.* [89] and Vurgaftman *et al.* [90]. InGaAs parameters obtained from Refs. [89] and [90] are summarized in Table 4.1.

	[89]	[90]
$E_{\mathrm{g},\Gamma}$ (eV)	0.730	0.830
$E_{\mathrm{g},L}$ (eV)	1.480	1.182
$E_{\mathrm{g},X}$ (eV)	1.980	1.563
m_Γ (m_0)	0.045	0.052
$m_{\mathrm{l},L}$ (m_0)	1.232	1.661
$m_{\mathrm{t},L}$ (m_0)	0.061	0.115
$m_{\mathrm{l},X}$ (m_0)	1.209	4.553
$m_{\mathrm{t},X}$ (m_0)	0.193	0.233
β_Γ (eV)	1	1
β_L (eV)	0.5	0.5
β_X (eV)	0.5	0.5

Table 4.1: $E_{\mathrm{g},v}$, m_v^* and β_v of $In_{0.53}Ga_{0.47}As$ obtained from Refs. [89] and [90].

The main differences in Table 4.1 regard the energy gaps and effective masses of the satellite valleys. These differences result in distinct onsets (due to E_g) and population rates (due to m) of the satellite valleys. Fig. 4.4 shows the gate capacitance C_g, as a

function of the gate voltage, V_g, for the two sets of parameters given in Table 4.1 for InGaAs cylindrical NWs with sizes $2R_s = 5$nm and $2R_s = 15$nm. Al_2O_3 is used as insulator, with $t_{ins} = 2$nm, and standard orientation is assumed.

When the parameters from Ref. [90] are considered, a shoulder is observed near $V_g \approx 0.9$V, for $2R_s = 5$nm; while using the parameters from Ref. [89] the shoulder appears at higher gate voltages ($V_g \approx 1.2$V for $2R_s = 5$nm and $V_g \approx 1.6$V for $2R_s = 15$nm). The position of the shoulder is related to the value of the L-valleys gap, which determines the L-valley population onset.

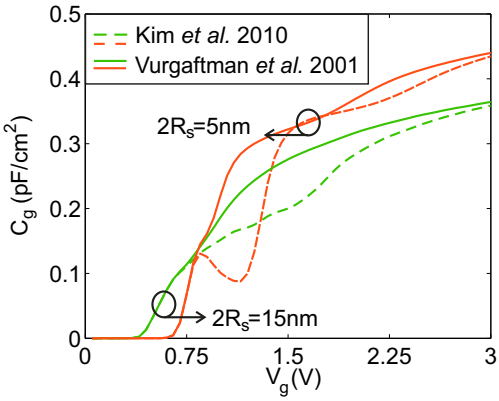

Figure 4.4: C_g as a function of V_g for two InGaAs NW sizes: $2R_s = 5$nm and $2R_s = 15$nm for the set of parameters given in Ref. [89] (dashed lines) and the one given in Ref. [90] (solid lines).

Once the importance of the material parameters in the simulation results is assessed, we have to choose a set of parameters to be considered by SP2D. To do it we have confronted SP2D results with the experimental ones provided by Radosavljevic *et al.* in Ref. [99]. In Fig. 4.5 we present the geometry implemented by SP2D to replicate that shown in Ref. [99]. The semiconductor device width, W_s, and height, H_s, are set to 45nm and 50nm, respectively and a tilt of 80° of the lateral sides is considered, similar to that depicted in Ref. [99]. In order to get the best fit with the experimental results, we have slightly reduced the EOT of the device from 1.2nm to 1.1nm. We use Tantalum silicate ($TaSiO_x$) as gate insulator, with a dielectric constant estimated as $\varepsilon_{ins} = 9\varepsilon_0$, from the EOT and the device geometries provided in Ref. [99]. The potential barrier height between the gate insulator and the semiconductor has been estimated as 1.97eV, following the procedure explained in Section 3.4 and assuming that all the parameters for $TaSiO_x$ can be calculated by a linear interpolation between those corresponding to SiO_2 and Ta_2O_5. As in Ref. [99], the gate penetrates into the

buried oxide, increasing the electrostatic control of the gate on the bottom region of the device.

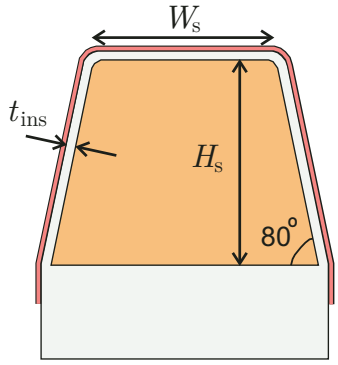

Figure 4.5: Cross-section of the Trigate with the gate penetrating into the buried oxide as in [99]. W_s and H_s are the semiconductor width and height respectively, t_{ins} is the oxide thickness. A tilt of 80° of the lateral sides has been considered.

Fig. 4.6 depicts C_g of the Trigate device as a function of the gate overdrive voltage, $V_{od} = V_g - V_T$ for the experimental results from Ref. [99] (solid line) and the simulations using both the sets of parameters in Table 4.1 from Refs. [89] (dotted line) and [90] (dashed line). For high gate voltages the simulation results for the set of parameters from Vurgaftman *et al* [90] show a hump, due to the occupation of the L valley which can be better appreciated in Fig. 4.7, where the total charge of each kind of valley is depicted versus V_g. The larger gap of the L valleys proposed in Ref. [89] increases the gate voltage range where only the Γ valley contributes to the capacitance and provides results closer to the experimental ones. Thus, hereinafter this set of parameters will be used for simulations of III-V materials in SP2D.

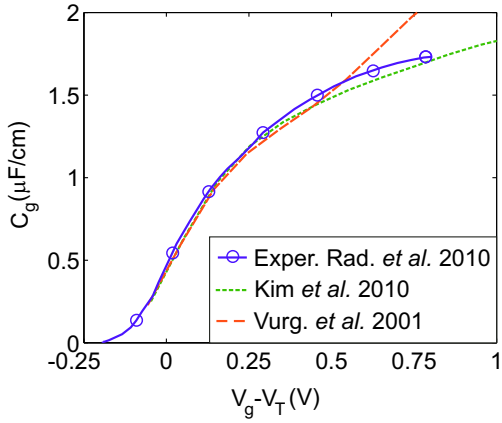

Figure 4.6: C_g versus V_g for the InGaAs Trigate of Fig. 4.5: comparison between experimental results from Ref. [99] (solid line) and simulations using the parameters in Table 4.1 from Ref. [89] (dotted line) and Ref. [90] (dashed line).

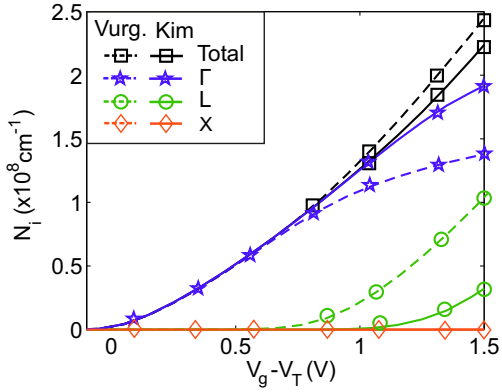

Figure 4.7: N_i of each kind of valley versus $V_g - V_T$ for the InGaAs Trigate of Fig. 4.5. The two sets of parameters shown in Table. 4.1 are used.

4.3 Comparison of III-V cylindrical NWs

In this Section we accomplish a brief study on the population of the Γ, L and X valleys in cylindrical NWs of different III-V materials and sizes. We also discuss its influence on the average conduction effective mass, m^*, and the gate capacitance, C_g. The NW geometries considered in this Section are as the one depicted in Fig. 4.2 and are oriented along the [100] crystallographic direction. Al_2O_3 was used as gate insulator with an insulator thickness $t_{ins} = 2$nm. A metal-gate work function $\Phi_m = 5.05$eV was assumed.

Fig. 4.8 shows the populations of the Γ-valley (dashed), the L-valley (dotted) and the X-valley (dash-dotted) together with the total electron population (solid) as a function of V_g for InAs (left), InGaAs (center) and GaAs (right) NWs of diameters $2R_s = 5$nm (top) and $2R_s = 15$nm (bottom).

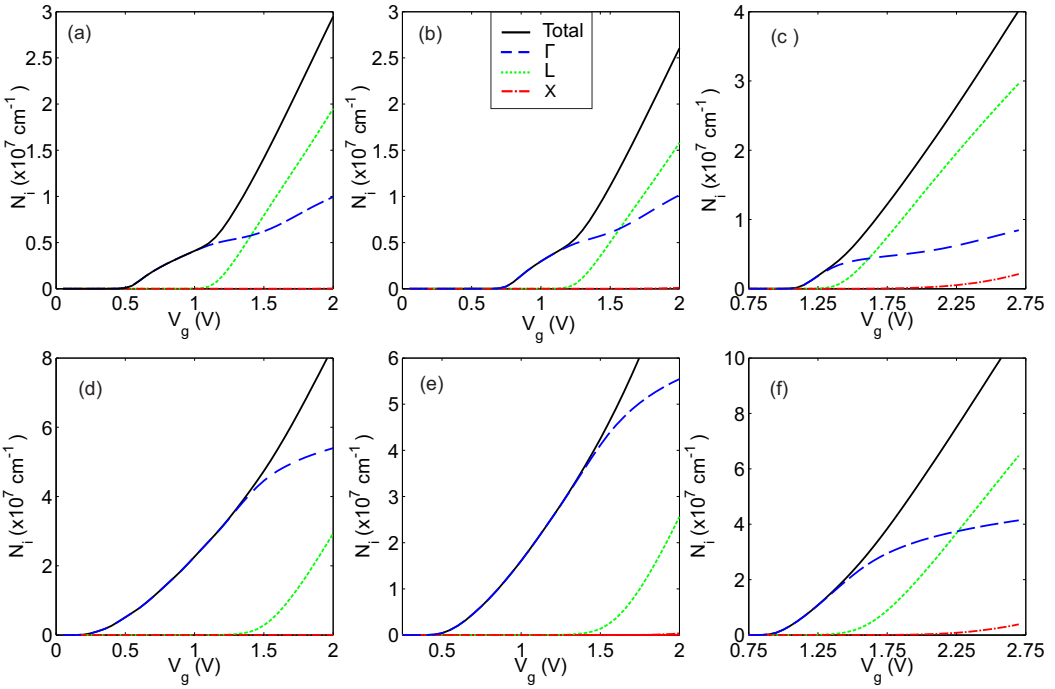

Figure 4.8: N_i of each kind of valley versus V_g for InAs (left) InGaAs (center) and GaAs (right) NWs of sizes $2R_s = 5$nm (top) and $2R_s = 15$nm (bottom). Total, Γ-valley, L-valley and X-valley electron populations are plotted as solid, dashed, dotted and dash-dotted lines respectively.

As can be seen in Fig. 4.8 the X-valley population is not relevant for the voltage

range analyzed, limiting its interest in practical purposes, and therefore it is obliterated in the forthcoming analysis. The main differences between curves for the different materials and sizes regards the valley population onsets. The threshold voltages of the Γ and L valleys, $V_{T,\Gamma}$ and $V_{T,L}$, were obtained from the maximum of the second derivative of the charge associated to each valley [156], and are summarized in Table 4.2. ΔV_T refers to the difference $V_{T,L} - V_{T,\Gamma}$

	$2R_s = 5$nm			$2R_s = 15$nm		
	$V_{T,\Gamma}$ (V)	$V_{T,L}$ (V)	ΔV_T (V)	$V_{T,\Gamma}$ (V)	$V_{T,L}$ (V)	ΔV_T (V)
InAs	0.53	1.14	0.61	0.22	1.51	1.19
InGaAs	0.75	1.24	0.49	0.52	1.58	1.06
GaA	1.12	1.41	0.29	0.94	1.59	0.65

Table 4.2: $V_{T,\Gamma}$ and $V_{T,L}$ (determined using the second derivative of the charge) for InAs, InGaAs and GaAs NWs of sizes $2R_s = 5$nm and $2R_s = 15$nm. ΔV_T refers to the difference $V_{T,L} - V_{T,\Gamma}$

As can be noted in Fig. 4.8 and Table 4.2, InAs devices achieve the highest difference between $V_{T,\Gamma}$ and $V_{T,L}$ for both sizes, due to its larger $E_{g,L} - E_{g,\Gamma}$ separation (see Appendix F). One interesting result concerns the decrease in the $V_{T,L} - V_{T,\Gamma}$ difference, with the device shrinking which is due to both the increase of $V_{T,\Gamma}$ and the decrease of $V_{T,L}$. This contra-intuitive result (for a decrease of device size we would expect an increase of V_T regardless the kind of valley) can be explained attending to the effect of the confinement on the first energy level, E_0, of Γ, $E_{0,\Gamma}$ and L, $E_{0,L}$, valleys. E_0, as is demonstrated in Section 6.5, mainly determines V_T for III-V NWs [156].

Fig. 4.9 shows the position of E_0 (referred to the bottom of the conduction band) in the sub-threshold regime (under flat well approximation) as a function of $2R_s$ and the confinement effective mass, m_v. As can be observed, only for small m_v there is a non-negligible change in the position of E_0 with $2R_s$. The values of m_v for Γ and L valleys for InAs are plotted as dashed lines [1]. From, Fig. 4.9 we would expect no meaningful change in $E_{0,L}$ and therefore $V_{T,L}$ with $2R_s$, but actually $V_{T,L}$ increases with $2R_s$. Therefore, we have to look for the explanation somewhere else.

Fig. 4.10 depicts the dependence of $E_{0,\Gamma}$ (solid) and $E_{0,L}$ (dashed) (referred to E_F which is the reference for energies as proposed in Chapter 3), and the surface potential

[1] An isotropic effective mass for the L valley ($m_L = 0.6m_0$) was considered for illustrative purposes in Fig. 4.9. Nevertheless the appropriate anisotropy of L-valley is taken into consideration by SP2D.

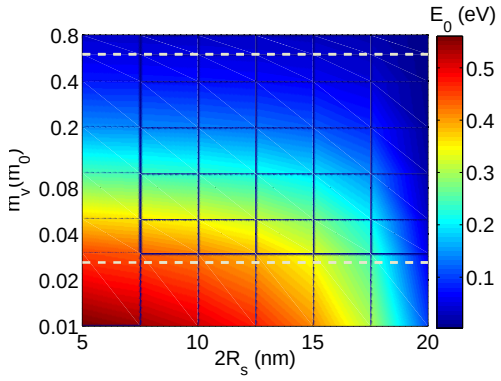

Figure 4.9: E_0 (referred to the bottom of conduction band) for a sub-threshold voltage (under flat well approximation) as a function of $2R_\mathrm{s}$ and m_v. The values of m_v for Γ (0.026) and L (0.6) valleys for InAs are plotted as white dashed lines.

ϕ_s (dash-dotted) as a function of V_g for two InAs NWs with sizes (a) $2R_\mathrm{s} = 5$nm and (b) $2R_\mathrm{s} = 15$nm. The V_g values corresponding to the threshold voltages of the Γ and L valleys are plotted as dotted lines. Two assertions can be done from Fig. 4.10: (a) the value E_0 for which the valley turns on is pretty similar in both sizes (around 0.03eV for the Γ-valley and around 0.075eV for the L-valley)[2]; (b) The dependence of E_0 with V_g is quite different from one size to the other.

The smaller the device, the sharper the decrease of $E_{0,\Gamma}$ and $E_{0,L}$ with V_g in the region between $V_{\mathrm{T},\Gamma}$ and $V_{\mathrm{T},L}$ due to the lower inversion charge and, consequently, potential screening. As the value $E_{0,L}$ for subtreshold regime and valley onset condition does not vary very much for both sizes[3], it is the slope of change of $E_{0,L}$ with V_g which mainly determines $V_\mathrm{T,}$ being V_T higher when the slope is softer (larger devices).

The V_g range between $V_{\mathrm{T},\Gamma}$ and $V_{\mathrm{T},L}$ is of interest because the conduction effective mass coincides with the Γ valley mass, thus providing its well-known beneficial effects on the transport properties (see Chapter 9). As a drawback, in the same V_g range where the higher mobility is expected, the so-called density of states bottleneck appears, limiting the gate capacitance. Fig. 4.11 shows C_g as a function of V_g for InAs (left), InGaAs (center) and GaAs (right) and different NW sizes: $2R_\mathrm{s} = 5$nm (solid) and $2R_\mathrm{s} = 15$nm

[2]Exact values are $E_{0,\Gamma} = 0.0371$eV and $E_{0,\Gamma} = 0.0292$eV for $2R_\mathrm{s} = 5$nm and 15nm and $E_{0,L} = 0.0828$eV and $E_{0,L} = 0.0675$eV for $2R_\mathrm{s} = 5$nm and 15nm.

[3]Some differences regarding the results from Fig. 4.9 are observed as here the anisotropy of the L-valley is taken into consideration

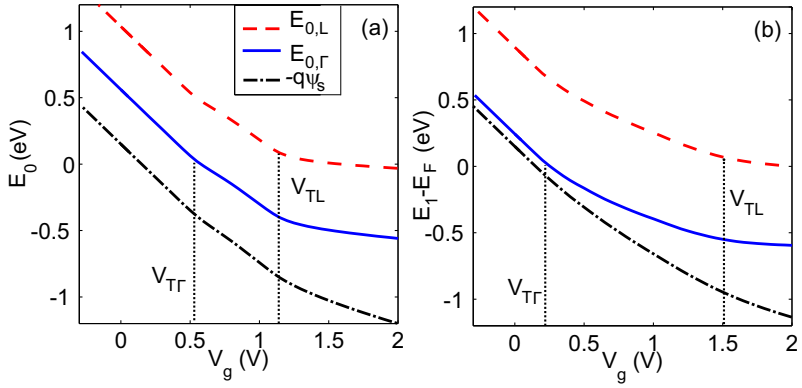

Figure 4.10: $E_{0,\Gamma}$ (solid) and $E_{0,L}$ (dashed) and the surface potential ψ_s (dash-dotted) as a function of $V_{\rm g}$ for two InAs NWs with sizes (a) $2R_{\rm s} = 5$nm and (b) $2R_{\rm s} = 15$nm. The $V_{\rm g}$ values corresponding to the threshold voltages of the Γ and L are plotted as dotted lines.

(dashed). As can be observed, in the range between $V_{\rm T,\Gamma}$ and $V_{\rm T,L}$ (see Table 4.2) the gate capacitance is degraded, showing oscillations in the transition between off and on states, and actually it only increases to acceptable values when L valleys get populated. It is for GaAs, with smaller $V_{\rm T,L}$-$V_{\rm T,\Gamma}$, that $C_{\rm g}-V_{\rm g}$ curves increases more sharply giving a better $C_{\rm g}$ behavior.

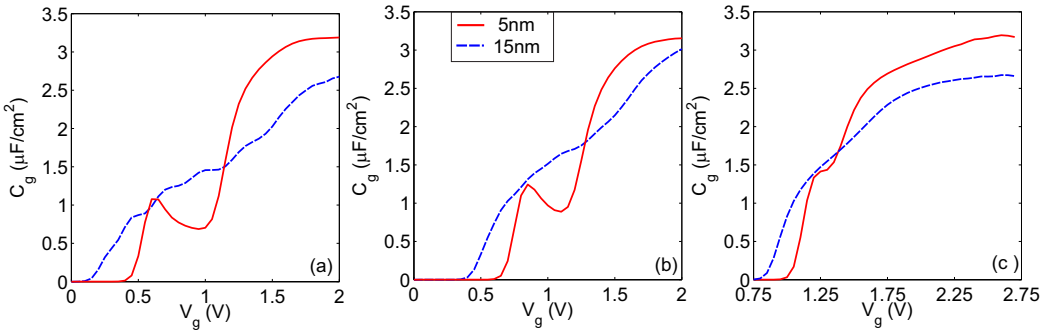

Figure 4.11: $C_{\rm g}$ versus $V_{\rm g}$ for (a) InAs, (b) InGaAs and (c) GaAs NWs of size $2R_{\rm s} = 5$nm (solid), and $2R_{\rm s} = 15$nm (dashed).

4.4 Comparison of Si and III-V Trigate MOSFETs

In this Section, guided by the good results obtained in the SP2D validation done in Section 4.2 for an InGaAs Trigate, we study the behavior of InGaAs, InGaSb and SOI Trigate FETs, as a function of the channel width, W_s. InGaSb has not been deeply studied in the literature for electron as majority carriers [157]. The inclusion in this comparison obeys to the technological expectations placed on it as a good alternative to Si in CMOS processes [157]. In addition to its well known hole mobility, InGaSb is characterized by a low Γ-valley effective mass, which can be controlled through the In molar fraction. On the contrary, the energy gap separation between Γ and L valleys is small for this material (see Appendix F) affecting negatively to the its potential high electron mobility.

Fig. 4.12 shows the Trigate geometry considered in this Section. H_s is the semiconductor channel height while t_{ins} and t_{box} are the gate and buried insulator thicknesses, respectively. All III-V semiconductors parameters are taken from Ref. [89] and summarized in Appendix F. For the sake of simplicity in the interpretation of the results, no tilt of the lateral sides of the Trigate is considered. The same, equivalent oxide thickness, EOT will be used for all devices, with SiO_2 as the gate insulator for the Si Trigates and $TaSiO_x$ for the InGaAs and InGaSb ones. The material parameters of $TaSiO_x$ are those used in Section 4.2.

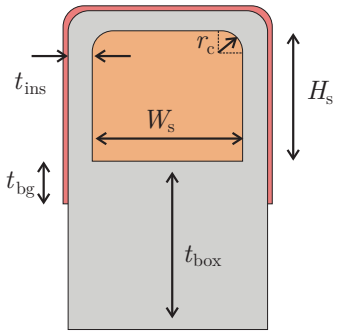

Figure 4.12: Trigate geometry. The channel size is $W_s \times H_s$. t_{ins} and t_{box} are the gate and buried insulator thickness, respectively. Following the experimental geometry from Ref. [99] the gate is extended along the buried insulator.

Fig. 4.13 compares the gate capacitance per unit area, $C_{g,sf}$ (which allows a fair comparison between sizes) as a function of V_g for InGaAs (solid), InGaSb (dotted) and

Si (dashed) Trigate devices. Several semiconductor widths, W_s, from 5nm to 30nm, are considered. The semiconductor height is kept constant to $H_s = 50$nm. As can be seen, the curves achieved for Si devices are very close and only for very small devices slight variations are found. However, W_s has a stronger impact on structures made of III-V alloys. Two main conclusions related to W_s can be deduced from these results:

(a) The threshold voltage variations associated to the higher quantization of narrower devices are more noticeable in InGaAs and InGaSb than in Si Trigates, due to the smaller effective masses of the InGaAs and InGaSb Γ valley. Fig. 4.14(a) shows the increment in the threshold voltage, ΔV_T, as the device width is reduced from 30nm to 5nm for Si (circles), InGaAs (squares) and InGaSb (diamonds) devices. The observed ΔV_T in InGaAs and InGaSb is three times higher than in Si for $W_s = 5$nm.

(b) At large V_g values an increase of C_g is found when the device dimensions are shrunk for InGaAs and InGaSb Trigates. This effect appears when satellite valleys get populated, primarily because the gate voltage at which the L valleys begin to be populated is reduced with the device width, as can be seen in Fig. 4.14(b). The effect is more clearly observed in InGaSb devices which have a lower L valley threshold voltages.

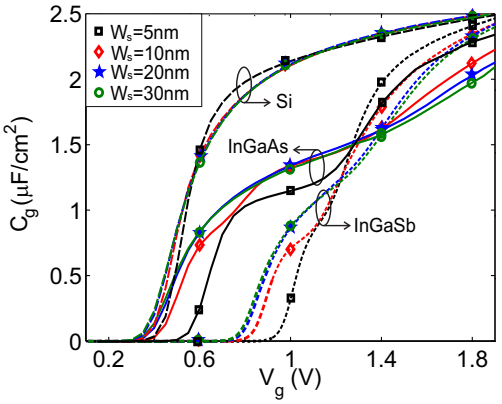

Figure 4.13: $C_{g,sf}$ versus V_g of InGaAs (solid), InGaSb (dotted), and Si (dashed) Trigate MOSFETs with $H_s = 50$nm and W_s ranging from 5nm to 30nm.

As also shown in Fig. 4.13, higher values for C_g are achieved for Si Trigates compared to III-V materials, in agreement with the results presented in the literature for

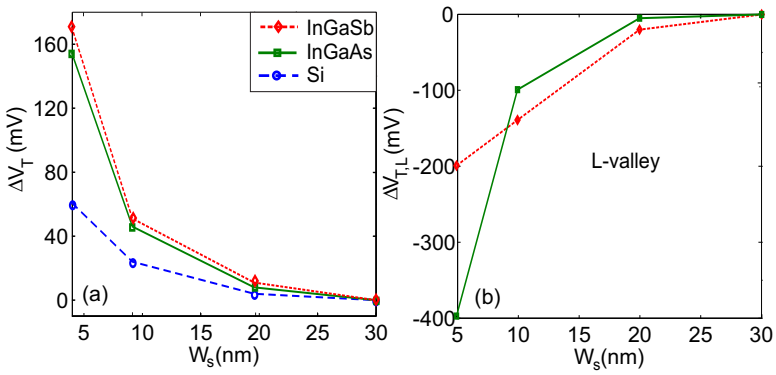

Figure 4.14: (a) ΔV_{T} of the Γ valley as a function of W_{s} for InGaAs (solid lines), InGaSb (dotted lines) and of Δ-valley for Si (b) ΔV_{T} of the L valley as a function of W_{s} for InGaAs (solid lines), InGaSb (dotted lines). $H_{\mathrm{s}} = 50$nm and W_{s} ranging from 5nm to 30nm.

both planar devices [158] and NWs [159]. The capacitance degradation for InGaAs and InGaSb devices is due to: 1) their larger inversion layer centroid [160], and 2) the density of states bottleneck [66]. Both effects are related to the reduced confinement effective mass of these materials.

Figs. 4.15 and 4.16 show the 2D charge distributions for InGaAs, InGaSb and Si Trigates (10nm×30nm only) and some horizontal slices of the charge distribution in the center of the devices, respectively.

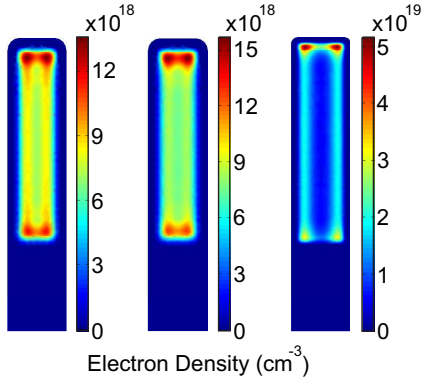

Figure 4.15: n (cm^{-3}) simulated at $V_{\mathrm{g}} - V_{\mathrm{T}} = 0.5$V for InGaAs (left) InGaSb (center) and Si (right) Trigate MOSFETs with $W_{\mathrm{s}} = 10$nm and $H_{\mathrm{s}} = 50$nm.

As can be seen in Fig. 4.15, the electron distribution for the Si, InGaAs and InGaSb

Trigates is not uniform. The increase of the electrostatic control in the regions close to the top gate and also to the bottom buried gate (especially near the corners) results in an enhancement of the charge density in those regions. The impact of this contribution should not be neglected for a correct modeling of Trigate geometries (see Section 4.5).

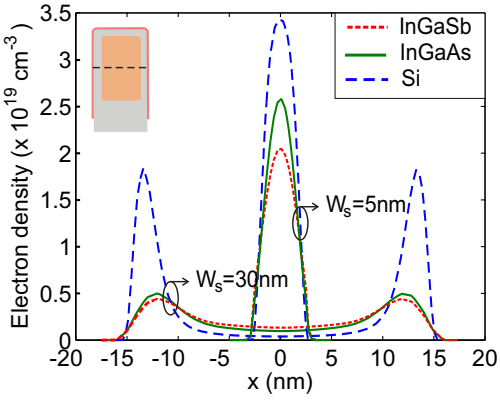

Figure 4.16: Slice of the electron density (cm^{-3}) at the center of the device (see inset), at $V_g = 1.2V$, for InGaAs (solid), InGaSb (dotted) and Si (dashed) Trigate MOSFETs with $H_s = 50nm$. Two different semiconductor widths are considered: $W_s = 5nm$ and $W_s = 30nm$.

In Fig. 4.16 the larger separation between the inversion charge and the semiconductor-insulator interface in InGaAs and InGaSb devices with respect to Si one is clearly depicted for $W_s = 30nm$. For $W_s = 5nm$ the spatial confinement is strong enough to obscure the influence of m_v^* on the charge distribution. The degradation of C_g in InGaAs and InGaSb for this size is therefore due to the density of states bottleneck.

4.5 Trigate versus DG comparison

To get a deeper understanding of the Trigate behavior, in this Section we have made a comparative study of Trigates and Double Gate (DG) FETs with similar sizes. The same kind of Trigates studied in Section 4.4 are considered (see Fig. 4.5). The electron density of the DG MOSFETs is calculated as the charge of a slice at the center of the Trigate (similar to the curves shown in Fig. 4.16), multiplied by the device height to account for the whole DG device charge.

Fig. 4.17 shows the electron density per unit length (N_i) achieved for 50nm height Trigates and the values obtained when DG devices are considered. W_s from 5nm to

30nm are simulated.

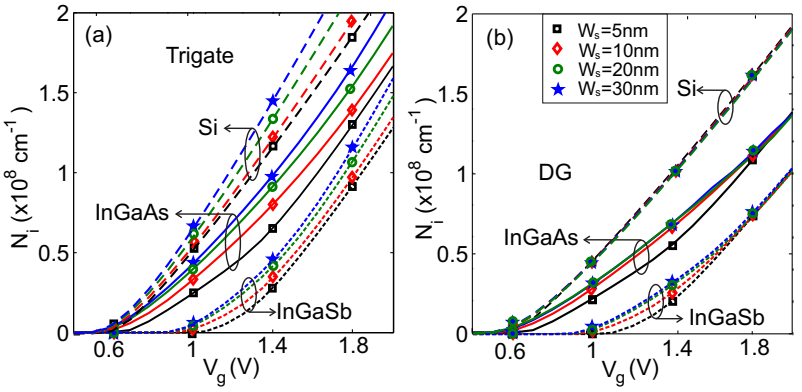

Figure 4.17: N_i as a function of V_g for (a) Trigates and (b) DGs with $H_\mathrm{s} = 50$nm and W_s ranging from 5nm to 30nm. Si and InGaAs are used as semiconductors.

Important differences are found depending on the description employed. The most obvious is the higher total charge of Trigate devices, which is primarily related to: 1) the increase on the device perimeter due to the top interface and 2) the non-negligible impact of the corners, due to their higher electron concentration. That higher electrostatic control of the gates on the corner regions also modifies the influence of the satellite valleys on the device performance, as L valleys are first populated near the corners of the device. To study this effect, Figs. 4.18 and 4.19 show the charge associated to the L valleys DG and Trigate devices made of InGaAs and InGaSb respectively. In all the cases, important differences are found that cannot be explained just by means of the increase in the total perimeter of the device.

Furthermore, from Figs. 4.18 and 4.19 we can asses that: 1) for InGaAs, the L-valley population in the top and lateral regions is quite reduced since nearly doubling the height (from 30nm to 50nm) or tripling the width (from 10nm to 30nm) does not notably increase the L-valley concentration (from $2.5 \times 10^7 \mathrm{cm}^{-1}$ to $3 \times 10^7 \mathrm{cm}^{-1}$ and from $2.8 \times 10^7 \mathrm{cm}^{-1}$ to $3 \times 10^7 \mathrm{cm}^{-1}$ for the largest polarization, respectively); 2) for InGaSb the L-valley population is disposed more uniformly through the different regions reducing the role of the corners, which explain the smaller differences between Trigate and DG.

The differences observed in the valleys population between Trigate and DG geometries may influence the estimation of the electron mobility. The larger effective mass of

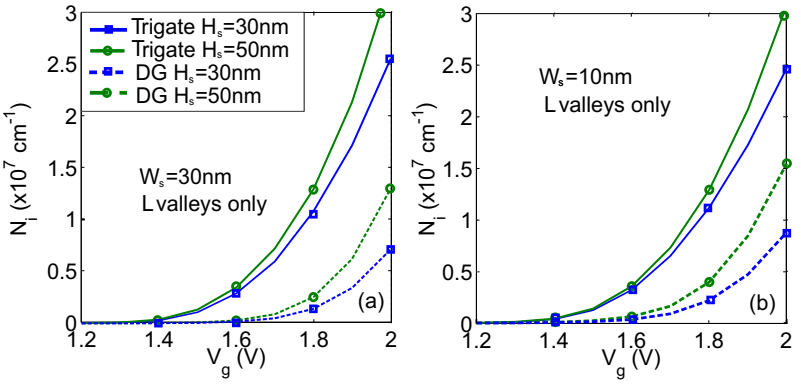

Figure 4.18: Electron density per unit length of the L valleys versus V_{g} for InGaAs Trigates and DGs with $H_{\mathrm{s}} = 30$nm and 50nm, and $W_{\mathrm{s}} = 30$nm (a) and 10nm (b).

the L valleys in the transport direction increases the average conduction effective mass, m^*, of the device which is calculated as:

$$m^* = \sum_v \frac{m_v^* N_v}{N_i} \tag{4.1}$$

where m_v^* and N_v are the conduction effective mass and electron concentration of the v-th valley. Therefore, the lack of precision when describing Trigate devices as DGs produces errors in the estimation of the conduction effective mass. Fig. 4.20 shows how the DG modeling of the devices underestimates m^* for InGaAs and InGaSb trigates but overestimates it for Si.

The large increase of m^* for large inversion charges observed in Fig. 4.20 points out a degradation of the electron mobility in III-V materials for high gate voltages. A thorough study of the transport properties of these devices will be carried out in Chapter 9.

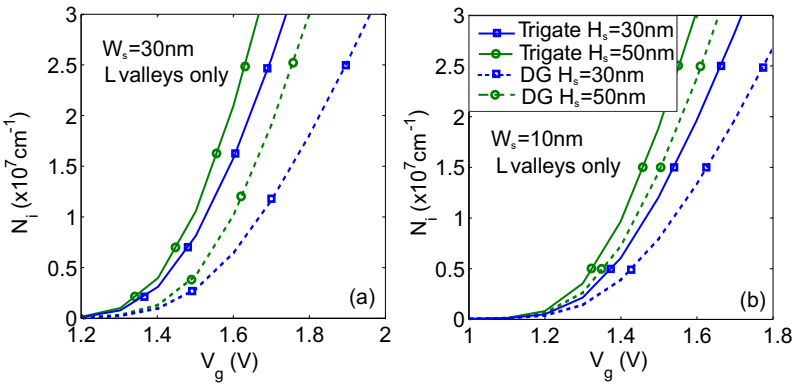

Figure 4.19: Electron density per unit length of the L valleys versus V_{g} for InGaSb Trigates and DGs with $H_{\mathrm{s}} = 30$nm and 50nm, and $W_{\mathrm{sc}} = 30$nm (a) and 10nm (b).

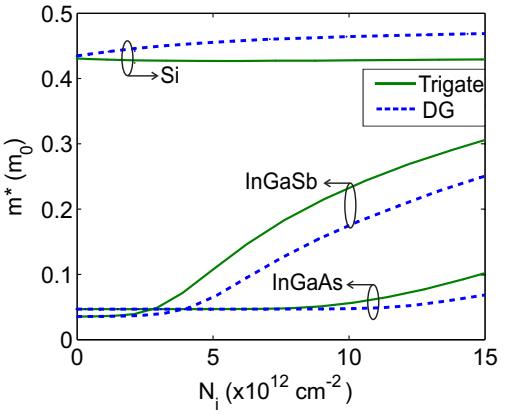

Figure 4.20: Conduction effective mass as a function of the inversion charge for InGaAs, InGaSb and Si trigate (solid lines) devices and comparison with their DG (dashed lines) counterpart ($W_{\mathrm{s}} = 30$nm, $H_{\mathrm{s}} = 50$nm).

4.6 Influence of the back-gate bias on the electrostatics of Si Trigates

Low-power applications require dynamic control of the threshold voltage to manage simultaneously power and performance [161], [162]. One potential solution is the back-gate biasing that modifies V_T due to the body effect. However, few works deal with this effect on MuG MOSFETs [163], [164]. This Section analyzes the influence of back gate bias on the performance of Si Trigate structures [165, 166].

Fig. 4.21 shows a cross-section of a Trigate with rectangular semiconductor channel, being W_s and H_s the semiconductor width and height respectively. t_{ins} and t_{box} are the thicknesses of the front gate and buried insulators, respectively. Back-gate bias (V_{bg}) is applied beneath the buried oxide. Si Trigates were oriented along the $[01\overline{1}]$ crystallographic direction ($\hat{z}$), being the top and bottom ($\hat{y}$) Si-insulator interfaces (100)-oriented, and the lateral ones ($\hat{x}$) (011)-oriented.

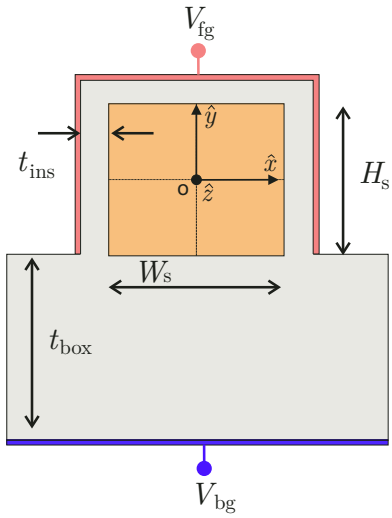

Figure 4.21: Trigate geometry. The channel size is $W_s \times H_s$. t_{ins} and t_{box} are the front gate insulator thickness and buried insulator thickness, respectively.

For Si Trigates, a midgap metal gate ($\Phi_m = 4.61$eV) is considered for the front gate and a p^+poly-Si for the back gate ($\Phi = 5.17$eV). SiO_2 is assumed as gate and buried insulator with thicknesses $t_{ox} = 1.2$nm and $t_{box} = 10$nm, respectively. The minimum channel width and height considered for Si is 5nm. The channel orientation has been taken into account rotating the effective mass tensor as explained in Section 3.6. Non-

parabolic corrections to the conduction band have also been included as explained in Section 3.7.

First, the inversion charge (N_i) versus front gate voltage (V_{fg}) curves have been studied as a function of the back gate bias (V_{bg}). Fig. 4.22 shows the results for a device with $W_s = 5$nm and $H_s = 5$nm. As can be seen, only the threshold voltage (V_T) is modified when V_{bg} changes, while the gate capacitance as a function of the overdrive gate voltage ($V_{fg} - V_T$) remains unaltered. Negative values of V_{bg} increase V_T, as they reduce the overall potential in the channel, while positive ones decrease V_T.

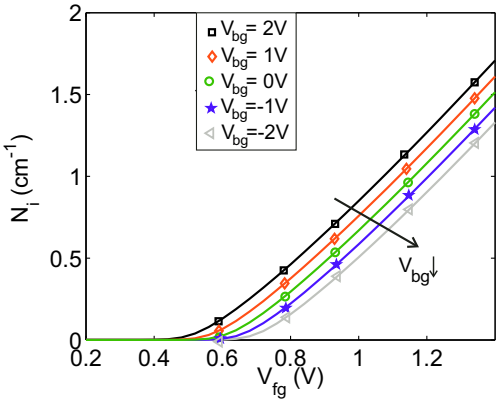

Figure 4.22: N_i versus V_{fg} in a device with $W_s = 5$nm, $H_s = 5$nm, as a function of V_{bg} (ranging from -2V to 2V).

The influence of the back-gate bias varies when different device widths are considered. This is due to a modification of the front-gate control on the back part of the channel. The overall behavior, however, is quite complex, as shown in Fig. 4.23, where different device widths are taken into account for a fixed device height, H_s=5nm, for (a) $V_{gb} = 2V$ and (b) $V_{gb} = -2V$. As can be observed, when W_s is raised, V_T slightly increases for negative values of V_{bg}, while it remarkably decreases for positive values of V_{bg}. To explain this behavior, the influence of the quantum confinement on the threshold voltage has to be taken into account. Hence, for negative V_{bg} values, there are two contributions that tend to cancel each other:

- Firstly, the increase of the device width produces a larger influence of the back-gate bias and thus, from a classical point of view, V_T should rise.

- Secondly, the wider the device, the lower the quantum confinement and therefore the lower its influence on the threshold voltage. In the absence of V_{bg}, this would

cause a reduction of V_T for wider devices.

As for positive V_{bg} values, the higher influence of the back gate in wider devices tends to reduce V_T, adding up to the quantum confinement effect.

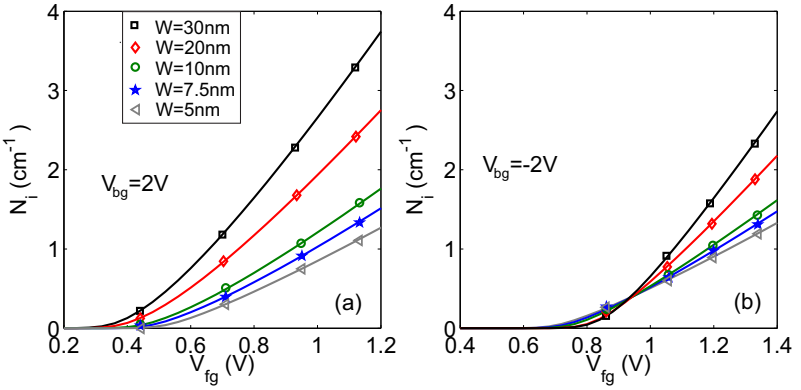

Figure 4.23: N_i versus V_{fg} in a device with $H_s = 5$nm and variable silicon width: (left) $V_{bg} = 2$V , (right) $V_{bg} = -2$V

The complete picture of V_T as a function of V_{bg} and W_s is shown in Fig. 4.24(a) for a $H_s = 5$nm device. Correspondingly the dependence of V_T on H_s for varying V_{bg} is plotted in Fig. 4.24(b) for a $W_s = 5$nm. It is easy to note for a given device size increasing the device width augments the control of V_{bg} on V_T while an increase of the device height reduces that control.

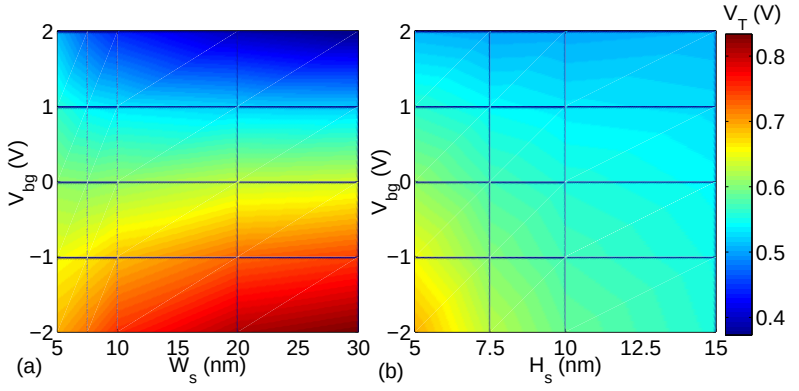

Figure 4.24: (a) V_T as a function of V_{bg} and W_s in a device with $H_s = 5$nm (b) V_T as a function of V_{bg} and H_s in a device with $W_s = 5$nm.

As already reported in Ref. [161], both the increase of W_s and the decrease of H_s

are useful to augment the body factor, which is defined as

$$\gamma = \left| \frac{\partial V_{\mathrm{T}}}{\partial V_{\mathrm{bg}}} \right| \tag{4.2}$$

Fig. 4.25 depicts the body factor as a function of the channel width and height. As can be seen, for the values of t_{ins} and t_{box} considered in this work, γ values higher than 0.1 can be achieved only for width/thin devices. However, devices with almost square aspect ratio (5nm×5nm or 20nm×15nm) can achieve γ values as large as 0.05 which may be worth for V_{T} control [**?**]. As the body factor is closely related to the ratio between the channel-to-back-gate capacitance (C_{bg}) and the channel-to-front-gate capacitance (C_{fg}) [162], the use of Ultra-Thin BOX is critical to even higher γ values.

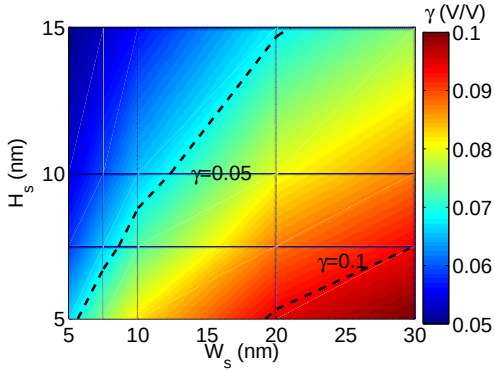

Figure 4.25: Body factor (γ) as a function of W_{s} and H_{s}. The dashed lines indicate the $\gamma = 0.05$ and $\gamma = 0.1$ isolines.

Apart from the influence of the back-gate bias on the threshold voltage, the use of V_{bg} also modifies the electron distribution in the channel. Figure 4.26 represents the normalized charge distribution along a vertical slice of a $W_{\mathrm{s}} \times H_{\mathrm{s}} = 5\mathrm{nm}\times5\mathrm{nm}$ device for different inversion charges (N_{i}) at $V_{\mathrm{bg}} = \pm 2\mathrm{V}$. For positive V_{bg} values (solid lines), the volume inversion effect is enhanced, being the charge more homogeneously distributed along the channel (even for large values of N_{i}, close to $10^7\mathrm{cm}^{-1}$). On the other hand, negative V_{bg} values (dashed lines) shift the charge towards the top interface.

The 2D normalized electron distribution for that device at an inversion charge of $N_{\mathrm{i}} = 10^6\mathrm{cm}^{-1}$ is depicted in Fig. 4.27 for (a) $V_{\mathrm{bg}} = -2$ and (b) $V_{\mathrm{bg}} = 2\mathrm{V}$. Not only the charge is closer to the top interface in the $V_{\mathrm{bg}} = -2\mathrm{V}$ case, but it is also more confined and closer to the lateral regions of the device. As it will be discussed in Chapter 9, this has a strong influence on the electron mobility.

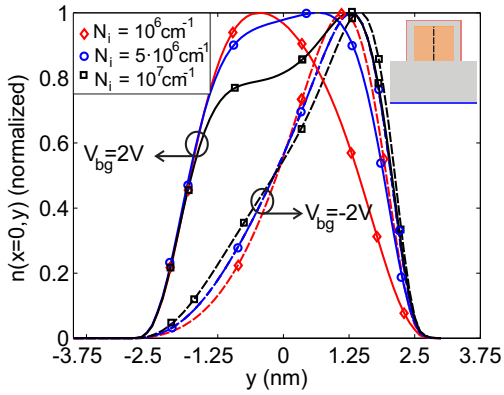

Figure 4.26: n along a vertical cut of a 5nm×5nm Trigate (see inset) at different inversion charges ($N_\mathrm{i} = 10^6\mathrm{cm}^{-1}$, $5 \times 10^6\mathrm{cm}^{-1}$ and $10^7\mathrm{cm}^{-1}$), with $V_\mathrm{bg} = \pm 2\mathrm{V}$.

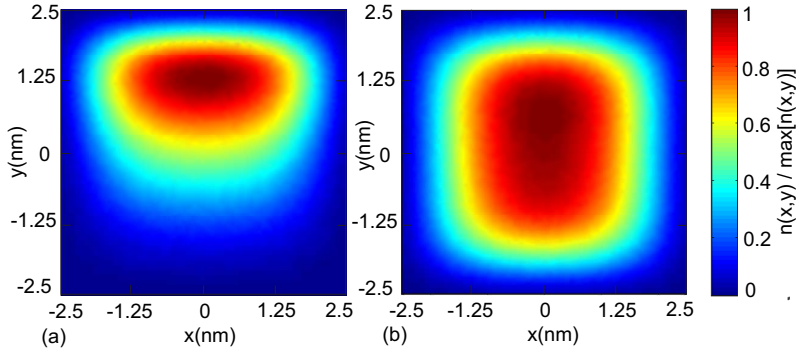

Figure 4.27: Normalized electron distribution at N_i=$10^6\mathrm{cm}^{-1}$ in a 5nm ×5nm device, with (a) $V_\mathrm{bg} = -2\mathrm{V}$ (b) $V_\mathrm{bg} = 2\mathrm{V}$.

4.7 Effects of interfacial states on the technological variability of Si Trigates

In this Section we study the influence of the interfacial states, D_it, on the performance of MuG FETs and, specifically, on the subthreshold Swing and threshold voltage [167]. To do it, we consider a Trigate Si-SiO_2 MOSFET as the one depicted in Fig. 4.12 but neglecting the buried gate. W_s and H_s are set to 10nm and t_ins to 1nm. Undoped body, corner rounding, a midgap metal gate and, otherwise stated, (100)/[011]-oriented devices are used. D_it has been modeled as a Gaussian function, with amplitude $A_\mathrm{g} = A_0$ and variance $\sigma_\mathrm{g} = \sigma_0$, following the experimental results from Ref. [102]. Other energetic profiles described in the literature must be highlighted [103, 141, 145, 168].

Fig. 4.28 shows experimental (solid) and modeled (dotted) (a) $D_{\rm it}$ and (b) $Q_{\rm it}$ as a function of the energy in the gap $E - E_{\rm i}$, being $E_{\rm i}$ the intrinsic level. As in Ref. [102] only acceptor kind traps are considered.

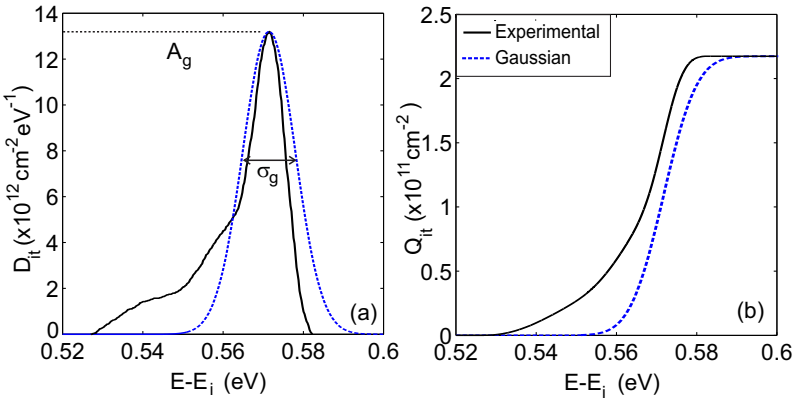

Figure 4.28: (a) $D_{\rm it}$ and (b) $Q_{\rm it}$ as a function of the energy in the gap, $E - E_{\rm i}$. Two $D_{\rm it}$ profiles are considered: an experimental one obtained from Ref. [102] and a Gaussian profile with the same peak and integrated charge.

Fig. 4.29 shows the SS calculated as a function of $V_{\rm g} - V_{\rm T}$ in the presence of the $D_{\rm it}$ at different temperatures, T ranging from 50K to 300K. Our simulations reproduce the behavior shown in Ref. [102]: for small $V_{\rm g}$, the SS values are close to the ideal SS limit, $\ln(10) \cdot k_{\rm B}T/q$. However, there is a kink close to $V_{\rm T}$ related to the presence of the $D_{\rm it}$, which is drifted to larger $V_{\rm g}$ values as T increases. Thus, at high T the influence of the $D_{\rm it}$ moves above threshold voltage, being obscured by the electron charge.

For that reason, the forthcoming results are obtained, otherwise stated, at $T = 50$K. First, we have compared SS for different Gaussian $D_{\rm it}$ profiles. Fig. 4.30 presents SS as a function of $V_{\rm g}$ for increasing values of $A_{\rm g}$: from $A_0/2$ to $2A_0$. The higher $A_{\rm g}$, the higher $Q_{\rm it}$ and, as expected from the $-Q_{\rm it}/C_{\rm ins}$ term of $V_{\rm T}$ (see Section **??**) the larger $\Delta V_{\rm T}$.

The amplitude and broadening in the $V_{\rm g}$ range of the SS kink increase with A. This effect degrades the on-off transition regime, as shown in Fig. 4.31, where the total charge density versus $V_{\rm g}$ is represented for the same $A_{\rm g}$ values considered in Fig. 4.30.

An alternative explanation of this effect can be found from the surface potential, $\psi_{\rm s}$, behavior along the Si-SiO_2 interface which is shown in Fig. 4.32. The linear relation between $\psi_{\rm s}$ and $V_{\rm g}$ is broken when $D_{\rm it}$ begins to fill: at that point, the increase of $Q_{\rm it}$

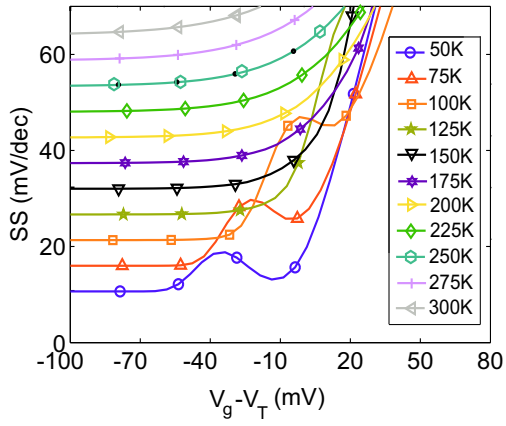

Figure 4.29: SS as a function of $V_{\rm g}$ for several T ranging from 50K to 300K for a 10nm×10nm Trigate device and a Gaussian profile as the shown in Fig. 4.28.

screens the potential, reducing $|d\psi_{\rm s}/dV_{\rm g}|$ and therefore the control of the gate on the inversion charge.

As a consequence, as depicted in Fig. 4.32, the subband energy levels E_j show a plateau region which extends through the $V_{\rm g}$ range where $D_{\rm it}$ keep filling up (see Fig. 4.30). The E_j rise is responsible for a lower level occupation and thus the charge reduction shown in Fig. 4.31.

A variation of $\sigma_{\rm g}$ also modifies the behavior of the SS kink, as shown in Fig. 4.34, where the high correlation between the SS kink and the shape of the $D_{\rm it}$ curve is evidenced. In this case, the $D_{\rm it}$ curves have been adjusted to have the same total integrated charge by modifying also the amplitude, and thus $\Delta V_{\rm T}$ is very similar for all the σ values.

Experimental results have shown that the $D_{\rm it}$ associated to lateral and top/bottom regions of MuG devices can be significantly different. Thus, some experimental results have shown a higher $D_{\rm it}$ concentration in the lateral regions compared to the top ones [102],[169]. Fig. 4.35 shows the simulation results when different amplitudes of the Gaussian profile are applied to the lateral and top regions. A higher lateral $D_{\rm it}$ increases the impact on both, the SS kink and in $\Delta V_{\rm T}$, mainly because the associate perimeter is larger $2W_{\rm s} > H_{\rm s}$.

It is more interesting to analyze the influence of each region of the device separately on the SS and potential. In Fig. 4.36 we compare the SS achieved when $D_{\rm it}$ are placed

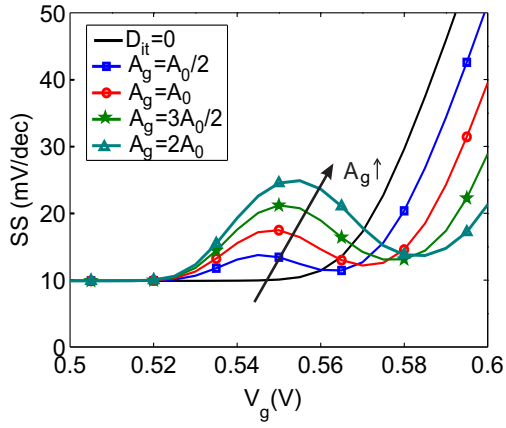

Figure 4.30: SS as a function of $V_{\rm g}$ for several $A_{\rm g}$ and $T = 50$K for a 10nm×10nm Trigate device.

in all the Si-SiO_2 interfaces and in each of them separately: corners, top, lateral and Si-BOX (bottom) regions are considered.

The maximum $\Delta V_{\rm T}$ and wider SS kink is produced by charges located at the Si-BOX interface. This result is related to the reduction of the gate control on such interface, which may be modeled as a reduction of the $C_{\rm ins}$ associated to that region, which would increase $V_{\rm T}$. The potential decrease due to $D_{\rm it}$ screening in each region is depicted in Fig. 4.37: lower values are found near the regions where the $D_{\rm it}$ is placed. Again, the stronger effect of $D_{\rm it}$ at the Si-BOX interface is perceived.

Moreover, we have considered two alternative transport orientations: [001] and [011] (both on (100) wafers, corresponding to the top surface of the Trigate): the results show that the orientation does not significantly impact neither the SS nor the $\Delta V_{\rm T}$, due to the fairly noticeable orientation dependence of the charge distribution in the subthreshold regime, as seen in Fig. 4.38 (the different peak value of the charge is related to a small $V_{\rm T}$ variation, shown in Fig. 4.36).

The relationship between the SS degradation and $\Delta V_{\rm T}$ has been analyzed in Ref [170], without successful results. One of the reasons may be the influence of the insulator thickness variability, also perceived in the TEM scans of Si NWs in Ref. [102]. We have modified the gate insulator geometry as shown in the insets of Fig. 4.39, where $t_{\rm ins}$ at the center of the top/lateral regions is increased or decreased to better fit fabricated devices. As shown in Fig. 4.39, the thicker insulator thickness provokes a degradation on the SS and a higher $\Delta V_{\rm T}$, as a consequence of the lower electrostatic control. This is

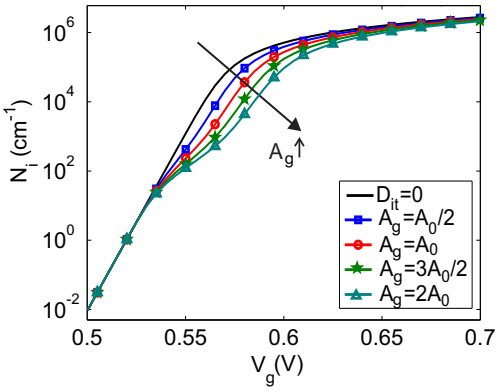

Figure 4.31: N_i as a function of V_g for several A_g and $T = 50$K for a 10nm×10nm Trigate device.

demonstrated in the inset of Fig. 4.38, where the potential along the device is plotted for the two extreme cases showing a larger screening in the device with thicker insulator thickness.

From all the aforementioned results, we conclude that:

(a) The reduction of the gate control increases the negative effects of the interface charges

(b) The increase of the gate insulator thickness or the presence of a noticeable interface charge at the Si-BOX interface of SOI devices degrades the device performance

(c) The improvement of the electrostatic control on the gate insulator interface reduces the technological variability associated to D_it.

Hence, we can expect that the increase of the number of gates helps to reduce both SS and ΔV_T. This hypothesis is confirmed in Fig. 4.40, where N_i is depicted as a function of V_g for different Mug structures with the same channel dimensions than the Trigate studied in this Section. In this Figure, the hump associated to the D_it presence is reduced as the gate control of the channel is increased, leading to the conclusion that the NW structure is the one with better immunity against the D_it influence.

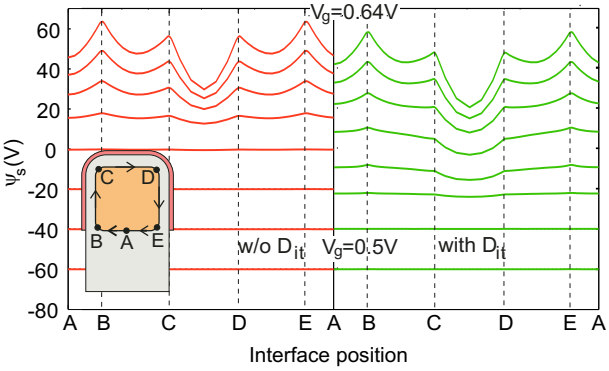

Figure 4.32: ψ_{s} along $\mathcal{C}_{i-s}$ as a function of V_{g} ranging from 0.5V to 0.64V without (left) and with (right) D_{it} at $T = 50$K for the 10nm×10nm Trigate. Inset: schematic depiction of the Trigate device with the semiconductor-insulator interface path marked with letters.

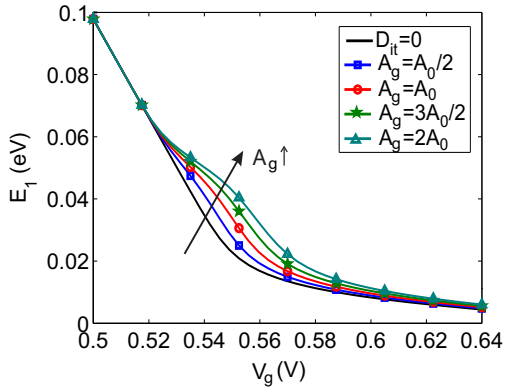

Figure 4.33: E_1 as a function of V_{g} for several A_{g} and $T = 50$K for a 10nm×10nm Trigate device.

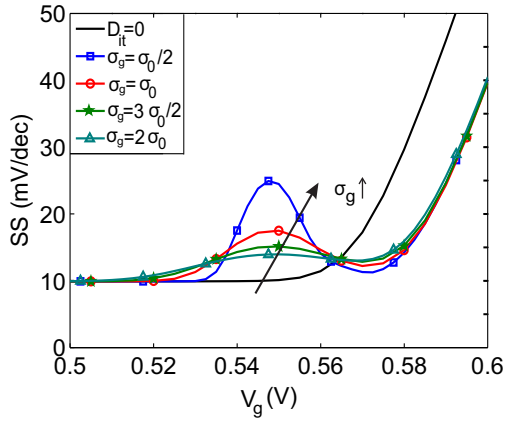

Figure 4.34: SS as a function of V_{g} for several σ_{g} and $T = 50$K for a 10nm×10nm Trigate device.

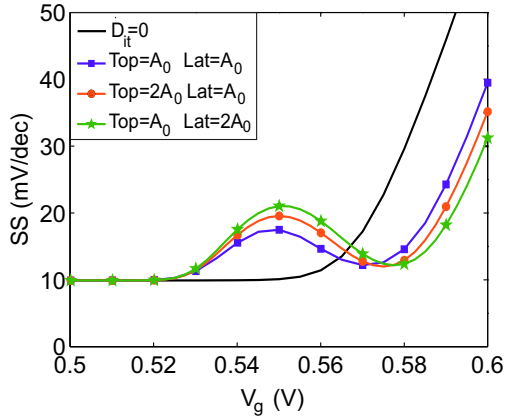

Figure 4.35: SS as a function of V_{g} for different profiles associated to lateral and top regions at $T = 50K$ for a 10nm×10nm Trigate device.

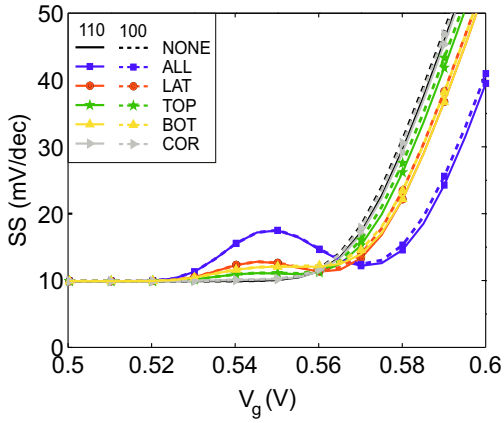

Figure 4.36: SS as a function of V_{g} for D_{it} placed at different region: all (named ALL), lateral (LAT), top (TOP), bottom (BOT) and top corners (COR) at $T = 50K$ for a 10nm×10nm Trigate device.

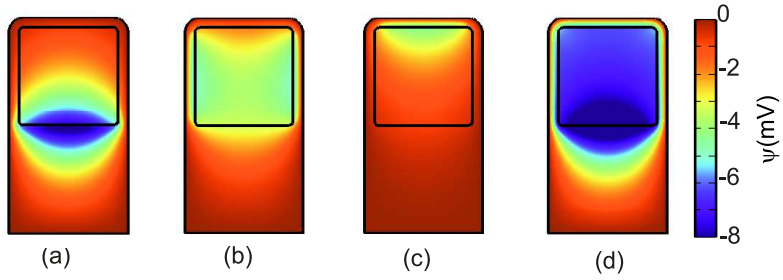

Figure 4.37: Potential decrease due to D_{it} screening for D_{it} located at: (a) in the Si-BOX region, (b) only in the lateral sides, (c) only in the top side, and (d) the whole Si-SiO_2 interface, for a 10nm×10nm Trigate device.

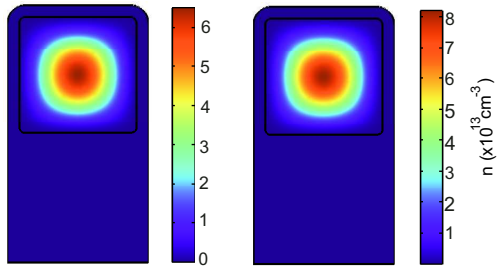

Figure 4.38: n for (a) (100)/[011] and (b) (100)/[001] Trigate FETs at $V_{\mathrm{g}} = 0.53$V without D_{it} for a 10nm×10nm Trigate device.

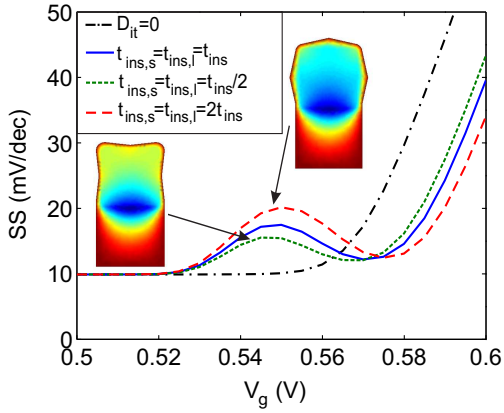

Figure 4.39: SS as a function of V_{g} for variable insulator thicknesses at the lateral top interfaces at $T = 50$K for a 10nm×10nm Trigate device. Inset: Potential along the device for the two extreme cases: $t_{\mathrm{ins,s}} = t_{\mathrm{ins,l}} = t_{\mathrm{ins}}/2$ (left) and $t_{\mathrm{ins,s}} = t_{\mathrm{ins,l}} = 2t_{\mathrm{ins}}$ (right)

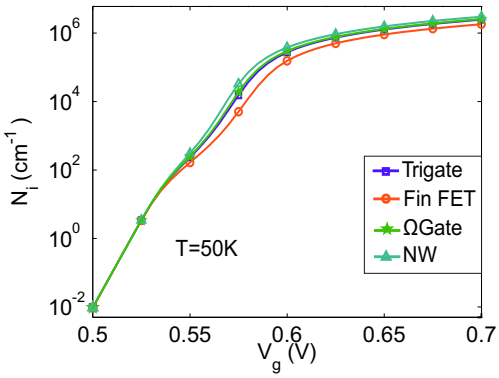

Figure 4.40: SS as a function of V_{g} for different MuG structures and $T = 50$K.

4.8 Conclusions

In this Chapter, Trigates and NWs made of Si and III-V semiconductors have been studied using the SP2D simulator. It has been demonstrated that the low density of states has a strong influence on the charge density and gate capacitance behavior of III-V NWs. Moreover, the population of higher energy valleys (in particular, of L valleys) can strongly modify the small conduction effective mass associated to III-V semiconductors. Additionally, we have studied the behavior of InGaAs, and SOI Trigate FETs, as a function of the channel width, showing that the semiconductor width has a strong impact on InGaAs Trigates: both the threshold voltage and the gate voltage at which the L valleys begin to be populated depend on the width. Besides, it has been demonstrated the importance of considering the two-dimensional confinement for III-V materials to accurately reproduce the electron distribution near the corners. This effect produces a noticeable impact on the conduction effective mass as a result of the different population of each valley. The control of the threshold voltage and the charge distribution of Trigate SOI devices by modifying the back-gate bias has been studied, confirming the possibility of achieving body factors higher than γ=0.1 as long as the channel width over height ratio is increased as much as possible. Finally, the influence of the interfacial states, D_{it}, on the performance of Si MuG FET and, specifically, on the subthreshold swing and threshold voltage has been analyzed observing relevant variations with the temperature and the oxide thickness. It is concluded that the higher the number of gates the lower the degradation due to the interface states.

Chapter 5

Charge, potential and current analytical models for III-V NWs

5.1 Introduction

In this Chapter, an analytical model is proposed to calculate the potential, inversion charge and drain current of III-V cylindrical NWs. To develop the model, we make use of the cylindrical symmetry of the device and the isotropic effective mass of Γ valley to solve the Poisson and Schrödinger equations in polar coordinates. From Schrödinger solution we obtain expressions for the subband energies and their corresponding wavefunctions, taking into account their penetration into the gate insulator and the effective mass discontinuity in the semiconductor-insulator interface. A complete expression for the potential in the NW is achieved by solving the Poisson equation for an arbitrary number of subbands. The model considers Fermi-Dirac Statistics, two-dimensional quantum confinement of the carriers, non-parabolicity effects and interface states.

Several differences must be highlighted between this work and other models proposed in the literature for cylindrical NWs [171]: 1) the inclusion of the wavefunction penetration into the gate insulator, which has to be considered to accurately model low-effective-mass materials [96]; 2) The non-parabolic dispersion relationship, which is non-negiglible in III-V materials [154]; and 3) The possibility of including an arbitrary analytical profile of interface states, which strongly affects the operation of III-V NWs [128].

The rest of the Chapter is organized as follows. In Section 5.2 we solve the

Schrödinger equation in a cylindrical potential well with a finite potential barrier. The solutions are expressed in terms of Bessel functions for the well and modified Bessel functions of the second kind for the barrier. The correction (by means of the perturbation theory) to the Schrödinger energy levels for a non-flat potential scenario is also discussed. In Section 5.3 the Poisson equation is solved for an arbitrary number of occupied subbands obtaining an expression for the potential in the NW. This potential is then used to correct the energy levels, as proposed in Section 5.2. Section 5.4 reviews the calculation of the electron charge considering parabolic and non-parabolic dispersion relationships. In Section 5.5 we deal with the inclusion of interface states in the model, allowing the introduction of any arbitrary analytical interface state profile. In Section 5.6 we briefly discuss the implementation of all equations from Section 5.2 and 5.3, using an iterative algorithm. Section 5.7 uses the results from the charge and potential model to build a current model for the NW. Section 5.8 validates the model by the comparison to the results of numerical simulations for different materials, sizes and applied gate voltages. Finally, the main conclusions of the work are presented in Section 5.9. Appendixes B.1, B.2 and B.3 include the mathematical details for: the normalization of the wavefunctions, the resolution of the Poisson equation and the determination of the boundary conditions, respectively.

5.2 Subband modeling

In this Section an analytical solution of the Schrödinger equation in a cylindrical NW is obtained, including the semiconductor, the gate insulator and the metal gate, as shown in Fig. 5.1.

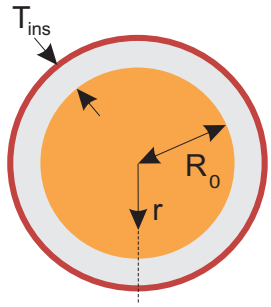

Figure 5.1: Geometry of the circular cross-section NW. R_0 is the semiconductor radius and T_{ins} the insulator thickness.

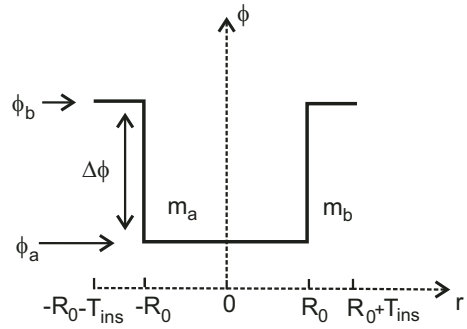

Figure 5.2: Potential energy profile along a radial slice of the NW in a finite potential well: $\Delta\phi = \phi_b - \phi_a$; where ϕ_a (ϕ_b) and m_a (m_b) correspond to the potential energy and effective mass in the semiconductor (insulator) respectively.

To do so, we consider a cylindrical well with finite potential barrier ($\Delta\phi$), as depicted in Fig. 5.2. Different effective masses are considered in the semiconductor (m_a) and the oxide (m_b), and the wavefunctions are allowed to penetrate into the gate insulator. This fact may impact the subband minimum energy as demonstrated by Mudanai *et al.* for planar devices [96]. For the system considered, the Schrödinger equation can be written as follows:

$$-\frac{\hbar^2}{2m_i}\nabla^2\xi(r,\theta) = (E-\phi_i)\,\xi(r,\theta) \tag{5.1}$$

where $\xi(r,\theta)$ is the wavefunction associated to an energy E, and m_i and ϕ_i are the confinement effective mass and the potential energy of each region $i = a, b$ (see Fig. 5.2). It is assumed here that neither m_i nor ϕ_i depend on the azimuthal angle, θ (i.e., the model is applied to isotropic bands). Therefore, $\xi(r,\theta)$ can be decomposed into its radial and angular components as:

$$\xi(r,\theta) = R(r)Y(\theta) \tag{5.2}$$

Using the previous factorization, Eq. (5.1) can be written as:

$$\frac{Y(\theta)}{r^2}\frac{\partial^2 R(r)}{\partial r^2} + \frac{Y(\theta)}{r}\frac{\partial R(r)}{\partial r} + \frac{R(r)}{r^2}\frac{\partial^2 Y}{\partial\theta^2} = -R(r)Y(\theta)\beta_i \tag{5.3}$$

where we have defined:

$$\beta_i = \sqrt{\frac{2m_i}{\hbar^2}(E-\phi_i)} \tag{5.4}$$

Rearranging terms we get:

$$\frac{1}{R(r)}\frac{\partial^2 R(r)}{\partial r^2} + \frac{r}{R(r)}\frac{\partial R(r)}{\partial r} + r^2\beta_i = \frac{1}{Y(\theta)}\frac{\partial^2 Y(\theta)}{\partial \theta^2} \tag{5.5}$$

which can be split into:

$$\frac{\partial^2 Y(\theta)}{\partial \theta^2} = -l^2 Y(\theta) \tag{5.6}$$

$$r^2\frac{\partial^2 R(r)}{\partial r^2} + r\frac{\partial R(r)}{\partial r} + \left(\beta_i r^2 - l^2\right) R(r) = 0 \tag{5.7}$$

The solution of Eq. (5.6) is:

$$Y(\theta) = \frac{1}{\sqrt{2\pi}} e^{\imath l\theta} \tag{5.8}$$

where $l \in \mathbb{Z}$ (to enforce Y is single-valued) and $\imath$ is the imaginary unit

Assuming $\phi_a < E < \phi_b$, the solution of Eq. (5.7) is:

$$R^i(r) = \begin{cases} A \cdot J_l(\gamma r) & \text{for} \quad i = a \\ C \cdot K_l(\alpha r) & \text{for} \quad i = b \end{cases} \tag{5.9}$$

being $J_l(\gamma r)$ the Bessel function of order l, $K_l(\alpha r)$ the modified Bessel function of the second kind and order l, $\gamma = \beta_a$ and $\alpha = j\beta_b$. Thus, the set of solutions for $\xi(r,\theta)$ in Eq. (5.1) is as wide as $\mathbb{Z}$.

The values of γ, α and E can be determined by applying the usual boundary conditions to ξ in the interface between media [115]:

$$\xi^a(R_\mathrm{s},\theta) = \xi^b(R_\mathrm{s},\theta) \tag{5.10}$$

$$\frac{1}{m_a}\left.\frac{d\xi^a(r,\theta)}{dr}\right|_{r=R_\mathrm{s}} = \frac{1}{m_b}\left.\frac{d\xi^b(r,\theta)}{dr}\right|_{r=R_\mathrm{s}} \tag{5.11}$$

Here, it is convenient to use the substitution $\hat{E} = E - \phi_a$. Then γ and α can be rewritten as:

$$\gamma^2 = \frac{2m_a}{\hbar^2}\hat{E}, \qquad \alpha^2 = \frac{2m_b}{\hbar^2}\left(\Delta\phi - \hat{E}\right) \tag{5.12}$$

where $\Delta\phi = \phi_b - \phi_a$ is the difference between the potential energies in both mediums, that is the barrier between their conduction band levels (see Fig. 5.2).

Then applying Eqs. (5.10) and (5.11) we get:

$$A \cdot J_l(\gamma R_\mathrm{s}) = C \cdot K_l(\alpha R_\mathrm{s}) \tag{5.13}$$

$$\frac{A}{m_a}\gamma\left[J_{l-1}(\gamma R_\mathrm{s}) - J_{l+1}(\gamma R_\mathrm{s})\right] = -\frac{C}{m_b}\alpha\left[K_{l-1}(\alpha R_\mathrm{s}) + K_{l+1}(\alpha R_\mathrm{s})\right] \tag{5.14}$$

The unknown constants, A and C, can be eliminated by dividing the two previous equations:

$$\frac{\eta}{m_a}\frac{J_{l-1}(\eta) - J_{l+1}(\eta)}{J_l(\eta)} = -\frac{\zeta}{m_b}\frac{K_{l-1}(\zeta) + K_{l+1}(\zeta)}{K_l(\zeta)} \tag{5.15}$$

where $\eta = \gamma R_\mathrm{s}$ and $\zeta = \alpha R_\mathrm{s}$. An additional relationship between η and ζ can be achieved from the definition of γ and α:

$$\eta^2 + \frac{m_a}{m_b}\zeta^2 = \frac{2m_a\Delta\phi R_\mathrm{s}^2}{\hbar^2} \tag{5.16}$$

Equations (5.15) and (5.16) form a system from which we can calculate η and ζ. The device dimensions and the semiconductor and insulator properties determine the right-hand-side of Eq. (5.16); and, consequently, the solution of the system. Some aspects must be taken into account when solving Eqs. (5.15) and (5.16):

(a) There are multiple solutions for the system: as many as values of l in Eq. (5.15).

(b) For a given l there are also several solutions as the Bessel functions involved in Eq. (5.15) are not monotonic.

(c) Every solution with $l = m$, being $m = 1, 2, \ldots$, is degenerate; having its degenerate solution $l = -m$. This result can be deduced from the properties of Bessel and modified Bessel functions:

$$J_v(x) = (-1)^v J_{-v}(x)$$

$$K_v(x) = K_{-v}(x) \qquad \text{with } v \in \mathbb{Z} \tag{5.17}$$

It is easy to observe that, applying these properties, Eq. (5.15) is completely equivalent for $l = m$ and $l = -m$

(d) For $l = 0$ the solution is non-degenerate.

For each solution pair η_j, ζ_j, with $j = 0, 1\ldots$, one can easily calculate a corre-

sponding pair γ_j and α_j and, using Eq. (5.12), a discrete energy level $\hat{E}_j$ as:

$$\hat{E}_j = \frac{\hbar^2}{2m_a}\frac{\eta_j^2}{R_{\rm s}^2} \tag{5.18}$$

For the sake of clarity, let us briefly explain the subscript notation used in this Chapter. On the one hand, we use the subscript j to enumerate the subbands, from the lowest ($j = 0$) to the highest ($j = N$) value of $\hat{E}_j$ (where N is the number of subbands considered). On the other hand, the subscript l indicates the order of the Bessel function associated to the j subband; in other words the value of l in Eq. (5.15) for which $\hat{E}_j$ is solution. Therefore, hereafter we assume $l = l(j)$.

To better appreciate the solutions provided by the system of Eqs. (5.15) and (5.16), Fig. 5.3 shows the first 24-th wavefunctions, sorted (left to right and top to bottom) attending to the value of $\hat{E}_j$, for a $In_{0.53}Ga_{0.47}As$-Al_2O_3 NW with $2R_{\rm s} = 20$nm and $t_{\rm ins} = 1$nm. The material parameters of $In_{0.53}Ga_{0.47}As$ and Al_2O_3 are summed up in Appendix **??**. To get a more meaningful representation of the wavefunctions, we have plotted the real part of $\xi_j(r, j)$ for $l \geq 0$. Plotting $|\xi_j(r, \theta)|$ –which actually reflects the charge distribution– in its stead, will obscure the differences between l-values. Nevertheless, it is easy to figure out the corresponding imaginary parts of $\xi_j(r, \theta)$. As $R^i(r)$ is real and $Y(\theta) = e^{\imath l\theta}/\sqrt{2\pi}$, the imaginary parts are just a rotation given by $\pi/2l$ (with $l \neq 0$) of the plotted real parts. For $l = 0$ the wavefunction is real. Each wavefunction in Fig. 5.3 is labeled with its corresponding values of j and l. The missing values of j correspond to the $l < 0$ results which are not plotted. The wavefunctions for $l < 0$ will be equal to their $l > 0$ counterparts except for a factor -1 multiplying the real parts for odd l and the imaginary parts for even l. As expected the cylindrical symmetry of $|\xi_j(r, \theta)|$ is always preserved.

Hitherto, the values of the constants A and C in Eq. (5.9) have not been determined. They can be obtained from the normalization of the wavefunction:

$$\int\int |\xi_j(r,\theta)|^2 r dr d\theta = 1 \tag{5.19}$$

Using Eqs. (5.2), (5.8) and (5.9), Eq. (5.19) is rewritten as:

$$A_j^2 \int_0^{R_{\rm s}} r J_l^2(\gamma_j r)\, dr + C_j^2 \int_{R_{\rm s}}^{R_{\rm s}+t_{\rm ins}} r\, K_l^2(\alpha_j r)\, dr = 1 \tag{5.20}$$

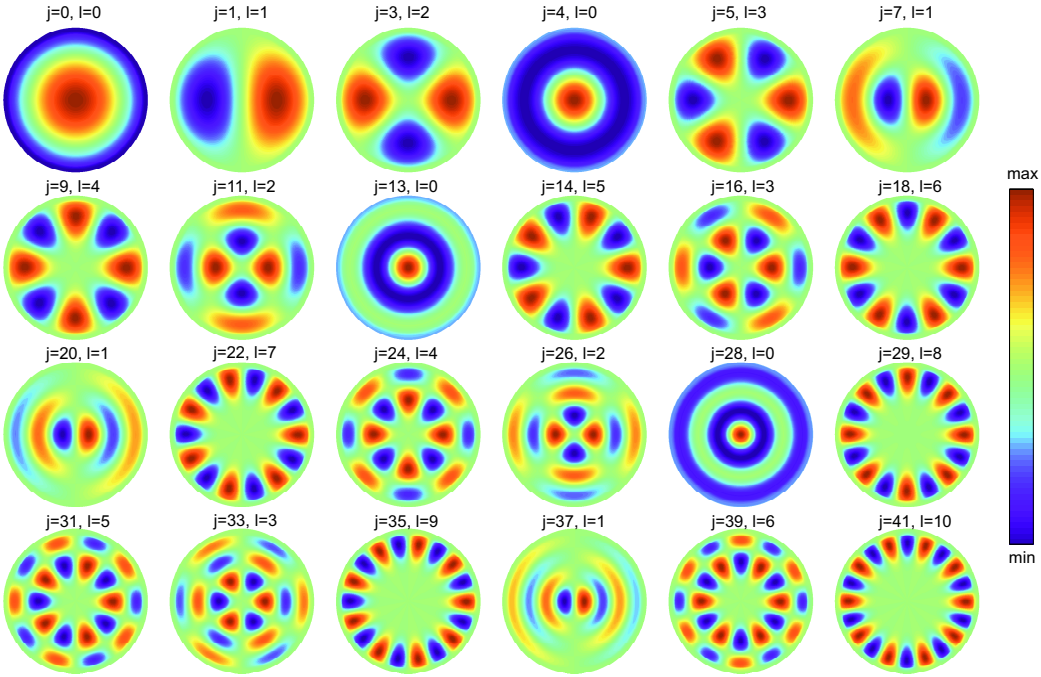

Figure 5.3: First 24-th wavefunctions, sorted (left to right and top to bottom) attending to the value $\hat{E}_j$, for a InGaAs-Al_2O_3 NW with $2R_s = 20$nm and $t_{ins} = 1$nm. Only the real part of the wavefunction is represented.

where A_j and C_j are related by Eq. (5.13). The integration of Eq. (5.20) is detailed in Appendix B.1. The results for A_j and C_j are:

$$A_j = \left(\frac{R_s^2}{2} \left[2J_l^2(\gamma_j R_s) - J_{l-1}(\gamma_j R_s) J_{l+1}(\gamma_j R_s) - J_l^2(\gamma_j R_s) \frac{K_{l-1}(\alpha_j R_s) K_{l+1}(\alpha_j R_s)}{K_l^2(\alpha_j R_s)} \right] \right.$$
$$\left. - \frac{J_l^2(\gamma_j R_s)}{K_l^2(\alpha_j R_s)} \frac{(R_s + t_{ins})^2}{2} \left[K_l^2(\alpha_j (R_s + t_{ins})) - K_{l-1}(\alpha_j (R_s + t_{ins}) K_{l+1}(\alpha_j (R_s + t_{ins})) \right] \right)^{-1/2} \tag{5.21}$$

$$C_j = \left(\frac{R_s^2}{2} \left[2K_l^2(\alpha_j R_s) - K_l^2(\alpha_j R_s) \frac{J_{l-1}(\gamma_j R_s) J_{l+1}(\gamma_j R_s)}{J_l^2(\gamma R_s)} - K_{l-1}(\alpha_j R_s) K_{l+1}(\alpha_j R_s) \right] \right.$$
$$\left. - \frac{(R_s + t_{ins})^2}{2} \left[K_l^2(\alpha_j (R_s + t_{ins})) - K_{l-1}(\alpha_j (R_s + t_{ins}) K_{l+1}(\alpha_j (R_s + t_{ins})) \right] \right)^{-1/2} \tag{5.22}$$

Up to now we have solved the Schrödinger equation for a flat potential well obtaining expressions for the energy levels, Eq. (5.18), and the wavefunctions, Eqs. (5.8) and (5.9). However, the flat potential well is not a realistic scenario as far as the population associated to the subbands, and therefore the charge in the NW, becomes not negligible. Then, the potential in the NW gets curved in a way determined by the Poisson equation, and the solution of the simplified problem proposed in this Section is no longer accurate.

This variation of the potential in the NW can be taken in account using the perturbation theory. Here the perturbation is due to the non-flat potential, $\psi(r)$[1], in the NW. This term only affects the potential energy of the Hamiltonian. Thus, $\tilde{H} = -q\tilde{\psi}(r)$, being $\tilde{\psi}(r) = \psi(r) - \phi_a/q$. The term $-\phi_a/q$ enforces the precept that $\tilde{\psi}(r)$ is a difference between unperturbed and perturbed scenarios. $\Delta\phi$ is not included in $\tilde{H}$ as it was part of the original Hamiltonian. For a non-degenerate subband, the first-order correction of the energy level is given by [172]:

$$\Delta\hat{E}_j = \langle \xi_j^* | \tilde{H} | \xi_j \rangle \tag{5.23}$$

which for the NW can be written as,

$$\Delta\hat{E}_j = -q \int_0^{2\pi} \int_0^{R_s+t_{ins}} \xi_j(r,\theta)\ \tilde{\psi}(r)\ \xi_j^*(r,\theta)\ r\ dr d\theta = -q \int_0^{R_s+t_{ins}} R_j(r)\ \tilde{\psi}(r)\ R_j^*(r)\ r\ dr \tag{5.24}$$

where we have used:

$$\int_0^{2\pi} Y_j(\theta) Y_j^*(\theta) d\theta = \int_0^{2\pi} \frac{e^{\imath l\theta}}{\sqrt{2\pi}} \frac{e^{-\imath l\theta}}{\sqrt{2\pi}} d\theta = 1 \tag{5.25}$$

For degenerate energy levels $\hat{E}_j = \hat{E}_k$, the correction factors $\Delta\hat{E}_j$ and $\Delta\hat{E}_k$ can be obtained as [172]:

$$\Delta\hat{E}_{j,k} = \frac{1}{2}\left(V_{jj} + V_{kk}\right) \pm \frac{1}{2}\sqrt{(V_{jj} - V_{kk})^2 + 4\left|V_{jk}\right|^2} \tag{5.26}$$

where $V_{jk} = \langle \xi_j^* | \tilde{H} | \xi_k \rangle$. As previously explained, for degenerate energy levels k and j

[1] We have assumed no azimuthal dependence of ψ, as can be expected due to the cylindrical symmetry of the structure. This assumption will be demonstrated later in Section 5.3.

it holds that $l(j) = m$ and $l(k) = -m$. Then it is proved that:

$$V_{jk} = -q \int_0^{2\pi} \frac{e^{\imath m\theta}}{\sqrt{2\pi}} \left(\frac{e^{-\imath m\theta}}{\sqrt{2\pi}} \right)^* d\theta \int_0^{R_s+t_{ins}} R_j(r)\, \tilde{\psi}(r)\, R_k^*(r)\, r\, dr = 0 \tag{5.27}$$

Therefore:

$$\Delta \hat{E}_{j,k} = \frac{1}{2} (V_{jj} + V_{kk}) \tag{5.28}$$

But it can be readily checked that $V_{jj} = V_{kk}$ as $R_j(r)R_j^*(r) = R_k(r)R_k^*(r)$ –see Eqs. (5.9) and (5.17)–. Then,

$$\Delta \hat{E}_{j,k} = V_{jj} = V_{kk} = -q \int_0^{R_s+t_{ins}} R_j(r)\, \tilde{\psi}(r)\, R_j^*(r)\, r\, dr \tag{5.29}$$

Thus, to calculate the perturbation to the energy levels necessary to correct the flat potential well approximation, we need to determine the potential ψ in the structure. In the next Section we deal with the Poisson equation to determine the potential.

5.3 Potential modeling

In the present Section we undertake the calculation of the potential in the NW, ψ, due to the charge associated to an arbitrary number of subbands. The Poisson equation in cylindrical coordinates is:

$$\frac{1}{r^2}\frac{\partial^2 \psi}{\partial \theta^2} + \frac{1}{r}\frac{\partial}{\partial r}\left(r \frac{\partial \psi}{\partial r} \right) = -\frac{\rho_i(r,\theta)}{\epsilon_i} \tag{5.30}$$

where ϵ_i and ρ_i are the dielectric constant and charge density in the media i, respectively. ρ_i is given by:

$$\rho_i = -qn(r,\theta) - qN_a\, \delta_{i,a} \tag{5.31}$$

where $\delta_{i,a}$ is the Kronecker delta and $n(r,\theta)$ and N_a are the electron and acceptor impurities concentrations respectively. N_a is assumed constant and $n(r,\theta)$ is given by:

$$n(r,\theta) = \sum_{j=0}^{N} g(\hat{E}_j) |\xi_j(r,\theta)|^2 \tag{5.32}$$

which for the media i can be written as:

$$n(r,\theta) = \sum_{j=0}^{N} g(\hat{E}_j)|R_j^i(r)|^2|Y_j(\theta)|^2 \tag{5.33}$$

being $g(\hat{E}_j)$ the density of states associated to level j. Using $|Y(\theta)|^2 = 1/2\pi$, the resulting Poisson equation for the media i is:

$$\frac{1}{r^2}\frac{\partial^2\psi}{\partial\theta^2} + \frac{1}{r}\frac{\partial}{\partial r}\left(r\frac{\partial\psi}{\partial r}\right) = \frac{q}{2\pi\epsilon_i}\sum_{j=0}^{N} g(\hat{E}_j)|R_j^i(r)|^2 + \frac{q}{\epsilon_i}N_a\delta_{i,a} \tag{5.34}$$

As there is no azimuthal dependence of the charge density and taking into account the cylindrical symmetry of the NW, we can assume no azimuthal dependence for the potential (coherently with Section 5.2). Then, the resulting Poisson equation is:

$$\frac{1}{r}\frac{\partial}{\partial r}\left(r\frac{\partial\psi}{\partial r}\right) = \frac{q}{2\pi\epsilon_i}\sum_{j=0}^{N} g(\hat{E}_j)|R_j^i(r)|^2 + \frac{q}{\epsilon_i}N_a\delta_{i,a} \tag{5.35}$$

A first integration of Eq. (5.35) gives:

$$\int dr\frac{\partial}{\partial r}\left(r\frac{\partial\psi}{\partial r}\right) = \frac{q}{2\pi\epsilon_i}\sum_{j=0}^{N} g(\hat{E}_j)\int r|R_j^i(r)|^2dr + \frac{q\delta_{i,a}}{\epsilon_i}\int rN_a dr + C_i \tag{5.36}$$

where C_i is the integration constant in media i. A second integration of Eq. (5.36) results in:

$$\int\left(\frac{\partial\psi}{\partial r}\right)dr = \frac{q}{2\pi\epsilon_i}\sum_{j=0}^{N} g(\hat{E}_j)\int\frac{1}{\hat{r}}\int r|R_j^i(r)|^2drd\hat{r} + \frac{q\delta_{i,a}}{\epsilon_i}\int\frac{\hat{r}}{2}N_a d\hat{r} + \int\frac{C_i}{\hat{r}}d\hat{r} + D_i \tag{5.37}$$

where, in both cases, the integral and sum in the right-hand-side were interchanged as Fubini-Tonelli's theorem is satisfied, and we have used the symbol $\hat{}$ to distinguish the two integrations variables.

Therefore, the potential in the media i can be written as,

$$\psi^i(r) = \sum_{j=0}^{N}\frac{q}{2\pi\epsilon_i}g(\hat{E}_j)\varphi_j^i(r) + \frac{q}{\epsilon_i}\frac{r^2}{4}N_a\delta_{i,a} + C_i\ln(r) + D_i \tag{5.38}$$

where the term $\frac{q}{2\pi\epsilon_i} g(\hat{E}_j)\varphi_j^i(r)$ is the contribution of the j subband to the potential in media i; and,

$$\varphi_j^i(r) = \int \frac{1}{\hat{r}} \int r \left|R_j^i(r)\right|^2 dr d\hat{r} \tag{5.39}$$

determines the spatial distribution of this j subband contribution to the potential. Substituting Eq. (5.9) into Eq. (5.39) we have:

$$\varphi_j^i(r) = \begin{cases} A_j^2 \int \frac{1}{\hat{r}} \int r\, J_l^2\left(\gamma_j r\right) dr d\hat{r} & i = a \\ C_j^2 \int \frac{1}{\hat{r}} \int r K_l^2\left(\alpha_j r\right) dr d\hat{r} & i = b \end{cases} \tag{5.40}$$

We conclude from Eq. (5.17), that degenerate energy levels j and k (with $l(j) = m$ and $l(k) = -m$) have the same contribution to the potential. Eq. (5.40) is solved in detail in Appendix B.2 providing the following expression:

$$\varphi_j^i(r) = \begin{cases} A_j^2 \left(\frac{r^2}{2} J_l^2(\gamma_j r) + \frac{r^2}{2} J_{l-1}^2(\gamma_j r) + (-l + \frac{1}{2}) \frac{r}{\gamma_j} J_{l-1}(\gamma_j r) J_l(\gamma_j r) + \right. \\ \qquad \left. + \frac{l}{\gamma_j^2} \sum_{m=1}^{l} J_{m-1}^2(\gamma_j r) - \frac{l}{2\gamma_j^2} J_0^2(\gamma_j r) \right) & i = a \\ C_j^2 \left(\frac{r^2}{2} K_l^2(\alpha_j r) - \frac{r^2}{2} K_{l-1}^2(\alpha_j r) + (-l + \frac{1}{2}) \frac{r}{\alpha_j} K_{l-1}(\alpha_j r) K_l(\alpha_j r) + \right. \\ \qquad \left. + \frac{l}{\alpha_j^2} \sum_{m=1}^{l} (-1)^{l-m} K_{m-1}^2(\alpha_j r) - (-1)^{l-1} \frac{l}{2\alpha_j^2} K_0^2(\alpha_j r) \right) & i = b \end{cases} \tag{5.41}$$

To clarify the contribution of each subband to the potential, Fig. 5.4 shows φ_j for the first 24-th subbands, sorted left to right and top to bottom, for an InGaAs-Al_2O_3 NW with $2R_s = 20$nm and $t_{ins} = 1$nm. Each φ_j was labeled with its corresponding value of j and l. Since degenerate subbands contribute equally to the potential, their corresponding φ_j was plotted just once.

Two conclusions can be extracted from Fig. 5.4: (a) As the order l of the Bessel function associated to the subband increases, its contribution to the potential is more step-like; (b) For a given l, φ_j depends softly on r for higher j. Nevertheless, φ_j is weighted by the population of the corresponding subbands $g(\hat{E}_j)$, as proposed in Eq. (5.38), being the first contributions always more relevant than the last ones.

Once the expression for the spatial distribution of the contribution of the subband

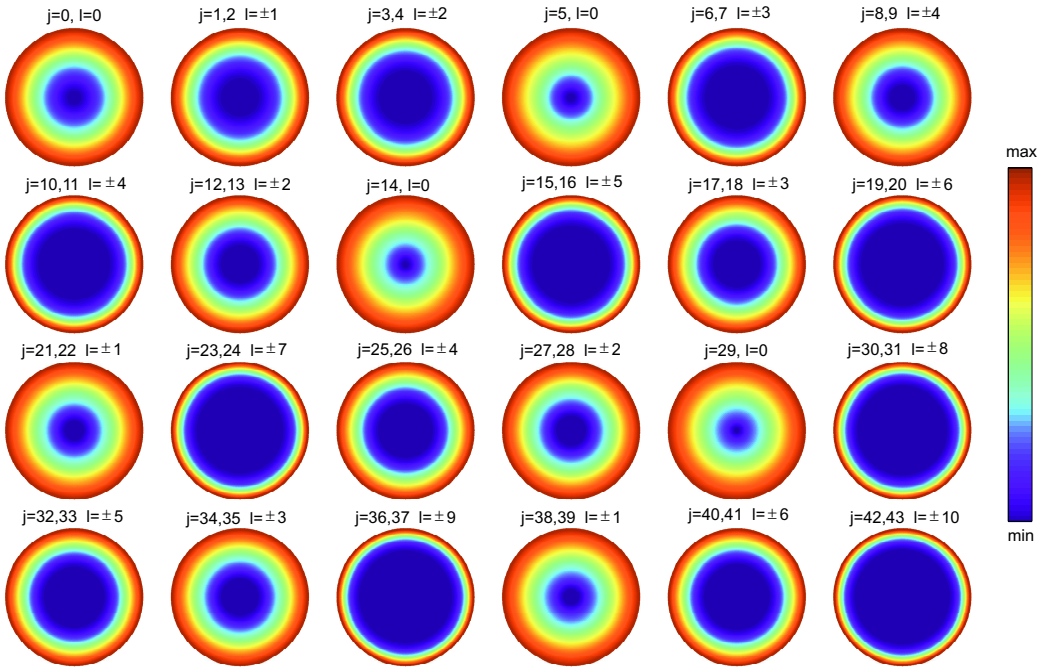

Figure 5.4: φ_j due to first 24-th subbands, sorted (left to right and top to bottom) attending to the value $\hat{E}_j$, for a $2R_{\mathrm{s}} = 20$nm InGaAs-Al_2O_3 NW with $t_{\mathrm{ins}} = 1$nm.

j to the potential in the semiconductor and the insulator has been achieved, we need to calculate the integration constants C_i and D_i in both media. To do it, we apply the following boundary conditions

$$\left.\frac{d\psi^a(r)}{dr}\right|_{r=0} = 0 \tag{5.42}$$

$$\psi^a(R_{\mathrm{s}}) = \psi^b(R_{\mathrm{s}}) \tag{5.43}$$

$$\epsilon_a \left.\frac{d\psi^a(r)}{dr}\right|_{r=R_{\mathrm{s}}} = \epsilon_b \left.\frac{d\psi^b(r)}{dr}\right|_{r=R_{\mathrm{s}}} \tag{5.44}$$

$$\psi^b(R_{\mathrm{s}} + t_{\mathrm{ins}}) = V_{\mathrm{g}} - \Phi_{\mathrm{ms}} \tag{5.45}$$

where:

(a) Eq. (5.42) is set by the cylindrical symmetry of the structure;

(b) Eqs. (5.43) and (5.44) are imposed by the continuity of the solution of the Poisson

equation in the interface between media

(c) Eq. (5.45) is obtained from the polarization of the NW, being V_g the voltage applied in the gate contact located at the outer shell of the NW and Φ_{ms} the difference between the metal gate work function and the semiconductor electron affinity.

The step by step procedure to determine C_a, D_a, C_b and D_b from these equations is accomplished in Appendix B.3. For the sake of clarity, we write here just the final solutions.

$$C_a = 0 \tag{5.46}$$

$$D_a = \frac{q}{2\pi\epsilon_b}\sum_{j=0}^{N} g(\hat{E}_j)\varphi_j^b(R_s) + C_b\ln(R_s) + D_b - \frac{q}{2\pi\epsilon_a}\sum_{j=0}^{N} g(\hat{E}_j)\varphi_j^a(R_s) - \frac{q}{\epsilon_a}\frac{R_s^2}{4}N_a \tag{5.47}$$

$$C_b = \frac{R_s}{\epsilon_b}\left(\frac{1}{2\pi}\sum_{j=0}^{N} g(\hat{E}_j)\varphi_j'^a(R_s) + \frac{qN_aR_s}{2} - \frac{1}{2\pi}\sum_{j=0}^{N} g(\hat{E}_j)\varphi_j'^b(R_s)\right) \tag{5.48}$$

$$D_b = V_g - \Phi_{ms} - \frac{1}{2\pi\epsilon_b}\sum_{j=0}^{N} g(\hat{E}_j)\varphi_j^b(R_s + t_{ins}) - C_b\ln(R_s + t_{ins}) \tag{5.49}$$

where $\psi_j'^a$ and $\psi_j'^b$ are the derivatives of ψ_j^a and ψ_j^b and their expressions are proposed in Appendix B.3. Summing up, the potential in the semiconductor can be calculated as:

$$\psi^a(r) = \frac{q}{2\pi\epsilon_a}\sum_{j=0}^{N} g(\hat{E}_j)\varphi_j^a(r) + \frac{q}{\epsilon_a}\frac{r^2}{4}N_a + D_a \tag{5.50}$$

where φ_j^a and D_a are given by Eqs. (5.41) and (5.47). Correspondingly, the potential in the insulator is given by:

$$\psi^b(r) = \frac{q}{2\pi\epsilon_b}\sum_{j=0}^{N} g(\hat{E}_j)\varphi_j^b(r) + C_b\ln(r) + D_b \tag{5.51}$$

where φ_j^b, C_b and D_b are given by Eqs. (5.41), (5.48) and (5.49).

Once we have a complete close expression for the potential in the NW, we can briefly discuss about the main factors influencing its behavior. In the semiconductor, the radial dependence of $\psi(r)$ is governed by two terms (remind that D_a is just a constant): the first of them is associated to the electron concentration, the second one is controlled

by the acceptor impurities. For low gate voltages the acceptor impurities term is the main contribution to Eq. (5.50), and the potential has a quadratic dependence on the radial coordinate. However, for low N_a concentrations ($< 10^{14}\text{cm}^{-3}$) the total variation of the potential due to N_a is of the order of 10^{-6}V or 10^{-7}V. This variation is negligible and the flat band approximation works well. When higher gate voltages are considered, the potential is controlled by the first term of Eq. (5.50). Then, the potential curvature along the semiconductor radius cannot be neglected and the flat potential well approximation starts to fail, being necessary to correct the energy levels as explained in Section 5.2. Regarding the potential in the insulator, there are also two contributions, one controlled by the electron concentration and one with logarithmic dependence on r. However, in the insulator, due to the low penetration of the wavefunctions, the electron concentration term is, even for large V_g, much smaller than the logarithmic term, being the potential controlled by this one.

5.4 Charge modeling

In this Section we model the electron charge, Q_i, considering a parabolic and a non-parabolic dispersion relationship. The electron charge can be calculated as:

$$Q_i = -q\int_0^{2\pi}\int_0^{R_\text{s}+t_\text{ins}} n(r,\theta)\, r dr d\theta = -q\sum_{j=0}^{N} g(\hat{E}_j)\int_0^{2\pi}\int_0^{R_\text{s}+t_\text{ins}} |\xi_j(r,\theta)|^2\, r dr d\theta = -q\sum_{j=0}^{N} g(\hat{E}_j) \tag{5.52}$$

where we have used Eq. (5.19). For a parabolic dispersion relationship the density of states associated to an energy level E_j is well known:

$$g(E) = g_v\left(\frac{2m_a^* k_B T}{\pi\hbar^2}\right)^{1/2}\mathcal{F}_{-1/2}\left(\frac{E_F - E_j}{k_B T}\right) \tag{5.53}$$

where g_v is the valley degeneracy ($g_v = 1$ for the Γ valley) and m_a^* the transport effective mass in the semiconductor. The rest of the terms keep their usual meaning. This expression can be related to the solution, $\hat{E}_j$, obtained in Section 5.2, by rearranging the term $E_F - E_j$ in the following way:

$$E_j - E_F = (E_j - \phi_a) + (\phi_a - E_F) = \hat{E}_j + \phi_a = \hat{E}_j - q\psi_c \tag{5.54}$$

where $E_F = 0$ is assumed as a reference for energies, and $\phi_a = -q\psi_c$, being $\psi_c = \psi^a(0)$ the potential at the center of the NW. Then, for a parabolic approximation, $g(\hat{E}_j)$ can be written as:

$$g(\hat{E}_j) = g_v \left(\frac{2m_a^* k_B T}{\pi \hbar^2} \right)^{1/2} \mathcal{F}_{-1/2} \left(-\frac{\hat{E}_j - q\psi_c}{k_B T} \right) \tag{5.55}$$

However, as discussed in Section 5.2, the solution $\hat{E}_j$ is not accurate if the potential is not flat, which is the case whenever the semiconductor charge is not negligible. The energy level $\hat{E}_j$ must be corrected by the perturbation energy $\Delta\hat{E}_j$. Then:

$$g(\hat{E}_j) = g_v \left(\frac{2m_a^* k_B T}{\pi \hbar^2} \right)^{1/2} \mathcal{F}_{-1/2} \left(-\frac{\hat{E}_j + \Delta\hat{E}_j - q\psi_c}{k_B T} \right) \tag{5.56}$$

Up to this point, we have considered a parabolic band approximation. However, the non-parabolicity of the conduction band in III-V materials modifies the energy levels and the dispersion relationship. To study its effects, we recall here the model presented by Jin *et al.* [95], where the following expression for the non-parabolic dispersion relationship is proposed (see Section 2.6):

$$\hat{E}_j^{\mathrm{NP}}(k) = \hat{\phi}_j + \frac{-1 + \sqrt{1 + 4\beta_v \left(\frac{\hbar^2 k^2}{2m_a^*} + \hat{E}_j - \hat{\phi}_j \right)}}{2\beta_v} \tag{5.57}$$

where β_v is the non-parabolicity factor of the v valley; k is the wavevector component in the non-confined dimension; and $\hat{\phi}_j$ is the expectation value of the potential energy with respect to the wavefunction of the j subband, defined as:

$$\hat{\phi}_j = \int_0^{2\pi} \int_0^{R_\mathrm{s}+t_\mathrm{ins}} \xi_j(r,\theta)\hat{\phi}(r)\xi_j^*(r,\theta) r\, dr\, d\theta \tag{5.58}$$

where $\hat{\phi}(r)$ is the total potential energy:

$$\hat{\phi}(r) = \begin{cases} -q(\psi^a(r) - \psi_\mathrm{c}) & 0 < r < R_\mathrm{s} \\ -q(\psi^b(r) - \psi_\mathrm{c}) + \Delta\phi & R_\mathrm{s} < r < R_\mathrm{s} + t_\mathrm{ins} \end{cases} \tag{5.59}$$

which, to be coherent with $\hat{E}_j$, is referred to the potential energy at the center of the NW, $-q\psi_\mathrm{c}$. $\hat{\phi}_j$ should not be confused with $-q\tilde{\psi}(r)$ as here the potential barrier

between the semiconductor and the insulator must be taken into consideration.

To introduce the non-parabolicity in the model, we have considered two different approaches. In the first approximation we introduced a non-parabolic correction which only shifts the parabolic energy minimum:

$$\Delta\hat{E}_j^{\mathrm{NP}} = \hat{E}_j^{\mathrm{NP}}(0) - \hat{E}_j = \hat{\phi}_j + \frac{-1+\sqrt{1+4\beta_v\left(\hat{E}_j-\hat{\phi}_j\right)}}{2\beta_v} - \hat{E}_j \tag{5.60}$$

Then $\Delta\hat{E}_j^{\mathrm{NP}}$ is introduced into (5.56) leading to:

$$g(\hat{E}_j) = g_v\sqrt{\frac{2m_a^* k_{\mathrm{B}}T}{\pi\hbar^2}}\mathcal{F}_{-\frac{1}{2}}\left(-\frac{\hat{E}_j+\Delta\hat{E}_j-q\psi_{\mathrm{c}}+\Delta\hat{E}_j^{\mathrm{NP}}}{k_{\mathrm{B}}T}\right) \tag{5.61}$$

The second approximation takes into consideration the non-parabolic dispersion relationship defined in Eq. (5.57). Therefore, $g(\hat{E}_j)$ is not determined by Eq. (5.61) and it cannot be expressed as a function of a Fermi integral of any order. In its stead, it is given by:

$$g(\hat{E}_j) = \frac{g_v}{\pi}\int_{-\infty}^{\infty}\left(1+e^{\frac{-\hat{E}_j^{\mathrm{NP}}(k)}{k_{\mathrm{B}}T}}\right)^{-1}dk \tag{5.62}$$

where $\hat{E}_j^{\mathrm{NP}}(k)$ is calculated as in Eq. (5.57) and again $E_{\mathrm{F}}=0$. The first approximation is simpler than the second one, but it is not accurate for large gate voltages. For this reason, it will only be used for the threshold voltage model presented in Chapter 6. In any other case involving non-parabolicity, the second approximation is the most appropriate.

5.5 Interfacial states modeling

In this Section, we deal with the inclusion of interfacial states, D_{it}, in the model. The presence of a non null surface charge, Q_{it}, at the semiconductor-insulator interface modifies the boundary condition which imposes the continuity of the electric displacement field at the interface. This boundary condition must be, then, reformulated taking into consideration Q_{it}:

$$\epsilon_a\left.\frac{d\psi^a(r)}{dr}\right|_{r=R_{\mathrm{s}}} - \epsilon_b\left.\frac{d\psi^b(r)}{dr}\right|_{r=R_{\mathrm{s}}} = Q_{\mathrm{it}} \tag{5.63}$$

with $Q_{\rm it}$ and $D_{\rm it}$ are related by

$$Q_{\rm it} = q \int_{E_{\rm v}(R_{\rm s})}^{E_{\rm i}(R_{\rm s})} D_{\rm it}^{d}(E)[1 - f(E)]dE - q \int_{E_{\rm i}(R_{\rm s})}^{E_{\rm c}(R_{\rm s})} D_{\rm it}^{a}(E) f(E) dE \tag{5.64}$$

where the superscript d (a) refers to donors (acceptors) traps, and $f(E)$ is the Fermi function. $E_{\rm c}$, $E_{\rm v}$ and $E_{\rm i}$ are the conduction band, the valence band and the intrinsic Fermi level respectively. Using the references for energies proposed in Section 5.4, we can write $E_{\rm c}(r) = -q\psi(r)$. Then $E_{\rm c}(R_{\rm s}) = -q\psi(R_{\rm s}) = -q\psi_{\rm s}$. Thus, Eq. (5.64) can be rewritten in terms of $\psi_{\rm s}$ as:

$$Q_{\rm it} = q \int_{-q\psi_s - E_g}^{-q\psi_s - E_g/2} D_{\rm it}^{d}(E) \frac{e^{\frac{E}{k_{\rm B}T}}}{1 + e^{\frac{E}{k_{\rm B}T}}} dE - q \int_{-q\psi_s - E_g/2}^{-q\psi_s} D_{\rm it}^{a}(E) \frac{1}{1 + e^{\frac{E}{k_{\rm B}T}}} dE \tag{5.65}$$

where $E_{\rm g}$ is the band gap. The new boundary condition in Eq. (5.63) modifies the determination of C_b in Eq. (5.48) which now is reformulated as:

$$C_b = \frac{R_{\rm s}}{\epsilon_b} \left(\frac{1}{2\pi} \sum_{j=0}^{N} g(\hat{E}_j) \varphi_j'^{b}(R_{\rm s}) + \frac{qN_a R_{\rm s}}{2} - \frac{1}{2\pi} \sum_{j=0}^{N} g(\hat{E}_j) \varphi_j'^{b}(R_{\rm s}) \right) - \frac{R_{\rm s}}{\epsilon_b} Q_{\rm it} \tag{5.66}$$

The remaining solutions from the Poisson equation obtained in Section 5.3 are kept as aforementioned.

5.6 Iterative scheme

In this Section we discuss the implementation of the model. It is straightforward to appreciate that the expressions for $g(\hat{E}_j)$ and $\psi(r)$ are coupled. This interdependency is observed in the factor ψ_c in Eq. (5.56) and $g(\hat{E}_j)$ in Eqs. (5.50) and (5.51). Therefore, the model requires an iterative solution scheme. Fig. 5.5 shows a flux diagram of the procedure employed to solve the model.

The initial solution considers a flat potential well $\psi(r) = 0$ (therefore $\Delta\hat{E}_j = 0$) and a given polarization in the outer shell of the NW (given by $V_{\rm g}$). Then we solved the Schrödinger equation obtaining $\hat{E}_j$ and ξ_j from Eqs. (5.18) and (5.2). In the next step we determine $g(\hat{E}_j)$ using Eq. (5.56) for parabolic bands or Eq. (5.62) for non-parabolic

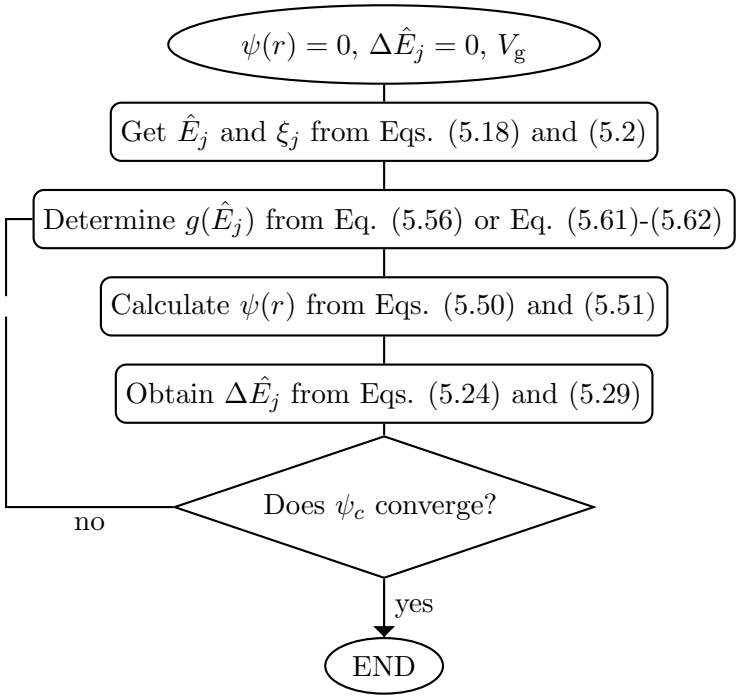

Figure 5.5: Iterative scheme for the implementation of the model.

bands. Once we get $g(\hat{E}_j)$, we obtain $\psi(r)$ in both media using Eqs. (5.50) and (5.51). This allows us to recalculate $\Delta\hat{E}_j$ using Eqs. (5.24) and (5.29) for non-degenerate and degenerate energy levels respectively. The new $\Delta\hat{E}_j$ values would imply a variation of $g(\hat{E}_j)$ as given by Eqs. (5.56) and (5.62), restarting the loop. The stop condition is the convergence of any of the variables involved, for example the potential ψ_c. This iterative scheme can be optimized introducing a convergence accelerator algorithm as Gauss-Seidel [173].

5.7 Drain current model

In this Section we propose an analytical model for the drain current, I_{ds}, of III-V NWs in two scenarios: 1) when no D_{it} is considered; and 2) when a constant D_{it} is assumed.

Fig. 5.6 depicts a long channel cylindrical NW where L is the NW channel length, and V_{s} and V_{d} are the source and drain voltages respectively. V is a gradual potential which varies from the source, $V = V_{\mathrm{s}}$, to the drain, $V = V_{\mathrm{d}}$. This gradual potential (plotted as a dashed line between the two ends of the NW in Fig. 5.6) can be modeled as a variation in the pseudo Fermi level [174]:

$$E_{\mathrm{F}}(z) = E_{\mathrm{F}}(0) - qV \tag{5.67}$$

The cross-section potentials at two arbitrary NW axial positions are also plotted (they were obtained by solving the analytical charge and potential models for two arbitrary $V(z)$ values).

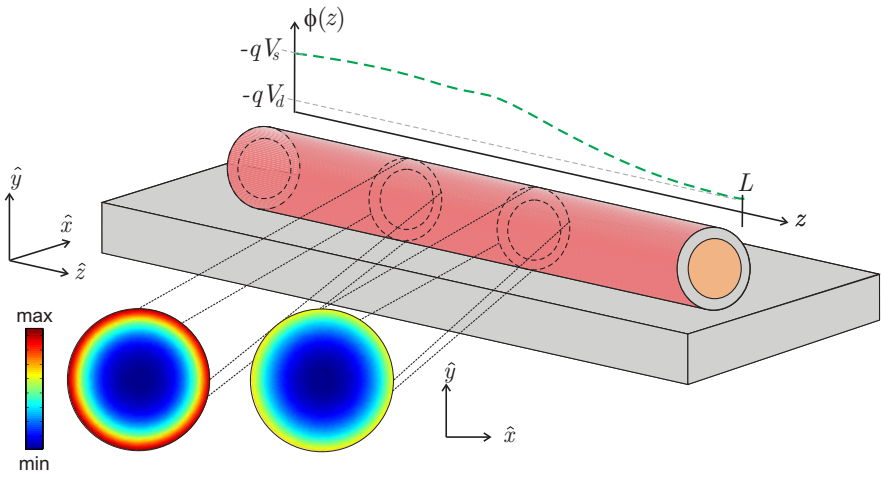

Figure 5.6: 3D schematic view of a long channel cylindrical NW. The semiconductor and insulator media are plotted as orange and gray, respectively while the gate contact is plotted as red. A 2D cross-section of the potential, V is plotted for two z positions. An arbitrary ϕ dependence on z is plotted as a dashed line between the two ends of the NW.

To determine I_{ds} we use the (drift-diffusion) current continuity condition which

imposes [175], [176], [177]:

$$\mu 2\pi R_{\mathrm{s}} Q_{\mathrm{i}} \frac{dV}{dz} = \text{constant} \tag{5.68}$$

being μ the mobility (which for the sake of simplicity is assumed to be constant[2]). To determine I_{ds} we integrate Eq. (5.68) from the source, $z = 0$, to the drain, $z = L$, getting:

$$I_{\mathrm{ds}} = \frac{2\pi R_{\mathrm{s}} \mu}{L} \int_{V_{\mathrm{s}}}^{V_{\mathrm{d}}} Q_{\mathrm{i}}(V) dV \tag{5.69}$$

The electron charge per unit surface is given by Eq. (5.52):

$$Q_{\mathrm{i}}(V) = -\frac{qN_{\mathrm{c}}}{2\pi R_{\mathrm{s}}} \sum_{j=0}^{N} \mathcal{F}_{-\frac{1}{2}} \left(-\frac{\hat{E}_j + \Delta\hat{E}_j - q\psi_{\mathrm{s}} + qV}{k_{\mathrm{B}}T} \right) \tag{5.70}$$

where E_{F} has been replaced by the pseudo Fermi level $E_{\mathrm{F}}(z) = E_{\mathrm{F}}(0) - qV$ to take into consideration its variation along the NW length; and, consistently with the previous Section, the Fermi level at the source was used as a reference for energies, $E_{\mathrm{F}}(0) = 0$.

The surface potential, ψ_{s}, can be calculated as:

$$\psi_{\mathrm{s}} = V_{\mathrm{gs}} - (\Phi_{\mathrm{m}} - \chi_{\mathrm{s}}) - \frac{Q_{\mathrm{i}}}{C_{\mathrm{ins}}} - \frac{Q_{\mathrm{it}}}{C_{\mathrm{ins}}} \tag{5.71}$$

being Q_{it} the surface charge due to interface states given, as in Eq. (5.64), by:

$$Q_{\mathrm{it}} = q \int D_{\mathrm{it}}^{\mathrm{d}}(E)[1 - f(E)]dE - q \int D_{\mathrm{it}}^{\mathrm{a}}(E) f(E) dE \tag{5.72}$$

As already seen in Section 5.6, Eqs. (5.70) and (5.71) are coupled. Furthermore, Q_{it} can have an arbitrary dependence on V. Therefore, the integration in Eq. (5.69) is not straightforward. However there are at least two cases where the integration can be successfully accomplished:

(A) If no interface traps are considered.

(B) If a constant profile for the interface traps is assumed and the Fermi function is approximated by a step function.

The integration procedure in both cases is detailed in Appendix B.4. Here we recall

[2]This simplification, although not pretty realistic (see Chapter 7), is quite used in the literature for long channel devices [174, 176].

the resulting expressions.

5.7.1 Drain current when $D_{\mathbf{it}} = 0$

When no interface traps are considered, I_{ds} is given by:

$$I_{\mathrm{ds}} = \frac{\mu}{L}\left(f_1(V_{\mathrm{d}}) + f_2(V_{\mathrm{d}}) - f_1(V_{\mathrm{s}}) - f_2(V_{\mathrm{s}})\right) \tag{5.73}$$

where f_1 and f_2 are defined as:

$$f_1(V) = -\frac{k_{\mathrm{B}}T}{q}\sum_{j=0}^{N}\mathcal{F}_{\frac{1}{2}}\left(-\frac{\hat{E}_j + \Delta\hat{E}_j - q\psi_{\mathrm{s}} + qV}{k_{\mathrm{B}}T}\right) \tag{5.74}$$

$$f_2(V) = -\frac{1}{C_{\Upsilon}}\left[\sum_{j=0}^{N}\mathcal{F}_{-\frac{1}{2}}\left(-\frac{\hat{E}_j + \Delta\hat{E}_j - q\psi_{\mathrm{s}} + qV}{k_{\mathrm{B}}T}\right)\right]^2 \tag{5.75}$$

being C_{Υ} a capacitance term defined in Eq. (B.75) in Appendix B.4. It is important to remind that ψ_{s} and $\Delta\hat{E}_j$ in Eqs. (5.74) and (5.75) are the surface potential and the correction of the energy level j for a given value V of the pseudo Fermi level. Therefore, when evaluating f_1 and f_2 at V_{s} (V_{d}) in Eq. (5.73), ψ_{s} and $\Delta\hat{E}_j$ would be ψ_{ss} (ψ_{sd}) and $\Delta\hat{E}_j^{\mathrm{s}}$ ($\Delta\hat{E}_j^{\mathrm{d}}$), that is the surface potential and the correction to the energy level at the source (drain) respectively. Thus, Eq. (5.73) requires the resolution of the charge model for $V = V_{\mathrm{s}}$ and $V = V_{\mathrm{d}}$.

5.7.2 Drain current for a constant $D_{\mathbf{it}}$ profile

When a constant D_{it} profile is assumed in a certain range of energies between E_{a} and E_{b}, I_{ds} is given by:

$$I_{\mathrm{ds}} = \frac{\mu}{L}\left[f_1(V_{\mathrm{d}}) + f_2(V_{\mathrm{d}}) - f_1(V_{\mathrm{s}}) - f_2(V_{\mathrm{s}}) + \frac{f_1(V_{\mathrm{b}}) + f_2(V_{\mathrm{b}}) - f_1(V_{\mathrm{a}}) - f_2(V_{\mathrm{a}})}{1 + \dfrac{qD_{\mathrm{it}}}{C_{\mathrm{ins}}}}\right] \tag{5.76}$$

being f_1 and f_2 already defined in Eqs. (5.74) and (5.75) respectively. V_{b} and V_{a} are the gradual potentials corresponding to the pseudo Fermi potential for which $E_{\mathrm{F}}(z) = E_{\mathrm{b}}$

and $E_{\mathrm{F}}(z) = E_{\mathrm{a}}$, respectively.

It is worth to particularize the range of energies where the traps are present to the upper half of the band gap, in accordance with an amphoteric perspective of the interface traps nature [178]. Then, $E_{\mathrm{a}} = E_{\mathrm{i}}$ and $E_{\mathrm{b}} = E_{\mathrm{c}}$ being E_{i} and E_{c} the intrinsic Fermi level and the conduction band edge, respectively. Then, I_{ds} will be:

$$I_{\mathrm{ds}} = \frac{\mu}{L}\left[f_1(V_{\mathrm{d}}) + f_2(V_{\mathrm{d}}) - f_1(V_{\mathrm{s}}) - f_2(V_{\mathrm{s}}) + \frac{f_1(V_{\mathrm{c}}) + f_2(V_{\mathrm{c}}) - f_1(V_{\mathrm{i}}) - f_2(V_{\mathrm{i}})}{1 + \dfrac{qD_{\mathrm{it}}}{C_{\mathrm{ins}}}} \right] \tag{5.77}$$

Now, V_{c} and V_{i} are the gradual potentials for which the pseudo Fermi level crosses trough E_{c} and E_{i}, respectively. Using the references for energies in the charge mode, where $E_{\mathrm{c}}(r) = -q\psi(r)$, it is easy to check that $-qV_{\mathrm{c}} = -q\psi_{\mathrm{s}}$ and $-qV_{\mathrm{i}} = -q\psi_{\mathrm{s}} + E_{\mathrm{g}}/2$. It is noted that Eqs. (5.74) and (5.75) are pretty simplified when V is evaluated at V_{i} and V_{c}. In fact, $\Delta\hat{E}_j$ can be obliterated for $V = V_{\mathrm{i}}$, as $E_{\mathrm{F}}(z) = E_{\mathrm{i}}$ and no relevant charge concentration or potential curvature is expected; thus the arguments of $\mathcal{F}_{\frac{1}{2}}$ are simplified and $\mathcal{F}_{-\frac{1}{2}}$ to $\hat{E}_j$. For $V = V_{\mathrm{c}}$, $\Delta\hat{E}_j$ cannot be neglected and the solution of the charge model is mandatory.

5.8 Results and discussion

In this Section, the results from the proposed analytical models are compared with the solution of the 2D self-consistent Schrödinger-Poisson solver (see Chapter 3) for different NW sizes and gate voltages. InAs and $In_{0.53}Ga_{0.47}As$ are considered as semiconductor materials while Al_2O_3 is used as gate insulator. The parameters of the simulation of Γ, X and L valleys are summarized in Appendix F.

First we study the validity of the proposed solution of the Schrödinger equation. A subthreshold gate voltage ($V_{\mathrm{g}} = 0.2\mathrm{V}$) was considered to limit the effect of: 1) the conduction band curvature in the semiconductor and 2) the logarithmic potential well in the insulator as much as possible. Fig. 5.7(a) shows the three lower energies calculated with the developed analytical model (solid lines) and with the self consistent simulator (symbols) as a function of the device size. The model energy levels corresponding to an infinite potential well are also plotted (dashed lines). The infinite potential well

strongly overestimates the energy levels while an excellent agreement is found for the finite potential well model presented in this Chapter.

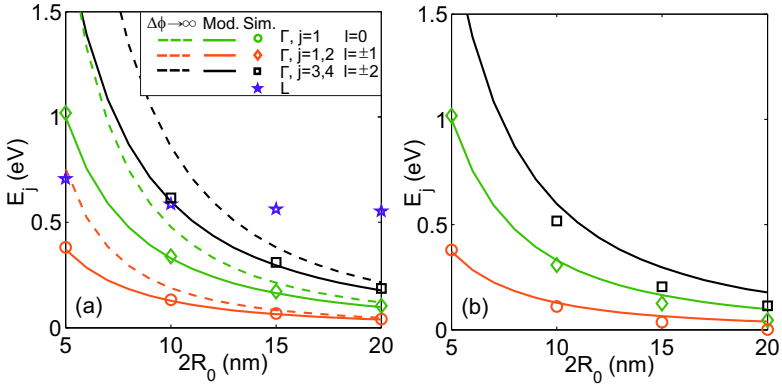

Figure 5.7: Energy minimum of the first subbands of InGaAs NWs as a function of the device size at (a) $V_g = 0.2$V and (b) $V_g = 0.8$V. Comparison between simulation (symbols), and model results (solid lines) considering a finite (solid) and infinite (dashed) potential well. The first L valley energy level (not modeled) is also depicted.

The first L-valley energy level (not modeled) is also depicted in Fig. 5.7. It should be noted that, for small devices ($2R_s \leq 10$nm), the second and third subbands of the Γ valley (i.e., the one that is modeled here) are more energetic than the first subband of L valleys, and therefore a model accounting for L valleys would be needed to reproduce more exactly the simulation results for small NWs. Nevertheless, this would imply a complete new resolution of the Schrödinger and Poisson equations since L-valleys are anisotropic.

While the results for $\hat{E}_j$ obtained from Eq. (5.18) are quite accurate for low gate voltages (where the potential is roughly planar), for higher gate voltages the expressions above are not so well suited, as shown in Fig. 5.7(b). The reason is that, when higher V_g are considered, the electron concentration in the semiconductor increases, affecting the potential that is not flat anymore.

Then, the energy levels must be corrected (using the perturbation theory) as proposed by Eqs. (5.24) and (5.29). In Fig. 5.8 we show the first two energy levels as a function of the device size (for InGaAs NWs), before (dashed) and after (solid) introducing the corrections due to the curved potential. The gate voltage is $V_g = 0.8$V, as in Fig. 5.7(b). As can be seen, an excellent agreement is found between model and

simulation results when the correction in the energy levels is introduced.

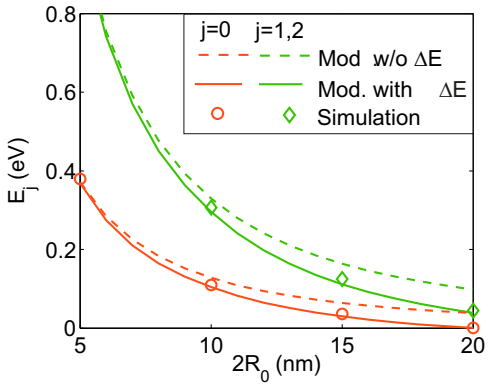

Figure 5.8: Energy minimum of the first subbands of InGaAs NWs at $V_g = 0.8$V. Comparison between simulation (symbols) and modeled (lines) values before (dashed) and after (solid) the energy correction.

Since the energy levels from Eq. (5.1) need a correction for large V_g, it is interesting to look at the validity of their corresponding wavefunctions in a similar scenario. Fig. 5.9, shows $|R_j|^2$ as a function of the radial position, r, $j = 0$ (left) and $j = 1, 2$ (right) subbands of $2R_s = 10$nm InGaAs NWs, considering infinite and finite potential barriers for $V_g = 0.8$V. Simulation and model results are plotted as solid and dashed lines, respectively. Even for this gate voltage (where a non-flat potential well in the NW is expected) the wavefunctions obtained from Eq. (5.1) fit the simulation results. That agreement reinforces the assumption, made in Section 5.2, when just the energy levels and not the wavefunctions from Schrödinger equation were corrected. Finally, it can be observed that for infinite potential barrier, the wavefunction is displaced away from the semiconductor-insulator interface, highlighting the relevance of the wavefunction penetration for a good modeling.

Once the energy levels obtained from Eq. (5.18) and corrected by Eqs. (5.24) and (5.29) and the wavefunctions determined by Eq. (5.9) are validated, we deal with the assessment of $g(\hat{E})$ for parabolic and non-parabolic bands. Fig. 5.10 shows N_i versus V_g for a $2R_s = 10$nm InGaAs NW. Model results are plotted as dashed lines while simulation ones correspond to solid lines. Dash-dotted line correspond to the first non-parabolic approach (which just corrects the energy minimum.) Only three energy levels were considered in this figure.

As can be seen, when non-parabolic effects are included, N_i as well as its slope in-

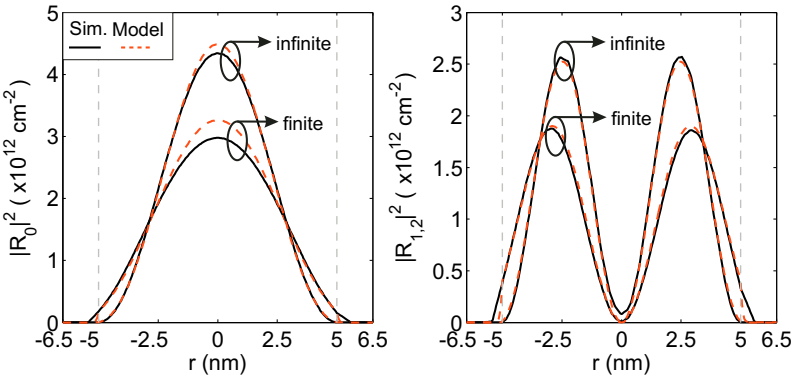

Figure 5.9: $|R_j(r)|^2$ versus radial position for $j = 0$ (a) and $j = 1, 2$ (b) subbands, considering a finite and an infinite potential well. Simulation and model results are plotted as solid and dashed lines respectively for a $2R_s = 10$nm InGaAs NW for $V_{\mathbf{G}} = 0.8$V.

crease due to the higher density of states. Regarding the two approximations employed to include the non-parabolicity, the first one fits well the non-parabolic simulation results up to $V_g \simeq 0.9$V. However, for higher gate voltages N_i is underestimated. The advantage of this first non-parabolic description is the simplicity of the resulting mathematical expression. For these reason it will be employed when determining V_T in Chapter 6. On the contrary, the second one accurately reproduces the simulation results in a higher range, at the cost of a more complex expression. Due to its simplicity we use the parabolic description in the forthcoming results of the model in this Chapter.

We now study the accuracy of the model expressions for the potential. Fig. 5.11 shows the potential along r for a $2R_s = 10$nm InAs (left) and a InGaAs (right) NWs with $t_{ins} = 1.5$nm at overdrive gate voltages $V_g - V_T = 0.1$V (top) and $V_g - V_T = 0.5$V (bottom). InAs and InGaAs present notably differences in magnitudes such as the band gap and the effective mass, allowing to test the model in distinct scenarios. V_T is the threshold voltage and its value has been calculated for InAs ($V_T = 0.32$V) and InGaAs ($V_T = 0.56$V) using the maximum of the second derivative of the charge. Excellent agreement was found between simulation and model results for the V_T (see Chapter 6 for a detailed study of V_T). Solid and dashed curves correspond to the simulation and model results under consideration. The transition between semiconductor and insulator is marked by thin dashed vertical lines. As can be seen, the model fits the potential quite well for both materials and bias conditions. Even for higher overdrive gate voltages, $V_g - V_T > 0.5$V, the model is expected to work properly till the L-valley

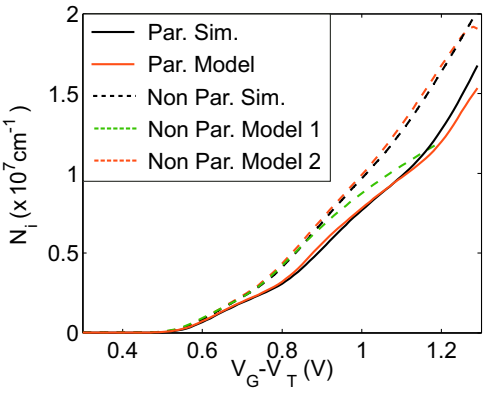

Figure 5.10: N_i versus gate voltage for a $2R_s = 10$nm InGaAs NW. Dashed and solid lines correspond to non-parabolic and parabolic results respectively

levels begin to be populated.

The role of the different energy levels is better appreciated from the charge distribution in the structure. Fig. 5.12 shows the electron density along the radial coordinate of the NW for InAs (left) and InGaAs (right) NWs at the same overdrive gate voltages. Again, solid and dashed curves correspond to the simulation and model results respectively, and the transition between media are plotted as thin dashed vertical lines. The contribution of the first energy level is also plotted (dotted line). For low overdrive gate voltages ($V_g - V_T = 0.1$V) nearly all the charge is due to the filling of the first energy level ($j = 0$, $l = 0$). When a higher voltage is considered ($V_g - V_T = 0.5$V) the charge is pushed away from the center of the NW, due to the occupancy of the second degenerate energy level ($j = 1, 2$, $l = \pm 1$). At both values of $V_g - V_T$, it is easy to appreciate the differences in the electron charge distribution inside the insulator for each material: the InGaAs device has a softer charge profile in the semiconductor-insulator interface than the InAs one due to the smaller discontinuity in the oxide-semiconductor effective masses ($m_a = 0.0468$ for InGaAs, $m_a = 0.026$ for InAs and $m_b = 0.2$ for Al_2O_3).

Let us evaluate the electron density per unit length, N_i, as a function of the overdrive gate voltage. Fig. 5.13 shows N_i versus $V_g - V_T$ for several InGaAs and InAs NW sizes. The model fits well the simulation results in all the operation regimes. The differences observed in Fig. 5.13 for large $V_g - V_T$ in the smallest device are explained by the occupation of higher energy levels belonging to the L valley (not considered in this model). As it is discussed in Chapter 4, for a given overdrive gate voltage, L valley

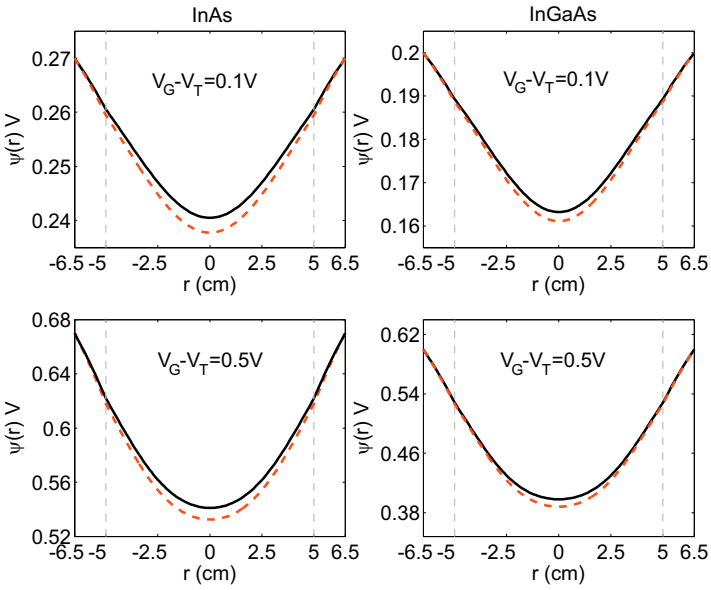

Figure 5.11: Potential along a slice for $2R_s = 10$nm InAs (left) InGaAs (right) NW at $V_g - V_T = 0.1$V and $V_g - V_T = 0.5$V. Solid lines have been used for the simulation while dashed lines represent the results of the model.

population increases with decreasing size. For this reason, larger differences between model and simulation results are observed (at the same $V_g - V_T$) for small NWs in Fig. 5.13. Therefore, the model is expected to work properly (if a good convergence is achieved) for much larger sizes than those shown in Fig. 5.13. For them the L-valley population is less meaningful and the model would only be limited for very large overdrive voltages due to a strong curvature of the potential (which cannot be taken into account by a first order correction). The better fit obtained for the InAs NW in Fig. 5.13 is due to its lower confinement effective mass. The lower the effective mass, the higher the separation between the energy levels, and the larger the gate voltage range where the model is accurate.

Now we briefly study (and validate) the model when D_{it} is included. Fig. 5.14 shows the subthreshold swing and the surface potential, $\psi_s = \psi(R_s)$ when D_{it} is considered and when it is not, for a 15nm InAs NW ($t_{ins} = 1$nm). Simulation and model results are plotted as solid and dashed lines respectively.

We have considered a Gaussian D_{it} distribution of acceptors traps centered in the middle of the upper part of the gap with variance 20meV and amplitude of $5 \cdot$

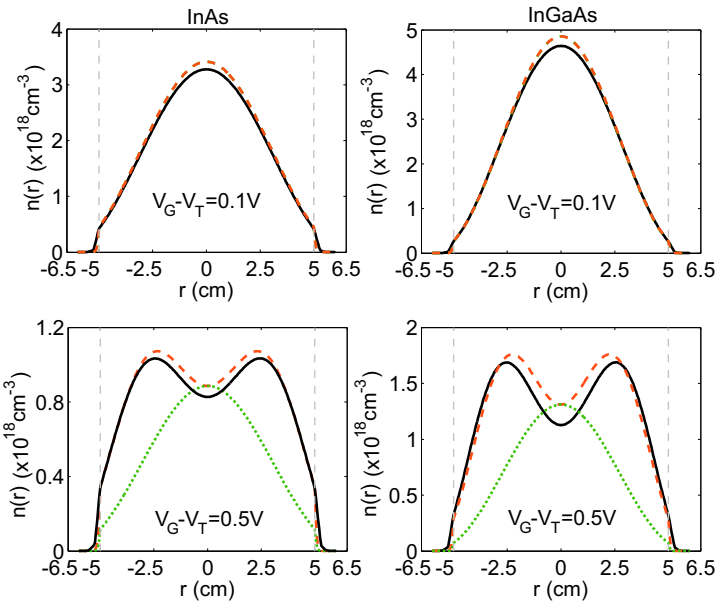

Figure 5.12: Electron density along a slice for $2R_s = 10$nm InAs (left) and InGaAs (right) NWs at $V_g - V_T = 0.1$V and $V_g - V_T = 0.5$V. Comparison between simulation (solid) and model (dashed) results. The contribution of the first energy level is plotted sd dotted line.

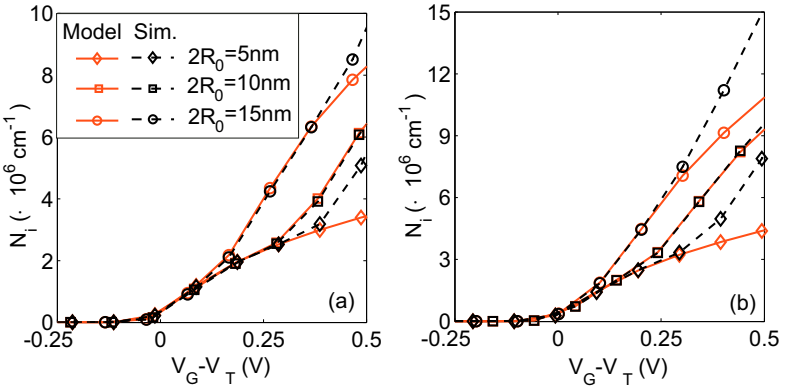

Figure 5.13: Comparison between the simulated (dashed) and modeled (solid) inversion charge for (a) InAs and (b) InGaAs NWs with different sizes. Dashed and solid lines correspond to simulation and model results respectively

$10^{13}\text{cm}^{-2}\text{eV}^{-1}$. It is in good correspondence with experimental profiles reported in the literature [102]. A good agreement between model and simulation results is observed.

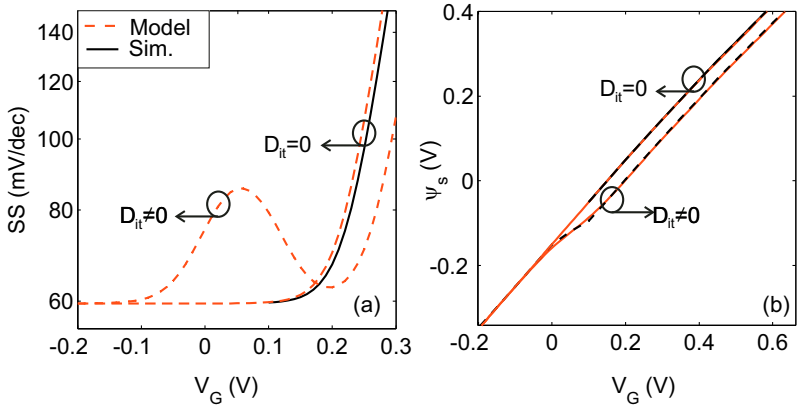

Figure 5.14: (a) SS and (b) ψ_s as a function of $V_{\rm g}$ when $D_{\rm it}$ is considered and when it is not for a InAs NW with $2R_{\rm s} = 15$nm and $t_{\rm ins} = 1$nm. Simulation and model results are plotted as solid and dashed lines respectively.

The $D_{\rm it}$ shape is well reproduced by the SS curves. Regarding the surface potential, the effect of $D_{\rm it}$ can be appreciated as a decrease of ψ_s as a consequence of the charge screening.

Finally, the results from the drain current analytical model are validated with the numerical results obtained using the solution of the SP2D solver for different NW sizes and gate and drain voltages. The numerical current from the 2D simulator is obtained by using Eq. (5.69). We set $L = 100$nm and $\mu = 200{\rm cm}^2/{\rm V\,s}$ for both simulation and model results.

First, we compare the model and simulation results when no interface states are present. Fig. 5.15 shows $I_{\rm ds}$ as a function of $V_{\rm ds}$ from model (dashed) and simulation (solid) for several $V_{\rm gs}$ values from 0.6V (stars) to 1.2V (circles), for a $2R_{\rm s} = 15$nm InAs NW with $t_{\rm ins} = 1.5$nm and no interface traps. It can be observed that the model fits the simulation results in all operation regimes and for all $V_{\rm gs}$. Only a small misfit is observed for $V_{\rm gs} = 1.2$V, which is due to the non-negligible population of the L-valley subbands.

Let us now validate $I_{\rm ds}$ results when a constant $D_{\rm it}$ profile is assumed. Fig. 5.16 shows $I_{\rm ds}$ as a function of $V_{\rm ds}$ from model (dashed lines) and simulation (solid lines) for a $2R_{\rm s} = 15$nm InAs NW, assuming a constant $D_{\rm it} = 10^{13}{\rm eV}^{-1}{\rm cm}^{-2}$ in the upper half of the band gap and 0 otherwise. Similar $V_{\rm gs}$ values to those of Fig. 5.15 are considered. Once more, a good fit is observed for $I_{\rm ds}$ in a wide range of $V_{\rm ds}$ and $V_{\rm gs}$

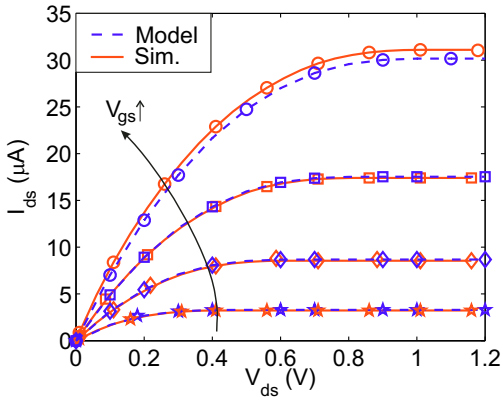

Figure 5.15: I_{ds} as a function of V_{ds} from model (dashed) and simulation (solid) for several V_{gs}: 0.6V (stars), 0.8V (diamonds), 1V (squares) and 1.2V (circles), with $D_{it} = 0$ for a $2R_s = 15$nm InAs NW.

values. Again, the small misfit between model and simulation results for $V_{gs} = 1.2$V is due to the L-valley population.

To better appreciate the influence of the interface states on the drain current, Fig. 5.17 compares I_{ds} results achieved by the model (dashed lines) and simulation (solid lines) as a function of V_{ds} at $V_{gs} = 0.8$V for several D_{it} values: $D_{it} = 0$ (circles), $D_{it} = 10^{13}\text{eV}^{-1}\text{cm}^{-2}$ (squares) and $D_{it} = 1.5{\cdot}10^{13}\text{eV}^{-1}\text{cm}^{-2}$ (diamonds). The presence of interface states results in a decrease of I_{ds} in all regimes. As can be expected, the larger the interface states concentration the larger the decrease in the linear and saturated current. This dependence could be exploited to try to determine the mean D_{it} value in the NW from drain current measurements.

Now we asses the validity of the model for other semiconductor materials and sizes. Fig. 5.18 presents I_{ds} as a function of V_{ds} for $2R_s = 15$nm (a) InGaAs and (b) GaAs NWs at $V_{gs} - V_T = 0.5$V, being $V_T = 0.52$V for the InGaAs NW and $V_T = 0.90$V for the GaAs NW (both V_T values were obtained from the maximum of the transconductance [179],[156]). Simulation and model results are plotted as solid and dashed lines for $D_{it} = 0$ (squares) and $D_{it} = 10^{13}\text{cm}^{-2}\text{eV}^{-1}$ (circles). The model reproduces well the simulation results for both materials.

The larger difference between I_{ds} with and without D_{it} in GaAs (regarding that of InGaAs) is due to its wider gap. If a constant D_{it} in the upper half of the gap is considered, the total interface charge is $Q_{it} = D_{it} \times E_g/2$. Thus, the higher total Q_{it}

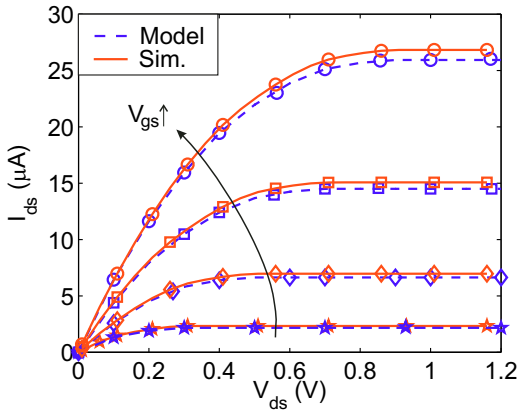

Figure 5.16: $I_{\rm ds}$ as a function of $V_{\rm ds}$ from model (dashed) and simulation (solid) for several $V_{\rm gs}$: 0.6V (stars), 0.8V (diamonds), 1V (squares) and 1.2V (circles), for $D_{\rm it} = 10^{13}{\rm eV}^{-1}{\rm cm}^{-2}$ for a $2R_{\rm s} = 15$nm InAs NW.

for GaAs implies, as was discussed in Fig. 5.17, a higher decrease in the saturation drain current, explaining the differences between InGaAs and GaAs in Fig. 5.18.

Fig. 5.19 depicts the results for several InAs NWs ranging from $2R_{\rm s} = 15$nm to $2R_{\rm s} = 60$nm considering (a) no $D_{\rm it}$ and (b) a constant $D_{\rm it} = 10^{13}{\rm cm}^{-2}{\rm eV}^{-1}$ profile in the upper half of the band gap. $I_{\rm ds}$ as a function of $V_{\rm ds}$ is plotted for $V_{\rm gs} - V_{\rm T} = 0.5$V being $V_{\rm T} = 0.23$V, 0.18V, and 0.15V for the $2R_{\rm s} = 15$nm, 30nm and 60nm NWs, respectively. The model fits the simulation results for $2R_{\rm s} = 15$nm to $2R_{\rm s} = 30$nm in both scenarios. Some inaccuracy in the model results, regarding the simulated ones, is observed for the largest size: $2R_{\rm s} = 60$nm. In this case the source of inaccuracy in the model is not due to the L-valley population (which is less relevant in larger NWs as explained in Section 4.3) but to the approximation made in Appendix B.4 to analytically integrate the current.

Although the analytical $I_{\rm ds}$ expression underestimates non-negligibly the current for large NWs, it is worth to look that the $I_{\rm ds}$ difference with and without $D_{\rm it}$ is not so distinct in model and simulation results. Fig. 5.20 shows $I_{\rm ds}^{\rm w/o} - I_{\rm ds}^{\rm w}$ in the saturation region as a function of $2R_{\rm s}$, being $I_{\rm ds}^{\rm w/o}$ and $I_{\rm ds}^{\rm w}$ the drain currents in absence and presence of $D_{\rm it}$ respectively. As can be observed, the model reproduces the tendency of the curve also for larger NWs, reinforcing its validity to extract $D_{\rm it}$ from $I_{\rm ds}$.

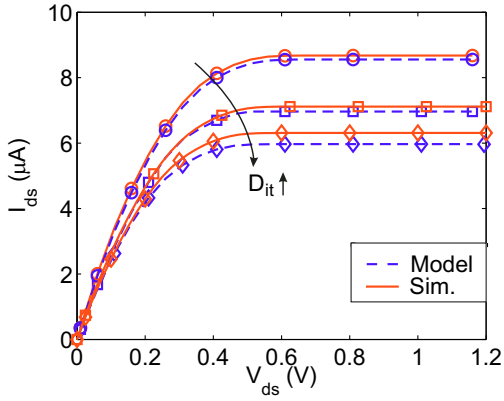

Figure 5.17: $I_{\rm ds}$ as a function of $V_{\rm ds}$ for a $V_{\rm gs} = 0.8$V for the model (dashed) and simulation (solid) results for several $D_{\rm it}$ values: $D_{\rm it} = 0$ circles, $D_{\rm it} = 10^{13}{\rm eV}^{-1}{\rm cm}^{-2}$ (squares) and $D_{\rm it} = 1.5 \cdot 10^{13}{\rm eV}^{-1}{\rm cm}^{-2}$ (diamonds)

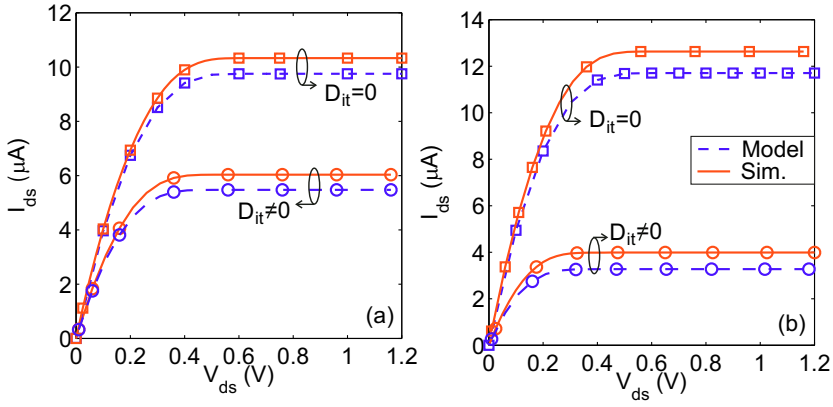

Figure 5.18: $I_{\rm ds}$ as a function of $V_{\rm ds}$ for $2R_{\rm s} = 15$nm InGaAs (a) and GaAs respectively (b) NWs at $V_{\rm gs} - V_{\rm T} = 0.5$V. Simulation and model results are plotted as solid and dashed lines for $D_{\rm it} = 0$ (squares) and $D_{\rm it} = 10^{13}{\rm cm}^{-2}{\rm eV}^{-1}$ (circles).

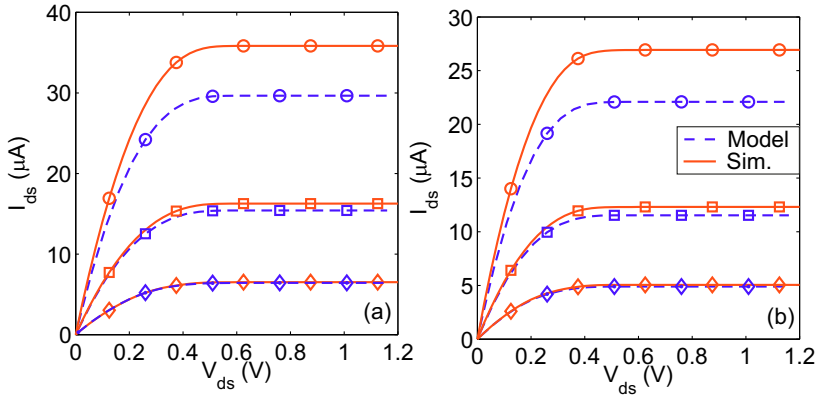

Figure 5.19: $I_{\rm ds}$ as a function of $V_{\rm ds}$ for several InAs NW sizes: $2R_{\rm s}$ = 15nm (diamonds), $2R_{\rm s}$ = 30nm (circles) and $2R_{\rm s}$ = 60nm (squares) considering (a) no $D_{\rm it}$ and (b) a constant $D_{\rm it}$ = $10^{13}{\rm cm}^{-2}{\rm eV}^{-1}$ profile in the upper half of the band gap.

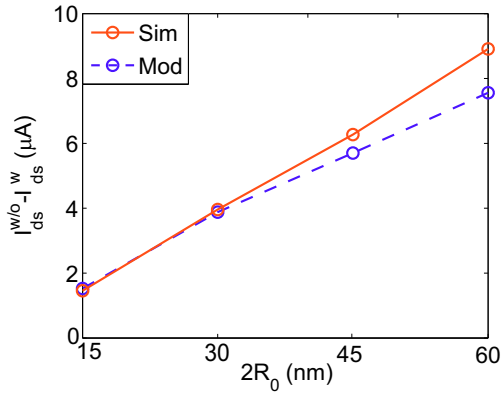

Figure 5.20: $I_{\rm ds}^{\rm w/o} - I_{\rm ds}^{\rm w}$ in the saturation region as a function of $2R_{\rm s}$ from model (dashed) and simulation (solid) for InAs NWs biased at $V_{\rm gs} - V_{\rm T} = 0.5$V.

5.9 Conclusions

In this Chapter we have proposed a complete model for the potential, the inversion charge and the drain current in NWs made of III-V materials. This model presents analytical expressions for the calculation of the subband energies and their corresponding wavefunctions, taking into account their penetration into the gate insulator and the effective mass discontinuity in the semiconductor-oxide interface. The model considers Fermi-Dirac statistics, two-dimensional confinement of the carriers and non-parabolic effects. It also allows the inclusion of arbitrary analytical profiles of interfacial states. We have demonstrated that our analytical solution fits very well the numerical simulations in all operating regimes and for a wide range of NW sizes and gate voltages. The main limitation of the potential and charge models is related to the population of energy levels associated to the L-valley, and the strong curvature of the potential in the semiconductor (which cannot be considered by a first order correction) for very large V_{g} values. As for the drain current model, it is limited for large NWs by the approximation made when solving the long channel integral.

Chapter 6

Gate capacitance and threshold voltage models

6.1 Introduction

In this chapter, we develop physically based analytical models for the gate capacitance (C_{g}), and the threshold voltage (V_{T}), in III-V NWs. To do so, we use the results from charge, potential and drain current achieved in Chapter 5. All the features from the analytical model of Chapter 5 are kept: two-dimensional quantum confinement of the carriers, wavefunction penetration into the gate insulator, Fermi-Dirac statistics and the conduction band non-parabolicity.

There are two main concepts that strongly affect the behavior of electrostatic magnitudes in III-V NWs:

(1) The 2D quantum confinement of the carriers which leads to: (a) a displacement of the charge density, pushed away from the semiconductor-insulator interface [62] and (b) a change (regarding bulk) in the behavior of the density of states, which decrease with increasing energy [140].

(2) The low effective mass (characteristic of III-V materials) which reduces the density of states, leading to the so-called density of states bottleneck [66].

Regarding the gate capacitance, this scenario implies that C_{g} is reduced much below the insulator capacitance (C_{ins}) and the so called quantum capacitance limit can be reached [180]. That possibility may degrade the device performance, although some

authors have found positive consequences regarding the control of SCEs and power-delay product [181],[182]. In the gate capacitance model presented here we try to achieve a better understanding, shedding light on the different terms that contribute to C_{g}.

As for the threshold voltage, the traditional definition of V_{T} (as V_{g} for which $\psi_s = 2\psi_F$ being ψ_F the Fermi potential [183–185]) is no longer valid for III-V NWs. The low density of states implies high surface band bendings to reach a non-negligible electron concentration, and, consequently, a reformulation of the concept is required. To overcome this issue, several new proposals to estimate V_{T} have recently come up and various articles have reviewed the different V_{T} definitions and methods available for its extraction [97, 179, 186–196]. However, to the best of our knowledge there is no analytical physically based study in the literature on III-V NWs V_{T} modeling. In the threshold voltage model presented here we analyze the various factors which are involved in the onset condition of the NWs providing a complete analytical expression.

The rest of this Chapter is organized as follows. Section 6.2 explains the procedure to achieve the gate capacitance model for III-V NWs, and the different capacitance terms are defined. In Section 6.3 we validate the gate capacitance model results with those from the simulator presented in Chapter 3. In Section 6.4 we evaluate the contribution of the different capacitance terms (the insulator capacitance, the finite density of states and the charge distribution in the NW) to the total gate capacitance and compare the model results with those corresponding to a Si NW. Section 6.5 explains the process followed to achieve a V_{T} model for III-V NWs under the parabolic band assumption. In Section 6.6 we propose a non-parabolic band correction to V_{T}. In Section 6.7 we discuss the variation on V_{T} due to a non-null D_{it}. In Section 6.8 we validate the model results with those obtained from simulation for several semiconductor materials, NW sizes and insulator thicknesses. We also evaluate the different contributions to V_{T}, discuss the influence of the wavefunction penetration into the gate insulator on V_{T} and its dependence on the confinement effective mass of the Γ-valley. Section 6.9 sums up the main conclusions of this Chapter. Finally, in Appendix **??** is included some calculi related to the capacitance and threshold voltage models.

6.2 Gate Capacitance Model

In this section we propose an analytical model for the gate capacitance of III-V cylindrical NWs. The NW structure is the same presented in Fig. 5.1 of Chapter 5, where R_{s} was the semiconductor radius and t_{ins} the insulator thickness.

The gate capacitance is defined as:

$$C_{\mathrm{g}} = \frac{\partial Q_{\mathrm{G}}}{\partial V_{\mathrm{g}}} = -\frac{\partial Q_{\mathrm{s}} + Q_{\mathrm{ins}}}{\partial V_{\mathrm{g}}} \simeq -\frac{\partial Q_{\mathrm{s}}}{\partial V_{\mathrm{g}}} \tag{6.1}$$

being $Q_{\mathrm{G}} = -Q_{\mathrm{s}} - Q_{\mathrm{ins}}$ the gate charge; $Q_{\mathrm{s}} = Q_{\mathrm{d}} + Q_{\mathrm{i}}$ the total charge in the semiconductor; Q_{ins} the charge in the insulator; and Q_{i} and Q_{d} the inversion and depletion charges in the semiconductor, respectively. In Eq. (6.1) we assumed that the charge in the insulator is negligible compared to the charge in the semiconductor (see Appendix C.2 for details on the goodness of the approximation). Using some trivial algebra, we can write:

$$\frac{1}{C_{\mathrm{g}}} = -\frac{\partial V_{\mathrm{g}}}{\partial Q_{\mathrm{s}}} = -\frac{\partial (V_{\mathrm{g}} - \psi_{\mathrm{s}})}{\partial Q_{\mathrm{s}}} - \frac{\partial \psi_{\mathrm{s}}}{\partial Q_{\mathrm{s}}} \tag{6.2}$$

where ψ_{s} is the semiconductor surface potential that can be related to V_{g} by means of the Gauss's law:

$$V_{\mathrm{g}} - \Phi_{\mathrm{ms}} = \psi_{\mathrm{s}} - \frac{Q_{\mathrm{s}}}{C_{\mathrm{ins}}} \tag{6.3}$$

being $C_{\mathrm{ins}} = 2\pi\epsilon_{\mathrm{ins}} / \ln\left(1 + \frac{T_{\mathrm{ins}}}{R_{\mathrm{s}}}\right)$ the insulator capacitance per unit length [1]. Assuming that Q_{d} does not depend on V_{g}, Eq. (6.2) can be rewritten as:

$$\frac{1}{C_{\mathrm{g}}} = \frac{1}{C_{\mathrm{ins}}} + \frac{1}{C_{\mathrm{inv}}} \tag{6.4}$$

where $C_{\mathrm{inv}} = -\partial Q_{\mathrm{i}} / \partial \psi_{\mathrm{s}}$ is the inversion capacitance [62]. The term C_{inv} has been modeled in the literature in different ways [159, 197, 198]. Based on Ref. [159], C_{inv} is written as:

$$\frac{1}{C_{\mathrm{inv}}} = -\frac{\partial \psi_{\mathrm{s}}}{\partial Q_{\mathrm{i}}} = -\frac{\partial \psi_{\mathrm{c}}}{\partial Q_{\mathrm{i}}} - \frac{\partial (\psi_{\mathrm{s}} - \psi_{\mathrm{c}})}{\partial Q_{\mathrm{i}}} \tag{6.5}$$

where ψ_{c} is the potential at the center of the NW. Following the nomenclature proposed in Ref. [159], the reciprocal of the first term is the quantum capacitance, $C_{\mathrm{Q}} = -\partial Q_{\mathrm{i}} / \partial \psi_{\mathrm{c}}$, due to the finite density of states; and the reciprocal of the sec-

[1] Otherwise stated the capacitance terms mentioned throughout this Chapter are capacitances per unit length.

ond term is denoted by C_{e}, which can be expressed as [197]:

$$\frac{1}{C_{\mathrm{e}}} = -\frac{\partial(\psi_{\mathrm{s}} - \psi_{\mathrm{c}})}{\partial Q_{\mathrm{i}}} = \frac{1}{\epsilon_{\mathrm{s}}}\frac{\partial(x_{\mathrm{i}} Q_{\mathrm{i}})}{\partial Q_{\mathrm{i}}} \tag{6.6}$$

where ϵ_{s} is the dielectric constant in the semiconductor; and x_{i} is calculated as:

$$x_{\mathrm{i}} = \frac{1}{2\pi}\frac{\int_0^{R_{\mathrm{s}}} r\ln\left(\frac{R_{\mathrm{s}}}{r}\right) n(r)dr}{\int_0^{R_{\mathrm{s}}} r n(r)dr} \tag{6.7}$$

in which, coherently with Chapter 5, no dependence with the azimuthal coordinate for n was assumed. We recall here the expression for n achieved in Chapter 5, Eq. (5.33)

$$n(r) = \frac{1}{2\pi}\sum_{j=0}^{N} g(\hat{E}_j)|R_j(r)|^2 \tag{6.8}$$

Thus, the electron charge Q_{i} in the semiconductor can be calculated as:

$$Q_{\mathrm{i}} = q\int_0^{2\pi}\int_0^{R_{\mathrm{s}}} r n(r)drd\theta = q\,2\pi\int_0^{R_{\mathrm{s}}} r n(r)dr \tag{6.9}$$

Then, substituting Eqs. (6.7) and (6.9) into Eq. (6.6) we get:

$$\frac{1}{C_{\mathrm{e}}} =\cong \frac{q}{2\pi\epsilon_{\mathrm{s}}}\left(\sum_j \int_0^{R_{\mathrm{s}}} r\ln\left(\frac{R_{\mathrm{s}}}{r}\right)|R_j(r)|^2 dr\frac{\partial g(\hat{E}_j)}{\partial\psi_{\mathrm{c}}}\right)\frac{\partial\psi_{\mathrm{c}}}{\partial Q_{\mathrm{i}}} \tag{6.10}$$

where it has been assumed that $|R_j(r)|^2$ does not depend on ψ_{c} for III-V NWs, which is consistent with the analytical model of Chapter 5 (see Fig. 5.9). It is useful to define a quantum capacitance due to each subband j as: $C_{\mathrm{Q}j} = -q\,\partial g(\hat{E}_j)/\partial\psi_{\mathrm{c}}$. Therefore, using the definition of C_{Q}, we have:

$$\frac{1}{C_{\mathrm{e}}} \cong \frac{1}{C_{\mathrm{Q}}}\sum_j \frac{C_{\mathrm{Q}j}}{2\pi\epsilon_{\mathrm{s}}}\int_0^{R_{\mathrm{s}}} r\ln\left(\frac{R_{\mathrm{s}}}{r}\right)|R_j(r)|^2 dr \tag{6.11}$$

where the integral term is, as proposed by Lee *et al.* in Ref. [159], closely related to an

effective inversion-layer centroid. In a similar way, it is possible to define an effective centroid capacitance associated to each subband j given by:

$$C_{Cj} = \frac{2\pi\epsilon_{\mathrm{s}}}{\int_0^{R_{\mathrm{s}}} r \ln\left(\frac{R_{\mathrm{s}}}{r}\right) |R_j(r)|^2 dr} \tag{6.12}$$

Therefore:

$$\frac{1}{C_{\mathrm{e}}} \cong \frac{1}{C_{\mathrm{Q}}} \left(\sum_{j=0}^{N} \frac{C_{\mathrm{Q}j}}{C_{\mathrm{C}j}} \right) \tag{6.13}$$

and the inversion capacitance is expressed as:

$$\frac{1}{C_{\mathrm{inv}}} \cong \frac{1}{C_{\mathrm{Q}}} + \frac{1}{C_{\mathrm{Q}}} \left(\sum_{j=0}^{N} \frac{C_{\mathrm{Q}j}}{C_{\mathrm{C}j}} \right) \tag{6.14}$$

Using the definitions for C_{Q} and $C_{\mathrm{Q}j}$, we know that $C_{\mathrm{Q}} = \sum C_{\mathrm{Q}j}$. Therefore the second term in the right-hand-side of Eq. (6.14) is a weighted mean of the centroid capacitances of all subbands, where the weight of each subband j is controlled by the rate of change of $g(\hat{E}_j)$ with ψ_c. This expression is equivalent to those proposed in Refs. [197] and [159]. However, this one dissociates the C_{inv} dependence on the density of states and on the charge distribution. Indeed, $C_{\mathrm{C}j}$ just depends on $|R_j(r)|^2$ for each sub-band. If $|R_j(r)|^2$ does not change with V_{g} (as it is the case for III-V NWs under not too high V_{g} values, as it is shown in Chapter 5) then $C_{\mathrm{C}j}$ is a purely geometric capacitance.

From the previous expression we can propose the circuit model for the total gate capacitance shown in Fig. 6.1. Although this model is less simple than others found in the literature [198], it is physically more meaningful. C_{g} is given by the series connection of the insulator capacitance, the quantum capacitance, and a contribution that depends on the effective position of the charge. Here, the centroid capacitances associated to each subband j are connected in series and they are weighted by the inverse of the contribution of their subband quantum capacitance to the whole quantum capacitance. Then, the series association of the centroid capacitances is controled by those subbands with the highest $C_{\mathrm{Q}j}/C_{\mathrm{Q}}$ ratio. Therefore, the larger (the smaller) $C_{\mathrm{Q}j}$, the larger (the smaller) the influence of $C_{\mathrm{C}j}$ associated to this level. Thus, the quantum capacitance due to each level determines not only C_{Q} but also how relevant $C_{\mathrm{C}j}$ is for the total C_{g}.

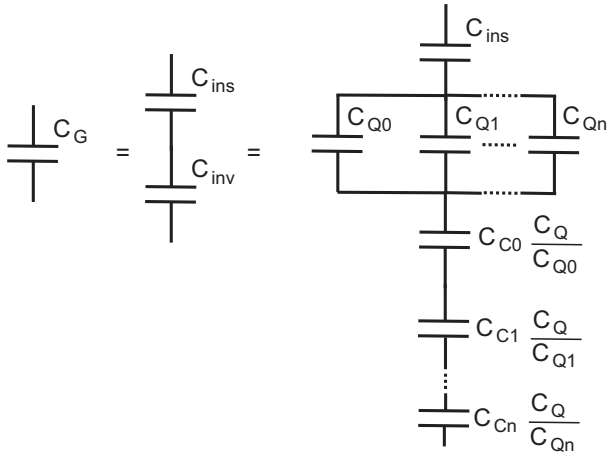

Figure 6.1: Capacitance model for III-V cylindrical NWs.

It is interesting to note that in the quantum limit $C_{\mathrm{Q}} = C_{\mathrm{Q0}}$ and C_{inv} is reduced to the series connection of C_{Q0} and C_{C0}. This particular case is consistent with other studies of III-V MOSFETs [198, 199] and double gate MOSFETs [96] found in the literature.

Based on the analytical model of Chapter 5, we are able to achieve analytical expressions for C_{inv}, C_{Q} and C_{C} in this kind of structures. We recall here the expressions obtained in Chapter 5 for the electron wavefunction $\xi_j(r,\theta)$

$$\xi_j(r,\theta) = R(r)\cdot Y(\theta) = \begin{cases} A_j J_l\left(\gamma_j r\right)\cdot e^{\imath l\theta}/\sqrt{2\pi} & 0 < r < R_{\mathrm{s}} \\ C_j K_l\left(\alpha_j r\right)\cdot e^{\imath l\theta}/\sqrt{2\pi} & r > R_{\mathrm{s}} \end{cases} \tag{6.15}$$

and for the density of occupied states, $g(\hat{E}_j)$:

(a) under parabolic dispersion relationship:

$$g(\hat{E}_j) = \; g_v\sqrt{\frac{2m^* k_{\mathrm{B}}T}{\pi\hbar^2}}\mathcal{F}_{-\frac{1}{2}}\left(-\frac{\hat{E}_j + \Delta\hat{E}_j - q\psi_{\mathrm{c}}}{k_{\mathrm{B}}T}\right) \tag{6.16}$$

(b) introducing a non-parabolicity correction factor of the minimum energy level

$$g(\hat{E}_j) = g_v\sqrt{\frac{2m^* k_{\mathrm{B}}T}{\pi\hbar^2}}\mathcal{F}_{-\frac{1}{2}}\left(-\frac{\hat{E}_j + \Delta\hat{E}_j - q\psi_{\mathrm{c}} + \Delta\hat{E}_j^{\mathrm{NP}}}{k_{\mathrm{B}}T}\right) \tag{6.17}$$

(c) considering a full non-parabolic dispersion relationship

$$g(\hat{E}_j) = \frac{g_v}{\pi} \int_{-\infty}^{\infty} \left(1 + e^{\frac{-\hat{E}_j^{\mathrm{NP}}(k)}{k_{\mathrm{B}}T}}\right)^{-1} dk \tag{6.18}$$

In Eqs. (6.15)-(6.18) we have kept the nomenclature introduced in Chapter 5. Now we proceed to obtain an analytical expressions for $C_{\mathrm{C}j}$ and $C_{\mathrm{Q}j}$ from the previous equations. First, substituting Eq. (6.15) in Eq. (6.12), the centroid capacitance associated to level j is found:

$$C_{\mathrm{C}j} = \frac{2\pi\epsilon_{\mathrm{s}}}{\int_0^{R_{\mathrm{s}}} r \ln\left(\frac{R_{\mathrm{s}}}{r}\right) |A_j J_l(\gamma_j r)|^2 dr} \tag{6.19}$$

where the integral in the denominator is solved for any level j in Appendix (C.1). The resulting expression is:

$$C_{\mathrm{C}j} = \frac{2\pi\epsilon_{\mathrm{s}}}{A_j^2}\left(\frac{R_{\mathrm{s}}^2}{2}J_l^2(\gamma_j R_{\mathrm{s}}) + \frac{R_{\mathrm{s}}^2}{2}J_{l-1}^2(\gamma_j R_{\mathrm{s}}) + (-l+\frac{1}{2})\frac{R_{\mathrm{s}}}{\gamma_j}J_{l-1}(\gamma_j R_{\mathrm{s}})J_l(\gamma_j R_{\mathrm{s}}) + \right.$$
$$\left. + \frac{l}{\gamma_j^2}\sum_{m=1}^{l} J_{m-1}^2(\gamma_j R_{\mathrm{s}}) - \frac{l}{2\gamma_j^2}J_0^2(\gamma_j R_{\mathrm{s}}) - \frac{l}{2\gamma_j^2}J_0^2(0)\right)^{-1} \tag{6.20}$$

To calculate the quantum inversion-layer capacitance due to level j we derive Eqs. (6.16), (6.17) and (6.18) with respect to ψ_c getting:

(a) under parabolic dispersion relation:

$$C_{\mathrm{Q}j} = q^2 g_v \sqrt{\frac{2m_a^*}{k_{\mathrm{B}}T\pi\hbar^2}}\mathcal{F}_{-\frac{3}{2}}\left(-\frac{\hat{E}_j + \Delta\hat{E}_j - q\psi_{\mathrm{c}}}{k_{\mathrm{B}}T}\right)\left(1 - \frac{1}{q}\frac{\partial\Delta\hat{E}_j}{\partial\psi_{\mathrm{c}}}\right) \tag{6.21}$$

(b) introducing a non-parabolicity correction factor of the minimum energy level

$$C_{\mathrm{Q}j} = q^2 g_v \sqrt{\frac{2m_a^*}{k_{\mathrm{B}}T\pi\hbar^2}}\mathcal{F}_{-\frac{3}{2}}\left(-\frac{\hat{E}_j + \Delta\hat{E}_j - q\psi_{\mathrm{c}} + \Delta\hat{E}_j^{\mathrm{NP}}}{k_{\mathrm{B}}T}\right)\left(1 - \frac{1}{q}\frac{\partial(\Delta\hat{E}_j + \Delta\hat{E}_j^{\mathrm{NP}})}{\partial\psi_{\mathrm{c}}}\right) \tag{6.22}$$

(c) considering a full non-parabolic dispersion relation as proposed by Jin *et al.* [95]

$$C_{\mathrm{Q}j} = \frac{1}{k_{\mathrm{B}}T}\frac{g_v}{\pi}\int_{-\infty}^{\infty} e^{\frac{-\hat{E}_j^{\mathrm{NP}}(k)}{k_{\mathrm{B}}T}}\left(\frac{\partial \hat{E}_j^{\mathrm{NP}}(k)}{\partial \psi_c}\right)\left(1+e^{\frac{-\hat{E}_j^{\mathrm{NP}}(k)}{k_{\mathrm{B}}T}}\right)^{-2} dk \tag{6.23}$$

where the derivative rule for the Fermi-Dirac integral, $\mathcal{F}_{i-1}(x) = d\mathcal{F}_i(x)/dx$, was used. It should be noted that centroid capacitances are not modified regardless the dispersion relation considered.

6.3 Capacitance model validation

Our intention here is to validate the analytical gate capacitance model by comparing its results with those provided by the simulator presented in Chapter 3. To do so, three different semiconductor materials (InAs, $\mathrm{In}_x\mathrm{Ga}_{1-x}\mathrm{As}$ ($x = 0.53$) and GaAs) and three NW diameters ($2R_{\mathrm{s}}$ = 5nm, 10nm and 15nm) have been considered. Γ, X and L valleys were taken into consideration in the simulations. Al_2O_3 was used as gate insulator and t_{ins} was held to 1.5nm, which corresponds to an EOT of 0.6nm [200], following to previous works [201]. The validity of the model was also checked for other insulator materials and thicknesses. All material parameters are presented in Appendix (F).First, a parabolic conduction band is assumed.

Fig. 6.2 shows the simulated (solid lines) and modeled (dashed lines) gate capacitance results as a function of the gate voltage for three different InGaAs NW sizes. A good agreement is found for $V_{\mathrm{g}} < 0.7$V in the $2R_{\mathrm{s}} = 15$nm case, and $V_{\mathrm{g}} < 1$V in the $2R_{\mathrm{s}} = 5$nm and $2R_{\mathrm{s}} = 10$nm cases. In its range of validity, the model accurately reproduces the humps in the gate capacitance which are due to the occupation of the first three energy levels. They are better observed in the $2R_{\mathrm{s}} = 10$nm NW for $j = 0$ around $V_{\mathrm{g}} = 0.6$V and for $j = 1$, 2 around $V_{\mathrm{g}} = 0.9$V (the inset of Fig. 6.2 shows $g(\hat{E}_j)$ associated to these levels versus the gate voltage for this NW size). As shown in the figure, the range of validity for the $2R_{\mathrm{s}} = 15$nm device can be extended taking into account higher energy levels of the Γ-valley ($j = 3, 4$, $l = \pm 2$ and $j = 5, 6$, $l = \pm 3$). However, for the $2R_{\mathrm{s}} = 5$nm and $2R_{\mathrm{s}} = 10$nm NWs, the upper energy levels are the first sub-bands of the L-valley, which are not modeled in this work, and therefore considering higher energy levels of the Γ-valley does not improve the results.

Fig. 6.3 compares the model (dashed lines) and simulation (solid lines) results for

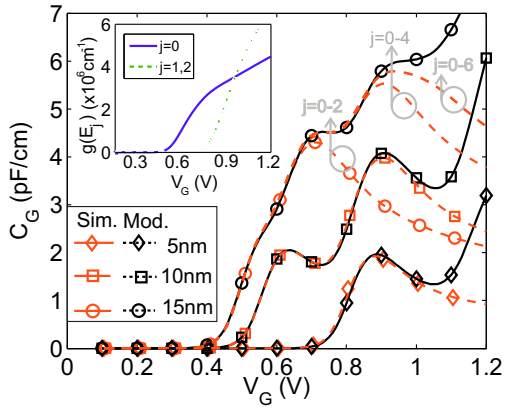

Figure 6.2: Gate capacitance versus gate voltage for a $2R_s = 5$nm (diamonds), $2R_s = 10$nm (squares), $2R_s = 15$nm (circles) InGaAs nanowires. Solid and dashed lines correspond to simulation and model results respectively. The results of the $2R_s = 15$nm NW also include the $j = 3, 4$, $l = \pm 2$ and $j = 5, 6$, $l = \pm 3$ degenerate Γ-valley energy level. Inset: $g(\hat{E})$ due to level $j = 0$ and $j = 1, 2$ versus gate voltage for the $2R_s = 10$nm InGaAs NW.

$2R_s = 10$nm NWs made of different III-V materials. The gate capacitance is plotted as a function of the gate overdrive voltage $(V_g - V_T)$. The V_T values were numerically calculated from the maximum of the second derivative of the charge respect to the gate voltage. V_T values were: 0.32V, 0.55V and 0.96V for the InAs, InGaAs and GaAs NWs, respectively. A detailed discussion on V_T is proposed in Section 6.5. Again, the gate capacitance model fits quite well the simulation results for the three materials. The InAs NW presents the larger range of validity for the model (up to $V_g - V_T = 0.6$V), when only three energy levels are considered. This is due to its lower confinement effective mass, which increases the separation among energy levels and extends the range of V_g where just three energy levels are enough to describe the gate capacitance behavior (see Chapter 5).

In Fig. 6.4 we proceed to asses the capacitance model results including the non-parabolic effects. Specifically, Fig. 6.4 shows C_g versus V_g for a $2R_s = 10$nm InGaAs NW. Non-parabolic results are plotted as dashed lines while parabolic ones correspond to solid lines. The model results are represented as solid red in the parabolic approach, and dashed green and red in the non-parabolic approach using the first and second approximation, respectively. As can be seen, when non-parabolic effects are included, the gate capacitance curve shows a shift in the position of the peaks, displaced to lower gate

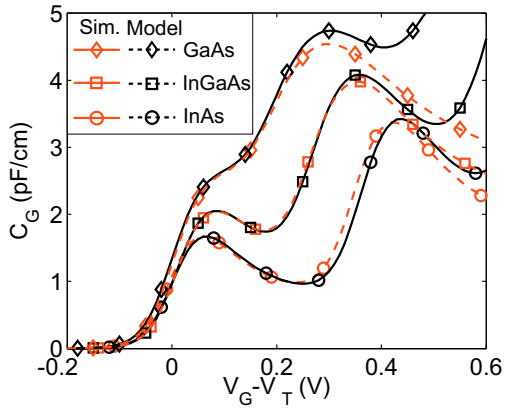

Figure 6.3: Gate capacitance versus gate overdrive voltage for InAs (circles), InGaAs (squares) and GaAs (diamonds) $2R_s = 10$nm NWs. Solid and dashed lines correspond to simulation and model results respectively.

voltages, and in their values, that are increased. Regarding the two approximations employed to include the non-parabolicity, the first one fits well the non-parabolic simulation results up to $V_g = 0.8$V. However, for higher gate voltages C_g is underestimated in the same amount than the parabolic description. The advantage of this first non-parabolic description is the simplicity of the resulting mathematical expression which is accurate for low V_g, being later used in Section 6.5 for the threshold voltage calculation. On the contrary, the second one accurately reproduces the simulation results up to $V_g \simeq 1$V, at the cost of a more complex expression. Hereinafter, the parabolic description is used to discuss the model and gain some further insight on the different terms that determine the gate capacitance behavior.

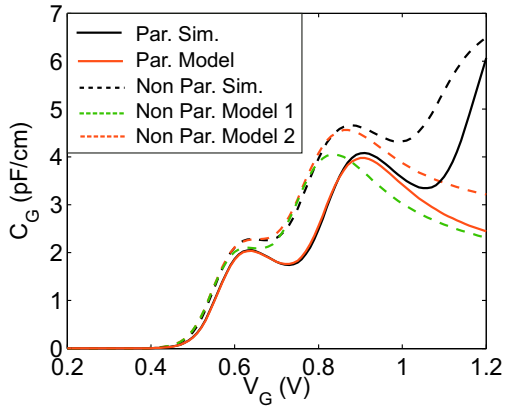

Figure 6.4: Gate capacitance versus gate voltage for a $2R_s = 10$nm InGaAs NW. Dashed and solid lines correspond to non-parabolic bands and parabolic results respectively. Model results are plotted as red and green while simulation results are plotted as black.

6.4 Results and discussion of the C_g model

6.4.1 Assessment of gate capacitance components.

Once the model has been validated, it is interesting to gain some further insight into the different components of the total gate capacitance. First, we shall examine how Eqs. (6.20) and (6.21) corresponding to C_{Cj} and C_{Qj} respectively reproduce the different terms of Eqs. (6.4) and (6.14). Fig. 6.5 shows the modeled C_g, C_Q and C_e in blue, red and green dashed lines respectively, for the $2R_s = 10$nm InGaAs nanowire. Numerical simulation results are plotted as symbols.

A good correspondence is found between the model and the simulations results. The misfit observed for $V_g > 1$V is due to the occupancy of higher L-valley energy levels included in the simulator. It can be clearly observed that C_Q mainly determines the C_g behavior of the InGaAs NW. This situation is directly related to the density of states bottleneck phenomenon of III-V materials [159]. The humps in C_Q are reproduced by C_g. However, their amplitude and width are modulated by C_e, which cannot be neglected, and by C_{ins}. Some differences between the model and the simulation results are observed for C_e in the range $0.8\text{V} < V_g < 1\text{V}$. This discrepancy arises from the initial assumption that considers $|R_j(r)|^2$ independent on ψ_c, and therefore on V_g, –see Eq. (6.10)–. To achieve a better fit between model and simulation for C_e, this dependence

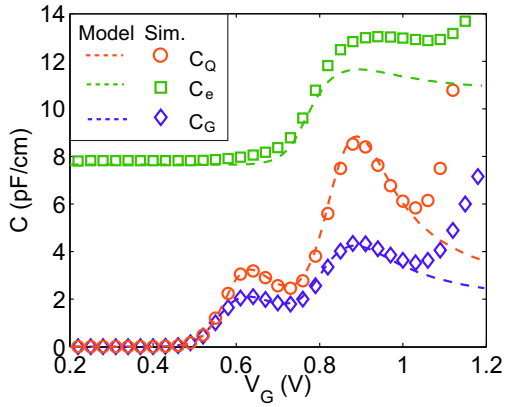

Figure 6.5: Simulation (symbols) and model (dashed lines) results for C_g (blue), C_Q (red) and C_e (green) as a function of V_g for a $2R_s$ = 10nm InGaAs NW

should be taken into consideration, increasing notably the complexity of the model. Nevertheless C_e is not the dominant contribution to C_g and therefore the agreement between model and simulation for C_g is still good in that range of applied bias.

Fig. 6.6 presents the results of a more detailed insight in the behavior of C_e. Specifically, it shows the contribution of each $C_{Cj}C_Q/C_{Qj}$ term achieved from the simulation (squares) and model (red and blue dashed lines). Again, just the first three energy levels ($j = 0$ and $j = 1, 2$) were considered. C_e is plotted as a dashed green line. The C_{Cj} terms are also shown (solid lines and circles for model and simulation respectively). As can be seen, a good fit between the model and the simulation results is observed for all terms until V_g reaches 1V. For small V_g, only the first energy level ($j = 0$) is populated, and therefore $C_Q = C_{Q0}$ and $C_e = C_{C0}$. In this range, it is possible to consider C_{inv} as the series combination of C_{Q0} and C_{C0}, which is the quantum limit scenario [180]. As soon as the $j = 1, 2$ doubly degenerate energy levels are occupied, its quantum capacitance, C_{Q1}, is not negligible. Then, the ratio C_Q/C_{Q0} rises and so does the term $C_{C0}C_Q/C_{Q0}$ which is no longer equal to C_{C0}. Moreover, $C_{C1}C_Q/C_{Q1}$ is higher than the centroid capacitance C_{C1}, because $C_Q > C_{Q1}$. For $V_g \gtrsim 0.8$V $C_{Q1} > C_{Q0}$ (see the rate of increase of the charge in the inset of Fig. 6.2) and, as a consequence, $C_{C1}C_Q/C_{Q1} < C_{C0}C_Q/C_{Q0}$. Then, C_e increases from its C_{C0} initial value, and tends to C_{C1}. For $V_g > 1$V, the C_Q/C_{Qj} ratio is underestimated by the model (as more energy levels –belonging to L-valley– are being occupied while the model considers $C_Q = C_{Q0} + C_{Q1}$) and so are the terms $C_{Cj}C_Q/C_{Qj}$.

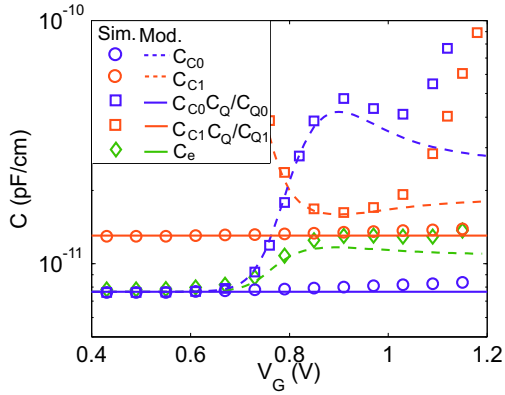

Figure 6.6: Contribution of each term to C_{e}. Model and simulation results are plotted as lines and symbols respectively for the same device as in Fig. 6.5.

Regarding the values calculated for $C_{\mathrm{C}j}$, the simulated $C_{\mathrm{C}j}$ remains almost constant with V_{g}. This is consistent with the model proposed in Chapter 5 which assumes that ξ_j does not depend on V_{g} in III-V NWs. As a consequence, the model fits well the simulated results. Moreover, $C_{\mathrm{C}j}$ can be closely associated to an inversion layer position [159]: Fig. 6.7 shows the first three simulated wavefunctions at $V_{\mathrm{g}} = 0.8$V and their corresponding inversion layer effective centroid determined in the way proposed by Lee *et al.* [159] from the model Eqs. (C.9), (C.10) and (C.11). The larger separation of the effective position of the charge respect to the semiconductor-insulator interface of level $j = 0$ is consistent with the smaller C_{C0} (dashed blue) observed in Fig. 6.6.

6.4.2 Material comparison

To achieve a better understanding of the performance limits of III-V NWs, it is interesting to compare some of the previous results with those of a Si NW. To do it, we have assumed an isotropic effective mass model for Si, with a confinement effective mass for Δ_4 valleys given by $m^* = (2m_{\mathrm{l}} + m_{\mathrm{t}})/(m_{\mathrm{l}} + m_{\mathrm{t}})$ [95, 202]. In this way the electron density does not depend on the azimuthal coordinate; and a capacitance model similar to the proposed here can be considered [197]. It should be noted that in Si the wavefunction depends strongly on V_{g} and therefore C_{e} cannot be expressed as in Eq. (6.13). SiO_2 is considered as gate insulator with a thickness of $T_{\mathrm{ins}} = 0.6$nm, which is the EOT corresponding to the 1.5nm thick Al_2O_3 gate insulator used for the III-V NWs [200].

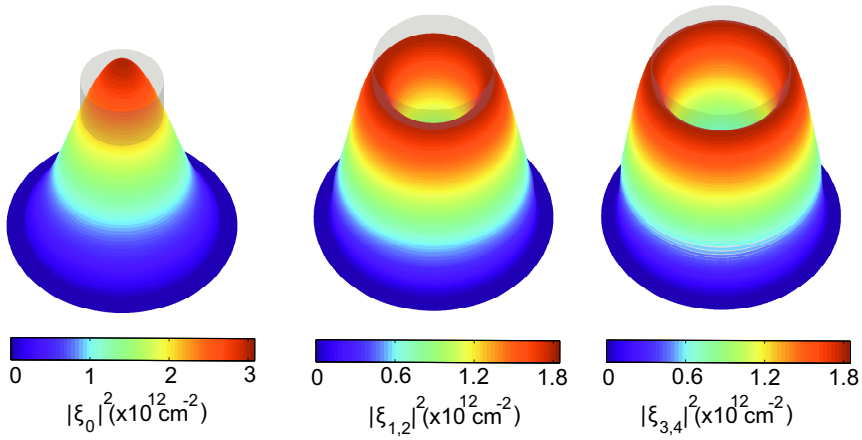

Figure 6.7: Simulated $|\xi_j|^2$ at $V_g = 0.8$V for $j = 0$ (left) and $j = 1, 2$ (center) and $j = 3, 4$ (right) subbands for the same device of Fig.6.5. The inversion layer effective centroid position is plotted as a semitransparent gray cylinder.

Fig. 6.8 shows the two contributions to C_{inv} in Eq. (6.14): C_Q (solid lines) and C_e (dashed lines), for Si (circles), InAs (diamonds), InGaAs (squares) and GaAs (stars) NWs, all with $2R_s = 10$nm, as a function of $V_g - V_T$. It is important to note that the Si curves were obtained numerically from Eqs. (6.5) and (6.6), while the corresponding InAs, InGaAs and GaAs curves were calculated using the analytical expressions, as proposed previously. For the III-V nanowires, the values of V_T commented in Section 6.3 are used again. For Si, V_T is numerically determined obtaining a value $V_T = 0.52$V.

It can be observed that while C_Q is the dominant term for the III-V nanowires, it is negligible for Si in the strong inversion regime. The different values of C_Q in InAs, InGaAs and GaAs can be explained attending to the differences in their Γ-valley effective masses. First, the lowest confinement effective mass of InAs increases the separation between humps in C_Q with respect to InGaAs or GaAs. Second, the largest density of states effective mass of GaAs rises C_Q up to values above C_e. Hence, in this material C_{inv} is controled simultaneously by C_Q and C_e.

It is interesting to analyse the contribution of C_e for the different materials. For gate voltages below V_T, in III-V NWs as well as in Si, C_e remains almost constant. In the III-V NWs $C_e = C_{C0}$ and the differences observed among InAs, InGaAs and InAs are mainly due to ϵ_s in Eq. (6.29) and slightly to their effective mass and the wavefunction penetration into the gate insulator. The dependence of C_e with V_g is strongly influenced

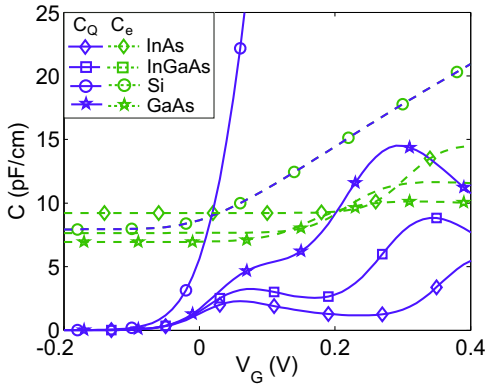

Figure 6.8: Gate capacitance as a function of the gate overdrive voltage. $C_{\rm Q}$ and $C_{\rm e}$ are plotted as solid blue and dashed green, respectively, for a $2R_{\rm s}$ = 10nm Si (circles), InAs (diamonds), InGaAs (squares) and GaAs (stars) NW.

by $C_{\rm Q}$. In this way, $C_{\rm e}$ in InAs remains constant until $V_{\rm g} - V_{\rm T} \simeq 0.25$V where the second energy level starts to get populated, while in GaAs this variation in $C_{\rm e}$ appears for $V_{\rm g} - V_{\rm T} \simeq 0.1$V.

In Si the situation is completely different. $C_{\rm e}$ remains constant only in the subthreshold region and then it grows linearly with $V_{\rm g} - V_{\rm T}$. Moreover, since $C_{\rm Q}$ is very high, $C_{\rm e}$ determines $C_{\rm inv}$ in the inversion regime for the Si NW. $C_{\rm e}$ is closely related –see Eq. (6.13)– to the difference between the surface and the center potential in the NW. Therefore, to understand the differences in the $C_{\rm e}$ behavior in Si with respect to III-V materials it is interesting to analyze the behavior of $\psi_{\rm s}$ and $\psi_{\rm c}$ with $V_{\rm g}$. Fig. 6.9 shows $\psi_{\rm s}$ (circles) and $\psi_{\rm c}$ (squares) in the Si (solid lines) and InGaAs (dashed lines) NWs as a function of the gate voltage. In strong inversion, $\psi_{\rm c}$ is screened by the charge in Si, and therefore it becomes constant while for InGaAs $\psi_{\rm c}$ keeps on increasing although at a lower rate than $\psi_{\rm s}$. This is the reason why $C_{\rm e}$ increases almost linearly with $V_{\rm g}$ in Si but not in InGaAs. As proposed by Knoch *et al.* [181], this fact could be an interesting advantage to allow a better electrostatic control of the channel and then to reduce the short channel effects in III-V NWs.

We can complete the comparison between Si and III-V materials by studying the gate capacitance dependence on the EOT. Fig. 6.10 shows $C_{\rm g}$, for $V_{\rm g} - V_{\rm T} = 0.3$V, as a function of the EOT for $2R_{\rm s}$ = 10nm Si (circles), InAs (diamonds), InGaAs (squares) and GaAs (stars) NWs. The insulator capacitance $C_{\rm ins}$ is also plotted as a dashed

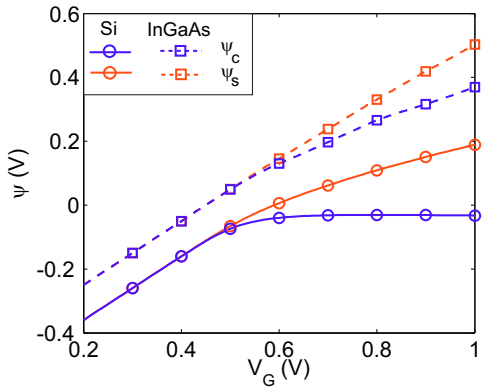

Figure 6.9: Surface (circles) and center (squares) potential in a Si (solid) and an InGaAs (dashed) $2R_s = 10$nm NW.

line. Again the Si curve was numerically obtained –from Eq. (6.2)– while for the InAs, InGaAs and GaAs NWs, C_g was determined using the analytical model. For the

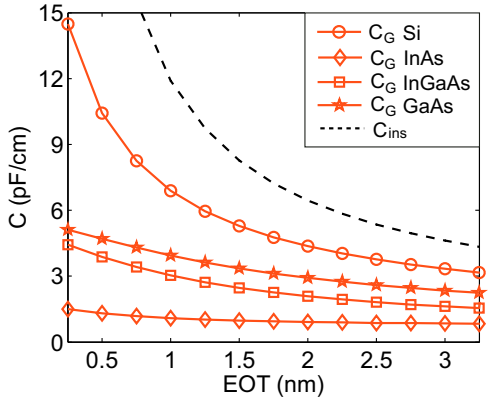

Figure 6.10: Gate capacitance as a function of the EOT for a $2R_s = 10$nm Si (circles), InAs (diamonds), InGaAs (squares) and GaAs (stars) NW. C_{ins} is also plotted as dashed a line.

Si NW the gate capacitance strongly depends on the EOT, mimicing the behavior of C_{ins}. However, for III-V materials, C_g is slightly affected by C_{ins}, or by a change in the EOT, since C_{inv} is the dominant contribution and it is almost independent of the EOT, as already shown by the analytical model here proposed. This is an important result which demonstrates the restricted impact of the continuous EOT scaling on the performance improvement of III-V NWs, in contrast to the traditional trend of silicon

devices.

6.4.3 Effect of the wavefunction penetration

Finally, we have performed a comparison of the results with and without wavefunction penetration into the gate oxide. Fig. 6.11 shows the gate capacitance as a function of the gate voltage for the $2R_s = 10$nm InGaAs NW considering a finite (squares) and infinite (circles) potential barrier. In both scenarios the model (dashed lines) fits well the simulation results (solid lines) until $V_g \simeq 1$V. It should be noticed that while the second hump is clearly present in the simulation results for the finite potential well case, it is not in the infinite one. In the former case, the upper energy levels are due to the Γ-valley, while in the later case they are due to the L-valley. The higher conduction effective mass of this valley tends to strongly increase C_Q, hiding the second hump. Furthermore, the position of the humps is modified when no wavefunction penetration is considered. This is because the resulting energy levels differ significantly (see Fig. 5.7 in Chapter 5) as it was also observed for planar devices [96]. Moreover, the amplitude of the humps is reduced when no wavefunction penetration is included. This can be explained attending to a displacement of the charge position in the semiconductor farther from the semiconductor-insulator interface (as it was shown in Fig. 5.9 in Chapter 5),

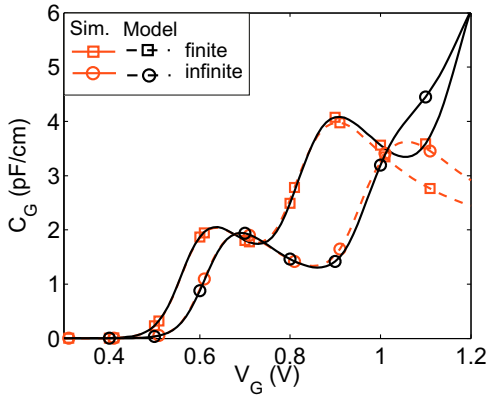

Figure 6.11: Gate capacitance versus gate voltage for a $2R_s = 10$nm InGaAs NW. Solid and dashed lines correspond to simulation and model results respectively. Infinite and finite potential barrier are plotted as circles and squares respectively.

6.5 Threshold voltage modeling

In this Section we propose an analytical model for the threshold voltage of III-V NWs under a parabolic dispersion relation. Due to the relevance of non-parabolicity in III-V materials, the resulting expression will be modified in Sections 6.6 and 6.7 to consider non-parabolicity of the conduction band and interface states, respectively. The NW structure is the same as depicted in Fig. 5.1. As mentioned in the Introduction of the present Chapter, when small MuG devices are considered, the traditional definition of V_{T} corresponding to a semiconductor surface potential band bending equal to two times the Fermi potential is no longer valid [183–185].

Here, V_{T} is calculated as the maximum of the second derivative of the electron charge per unit length as a function of the gate voltage, $d^2Q_{\mathrm{s}}/dV_{\mathrm{g}}^2$, where $Q_{\mathrm{s}} = Q_{\mathrm{i}} + Q_{\mathrm{d}}$, is the total charge in the semiconductor. Here Q_{i} and Q_{d} are the inversion and depletion charges in the semiconductor and we assume that $Q_{\mathrm{d}} = qN_{\mathrm{a}}\pi R_{\mathrm{s}}^2$ does not depend on V_{g}. This definition of V_{T} has been satisfactorily used in the study of the corner effects in MuG MOSFETs [203]. We recall the expression for Q_{i} under parabolic dispersion relation introduced in Chapter 5. There, we showed that, around V_{T}, Q_{i} can be calculated by the carriers in the first subband (see Fig. 5.7 in Chapter 5). Thus, the resulting expression for Q_{i} around threshold is:

$$Q_{\mathrm{i}} = qg(\hat{E}_0) = qg_v\sqrt{\frac{2m_{\mathrm{t}}k_{\mathrm{B}}T}{\pi\hbar^2}}\mathcal{F}_{-\frac{1}{2}}\left(-\frac{\hat{E}_0 + \Delta\hat{E}_0 - q\psi_{\mathrm{c}}}{k_{\mathrm{B}}T}\right) \tag{6.24}$$

where the nomenclature introduced in Chapter 5 is kept.

However, in order to develop a simple compact model, Q_{i} in Eq. (6.24) can be further simplified. For low gate voltages $\Delta\hat{E}_0$ can be neglected since the potential in the cross section of the NW is nearly flat and, consequently, this factor is not relevant (see Fig. 5.7a in Chapter 5). So, after renaming $N_{\mathrm{c}} = qg_v\sqrt{2m_{\mathrm{t}}k_{\mathrm{B}}T/\pi\hbar^2}$, we can write

$$Q_{\mathrm{i}} = N_{\mathrm{c}}\,\mathcal{F}_{-\frac{1}{2}}\left(-\frac{\hat{E}_0 - q\psi_{\mathrm{c}}}{k_{\mathrm{B}}T}\right) \tag{6.25}$$

Additionally, the gate capacitance, C_{g}, was defined in Eq. (6.1) as:

$$C_{\mathrm{g}} \equiv \frac{dQ_{\mathrm{G}}}{dV_{\mathrm{g}}} = -\frac{dQ_{\mathrm{s}}}{dV_{\mathrm{g}}} = -\frac{dQ_{\mathrm{i}}}{dV_{\mathrm{g}}} \tag{6.26}$$

where Q_{G} is the gate charge. For just one subband, we got in Section 6.2 that C_{g} can be expressed as:

$$C_{\mathrm{g}} = \left(\frac{1}{C_{\mathrm{ins}}} + \frac{1}{C_{\mathrm{Q0}}} + \frac{1}{C_{\mathrm{C0}}} \right)^{-1} \tag{6.27}$$

where C_{Q0} and C_{C0} were the quantum and centroid capacitances due to the first subband:

$$C_{\mathrm{Q0}} = \frac{dQ_{\mathrm{i}}}{d\psi_{\mathrm{c}}} = \frac{q}{k_{\mathrm{B}}T} N_{\mathrm{c}} \mathcal{F}_{-\frac{3}{2}} \left(-\frac{\hat{E}_0 - q\psi_{\mathrm{c}}}{k_{\mathrm{B}}T} \right) \tag{6.28}$$

$$C_{\mathrm{C0}} = \frac{4\pi\epsilon_{\mathrm{s}}}{A_0^2 R_{\mathrm{s}}^2 \left(J_1^2(\gamma_0 R_{\mathrm{s}}) + J_0^2(\gamma_0 R_{\mathrm{s}}) - \dfrac{J_0(\gamma_0 R_{\mathrm{s}}) J_1(\gamma_0 R_{\mathrm{s}})}{\gamma_0 R_{\mathrm{s}}} \right)} \tag{6.29}$$

For the sake of simplicity we define:

$$\frac{1}{C_{\mathrm{geom}}} \equiv \frac{1}{C_{\mathrm{ins}}} + \frac{1}{C_{\mathrm{C0}}} \tag{6.30}$$

Then:

$$\frac{d^2 Q_{\mathrm{i}}}{dV_{\mathrm{g}}^2} = -\frac{d}{dV_{\mathrm{g}}} \left(\frac{1}{\dfrac{1}{C_{\mathrm{geom}}} + \dfrac{1}{C_{\mathrm{Q0}}}} \right) = \frac{\dfrac{dC_{\mathrm{Q0}}}{dV_{\mathrm{g}}}}{\left(1 + \dfrac{C_{\mathrm{Q0}}}{C_{\mathrm{geom}}} \right)^2} \tag{6.31}$$

Using the Gauss law we can write:

$$V_{\mathrm{g}} - \Phi_{\mathrm{ms}} - \psi_{\mathrm{s}} = \frac{Q_{\mathrm{i}}}{C_{\mathrm{ins}}} + \frac{Q_{\mathrm{d}}}{C_{\mathrm{ins}}} \tag{6.32}$$

The surface potential can be expressed in terms of ψ_{c} as:

$$\psi_{\mathrm{s}} = \psi(R_{\mathrm{s}}) = \frac{qg(\hat{E}_0)}{2\pi\epsilon_s} \frac{R_{\mathrm{s}}^2}{2} \left(J_1^2(\gamma_0 R_{\mathrm{s}}) + J_0^2(\gamma_0 R_{\mathrm{s}}) - \frac{J_0(\gamma_0 R_{\mathrm{s}}) J_1(\gamma_0 R_{\mathrm{s}})}{\gamma_0 R_{\mathrm{s}}} \right) + \frac{qN_{\mathrm{a}} R_{\mathrm{s}}^2}{4\epsilon_{\mathrm{s}}} + \psi_{\mathrm{c}} \tag{6.33}$$

where we have particularized Eq. (5.50) for just one subband. Using Eqs. (6.24) and (6.29) we can reformulate:

$$\psi_{\mathrm{s}} = \frac{Q_{\mathrm{i}}}{C_{\mathrm{C0}}} + \frac{Q_{\mathrm{d}}}{4\pi\epsilon_{\mathrm{s}}} + \psi_{\mathrm{c}} \tag{6.34}$$

Therefore, using Eq. (6.32) and assuming $dQ_{\mathrm{d}}/d\psi_{\mathrm{c}} = 0$, Eq. (6.34) can be rewritten as:

$$\frac{dV_{\mathrm{g}}}{d\psi_{\mathrm{c}}} = \frac{dQ_{\mathrm{i}}}{d\psi_{\mathrm{c}}} \frac{1}{C_{\mathrm{ins}}} + \frac{dQ_{\mathrm{i}}}{d\psi_{\mathrm{c}}} \frac{1}{C_{\mathrm{C0}}} + 1 \tag{6.35}$$

Using Eqs. (6.28) and (6.30) Eq. (6.35) transforms into:

$$\frac{dV_{\mathrm{g}}}{d\psi_{\mathrm{c}}} = \left(1 + \frac{C_{\mathrm{Q0}}}{C_{\mathrm{geom}}}\right) \tag{6.36}$$

So, applying the chain rule to $dC_{\mathrm{Q0}}/dV_{\mathrm{g}}$ in Eq. (6.31) and substituting Eq. (6.36) we get:

$$\frac{d^2Q_{\mathrm{i}}}{dV_{\mathrm{g}}^2} = \frac{\dfrac{dC_{\mathrm{Q0}}}{d\psi_{\mathrm{c}}}}{\left(1 + \dfrac{C_{\mathrm{Q0}}}{C_{\mathrm{geom}}}\right)^3} \tag{6.37}$$

Although the maximum of $d^2Q_{\mathrm{s}}/dV_{\mathrm{g}}^2$ could be determined differentiating Eq. (6.37) with respect to V_{g} and equaling the resulting expression to zero, the procedure would result in a non linear second order differential equation. Obtaining V_{T} from such expression is non trivial.

In its stead, we can consider having a deeper insight in the behavior of $d^2Q_{\mathrm{i}}/dV_{\mathrm{g}}^2$. Substituting Eq. (6.28) into Eq. (6.37) leads to:

$$\frac{d^2Q_{\mathrm{i}}}{dV_{\mathrm{g}}^2} = \frac{\left(\dfrac{q}{k_{\mathrm{B}}T}\right)^2 N_{\mathrm{c}} \mathcal{F}_{-\frac{5}{2}}\left(-\dfrac{\hat{E}_0 - q\psi_{\mathrm{c}}}{k_{\mathrm{B}}T}\right)}{\left[1 + \dfrac{\frac{q}{k_{\mathrm{B}}T}N_{\mathrm{c}}}{C_{\mathrm{geom}}}\mathcal{F}_{-\frac{3}{2}}\left(-\dfrac{\hat{E}_0 - q\psi_{\mathrm{c}}}{k_{\mathrm{B}}T}\right)\right]^3} \tag{6.38}$$

where we have used the derivative rule for the Fermi-Dirac integral: $\mathcal{F}_{i-1}(u) = d\mathcal{F}_i(u)/du$. The value of ψ_{c} that maximizes this expression is the center potential at threshold voltage: $\psi_{\mathrm{c}}^{(\mathrm{T})}$. Hereinafter we use the superscript $^{(\mathrm{T})}$ to denote the value of a potential at $V_{\mathrm{g}} = V_{\mathrm{T}}$.

For the sake of clarity let us define: $x = \left(-\hat{E}_0 + q\psi_{\mathrm{c}}\right)/k_{\mathrm{B}}T$, and $A = \frac{q}{k_{\mathrm{B}}T}\frac{N_{\mathrm{c}}}{C_{\mathrm{geom}}}$. Then, determining $\psi_{\mathrm{c}}^{(\mathrm{T})}$ in (6.38) is equivalent to obtaining the value x_{m} that maximizes

$$f(x) = \frac{\mathcal{F}_{-\frac{5}{2}}(x)}{\left[1 + A\,\mathcal{F}_{-\frac{3}{2}}(x)\right]^3} \tag{6.39}$$

The inset of Fig. 6.12 shows $f(x)$ around its maximum for four values of A. As can be seen, x_{m} varies with A, which is a function of device geometry (through C_{geom}) and of the material parameters (through N_{c}). We have found that for all device geometries

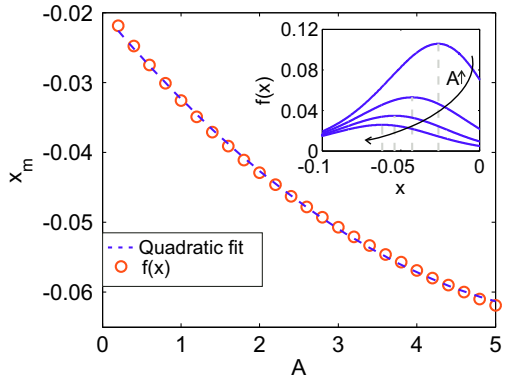

Figure 6.12: x_{m} as a function of A (red circles); quadratic fit for this dependency (blue dashed line). Inset: Detail around the maximum of $f(x)$ for the following values of A: 0.5, 2, 3.5, 5.

and material parameters considered in this study the term A is in a range from 0.2 to 5 where x_{m} varies as shown in Fig. 6.12 (symbols). This dependence can be fitted by a quadratic approximation, shown as a dashed line in Fig. 6.12 and given by:

$$x_{\mathrm{m}} = (0.038A^2 - 0.513A - 0.771) \tag{6.40}$$

Then, $\psi_{\mathrm{c}}^{(\mathrm{T})}$ can be calculated as:

$$\psi_{\mathrm{c}}^{(\mathrm{T})} = \frac{\hat{E}_0}{q} + \left[0.038\frac{q}{k_{\mathrm{B}}T}\left(\frac{N_{\mathrm{c}}}{C_{\mathrm{geom}}}\right)^2 - 0.513\frac{N_{\mathrm{c}}}{C_{\mathrm{geom}}} - 0.771\frac{k_{\mathrm{B}}T}{q}\right] \tag{6.41}$$

This expression accurately determines the center potential (referenced to E_{F}) at threshold voltage for all materials and nanowire sizes tested in this Chapter.

$\psi_{\mathrm{c}}^{(\mathrm{T})}$ and V_{T} can be related by means of the Gauss law evaluated at V_{g}=V_{T}:

$$V_{\mathrm{T}} - \Phi_{\mathrm{ms}} = \psi_{\mathrm{s}}^{(\mathrm{T})} + \frac{Q_{\mathrm{d}}}{C_{\mathrm{ins}}} + \frac{Q_{\mathrm{T}}}{C_{\mathrm{ins}}} \tag{6.42}$$

where $\psi_{\mathrm{s}}^{(\mathrm{T})}$ is the semiconductor surface potential at threshold which, from Eq. (6.34), is given by:

$$\psi_{\mathrm{s}}^{(\mathrm{T})} = \frac{Q_{\mathrm{T}}}{C_{\mathrm{C0}}} + \frac{Q_{\mathrm{d}}}{4\pi\epsilon_{\mathrm{s}}} + \psi_{\mathrm{c}}^{(\mathrm{T})} \tag{6.43}$$

being Q_{T} the inversion charge at threshold,

$$Q_{\mathrm{T}} = N_{\mathrm{c}}\, \mathcal{F}_{-\frac{1}{2}}\left(-\frac{\hat{E}_0 - q\psi_{\mathrm{c}}^{(\mathrm{T})}}{k_{\mathrm{B}}T}\right) \tag{6.44}$$

and where $\psi_{\mathrm{c}}^{(\mathrm{T})}$ was given in (6.41).

6.6 Non-parabolic correction for the V_{T} model

To provide a complete and accurate description of the threshold voltage in III-V NWs, the effect of non-parabolic bands should not be neglected. In this Section we propose a correction factor to Eq. (6.42) which takes into consideration the non-parabolicity of the Γ-valley dispersion relationship. To do it, we use the correction of the parabolic energy minimum introduced in Chapter 5, Eq. (5.60). As discussed in Fig. 5.10 in Chapter 5, this correction is accurate enough to model the Q_{i} versus V_{g} relation for low V_{g} values, and it is much simpler than the complete non-parabolic dispersion relation. Thus, using Eq. (5.60), the non-parabolic correction factor of the first energy level is:

$$\Delta\hat{E}_0^{\mathrm{NP}} = \hat{E}_0^{\mathrm{NP}} - \hat{E}_0 \tag{6.45}$$

where $\hat{E}_0$ is the parabolic band minimum and $\hat{E}_0^{\mathrm{NP}}$ is the non-parabolic band minimum given by:

$$\hat{E}_0^{\mathrm{NP}} = \hat{\phi}_0 + \frac{-1 + \sqrt{1 + 4\beta\left(\hat{E}_0 - \hat{\phi}_0\right)}}{2\beta} \tag{6.46}$$

being β the non-parabolic factor and $\hat{\phi}_0$ defined in Eq. (5.58):

$$\hat{\phi}_0 = \int_0^{2\pi}\int_0^{R_{\mathrm{s}}+t_{\mathrm{ins}}} \xi_0(r,\theta)\hat{\phi}(r)\xi_0^*(r,\theta) r\, dr\, d\theta \tag{6.47}$$

where $\hat{\phi}(r)$ is the total potential energy referred to ψ_c (see Section 5.4 for details). Consistently with the assumption made in Section 6.5 when neglecting the energy correction factor $\Delta\hat{E}_0$, we can approximate the potential in the semiconductor as flat and equal to ψ_{c}. In the insulator we have to add the potential barrier $\Delta\phi$ to consider the total potential energy. Therefore, $\hat{\phi}(r)$ can be approximated by zero inside the

semiconductor and by $\Delta\phi$ in the insulator. Then $\hat{\phi}_0$ is given by[2]:

$$\hat{\phi}_0 = \frac{1}{2\pi}\int_0^{2\pi}\int_{R_s}^{R_s+t_{ins}} C_0 K_0(\alpha_0 r)\Delta\phi C_0^* K_0^*(\alpha_0 r) r dr d\theta = \Delta\phi\, C_0^2 \int_{R_s}^{R_s+t_{ins}} |K_0(\alpha_0 r)|^2 r dr =$$
$$\Delta\phi\, C_0^2 \left(\frac{R_s^2}{2}[K_0^2(\alpha_0 R_s) + K_1^2(\alpha R_s)] - \frac{R_s + t_{ins}}{2}[K_0^2(\alpha_0(R_s + t_{ins})) + K_1^2(\alpha_0(R_s + t_{ins}))] \right) \tag{6.48}$$

where we have used Eqs. (6.15) and (B.5) However, a more compact expression for $\hat{\phi}_0$ can be easily obtained if we approximate K_0 by [204]:

$$K_0(\alpha_0 r) \cong \sqrt{\frac{\pi}{2\alpha_0 r}} e^{-\alpha_0 r} \tag{6.49}$$

which for the expected values of $\alpha_0 r > 10$ (all practical cases have been checked) introduces an error lower than 3%. The validation of such an approximation is showed in Appendix **??**. Therefore, substituting Eq. (6.49) into Eq. (6.48) gives:

$$\hat{\phi}_0 = \frac{\Delta\phi\, C_0^2 \pi}{4\alpha_0^2} e^{-2\alpha_0 R_s} \left(1 - e^{-2\alpha_0 t_{ins}}\right) \tag{6.50}$$

The term $e^{-2\alpha_0 t_{ins}}$ is actually much smaller than 1 for all practical values of the potential barrier, semiconductor radius, confinement effective mass (which determine α_0) and t_{ins} and therefore it can be neglected. Then, using Eq. (6.50) in Eqs. (6.46) and (6.45) the non-parabolic correction factor becomes:

$$\Delta\hat{E}_0^{NP} = \frac{\Delta\phi\, C_0^2 \pi}{4\alpha_0^2} e^{-2\alpha_0 R_s} - \hat{E}_0 + \frac{-1 + \sqrt{1 + 4\beta\left(\hat{E}_0 - \Delta\phi\, C_0^2 \pi e^{-2\alpha_0 R_s}/4\alpha_0^2\right)}}{2\beta} \tag{6.51}$$

This non-parabolic correction factor modifies the energy level in Eq. (6.25). But, as can be inferred from Eqs. (6.41) and (6.42), this is equivalent to a shift in V_T given by $\Delta\hat{E}_0^{NP}/q$. Therefore, the threshold voltage expression taking into consideration non-parabolic bands is:

$$V_T = \Phi_{ms} + \frac{Q_T}{C_{C0}} + \frac{Q_d}{4\pi\epsilon_s} + \frac{Q_T}{C_{ins}} + \frac{Q_d}{C_{ins}} + \psi_c^{(T)} + \frac{\Delta\hat{E}_0^{NP}}{q} \tag{6.52}$$

[2]Please remind that C_0 is not a capacitance, but the normalization constant of the wavefunction in the insulator

where $\psi_{\mathrm{c}}^{(\mathrm{T})}$ is given by Eq. (6.41), Q_{T} by Eq. (6.44) and $\Delta\hat{E}_{\mathrm{NP}}$ by Eq. (6.51).

6.7 Influence of interface states on V_{T}

In this Section we discuss the effect of an arbitrary profile of interface states on the threshold voltage. To this end we first determine the variation of ψ_{c} due to a non-null D_{it}. As shown by Eq. (6.52) this variation of ψ_{c} can be right away translated into a variation in V_{T}. Therefore, we define the correction factor of V_{T} due to a non-null D_{it} as:

$$\Delta V_{D_{\mathrm{it}}} = \psi_{\mathrm{c}}^{\mathrm{w}D_{\mathrm{it}}} - \psi_{\mathrm{c}}^{\mathrm{w/o}D_{\mathrm{it}}} \tag{6.53}$$

where the superscript wD_{it} and w/oD_{it} are used henceforth to refer to quantities with and without D_{it}. To determine this difference we make use the model equations from Sections 5.3 and 5.5. From Eq. (5.50) we get a generic expression for the center potential, which taking into account that $J_v(0) = 0$ for $v \neq 0$ and $J_0(0) = 1$:

$$\psi_{\mathrm{c}} = \frac{q}{2\pi\epsilon_a}\sum_{j=0}^{N} g(\hat{E}_j)\frac{A_j^2 l}{2\gamma_j^2} + D_a \tag{6.54}$$

The first term in the right-hand-side of Eq. (6.54) is not modified if D_{it} is considered. As explained in Section 5.5 the presence of a non-null D_{it} modify the insulator integration constant C_b, see Eq. (5.48), and consequently constants D_b and D_a which depend on it, see Eqs. (5.47) and (5.49). Therefore, we can reformulate Eq. (6.53) as:

$$\Delta V_{D_{\mathrm{it}}} = D_a^{\mathrm{w}D_{\mathrm{it}}} - D_a^{\mathrm{w/o}D_{\mathrm{it}}} \tag{6.55}$$

where D_a is given by:

$$D_a = \frac{q}{2\pi\epsilon_b}\sum_{j=0}^{N} g(\hat{E}_j)\varphi_j^b(R_{\mathrm{s}}) + C_b\ln(R_{\mathrm{s}}) + D_b - \frac{q}{2\pi\epsilon_a}\sum_{j=0}^{N} g(\hat{E}_j)\varphi_j^a(R_{\mathrm{s}}) - \frac{q}{\epsilon_a}\frac{R_{\mathrm{s}}^2}{4}N_a \tag{6.56}$$

Since the expression for φ_j^a, φ_j^b and $g(\hat{E}_j)$ do not depend on D_{it} we get:

$$D_a^{\mathrm{w}D_{\mathrm{it}}} - D_a^{\mathrm{w/o}D_{\mathrm{it}}} = (C_b^{\mathrm{w}D_{\mathrm{it}}} - C_b^{\mathrm{w/o}D_{\mathrm{it}}})\ln(R_{\mathrm{s}}) + (D_b^{\mathrm{w}D_{\mathrm{it}}} - D_b^{\mathrm{w/o}D_{\mathrm{it}}}) \tag{6.57}$$

with $C_b^{\mathrm{w}D_{\mathrm{it}}}$ and $C_b^{\mathrm{w/o}D_{\mathrm{it}}}$ given by Eqs. (5.66) and (5.48). We recall them here:

$$C_b^{\mathrm{w}D_{\mathrm{it}}} = \frac{R_{\mathrm{s}}}{\epsilon_b}\left(\frac{1}{2\pi}\sum_{j=0}^{N} g(\hat{E}_j)\psi_j'^a(R_{\mathrm{s}}) + \frac{qN_aR_{\mathrm{s}}}{2} - \frac{1}{2\pi}\sum_{j=0}^{N} g(\hat{E}_j)\psi_j'^b(R_{\mathrm{s}})\right) - \frac{R_{\mathrm{s}}}{\epsilon_b}Q_{\mathrm{it}} \quad (6.58)$$

$$C_b^{\mathrm{w/o}D_{\mathrm{it}}} = \frac{R_{\mathrm{s}}}{\epsilon_b}\left(\frac{1}{2\pi}\sum_{j=0}^{N} g(\hat{E}_j)\psi_j'^a(R_{\mathrm{s}}) + \frac{qN_aR_{\mathrm{s}}}{2} - \frac{1}{2\pi}\sum_{j=0}^{N} g(\hat{E}_j)\psi_j'^b(R_{\mathrm{s}})\right) \quad (6.59)$$

where Q_{it} is the charge due to active interface traps. As discussed in Section 5.5 it comes from an integration of D_{it} whose limits depends on ψ_{s}. For the sake of simplicity, we consider here that all the traps are active at threshold voltage, which is not an unrealistic scenario looking at ψ_{s} for voltage values close to V_{T} (see Fig. 5.14 in Chapter 5). From Eq. (6.59) is it straightforward to find:

$$C_b^{\mathrm{w}D_{\mathrm{it}}} - C_b^{\mathrm{w/o}D_{\mathrm{it}}} = \frac{R_{\mathrm{s}}}{\epsilon_b}Q_{\mathrm{it}} \quad (6.60)$$

Finally, D_b was given by Eq. (5.49):

$$D_b = V_{\mathrm{g}} - \Phi_{\mathrm{ms}} - \frac{1}{2\pi\epsilon_b}\sum_{j=0}^{N} g(\hat{E}_j)\varphi_j^b(R_{\mathrm{s}} + t_{\mathrm{ins}}) - C_b\ln(R_{\mathrm{s}} + t_{\mathrm{ins}}) \quad (6.61)$$

None of the terms in the right hand side of Eq. (6.61), except C_b, depend on D_{it}. Then, introducing Eq. (6.60) into Eq. (6.61),

$$D_b^{\mathrm{w}D_{\mathrm{it}}} - D_b^{\mathrm{w/o}D_{\mathrm{it}}} = -\frac{R_{\mathrm{s}}}{\epsilon_b}Q_{\mathrm{it}}\ln(R_{\mathrm{s}} + t_{\mathrm{ins}}) \quad (6.62)$$

Substituting Eqs. (6.57), (6.60) and (6.62) into Eq. (6.55) we get:

$$\Delta V_{D_{\mathrm{it}}} = -\frac{Q_{\mathrm{it}}}{C_{\mathrm{ins,s}}} \quad (6.63)$$

being $C_{\mathrm{ins,s}} = \epsilon_b/R_{\mathrm{s}}\ln\left(1 + \frac{t_{\mathrm{ins}}}{R_{\mathrm{s}}}\right)$ the insulator capacitance per unit surface Although Eq. (6.63) is a commonly used formula in the literature, getting it reinforces the validity of the aforementioned model equations. The resulting threshold voltage expression

including D_{it} is:

$$V_{\mathrm{T}} = \Phi_{\mathrm{ms}} + \frac{Q_{\mathrm{T}}}{C_{C0}} + \frac{Q_{\mathrm{d}}}{4\pi\epsilon_s} + \frac{Q_{\mathrm{T}}}{C_{\mathrm{ins}}} + \frac{Q_{\mathrm{d}}}{C_{\mathrm{ins,s}}} + \psi_{\mathrm{c}}^{(\mathrm{T})} + \frac{\Delta\hat{E}_0^{\mathrm{NP}}}{q} - \frac{Q_{\mathrm{it}}}{C_{\mathrm{ins,s}}} \tag{6.64}$$

6.8 Validation and Results of the V_{T} model

In this section, the results obtained with the threshold voltage model have been compared with the solution of the simulator presented in Chapter 3. InAs, $In_xGa_{1-x}As$ (x=0.53) and GaAs were considered as semiconductor materials. The values of the Γ-valley effective masses, and non parabolicity factors are summed up in Appendix F. Al_2O_3 was used as gate insulator, although the validity of the V_{T} model was also checked for other insulator materials. Different NW sizes and oxide thicknesses were studied. The simulation results for V_{T} were obtained from the maximum of the second derivative of the charge with respect to the gate voltage.

The main assumption of the V_{T} model considers that Q_{i} can be described, around V_{T}, by just one energy sub-band. To check the validity of this premise, Fig. 6.13 shows the V_{T} simulation results when only the first sub-band (solid) and when all sub-bands (dashed) for a InAs NW. Some small differences are observed for large NW sizes ($2R_{\mathrm{s}} = 20$nm). To explain this behavior, the inset in Fig. 3 depicts the potential energy profile in the cross-section of two InAs NWs with $2R_{\mathrm{s}} = 5$nm and $2R_{\mathrm{s}} = 20$ nm at V_{T}, including the first subband energy level (solid) and the following ones (dotted). The Fermi level (dashed) is also depicted as the energy reference. For the smaller device, the separation between the first energy level and the following ones is quite large, reducing the population of the rest of the subbands and therefore confirming our assumption. For the larger device, the separation is reduced explaining the higher influence of the following subbands on the calculated V_{T} . Still, this discrepancy is small enough to validate the starting hypothesis.

Fig. 6.14 shows the modeled V_{T} (solid lines) as a function of the NW diameter for different III-V semiconductor materials: InAs (red), InGaAs (blue) and GaAs (green). Again $t_{\mathrm{ins}} = 1.5$nm was considered. Several NW sizes (from $2R_{\mathrm{s}}$ =5nm to 20nm) were simulated for each material (unfilled symbols). As can be seen, the model shows a good agreement for all NW sizes and materials.

To analyze the influence of the wavefunction penetration into the gate insulator on the determination of V_{T}, we have also plotted the infinite potential barrier case in

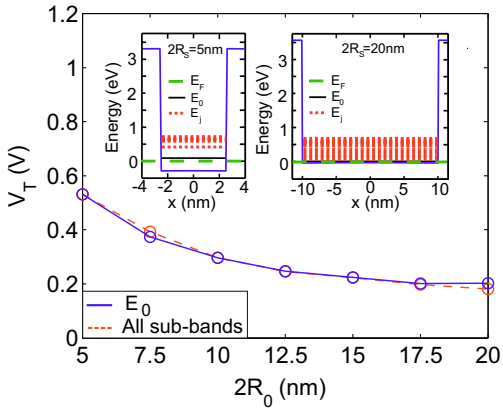

Figure 6.13: Threshold voltage versus NW diameter for a InAs NW considering the lowest subband (solid) or all the subbands (dashed). The inset shows the potential well, Fermi level (dashed), first energy level (solid) and following energy levels (red) for InAs NWs with $2R_{\rm s} = 5$nm (left) and $2R_{\rm s} = 20$nm (right) at $V_{\rm T}$ (dashed).

Fig. 6.14. Dashed lines and filled symbols correspond to model and simulation results respectively. We can see that the model also fits the simulation results for the infinite potential barrier [205],[98]. Larger differences in $V_{\rm T}$, between infinite and finite potential barrier cases, are observed for all materials when small NW sizes are considered. The higher influence of the infinite barrier in small NWs is due to their higher confinement that increases the value of the energy levels. The differences observed between the infinite and finite potential barrier cases are more relevant for the InAs NWs. The reason is that this material has the lowest confinement effective mass and therefore the largest wavefunction penetration into the gate insulator.

When very small devices are considered, the Γ-valley effective mass can notably differ from its bulk value [201]. This dependence can be included in the model. In fact, the model allows to consider different transport and confinement effective masses (m_a^* and m_a, respectively). Thereby, m_a^* affects to the $N_{\rm c}$ factor in Eq. (6.24) and m_a to $\hat{E}_0$ in Eq. (5.18)

Fig. 6.15 shows the threshold voltage as a function of the Γ-valley effective mass for two InGaAs NW sizes. To keep the figure simple, we have considered a isotropic effective mass: $m_a = m_a^*$. The rest of the material parameters (i.e. potential barrier, non-parabolicity factor, dielectric constant, etc.) are the characteristic ones of InGaAs. The simulation and model results are plotted as symbols and lines, respectively. A

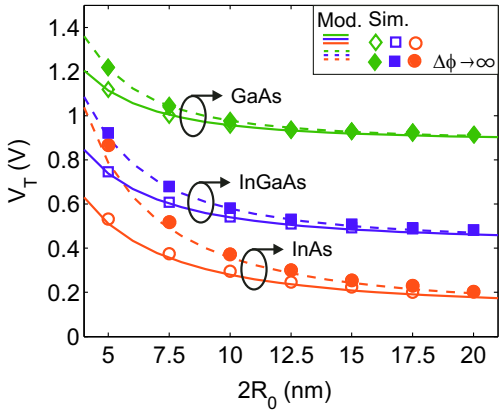

Figure 6.14: Threshold voltage versus NW diameter for InAs (circles), InGaAs (squares) and GaAs (diamonds) NWs. Solid lines and unfilled symbols correspond to model and simulation results with finite potential barrier respectively. Dashed lines and filled symbols are the model and simulation results when an infinite potential barrier case is considered.

good fit is observed for all effective mass values. As can be seen, a lower m_a increases the threshold voltage.

It is worthy to assess the contribution of the different components of Eq. (6.52) to V_T. Fig. 6.16 shows these contributions as a function of the nanowire diameter for: (a) InAs and (b) GaAs NWs. The contribution of the depletion charge term has not been plotted as it is several orders of magnitude lower than any other, for the doping level, $N_a = 10^{14}\text{cm}^{-3}$, considered in this Chapter. As can be seen, in general, just three terms control almost completely the V_T behavior: Φ_{ms}, $\psi_c^{(T)}$ and ΔE_0^{NP}. The influence of the inversion onset charge term, $Q_T\left(C_{C0}^{-1} + C_{ins}^{-1}\right)$, is negligible for all the NW sizes. The influence of the non-parabolic correction is much smaller in the GaAs devices (Fig. 6.16b) than in the InAs NWs (Fig. 6.16a). The reason is the lower value of the non-parabolicity factor of the Γ-valley, β, in GaAs (see Appendix F). Moreover, for GaAs NW sizes larger than $2R_s = 10$nm, V_T is roughly determined by Φ_{ms}.

Finally, the validity of the model for different insulator thicknesses is discussed. Fig. 6.17 shows the simulation (symbols) and model (solid lines) V_T results as a function of t_{ins} for $2R_s = 10$nm GaAs (green), InGaAs (blue) and a InAs (red) NWs. The results corresponding to two InGaAs NWs of $2R_s = 5$nm and $2R_s = 15$nm are also plotted as dashed lines (model) and as stars and triangles (simulation). As proposed

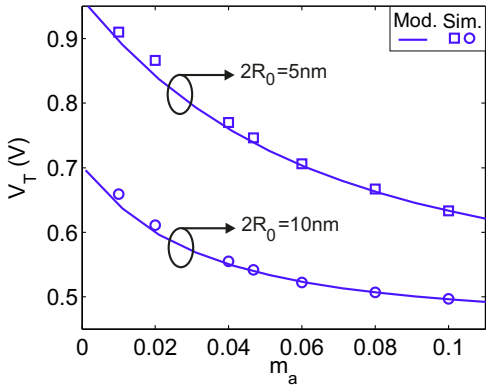

Figure 6.15: Threshold voltage for $2R_s = 5$nm and $2R_s = 10$nm InGaAs NWs considering different Γ-valley effective masses. Model and simulation results are plotted as solid lines and symbols, respectively.

in Section 6.5, V_T in III-V NWs remains approximately constant with t_{ins} as long as C_{ins} is not comparable to C_Q (see Section 6.2). The model reproduces the simulation results accurately for all proposed cases.

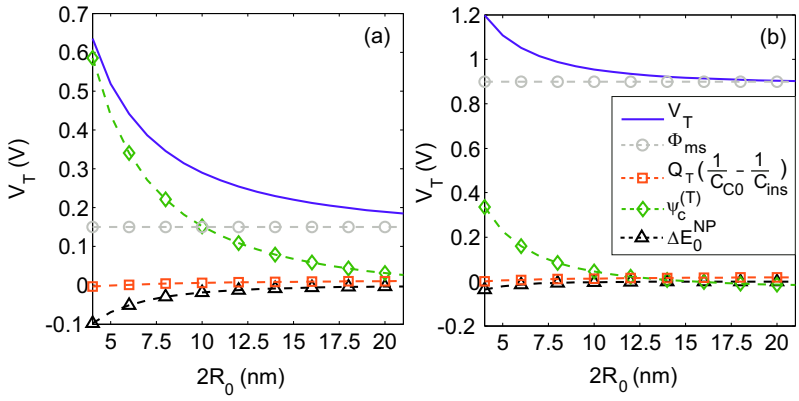

Figure 6.16: Contribution of the different terms of Eq. (6.52) to V_T for (a) a InAs and (b) a GaAs NW as a function of its size. The contribution of the depletion charge term to V_T has not been plotted as it is several orders of magnitude lower than any other.

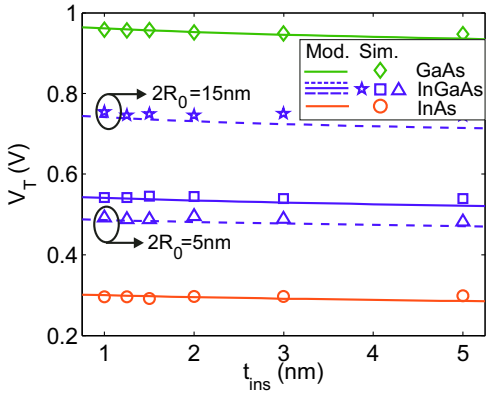

Figure 6.17: Threshold voltage versus insulator thickness for different $2R_s$ = 10nm GaAs (green), InGaAs (blue) and InAs (red) NWs. Model and simulation results are plotted as solid lines and symbols respectively. The results corresponding to two InGaAs NWs of $2R_s$ = 5nm and $2R_s$ = 15nm are also plotted as dashed lines (model) and as stars and triangles (simulation).

6.9 Conclusions

In this Chapter, we have proposed physically based analytical models for two electrostatic quantities in III-V NWs: the gate capacitance, and the threshold voltage. These models took into consideration Fermi-Dirac statistics, the conduction band non-parabolicity, and the two-dimensional quantum confinement of the carriers.

Regarding the gate capacitance model, it has been demonstrated that the model fits very well the numerical results for different NW sizes and materials, and for gate overdrive voltages up to 0.4V (in the worst case) without considering any fitting parameters. Its limitation was related to the occupancy of more than L-valley subbands and the presence of strong potential curvatures in the semiconductor which severely modify the wavefunctions obtained in Chapter 5. The different contributions to the total gate capacitance have been identified and modeled, showing their relation with the finite density of states and the charge distribution in the NWs. The capacitance behavior of III-V NWs has been compared with that of their Si counterparts. Significant differences have been found for the dominant contribution to the inversion capacitance, as well as for the semiconductor potential dependence on the gate voltage. Furthermore, we have shown the limited impact of the EOT reduction in the gate capacitance of III-V NWs, in contrast to the behavior observed in Si devices. Finally, the role of the wavefunction penetration into the gate insulator has been also analyzed, evidencing its relevance for an accurate description of the gate capacitance.

Concerning the threshold voltage model, after some reasonable approximations, we have come up with a simple expression of V_{T} that will be useful for the development of compact models for III-V cylindrical NWs. We have demonstrated that the threshold voltage expression accurately reproduces the numerical results for different III-V semiconductor materials, NW sizes, and oxide thicknesses. The influence of the wavefunction penetration into the gate insulator has been discussed, illustrating its relevance for an accurate modeling of V_{T}. The V_{T} variations due to the changes in the semiconductor effective mass have also been evaluated. We gave insight into the different contributions to the threshold voltage finding interesting differences among materials. Furthermore, we studied the V_{T} dependence on the insulator thickness, showing no relevant changes in a wide range of t_{ins} confirming that it is the quantum capacitance the main capacitance term controlling the behavior of III-V MOS structures.

Part III

Transport

Chapter 7

Boltzmann Transport Equation and Momentum Relaxation Time in a 1D electron gas

7.1 Introduction

The semi-classical study of the transport properties of a 1D electron gas implies the resolution of the Boltzmann Transport Equation (BTE) [88, 206] . As it happened with the Schrödinger and Poisson equations in the electrostatic part of this manuscript, the BTE is not straightforward to solve in complex structures. An analytical resolution is nearly unapproachable for most practical cases. For that reason, numerical solutions of the BTE are commonly used to analyze the transport behavior of electronic devices. Among them, we can highlight the Monte Carlo method, which solves the BTE collecting statistics [207–211] Deterministic approaches have also been implemented [212]. Other usual approach is the linearization of the BTE using the Momentum Relaxation Time (MRT) approximation [213–217]

In this work, we opted for evaluating the low-field electron mobility using the MRT approximation. Thus, the main goals of this Chapter are: 1) to set up the necessary background on the BTE in a 1D electron gas, spotlighting those issues which needs clear understanding and 2) present the linearization of the BTE which is used for its resolution showing the approaches needed to carry it out.

The rest of the Chapter is organized as follows. In Section 7.2 we introduce the

BTE and particularize it for the description of the electron transport in a 1D gas. Section 7.3 discuss the collision term of the BTE, that includes the effect of the the scattering phenomena and the perturbing potential that they induce through the Fermi Golden Rule. In Section 7.4, the linearization of the BTE and the definition of the MRT are presented, and highlighting their implications. Sections 7.5 and 7.6 compare two approaches (explicit and implicit) to solve the equations presented in Section 7.4. In Section 7.7, we introduce the Kubo-Greenwood formula for the calculation of the mobility from the solutions of the linearized BTE. This Chapter also includes Appendix D that deals with the scattering mechanism employed in this work. Finally, Section 7.8 recapitulate the main conclusions obtained thorough the Chapter.

7.2 Boltzmann Transport Equation

In this Section we introduce the BTE and we particularize it to characterize the transport phenomena in a 1D electron gas. The BTE describes the evolution in the real space, momentum space and time of a statistical distribution of classical particles. Its derivation can be found in several textbooks [88, 206, 218–220]. The most general formulation is:

$$\frac{df}{dt} = \left[\frac{\partial f}{\partial t}\right]_{\text{diffusion}} + \left[\frac{\partial f}{\partial t}\right]_{\text{forces}} + \left[\frac{\partial f}{\partial t}\right]_{\text{collisions}} \tag{7.1}$$

where f is the distribution function and describes the probability of finding a particle with a certain position and momentum at a given instant of time. Equation (7.1) reads as follows: the distribution function f changes with time by three different mechanisms: (i) particle's motion diffusion (which implies a change in position), (ii) external forces (which implies a change in momentum), and (iii) particle collisions.

When the particles to be modeled by the BTE are electrons in a semiconductor, $f = f(\mathbf{r}, \mathbf{k}, t)$, describes the electron distribution, and the first two factors of Eq. (7.1) can be particularized as [219], [206]:

$$\left[\frac{\partial f}{\partial t}\right]_{\text{diffusion}} = -\frac{1}{\hbar}\nabla_{\mathbf{k}} E_j(\mathbf{k}) \cdot \nabla f(\mathbf{r}, \mathbf{k}, t) \tag{7.2}$$

and

$$\left[\frac{\partial f}{\partial t}\right]_{\text{forces}} = -\frac{q\mathbf{F}}{\hbar} \cdot \nabla_{\mathbf{k}} f(\mathbf{r}, \mathbf{k}, t) \tag{7.3}$$

being $\mathbf{F}$ the external applied electric field.

The derivation of Eq. (7.2) reads as follows: the net change in the electron distribution due to electron diffusion is equal to the product of the spatial gradient, which points in the direction of spatial change of the electron distribution, times the velocity which determines the rate of spatial change of the position with time. A similar statement can be derived for Eq. (7.3).

Finally, distribution's change with time due to collisions can be written as:

$$\left[\frac{\partial f}{\partial t}\right]_{\text{collisions}} = S_{\text{in}}(\mathbf{r},\mathbf{k},t) - S_{\text{out}}(\mathbf{r},\mathbf{k},t) \tag{7.4}$$

where S_{in} and S_{out} stand for the rate of particles changing their wavevector to $\mathbf{k}$ and/or their position to $\mathbf{r}$ after a collision and the rate of particles changing their wavevector from $\mathbf{k}$ and/or their position from $\mathbf{r}$ after a collision, respectively.

Using Eqs. (7.2), (7.3) and (7.4), the BTE for electrons in semiconductors can be reformulated as [1]:

$$\frac{df(\mathbf{r},\mathbf{k},t)}{dt} + \frac{1}{\hbar}\nabla_{\mathbf{k}}E_j(\mathbf{k})\cdot\nabla f(\mathbf{r},\mathbf{k},t) + \frac{q\mathbf{F}}{\hbar}\cdot\nabla_{\mathbf{k}}f(\mathbf{r},\mathbf{k},t) = S_{\text{in}}(\mathbf{r},\mathbf{k},t) - S_{\text{out}}(\mathbf{r},\mathbf{k},t) \tag{7.5}$$

Equation (7.5) determines the change with time of the electron distribution in a 3D electron gas under a semi-classical approach[2]. However the object of interest along this manuscript is the study of MuG structures with 2D spatial confinement. The two paradigms, quantum mechanical (provided by the solution of the 2D Schrödinger and Poisson equations in the cross-section of the MuG structure in Chapter 2) and semi-classical (determined by the Boltzmann transport equation) need to be reassembled. The main assumption is to consider that the potential along the transport direction, z, of the MuG structure varies pretty slowly and thus the electron wavefunction in that direction can be approximated by a plane wave.

Then, the 2D Schrödinger and Poisson equations are solved for the NW cross-section (as proposed in Chapter 2) at each position z (and potential V) along the NW length. Since no dependence on z of the semiconductor Hamiltonian is expected, the inclusion of $V(z)$ can be modeled as a variation of the Fermi level along the NW length [213].

[1] The derivation of Eq. (7.5) is completely equivalent to that done by some authors in the literature [88] by just applying the chain rule to $df(\mathbf{r},\mathbf{k},t)/dt$ and assuming that $\mathbf{r}$ and $\mathbf{k}$ are independent and functions of time. We have opted for the one presented here as it provides a deeper understanding on the physics.

[2] Electrons in Eq. (7.5) are considered classical particles, but the collisions can be treated quantum mechanically, as will be shown in Section 7.3.

From the previous discussion we conclude that the six dimensional phase space $\mathbf{r}-\mathbf{k}$ of Eq. (7.5) is reduced to a 2D space $z-k_{\mathrm{z}}$ and Eq. (7.5) is particularized for the 1D electron gas as:

$$\frac{df_j(z,k_{\mathrm{z}},t)}{dt}+\frac{1}{\hbar}\frac{\partial E_j(k_{\mathrm{z}})}{\partial k_{\mathrm{z}}}\frac{\partial f_j(z,k_{\mathrm{z}},t)}{\partial z}+\frac{qF_{\mathrm{z}}}{\hbar}\frac{\partial f_j(z,k_{\mathrm{z}},t)}{\partial k_{\mathrm{z}}}= \\ =S_{\mathrm{in},j}(z,k_{\mathrm{z}},t)-S_{\mathrm{out},j}(z,k_{\mathrm{z}},t) \qquad (7.6)$$

where f, S_{in} and S_{out} are discretized for each subband j and $F_{\mathrm{z}}=-\partial V(z)/\partial z$ is the longitudinal component of the electric field.

In the next Section, the rates of change in the electron states due to collisions, S_{in} and S_{out}, are presented and their relation to the scattering phenomena and the perturbing potentials that they generate are discussed.

7.3 Scattering rate and perturbation potentials. Fermi Golden Rule

For an electron gas, S_{in} and S_{out} can be attributed to scattering events which perturb the electron free-flights, changing their ballistic trajectory. Three assumptions are made for the physical modeling of the scattering events: (a) the collisions occur in a very short time scale and can be considered as instantaneous; (b) the collisions produce a change in the particles trajectory modifying their wavenumber but they do not change the particles' position; and (c) the scattering interaction is weak [206].

Under these three assumptions, $S_{\mathrm{out},j}$ can be written as:

$$S_{\mathrm{out},j}(z,k_{\mathrm{z}},t)=f_j(z,k_{\mathrm{z}},t)\sum_{j',k'_{\mathrm{z}}}S_{j,j'}(k_{\mathrm{z}},k'_{\mathrm{z}})\left[1-f_{j'}(z,k'_{\mathrm{z}},t)\right] \qquad (7.7)$$

Eq. (7.7) reads as: the rate of electrons leaving the subband j and wavenumber k_{z} after a collision (also called the scattering output flux) at a given position z and time t, is equal to the probability of finding the (k_{z},j) state[3] occupied, $f_j(z,k_{\mathrm{z}},t)$, times the sum for all possible final states (k'_{z},j') of the probability of finding the state empty, $[1-f_{j'}(z,k'_{\mathrm{z}},t)]$, times the scattering rate from the state (j,k_{z}) to the state (j',k'_{z}),

[3]We use the notation (k_{z},j) to refer to an electron belonging to the subband j with wavenumber k_{z}.

$S_{j,j'}(k_z, k'_z)$. A similar reasoning can be used to obtain the scattering input flux, $S_{\text{in},j}$:

$$S_{\text{in},j}(z, k_z, t) = [1 - f_j(z, k_z, t)] \sum_{j', k'_z} S_{j',j}(k'_z, k_z) f_{j'}(z, k'_z, t) \tag{7.8}$$

Using Eqs. (7.7) and (7.8) into Eq. (7.6) the resulting 1D Boltzman equation for the subband j is:

$$\frac{df_j(z, k_z, t)}{dt} - \frac{1}{\hbar}\frac{\partial E_j(k_z)}{\partial k_z}\frac{\partial f_j(z, k_z, t)}{\partial z} + \frac{qF_z}{\hbar}\frac{\partial f_j(z, k_z, t)}{\partial k_z} =$$
$$[1 - f_j(z, k_z, t)] \sum_{j', k'_z} S_{j,j'}(k'_z, k_z) f_{j'}(z, k'_z, t) - f_j(z, k_z, t) \sum_{j', k'_z} S_{j',j}(k'_z, k_z) \left[1 - f'_j(z, k'_z, t)\right] \tag{7.9}$$

To determine $S_{j,j'}(k_z, k'_z)$ we use the Fermi Golden Rule which provides an expression for $S_{j,j'}(k, k')$ given the perturbation potential, $\tilde{\psi}$, caused by the corresponding scattering mechanism. A detailed derivation of the Fermi Golden Rule for systems confined in one dimension can be found in several textbooks [88], [206], [220]. Here we just present the main steps applied to the 2D MuG structures studied in this manuscript, where the electron is confined in two dimensions.

The derivation of the Fermi Golden Rule starts with the time dependent Schrödinger equation for the electron including a perturbing potential due to the scattering mechanism. Using the EMA and particularizing for a 1D electron gas, it can be rewritten as:

$$[H(\mathbf{r}) + \tilde{\phi}(\mathbf{r}, t)]\tilde{\Psi}_j(\mathbf{r}, t) = \imath\hbar\frac{d\tilde{\Psi}_j(\mathbf{r}, t)}{dt} \tag{7.10}$$

where $H(\mathbf{r})$ is the Hamiltonian operator of the electrostatic unperturbed problem presented in Chapter 2, in Eq. (2.9), and $\tilde{\phi} = -q\tilde{\psi}$ is the electron potential energy due to the perturbing potential. The solution of the perturbed problem can be written as a linear combination in the wavenumber space of the solutions of the unperturbed problem, $\Psi(\mathbf{r}, t)$ [206]. Thus:

$$\tilde{\Psi}(\mathbf{r}, t) = \sum_{i, k_z} c_{k_z}(t)\xi_{i,k_z}(x, y)\frac{e^{\imath k_z z}}{\sqrt{L}}e^{-\frac{\imath E_i(k_z)t}{\hbar}} \tag{7.11}$$

where the unperturbed solution was written as in Chapter 2 and assuming a plane wave dependency with time, where i and k_z are the indexes for the subband and wavenumber,

respectively. To determine the coefficients $c_{k_t extz}(t)$, Eq. (7.11) is substituted into Eq. (7.10) leading to:

$$\tilde{\phi}(\mathbf{r},t)\sum_{i,k_z} c_{k_z}(t)\xi_{i,k_z}(x,y)\frac{e^{\imath k_z z}}{\sqrt{L}}e^{-\frac{\imath E_i(k_z)t}{\hbar}} = \imath\hbar\sum_{i,k_z}\xi_{i,k_z}(x,y)\frac{e^{\imath k_z z}}{\sqrt{L}}e^{-\frac{\imath E_i(k_z)t}{\hbar}}\frac{dc_{k_z}(t)}{dt} \tag{7.12}$$

The scattering process moves the electron from an initial state (k_{zo}, j) to a final state (k'_{zo}, j'). Multiplying both sides of Eq. (7.12) by the electron wavefunction after the collision, $\xi^*_{j',k'_{zo}}(x,y)\frac{e^{\imath k'_{zo} z}}{\sqrt{L}}$, integrating over the volume of the device, $\mathcal{V}$, and taking into consideration the orthonormality of the solutions of the Schrödinger equation we get:

$$\sum_{i,k_z} c_{k_z}(t)\int_{\mathcal{V}}\xi_{i,k_z}(x,y)\frac{e^{\imath k_z z}}{\sqrt{L}}\tilde{\phi}(\mathbf{r},t)\xi^*_{j',k'_{zo}}(x,y)\frac{e^{-\imath k'_{zo} z}}{\sqrt{L}}dV\; e^{-\frac{\imath E_i(k_z)t}{\hbar}}e^{\frac{\imath E_{j'}(k'_{zo})t}{\hbar}} = \imath\hbar\frac{dc_{k'_{zo}}(t)}{dt} \tag{7.13}$$

For the mechanisms of interest, a plane wave time dependency of the perturbing potential is assumed [206]:

$$\tilde{\phi}(\mathbf{r},t) = \tilde{\phi}(\mathbf{r})e^{\pm\imath\omega t} \tag{7.14}$$

Then:

$$\sum_{i,k_z} c_{k_z}(t)M_{i,j'}(k_z,k'_{zo})e^{-\frac{\imath(E_i(k_z)-E_{j'}(k'_{zo})\pm\hbar\omega)t}{\hbar}} = \imath\hbar\frac{dc_{k'_{zo}}(t)}{dt} \tag{7.15}$$

where

$$M_{i,j'}(k_z,k'_{zo}) = \int_{\mathcal{V}}\xi_{i,k_z}(x,y)\frac{e^{\imath k_z z}}{\sqrt{L}}\tilde{\phi}(\mathbf{r},t)\xi^*_{j',k'_{zo}}(x,y)\frac{e^{-\imath k'_{zo} z}}{\sqrt{L}}dV \tag{7.16}$$

is the matrix element for the interaction between states (k_z, i) and (k_{zo}, j'). Since the scattering interaction is weak we can assume that the electron initial wavenumber k_{zo} is the main contribution to the sum in Eq. (7.12). In other words $c_k(t) \ll c_{k_{zo}}(t) = 1$ Then:

$$M_{j,j'}(k_{zo},k'_{zo})e^{-\frac{\imath(E_j(k_{zo})-E_{j'}(k'_{zo})\pm\hbar\omega)t}{\hbar}} = \imath\hbar\frac{dc_{k'_{zo}}(t)}{dt} \tag{7.17}$$

Integrating Eq. (7.15) for a certain period of time, T, in which the scattering event takes place, we can write:

$$c_{k'_{zo}}(T) = \frac{2}{\imath\hbar}M_{j,j'}(k_{zo},k'_{zo})e^{-\frac{\imath(E_j(k_{zo})-E_{j'}(k'_{zo})\pm\hbar\omega)T}{2\hbar}}\sin\left(\frac{E_j(k_{zo})-E_{j'}(k'_{zo})\pm\hbar\omega}{2\hbar}T\right) \tag{7.18}$$

The term $|c_{k'_{zo}}(T)|^2$ actually determines the probability of the transition from the (k_o, j) state to the (k'_o, j') state after a collision. The scattering rate $S_{j,j'}(k_z, k'_z)$ can be defined as the probability over time, therefore:

$$S_{j,j'}(k_z, k'_z) = \lim_{t\to\infty} \frac{|c_{k'_z}(T)|^2}{T} = \frac{2\pi}{\hbar}|M_{j,j'}(k_z, k'_z)|^2 \delta(E_j(k_z) - E_{j'}(k'_z) \pm \hbar\omega) \tag{7.19}$$

where we have used the properties of the sinc(x) function for $x \to \infty$ [221].

7.4 Momentum Relaxation Time

Once the BTE for a 1D electron gas has been presented, and the collisions term modeled, a method to solve Eq. (7.6) is needed. In this Section we present the linearization approximation, which provides a procedure to determine the electron momentum relaxation time that can be used to calculate the mobility as will be shown in Section 7.7.

Let us assume that only small displacements from equilibrium and uniform transport conditions are given. In this case, the distribution function, f, and other macroscopic quantities are independent of the transport position coordinate ($f \neq f(z)$). Under this approximation, the total derivative of the occupation function in the subband j-th, df_j/dt can be written as [88]:

$$\frac{df_j(k_z, t)}{dt} \simeq -\frac{\delta f_j(k_z)}{\tau_j(k_z)} = -\frac{f_j(k_z) - f_0(E_j(k_z))}{\tau_j(k_z)} \tag{7.20}$$

where $f_0(E)$ is the Fermi-Dirac occupation function in equilibrium, and $\delta f_j(k_z)$ is the deviation of the occupation function $f_j(k_z, t)$ respect to $f_0(E_j(k_z))$.

The MRT approach also assumes stationary behavior, $f \neq f(t)$, and small electric field F_z in the $\hat{z}$ direction so that $\partial f/\partial z \simeq 0$. Thus, under a small electric field F_z in the z direction, Eq. (7.6) can then be written as:

$$-\frac{qF_z}{\hbar}\frac{\partial f_j(k_z)}{\partial k_z} = -\frac{\delta f_j(k_z)}{\tau_j(k_z)} \tag{7.21}$$

We can develop the derivative in the left hand size as:

$$\frac{\partial f_j(k_z)}{\partial k_z} = \frac{\partial \delta f_j(k_z)}{\partial k_z} + \frac{\partial f_0(E_j(k_z))}{\partial k_z} = \frac{\partial \delta f_j(k_z)}{\partial k_z} + \frac{\partial f_0(E_j(k_z))}{\partial E_j(k_z)}\frac{\partial E_j(k_z)}{\partial k_z} \tag{7.22}$$

Introducing the previous equation into Eq. (7.21) and neglecting second-order terms, we get: -

$$-qF_z\frac{\partial f_0(E_j(k_z))}{\partial E_j(k_z)}v_j(k_z)\tau_j(k_z)=\delta f_j(k_z) \tag{7.23}$$

where the electron velocity definition: $v_j(k_z)=\hbar^{-1}\partial E_j(k_z)/\partial k_z$ has been used. From now on, we will simplify the notation to $E=E_j(k_z)$ and $E'=E_{j'}(k'_z)$.

Now, we will relate $\delta f_j(k_z)$ to the scattering rates in Eqs. (7.7) and (7.8), in order to achieve an expression for $\tau_j(k_z)$ as a function of the scattering rate $S_{j,j'}(k_z,k'_z)$. First, we replace $f_j(k_z)$ and $f_{j'}(k'_z)$ by $f_0(E)+\delta f_j(k_z)$ and $f_0(E')+\delta f_{j'}(k'_z)$, respectively.

$$\begin{aligned}S_{\text{in},j}-S_{\text{out},j}=&\left[1-f_0(E)-\delta f_j(k_z)\right]\sum_{j',k'}S_{j,i}(k'_z,k_z)\left[f_0(E')+\delta f_{j'}(k'_z)\right]-\\&-\left[f_0(E)+\delta f_j(k_z)\right]\sum_{j',k'}S_{j,j'}(k_z,k'_z)\left[1-f_0(E')-\delta f_{j'}(k'_z)\right]\end{aligned} \tag{7.24}$$

To simplify this equation we make use of the flux balance at equilibrium where the flux from state (k_z,j) to the state (k'_z,j') must equal the flux from (k'_z,j') to (k_z,j). Therefore:

$$f_0(E')S_{j',j}(k'_z,k_z)(1-f_0(E))=f_0(E)S_{j,j'}(k_z,k'_z)(1-f_0(E')) \tag{7.25}$$

Using Eq. (7.25) neglecting the second order terms $\delta f_j(k_z)\delta f_{j'}(k'_z)$ and making use of the condition of flux balance in equilibrium leads to:

$$\begin{aligned}S_{\text{in},j}-S_{\text{out},j}=&\sum_{j',k'_z}S_{j,j'}(k_z,k'_z)\frac{f_0(E)(1-f_0(E'))}{f_0(E')(1-f_0(E))}\left[\delta f_{j'}(k'_z)\left(1-f_0(E)\right)-f_0(E')\delta f_j(k_z)\right]-\\&-\sum_{j',k'_z}S_{j,j'}(k_z,k'_z)\left[\delta f_j(k_z)\left(1-f_0(E')\right)-f_0(E)\delta f_{j'}(k'_z)\right]\end{aligned} \tag{7.26}$$

After some algebra, we obtain:

$$S_{\text{in},j}-S_{\text{out},j}=-\delta f_j(k_z)\sum_{j',k'_z}S_{j,j'}(k_z,k'_z)\left\{\frac{1-f_0(E')}{1-f_0(E)}-\frac{\delta f_{j'}(k'_z)}{\delta f_j(k_z)}\frac{f_0(E)}{f_0(E')}\right\} \tag{7.27}$$

Using Eq. (7.23), we can rewrite the term $\delta f_{j'}(k'_z)/\delta f_j(k_z)$ as

$$\frac{\delta f_{j'}(k'_z)}{\delta f_j(k_z)} = \frac{q\tau_{j'}(k'_z)F_z v_{j'}(k'_z)\frac{\partial f_0(E')}{\partial E}}{q\tau_{j'}(k_z)F_z v_j(k_z)\frac{\partial f_0(E)}{\partial E}} = \frac{\tau_{j'}(k'_z)v_{j'}(k'_z)f_0(E')[1-f_0(E')]}{\tau_j(k_z)v_j(k_z)f_0(E)[1-f_0(E)]} \tag{7.28}$$

where the equality $\partial f_0(E)/\partial E = f_0(E)\,[1-f_0(E)]$ was used. Finally, substituting Eqs. (7.27) and (7.28) into Eq. (7.20), we get:

$$\frac{1}{\tau_j(k_z)} = \sum_{j',k'_z} S_{j,j'}(k_z,k'_z)\left(\frac{1-f_0(E')}{1-f_0(E)}\right)\left(1-\frac{\tau_{j'}(k'_z)v_{j'}(k'_z)}{\tau_j(k_z)v_j(k_z)}\right) \tag{7.29}$$

which is the final expression for $\tau_j(k_z)$.

The scattering probability $S_{j,j'}(k_z,k'_z)$ in Eq. (7.29) includes the cumulative effect of all the scattering mechanisms and can be written as:

$$S_{j,j'}(k_z,k'_z) = \sum_i S^i_{j,j'}(k_z,k'_z) \tag{7.30}$$

where the i index runs over the scattering mechanisms. Substituting Eq. (7.30) into Eq. (7.29) we get:

$$\frac{1}{\tau_j(k_z)} = \sum_{j',k'_z}\left[\sum_i S^i_{j,j'}(k_z,k'_z)\left(\frac{1-f_0(E')}{1-f_0(E)}\right)\left(1-\frac{\tau_{j'}(k'_z)v_{j'}(k'_z)}{\tau_j(k_z)v_j(k_z)}\right)\right] \tag{7.31}$$

Eq. (7.31) can be written as:

$$\frac{1}{\tau_j(k_z)} = \sum_i \frac{1}{\tau^i_j(k_z)} \tag{7.32}$$

being τ^i_j the contribution of the i-th scattering mechanism to τ_j:

$$\frac{1}{\tau^i_j(k_z)} = \sum_{j',k'_z} S^i_{j,j'}(k_z,k'_z)\left(\frac{1-f_0(E')}{1-f_0(E)}\right)\left(1-\frac{\tau_{j'}(k'_z)v_{j'}(k'_z)}{\tau_j(k_z)v_j(k_z)}\right) \tag{7.33}$$

Moreover, the calculation of τ^i_j depends on the total τ_j, and therefore, unless some approximation is done (see Section 7.5), a self consistent solution of τ_j including all the scattering mechanisms is needed. Once it is done, the contribution of a single scattering mechanism to $\tau_j(k_z)$, can be calculated as in Eq. (7.33).

The direct solution of Eq. (7.31) is not straightforward as it constitutes an implicit equation in $\tau_j(k_z)$. To reduce the problem, we distinguish three kinds of scattering mechanisms depending on the characteristic regarding energy and wavenumber. Thus, if we classify the scattering mechanism in three categories, isotropic (is), elastic anisotropic (ea) and inelastic anisotropic (ia), Eq. (7.31) can be rewritten as:

$$\begin{aligned}\frac{1}{\tau_j(k_z)} = &\sum_{is}\sum_{j',k'_z} S^{is}_{j,j'}(k_z,k'_z)\left(\frac{1-f_0(E')}{1-f_0(E)}\right)\left(1-\frac{\tau_{j'}(k'_z)v_{j'}(k'_z)}{\tau_j(k_z)v_j(k_z)}\right)+\\ &\sum_{ea}\sum_{j',k'_z} S^{ea}_{j,j'}(k_z,k'_z)\left(\frac{1-f_0(E')}{1-f_0(E)}\right)\left(1-\frac{\tau_{j'}(k'_z)v_{j'}(k'_z)}{\tau_j(k_z)v_j(k_z)}\right)+\\ &\sum_{ia}\sum_{j',k'_z} S^{ia}_{j,j'}(k_z,k'_z)\left(\frac{1-f_0(E')}{1-f_0(E)}\right)\left(1-\frac{\tau_{j'}(k'_z)v_{j'}(k'_z)}{\tau_j(k_z)v_j(k_z)}\right)\end{aligned} \tag{7.34}$$

The characteristics of the three kinds of scattering mechanisms can be readily deduced from their names and are summarized below.

- Inelastic anisotropic mechanism: the energy is not conserved, $E' \neq E$, and the scattering rate is wavenumber dependent, $S_{j,j'} \neq S_{j,j'}(k_z,k'_z)$.
- Elastic anisotropic mechanism: there is energy conservation, $E' \neq E$, an the scattering rate depends on the wavenumber, $S_{j,j'} = S_{j,j'}(k_z,k'_z)$.
- Isotropic mechanism: the scattering rate does not depend on the wavenumber, $S_{j,j'} = S_{j,j'}(k_z,k'_z)$. In this category, both the elastic and inelastic mechanism are included.

Taking into consideration these properties, Eq. (7.34) can be reformulated as:

$$\begin{aligned}\frac{1}{\tau_j(k_z)} = &\sum_{is}\sum_{j',k'_z} S^{is}_{j,j'}\left(\frac{1-f_0(E')}{1-f_0(E)}\right)+\sum_{ea}\sum_{j',k'_z} S^{ea}_{j,j'}(k_z,k'_z)\left(1-\frac{\tau_{j'}(k'_z)v_{j'}(k'_z)}{\tau_j(k_z)v_j(k_z)}\right)+\\ &\sum_{ia}\sum_{j',k'_z} S^{ia}_{j,j'}(k_z,k'_z)\left(\frac{1-f_0(E')}{1-f_0(E)}\right)\left(1-\frac{\tau_{j'}(k'_z)v_{j'}(k'_z)}{\tau_j(k_z)v_j(k_z)}\right)\end{aligned} \tag{7.35}$$

In Appendix D we go through a more detailed discussion of the simplifications that can be made in Eq. (7.35) for the different scattering mechanism kinds, while in the next two Sections we discuss the two approaches that we consider for the solution of Eq. (7.35).

7.5 Explicit calculation of the MRT

In this Section we present an explicit approximation for the calculation of the MRT that has been extensively used in the literature, see for example Refs. [213–217, 222]. Instead of solving the equation system previously proposed, the explicit approach manipulates Eq. (7.35) under some approximations to achieve a simpler explicit solution for τ_j.

The main assumption of the explicit calculation considers that there are small differences between $\tau_j(k_z)$ and $\tau_{j'}(k'_z)$ for all sub-bands, j, j' and wave-vectors k_z and k'_z. Using that approximation, $\tau_j(k'_z)/\tau_i(k_z) \simeq 1$, and the MRT of an elastic anisotropic mechanism can be written as:

$$\frac{1}{\tau_j^{ea}(k_z)} = \sum_{j',k'_z} S_{j,j'}^{ea}(k_z,k'_z)\left(1-\frac{v_{j'}(k'_z)}{v_j(k_z)}\right) \tag{7.36}$$

Equivalently, the MRT of an inelastic anisotropic mechanism is calculated as:

$$\frac{1}{\tau_j^{ia}(k_z)} = \sum_{j,k'_z} S_{j,j'}^{ia}(k_z,k'_z)\left(\frac{1-f_0(E')}{1-f_0(E)}\right)\left(1-\frac{v_{j'}(k'_z)}{v_j(k_z)}\right) \tag{7.37}$$

Then the total MRT for state (k_z,j) is:

$$\frac{1}{\tau_j(k_z)} = \sum_{ii}\frac{1}{\tau_j^{is}(k_z)} + \sum_{ea}\frac{1}{\tau_j^{ea}(k_z)} + \sum_{ia}\frac{1}{\tau_j^{ia}(k_z)} \tag{7.38}$$

where each contribution $\tau_j^{ia}(k_z)$, $\tau_j^{ea}(k_z)$ and $\tau_j^{ii}(k_z)$ is calculated as in Appendix D by just simplifying Eqs. (D.7), (D.10) and (D.14) using $\tau_j(k'_z) = \tau_i(k_z)$. Therefore, the explicit approach allows the independent and explicit calculation of the MRT due to each scattering mechanism. The total MRT is then obtained by applying the so-called Matthiessen rule at each k_z value [223] as in Eq. (**??**)

The assumption made in Eqs. (7.36) and (7.37) seems quite arguable as it implies that τ does not depend on k neither on the subband. However, the explicit calculation does work in many cases. The reason concerns the scattering rate $S_{j,j'}$ and the symmetry of the structures studied. When symmetric structures are considered, most of the scattering mechanisms result in a nearly diagonal $S_{j,j'}$ matrix. Consequently, the highest weight of the $\left(1-\frac{\tau_{j'}(k'_z)v_{j'}(k'_z)}{\tau_j(k_z)v_j(k_z)}\right)$ term in the (j',k'_z) sum correspond to $k'_z = k_z$ where the approximation $\tau_j(k')/\tau_i(k) \simeq 1$ is fully satisfied.

7.6 Implicit calculation of the MRT

In this Section we present a procedure to determine τ_j directly from Eq. (7.35) without any further approximations. Four important facts must be taken into consideration when approaching to the problem:

- Isotropic mechanisms do not depend on τ_j and can be calculated, for a given (k_z, j), in an independent way. In fact, we can define the contribution to τ_j of the is-th isotropic inelastic mechanism as:

$$\frac{1}{\tau_j^{is}(k_z)} = \sum_{j',k'_z} S_{j,j'}^{is}(k_z, k'_z) \tag{7.39}$$

- $\tau_j(k_z)$ depends on $\tau_{j'}(k'_z)$ through elastic anisotropic and inelastic anisotropic mechanisms.
- For elastic anisotropic mechanisms (k_z, j) and (k'_z, j') states have the same energy.
- For inelastic anisotropic mechanism $E' = E \pm \hbar\omega$ is satisfied, where E and E' are the energies corresponding to (k_z, j) and (k'_z, j') sates, respectively. For the sake of simplicity we just consider one inelastic anisotropic mechanism whose energy change is known and does not depend on the device geometry, size or any other variable: $\pm\hbar\omega_p$. A more general approach including several mechanism with distinct inelastic anisotropic mechanism with different energy changes would imply a discretization of the energy space and a resolution of the complete system of Eq. (7.35) for each discrete energy value as it is done in Ref. [224].

Fig. 7.1 shows a schematic depiction of the possible transitions from an arbitrary state, k_z (plotted as a blue filled dot). The final states resulting from an elastic anisotropic process are plotted as squares while those resulting from an inelastic anisotropic process are plotted as circles. Transitions for inelastic isotropic mechanisms are not plotted as they can be calculated separately. Additionally, the transitions starting from any of the final states must also be taken into account (and are plotted as diamonds) as they influence the calculation of τ_j at the initial state through $\tau_{j'}$ at the final states. It is clear that this nested interdependency leads to a discretization of the wavenumber space according to the discretization of the energy space (which is governed by $\pm\hbar\omega_p$). In Fig. 7.1 we use $k_{i,b/f}^j$ to refer to the k_z state in the backward/forward branch of the j-th subband with energy E_i. For example, the initial state

$k^0_{2,\mathrm{f}}$ refers to the k_z state in the positive branch of the 0-th subband with energy E_2. To keep the example simple enough to be afforded we have considered just three subbands and five energy steps. Nevertheless, the extension to a larger number of subbands and energy steps follows the same rules here proposed.

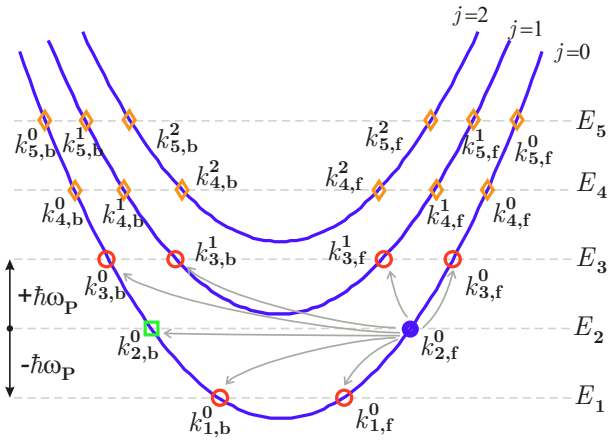

Figure 7.1: Schematic depiction of the possible transitions from the $k^0_{2,\mathrm{f}}$ state. The final states resulting from an elastic anisotropic process are plotted as squares while those resulting from an inelastic anisotropic process are plotted as circles. Other states resulting from the discretization of the wavenumber space are plotted as diamonds.

From a mathematical point of view, the set of transitions depicted in Fig. 7.1 can be formulated as an equation system. Looking for a matrix formulation of the problem, we rewrite Eq. (7.35) by multiplying both sides by $v_j(k_\mathrm{z})\tau_j(k_\mathrm{z})$ getting:

$$v_j(k_\mathrm{z}) = \tau_j(k_\mathrm{z})v_j(k_\mathrm{z})\left[\sum_{is}\frac{1}{\tau^{is}_j(k_\mathrm{z})} + \sum_{ea}\sum_{j',k'_\mathrm{z}} S^{ea}_{j,j'}(k_\mathrm{z},k'_\mathrm{z}) + \right.$$
$$\left.\sum_{ia}\sum_{j,k'_\mathrm{z}} S^{ia}_{j,j'}(k_\mathrm{z},k'_\mathrm{z})\left(\frac{1-f_0(E')}{1-f_0(E)}\right)\right] - \sum_{ea}\sum_{j',k'_\mathrm{z}} S^{ea}_{j,j'}(k_\mathrm{z},k'_\mathrm{z})\tau_{j'}(k'_\mathrm{z})v_{j'}(k'_\mathrm{z})$$
$$- \sum_{ia}\sum_{j',k'_\mathrm{z}} S^{ia}_{j,j}(k_\mathrm{z},k'_\mathrm{z})\left(\frac{1-f_0(E')}{1-f_0(E)}\right)\tau_{j'}(k'_\mathrm{z})v_{j'}(k'_\mathrm{z}) \qquad (7.40)$$

For the set of transitions introduced in Fig 7.1, we can write Eq. (7.40) as:

$$\begin{bmatrix} v_0(k^0_{1,\mathrm{f}}) \\ v_0(k^0_{1,\mathrm{b}}) \\ v_0(k^0_{2,\mathrm{f}}) \\ v_0(k^0_{2,\mathrm{b}}) \\ v_0(k^0_{3,\mathrm{f}}) \\ v_0(k^0_{3,\mathrm{b}}) \\ v_1(k^1_{3,\mathrm{f}}) \\ v_1(k^1_{3,\mathrm{b}}) \\ \vdots \\ v_2(k^2_{5,\mathrm{b}}) \end{bmatrix} = \begin{bmatrix} \Xi^{k^0_{1,\mathrm{f}}} & Z^{k^0_{1,\mathrm{f}}}_{k^0_{1,\mathrm{b}}} & \Lambda^{k^0_{1,\mathrm{f}}}_{k^0_{2,\mathrm{f}}} & \Lambda^{k^0_{1,\mathrm{f}}}_{k^0_{2,\mathrm{b}}} & 0 & 0 & 0 & 0 & \cdots & 0 \\ Z^{k^0_{1,\mathrm{b}}}_{k^0_{1,\mathrm{f}}} & \Xi^{k^0_{1,\mathrm{b}}} & \Lambda^{k^0_{1,\mathrm{b}}}_{k^0_{2,\mathrm{f}}} & \Lambda^{k^0_{1,\mathrm{b}}}_{k^0_{2,\mathrm{b}}} & 0 & 0 & 0 & 0 & \cdots & 0 \\ \Lambda^{k^0_{2,\mathrm{f}}}_{k^0_{1,\mathrm{f}}} & \Lambda^{k^0_{2,\mathrm{f}}}_{k^0_{1,\mathrm{b}}} & \Xi^{k^0_{2,\mathrm{f}}} & Z^{k^0_{2,\mathrm{f}}}_{k^0_{2,\mathrm{b}}} & \Lambda^{k^0_{2,\mathrm{f}}}_{k^0_{3,\mathrm{f}}} & \Lambda^{k^0_{2,\mathrm{f}}}_{k^0_{3,\mathrm{b}}} & \Lambda^{k^0_{2,\mathrm{f}}}_{k^1_{3,\mathrm{f}}} & \Lambda^{k^0_{2,\mathrm{f}}}_{k^1_{3,\mathrm{b}}} & \cdots & 0 \\ \Lambda^{k^0_{2,\mathrm{b}}}_{k^0_{1,\mathrm{f}}} & \Lambda^{k^0_{2,\mathrm{b}}}_{k^0_{1,\mathrm{b}}} & Z^{k^0_{2,\mathrm{b}}}_{k^0_{2,\mathrm{f}}} & \Xi^{k^0_{2,\mathrm{b}}} & \Lambda^{k^0_{2,\mathrm{b}}}_{k^0_{3,\mathrm{f}}} & \Lambda^{k^0_{2,\mathrm{b}}}_{k^0_{3,\mathrm{b}}} & \Lambda^{k^0_{2,\mathrm{b}}}_{k^1_{3,\mathrm{f}}} & \Lambda^{k^0_{2,\mathrm{b}}}_{k^1_{3,\mathrm{b}}} & \cdots & 0 \\ 0 & 0 & \Lambda^{k^0_{3,\mathrm{f}}}_{k^0_{2,\mathrm{f}}} & \Lambda^{k^0_{3,\mathrm{f}}}_{k^0_{2,\mathrm{b}}} & \Xi^{k^0_{3,\mathrm{f}}} & Z^{k^0_{3,\mathrm{f}}}_{k^0_{3,\mathrm{b}}} & Z^{k^0_{3,\mathrm{f}}}_{k^1_{3,\mathrm{f}}} & Z^{k^0_{3,\mathrm{f}}}_{k^1_{3,\mathrm{b}}} & \cdots & 0 \\ 0 & 0 & \Lambda^{k^0_{3,\mathrm{b}}}_{k^0_{2,\mathrm{f}}} & \Lambda^{k^0_{3,\mathrm{b}}}_{k^0_{2,\mathrm{b}}} & Z^{k^0_{3,\mathrm{b}}}_{k^0_{3,\mathrm{f}}} & \Xi^{k^0_{3,\mathrm{b}}} & Z^{k^0_{3,\mathrm{b}}}_{k^1_{3,\mathrm{f}}} & Z^{k^0_{3,\mathrm{b}}}_{k^1_{3,\mathrm{b}}} & \cdots & 0 \\ 0 & 0 & \Lambda^{k^1_{3,\mathrm{f}}}_{k^0_{2,\mathrm{f}}} & \Lambda^{k^1_{3,\mathrm{f}}}_{k^0_{2,\mathrm{b}}} & Z^{k^1_{3,\mathrm{f}}}_{k^0_{3,\mathrm{f}}} & Z^{k^1_{3,\mathrm{f}}}_{k^0_{3,\mathrm{b}}} & \Xi^{k^1_{3,\mathrm{f}}} & Z^{k^1_{3,\mathrm{f}}}_{k^1_{3,\mathrm{b}}} & \cdots & 0 \\ 0 & 0 & \Lambda^{k^1_{3,\mathrm{b}}}_{k^0_{2,\mathrm{f}}} & \Lambda^{k^1_{3,\mathrm{b}}}_{k^0_{2,\mathrm{b}}} & Z^{k^1_{3,\mathrm{b}}}_{k^0_{3,\mathrm{f}}} & Z^{k^1_{3,\mathrm{b}}}_{k^0_{3,\mathrm{b}}} & Z^{k^1_{3,\mathrm{b}}}_{k^1_{3,\mathrm{f}}} & \Xi^{k^1_{3,\mathrm{b}}} & \cdots & 0 \\ \vdots & \vdots & \vdots & \vdots & \vdots & \vdots & \vdots & \vdots & \ddots & \vdots \\ 0 & 0 & 0 & 0 & 0 & 0 & 0 & 0 & \cdots & \Xi^{k^2_{5,\mathrm{b}}} \end{bmatrix} \begin{bmatrix} \tau_0(k^0_{1,\mathrm{f}}) \\ \tau_0(k^0_{1,\mathrm{b}}) \\ \tau_0(k^0_{2,\mathrm{f}}) \\ \tau_0(k^0_{2,\mathrm{b}}) \\ \tau_0(k^0_{3,\mathrm{f}}) \\ \tau_0(k^0_{3,\mathrm{b}}) \\ \tau_1(k^1_{3,\mathrm{f}}) \\ \tau_1(k^1_{3,\mathrm{b}}) \\ \vdots \\ \tau_2(k^2_{5,\mathrm{b}}) \end{bmatrix} \tag{7.41}$$

The matrix elements Ξ, Z and Λ are determined from Eq. (7.40) following a completely equivalent procedure to that exposed in Appendix D:[4]

$$\Xi^{k^j_{i,\mathrm{f}}} = v_j(k^j_{i,\mathrm{f}}) \sum_{is} \frac{1}{\tau^{is}_j(k^j_{i,\mathrm{f}})} + \frac{L}{\hbar^2} \sum_{ea} \sum_{j'} \left[|M^{ea}_{j,j'}(k^j_{i,\mathrm{f}}, k^{j'}_{i,\mathrm{f}})|^2 - |M^{ea}_{j,j'}(k^j_{i,\mathrm{f}}, k^{j'}_{i,\mathrm{b}})|^2 \right] \frac{v_j(k^j_{i,\mathrm{f}})}{|v_{j'}(k^{j'}_{i,\mathrm{b}})|}$$
$$+ \frac{L}{\hbar^2} \sum_{ia} \sum_{j'} \left[|M^{ia}_{j,j'}(k^j_{i,\mathrm{f}}, k^{j'}_{i\pm1,\mathrm{f}})|^2 - |M^{ia}_{j,j'}(k^j_{i,\mathrm{f}}, k^{j'}_{i\pm1,\mathrm{b}})|^2 \right] \frac{v_j(k^j_{i,\mathrm{f}})}{|v_{j'}(k^{j'}_{i\pm1,\mathrm{f}})|} + Z^{k^j_{i,\mathrm{f}}}_{k^j_{i,\mathrm{f}}} \left(\frac{1 - f_0(E')}{1 - f_0(E)} \right) \tag{7.42}$$

$$Z^{k^j_{i,\mathrm{f}}}_{k^{j'}_{i',\mathrm{f}}} = -\mathrm{sign}(v_{j'}(k^{j'}_{i',\mathrm{f}})) \frac{L}{\hbar^2} \sum_{ea} |M^{ea}_{j,j'}(k^j_{i,\mathrm{f}}, k^{j'}_{i',\mathrm{f}})|^2 \tag{7.43}$$

$$\Lambda^{k^j_{i,\mathrm{f}}}_{k^{j'}_{i\pm1,\mathrm{f}}} = -\mathrm{sign}(v_{j'}(k^{j'}_{i\pm1,\mathrm{f}})) \frac{L}{\hbar^2} \sum_{ia} |M^{ia}_{j,j'}(k^j_{i,\mathrm{f}}, k^{j'}_{i',\mathrm{f}})|^2 \left(\frac{1 - f_0(E')}{1 - f_0(E)} \right) \tag{7.44}$$

[4] It must be noted that, due to the discretization of the energy space, k_z is reduced to k_i (being i the energy index); and the initial state upper and lower energies are notated as $i \pm 1$ instead of $^\pm$. Finally, in this notation the band index j/j' is explicitly introduced as a superscript in k instead of using the primed/unprimed notation of the Appendix.

The formulation of Ξ, Z and Λ for $k^j_{i,\mathrm{b}}$ and $k^{j'}_{i',\mathrm{b}}$ can be readily determine substituting $k^j_{i,\mathrm{f}}$ and $k^{j'}_{i',\mathrm{f}}$ by $k^j_{i,\mathrm{b}}$ and $k^{j'}_{i',\mathrm{b}}$ in the previous expressions. As for $1/\tau^{is}_j(k^j_{i,\mathrm{f}})$, it is calculated as in the explicit approximation. The dimension of the system is $[n\times 1] = [n\times n][n\times 1]$ where n is the number of elements of the discretized wavenumber space. To better illustrate the transitions with origin at the $k^0_{2,f}$ state shown in Fig. 7.1, we have shadowed the row which describes them in Eq. (7.41). In that row only the non-null elements are specified. Some other rows are written although, for the sake of simplicity, not all non-null elements of those rows are put down.

Under symmetric bands, as those depicted in Fig. 7.1, $\tau(k^j_{i,\mathrm{b}}) = \tau(k^j_{i,\mathrm{f}})$ and $v(k^j_{i,\mathrm{b}}) = -v(k^j_{i,\mathrm{f}})$. Thus, the previous equation system can be solved only for the positive k branch resulting into:

$$\begin{bmatrix} v_0(k^0_{1,\mathrm{f}}) \\ v_0(k^0_{2,\mathrm{f}}) \\ v_0(k^0_{3,\mathrm{f}}) \\ v_1(k^1_{3,\mathrm{f}}) \\ \vdots \\ v_2(k^2_{5,\mathrm{f}}) \end{bmatrix} = \begin{bmatrix} \tilde{\Xi}^{k^0_{1,\mathrm{f}}} & \tilde{\Lambda}^{k^0_{1,\mathrm{f}}}_{k^0_2} & 0 & 0 & \cdots & 0 \\ \tilde{\Lambda}^{k^0_{2,\mathrm{f}}}_{k^0_1} & \tilde{\Xi}^{k^0_{2,\mathrm{f}}} & \tilde{\Lambda}^{k^0_{2,\mathrm{f}}}_{k^0_3} & \tilde{\Lambda}^{k^0_{2,\mathrm{f}}}_{k^1_3} & \cdots & 0 \\ 0 & \tilde{\Lambda}^{k^0_{3,\mathrm{f}}}_{k^0_2} & \tilde{\Xi}^{k^0_{3,\mathrm{f}}} & \tilde{Z}^{k^0_{3,\mathrm{f}}}_{k^1_3} & \cdots & 0 \\ 0 & \tilde{\Lambda}^{k^1_{3,\mathrm{f}}}_{k^0_2} & \tilde{Z}^{k^1_{3,\mathrm{f}}}_{k^0_3} & \tilde{\Xi}^{k^1_3} & \cdots & 0 \\ \vdots & \vdots & \vdots & \vdots & \ddots & \vdots \\ 0 & 0 & 0 & 0 & \cdots & \tilde{\Xi}^{k^2_{5,f}} \end{bmatrix} \begin{bmatrix} \tau_0(k^0_{1,\mathrm{f}}) \\ \tau_0(k^0_{2,\mathrm{f}}) \\ \tau_0(k^0_{3,\mathrm{f}}) \\ \tau_1(k^1_{3,\mathrm{f}}) \\ \vdots \\ \tau_2(k^2_{5,\mathrm{f}}) \end{bmatrix} \tag{7.45}$$

where:

$$\tilde{\Xi}^{k^j_{i,\mathrm{f}}} = \Xi^{k^j_{i,\mathrm{f}}} + Z^{k^j_{i,\mathrm{f}}}_{k^j_{i,\mathrm{b}}} \tag{7.46}$$

$$\tilde{\Lambda}^{k^j_{i,\mathrm{f}}}_{k^{j'}_{i'}} = \Lambda^{k^j_{i,\mathrm{f}}}_{k^{j'}_{i',\mathrm{f}}} + \Lambda^{k^j_{i,\mathrm{f}}}_{k^{j'}_{i',\mathrm{b}}} \tag{7.47}$$

$$\tilde{Z}^{k^j_{i,\mathrm{f}}}_{k^{j'}_{i'}} = Z^{k^j_{i,\mathrm{f}}}_{k^{j'}_{i',\mathrm{f}}} + Z^{k^j_{i,\mathrm{f}}}_{k^{j'}_{i',\mathrm{b}}} \tag{7.48}$$

which is a $[n)/2\times 1] = [n/2\times n/2][n/2\times 1]$ system and is actually the equation system that we solve. Eq. (7.45) can be formulated in a matrix compact form as:

$$v = \Lambda\tau \tag{7.49}$$

where v and τ are the column vectors containing the velocities and the MRTs, respectively, of discretized wavenumbers shown in Fig. 7.1. Thus, we can determine τ

as:

$$\tau = \Lambda^{-1} v \tag{7.50}$$

It is worth to note that Eq. (7.45) has been proposed starting at an arbitrary wavenumber, k^0_{2f}, and it has resulted in the determination of τ for a set of n wavenumber values interdependent among them. This process is respected for different scattering wavenumbers, $k^0_{2,\mathrm{f}}$, until τ is modeled with enough precision for its numerical integration.

In Fig. 7.1 we have considered just five energy steps and three subbands, but the formulation of the matrix Λ for a more complex set of transitions, with more energy steps and more subbands can be performed following the same procedure already shown. One non-negligible issue regarding more complex formulations, concerns the truncation of the wavenumber set. In Fig. 7.1 we have considered just five energy steps, but from the monotonically increase of E with k_z (assumed for non-parabolic EMA), it is easy to conclude that a non-limited number of energy steps (and wavenumber values) result from the discretization of the wavenumber space. Moreover, due to the nested interdependency of the transitions, $\tau(k^0_{2,f})$ will depend on these higher k'_z. Nevertheless, $S_{j,j'}$ tends to decrease for anisotropic mechanisms with increasing $|k_\mathrm{z} - k'_\mathrm{z}|$, and therefore, the influence of higher states on the determination of τ for the initial state rapidly decreases, allowing the truncation of the discretized wavenumber space with a simple Neumann boundary condition, that is $\partial\tau_j(E)/\partial E \simeq 0$ [224].

7.7 Mobility calculation

As explained in Section 7.4, in the MRT approximation only small displacements from equilibrium are allowed and macroscopic quantities are assumed to not depend on the transport direction. This assumption is used by the so-called Kubo-Greenwood formula to determine the electron mobility, μ, of an electron gas [225],[226]. Here we summarize the main steps which lead to the Kubo-Greenwood formula modified for 1D transport under non-parabolic dispersion relation. In first place, the current density per unit length due to the j-th subband of a 1D electron gas can be defined as [219]:

$$J_j = -\frac{q}{L}\sum_{k_\mathrm{z}} v_j(k_\mathrm{z}) f_j(k_\mathrm{z}) = -\frac{q}{L}\sum_{k_\mathrm{z}} v_j(k_\mathrm{z}) \delta f_j(k_\mathrm{z}) \tag{7.51}$$

where $f_j(k_z) = f_0(E_j(k_z)) + \delta f_j(k_z)$ and the product term $v_j(k_z) f_0(E_j(k_z))$ vanishes due to its odd symmetry with k_z. Using Eq. (7.23) we can write:

$$J_j = \frac{q^2}{L} F_z \sum_{k_z} v_j^2(k_z) \tau_j(k_z) \frac{\partial f_0(E_j(k_z))}{\partial E} \tag{7.52}$$

Assuming a linear relation between current and electric field we have:

$$J_j = q N_j \mu_j F_z \tag{7.53}$$

where N_j is the population of the j-th band. So, equaling Eqs. (7.52) and (7.53) and solving for μ we get:

$$\mu_j = \frac{q}{N_j 2\pi} \int dk_z v_j^2(k_z) \tau_j(k_z) \frac{\partial f_0(E_j(k_z))}{\partial E} \tag{7.54}$$

So, the result is the Kubo-Greenwood formula for the mobility of a 1D electron gas [95, 225–227]:

$$\mu_j = \frac{q}{N_j 2\pi k_B T} \int dk_z v_j^2(k_z) \tau_j(k_z) f_0(E_j(k_z))(1 - f_0(E_j(k_z))) \tag{7.55}$$

The previous integral can be expressed in terms of energy using the relation $dk = dE/\hbar v_i(k)$:

$$\mu_j = \frac{q}{N_j \hbar \pi k_B T} \int dE v_j(E) \tau_j(E) f_0(E_j)(1 - f_0(E_j)) \tag{7.56}$$

where we keep the nomenclature of the previous Chapters.

7.8 Conclusions

In this Chapter, we have developed an approach to calculate the electron mobility of a 1D electron gas based on the linearization of the Boltzmann Transport Equation using the momentum relaxation time approximation (MRT). Besides the explicit approach for the calculation of the MRT which has been extensively used in the literature, we showed the implicit approach resolution. The formulation of the implicit equation system was exemplified, focusing on the nested interdependency of the transitions, and the truncation of the discretized wavenumber space with a simple Neumann boundary condition. The implicit resolution of the MRT must be highlighted for its rigorousness

and singularity in the literature.

Chapter 8

Modeling of scattering mechanisms in NWs

8.1 Introduction

In the previous Chapter we presented the procedure to determine the momentum relaxation time which depends on the matrix elements corresponding to the scattering mechanisms. In this Chapter we focus on the calculation of these matrix elements in a 1D electron gas due to five different processes: surface roughness, coulomb dispersion, bulk phonons (optical and acoustic), polar optical phonons and alloy disorder.

Although obtaining the final expression of the matrix element of each scattering element involves intricate mathematics, we have attempted to keep the derivations as rigorous as possible. Thus, in order to relieve the Chapter reading, we have moved to Appendix E some of the calculi. Despite of the mentioned mathematical complexity, the resulting matrix element expressions are in general simple functions which can be easily implemented. For that reason, we have not included, in this part of the manuscript, a description of the numerical particularities of the solution process. Thus, we utilize the wavefunctions and energy levels obtained using SP2D, and solve the expressions numerically using MATLAB®.

The rest of the Chapter is organized as follows. In Section 8.2, we discuss the surface roughness scattering mechanism assuming that it can be characterized by a random variable with an exponential power spectrum. In Section, 8.3 we determine the coulomb scattering element for a fully uncorrelated distribution of impurities in the confinement

plane and a hard-sphere model in the transport direction. Section 8.4 presents the matrix elements due to acoustic and optical phonons while Section 8.5 doest it for polar optical phonons. Section 8.6 introduces the matrix element due to alloy disorder in compound semiconductors. In Section 8.7, we introduce the tensorial dielectric screening for static mechanisms: surface roughness, coulomb and alloy disorder. Finally, Section 8.8 summarizes the main conclusions of the Chapter. Appendix E collects the mathematical details of some of the derivations.

8.2 Surface roughness

The set of irregularities found at the interface between the insulator and the semiconductor media in a MIS heterostructure (known as Surface Roughness, SR) is an unavoidable consequence of the fabrication process, which affects negatively to the carriers displacement in the direction parallel to the insulator-semiconductor interface [228]. Surface roughness is a very important scattering mechanism in bulk MOSFETs, specially at high gate voltages, when the carriers get closer to the semiconductor-insulator interface. This process gets even more relevant when the device size is reduced and thinner films are considered [95, 229]. Therefore, it is expected to play an important role in the transport as the size of nanowires decreases. On the one hand, the volume inversion, due to higher confinement, shifts electrons far from the aforementioned interface, potentially reducing the effect of SR. On the other hand, the ratio of device-surface to device-volume ratio is augmented with respect to that of planar structures increasing the relevance of surface related processes such as SR [230].

The modeling of the perturbing potential due to SR and the corresponding scattering matrix elements has been extensively visited in the literature for 1D-confined devices [208, 229, 231–234]. Nevertheless, only a few researchers have worked in the modeling of 2D confined devices. We can highlight the works in Ref. [95] in which the SR for cylindrical structures was modeled. Later works [235] extend their calculation for rectangular devices but considering only for Line Edge Roughness calculation. Alternatives approaches can be found in Ref. [214, 236], based on Ando's one [237], which, according to Ref. [95], cannot capture the body thickness dependence. Only very recently an alternative approach has been introduced almost simultaneously by Stanojevic and Kosina in Ref. [230] and Jin *et al.* in Ref. [238] without constraining the model to LER nor specific geometries or orientations. These two independent, but

coincident, studies are, to the best of our knowledge, the most realistic approximations to the SR physics in 2D confined devices.

In this manuscript, we have implemented this SR-model as follows. SR is defined by a random variable $\Delta^{\text{SR}}(\mathbf{r})$, being $\mathbf{r} \in S_{\text{i-s}}$ the position vector and $S_{\text{i-s}}$ the surface which delimits the insulator-semiconductor interface. The perturbing potential due to SR is:

$$\tilde{\psi}^{\text{SR}}(\mathbf{r}) = \Delta\phi\Delta^{\text{SR}}(\mathbf{r}) \tag{8.1}$$

where, as proposed previously in this manuscript, $\Delta\phi$ is the potential energy barrier between the semiconductor and the insulator, and $\tilde{\psi}^{\text{SR}}$ is only defined in $S_{\text{i-s}}$

The derivation of the SR scattering element between states (k_{z}, j) and (k'_{z}, j'), follows that proposed in Refs. [230] and [238]. Our aim is just to spotlight some key steps introducing minor modifications. As proposed in Section 7.3, under the Fermi golden rule, the scattering element is defined as:

$$M_{j,j'}(k_{\text{z}}, k'_{\text{z}}) = \Delta\phi \int_{\mathcal{S}_{\text{i-s}}} dS\ \xi_{j,k_{\text{z}}}(x,y)\frac{e^{-\imath k_{\text{z}} z}}{\sqrt{L}}\Delta(\mathbf{r})\xi^*_{j',k'_{\text{z}}}(x,y)\frac{e^{\imath k'_{\text{z}} z}}{\sqrt{L}} \tag{8.2}$$

where te volume integral has been reduced to a surface integration as $\tilde{\psi}^{\text{SR}}$ is only defined at the surface $S_{\text{i-s}}$. As $\Delta(\mathbf{r})$ is a random variable, Eq. (8.2) cannot be directly integrated. To avoid that problem Eq. (8.2) is reformulated as a function of $\Delta(\mathbf{r})$ autocorrelation function defined as:

$$C(\mathbf{r}) = \langle \Delta(\mathbf{r})\Delta(\mathbf{r}') \rangle \tag{8.3}$$

Keeping the random nature of $\Delta(\mathbf{r})$, $C(\mathbf{r})$ is the inverse transformation of the SR power spectrum, a quantity which can be realistically modeled (see Subsection 8.2.3).

Thus, squaring the matrix element and applying the expected value operator $\langle\rangle$ we get:

$$\left\langle \left| M_{j,j'}(k_{\text{z}}, k'_{\text{z}}) \right|^2 \right\rangle = \frac{\Delta\phi^2}{L^2} \int_{\mathcal{S}_{\text{i-s}}} dS \int_{\mathcal{S}_{\text{i-s}}} dS' \xi_{j,k_{\text{z}}}(x,y) e^{-\imath k_{\text{z}} z} \xi^*_{j',k'_{\text{z}}}(x,y) e^{\imath k'_{\text{z}} z} \langle \Delta(\mathbf{r})\Delta(\mathbf{r}') \rangle$$
$$\xi^*_{j,k_{\text{z}}}(x',y') e^{\imath k_{\text{z}} z'} \xi_{j',k'_{\text{z}}}(x',y') e^{-\imath k'_{\text{z}} z'} \tag{8.4}$$

The previous integral can be rewritten as.

$$\langle \left| M_{j,j'}(k_{\rm z}, k'_{\rm z}) \right|^2 \rangle = \frac{\Delta\phi^2}{L^2} \int_{\mathcal{C}_{\text{i-s}}} dc \int_{\mathcal{C}_{\text{i-s}}} dc' \int_0^L dz \int_0^L dz' \xi_{j,k_{\rm z}}(c) \xi^*_{j',k'_{\rm z}}(c) \xi^*_{j,k_{\rm z}}(c') \xi_{j',k'_{\rm z}}(c') \\ e^{\imath(k_{\rm z}-k'_{\rm z})(z'-z)} C(\mathbf{r}) \qquad (8.5)$$

where $C_{\text{i-s}}$ and L are the curve which describes the insulator-semiconductor interface in the cross-section and the device length, respectively; c is a 1D variable describing the confinement position (x, y) along $C_{\text{i-s}}$ and z is the transport coordinate. For the sake of clarity let us define the function:

$$f_{j,j',k_{\rm z},k'_{\rm z}}(c) = \Delta\phi \xi_{j,k_{\rm z}}(c) \xi^*_{j',k'_{\rm z}}(c) \qquad (8.6)$$

Then,

$$\langle \left| M_{j,j'}(k_{\rm z}, k'_{\rm z}) \right|^2 \rangle = \frac{1}{L^2} \int_{\mathcal{C}_{\text{i-s}}} dc \int_{\mathcal{C}_{\text{i-s}}} dc' \int_0^L dz \int_0^L dz' f_{j,j',k_{\rm z},k'_{\rm z}}(c) f_{j,j',k_{\rm z},k'_{\rm z}}(c') e^{\imath(k_{\rm z}-k'_{\rm z})(z'-z)} C(\mathbf{r}) \qquad (8.7)$$

The integration procedure for Eq. (8.5) requires the transformation of the real space into its reciprocal wavenumber space. In this transformation the periodicity of the real space variable determines the properties of the reciprocal space. For that reason, a distinction must be done between open and close $\mathcal{C}_{\text{i-s}}$ paths. This distinction, although not explicitly exposed, is the main difference in the approaches followed by Stanojevic *et al.* in Ref. [230] and Jin *et al.* in Ref. [238].

8.2.1 Derivation for open cross sections curves

Let us first consider the case when $\mathcal{C}_{\text{i-s}}$ is an open curve, for example, a bulk FinFET. Then the autocorrelation function can be expressed in terms of the SR power spectrum, $C(\mathbf{q})$, as:

$$C(c, z) = \frac{1}{4\pi^2} \int\int C(\mathbf{q}) e^{\imath q_{\rm c}(c'-c)} e^{\imath q_{\rm z}(z'-z)} dq_{\rm c} dq_{\rm z} \qquad (8.8)$$

where $\mathbf{q}$ is used here to denote the wavevector space of the scattering mechanism, keeping $\mathbf{k}$ to denote the wavevector space of electrons.

Introducing Eq. (8.8) into Eq. (8.5) one obtains:

$$\langle \left| M_{j,j'}(k_{\rm z},k'_{\rm z}) \right|^2 \rangle = \frac{1}{4\pi^2 L^2} \int_{\mathcal{C}_{\rm i\text{-}s}} dc \int_{\mathcal{C}_{\rm i\text{-}s}} dc' \int_0^L dz \int_0^L dz' \int dq_{\rm z} \int dq_{\rm c} f_{j,j',k_{\rm z},k'_{\rm z}}(c) f^*_{j,j',k_{\rm z},k'_{\rm z}}(c') \\ e^{-\imath q_{\rm c}(c-c')} e^{\imath (k_{\rm z}-k'_{\rm z}+q_{\rm z})(z'-z)} C(\mathbf{q}) \tag{8.9}$$

As shown in Appendix E the integration on z and z' leads to $2\pi L\delta(k_{\rm z}-k'_{\rm z}+q_{\rm z})$. Applying the δ function properties to the integral on $q_{\rm z}$, the following expression is achieved:

$$\langle \left| M_{j,j'}(k_{\rm z},k'_{\rm z}) \right|^2 \rangle = \frac{1}{2\pi L} \int_{\mathcal{C}_{\rm i\text{-}s}} dc \int_{\mathcal{C}_{\rm i\text{-}s}} dc' \int dq_{\rm c}\ f_{j,j',k_{\rm z},k'_{\rm z}}(c) f^*_{j,j',k_{\rm z},k'_{\rm z}}(c') e^{-\imath q_{\rm c}(c-c')} C(q_{\rm c}, q^f_{\rm z}) \tag{8.10}$$

being $q^f_{\rm z} = k'_{\rm z} - k_{\rm z}$. Rearranging Eq. (8.10) leads to:

$$\langle \left| M_{j,j'}(k_{\rm z},k'_{\rm z}) \right|^2 \rangle = \frac{1}{2\pi L} \int dq_{\rm c} C(q_{\rm c}, q^f_{\rm z}) \left[\int_{\mathcal{C}_{\rm i\text{-}s}} dc f_{j,j',k_{\rm z},k'_{\rm z}}(c) e^{-\imath q_{\rm c} c} \right] \\ \left[\int_{\mathcal{C}_{\rm i\text{-}s}} dc' f^*_{j,j',k_{\rm z},k'_{\rm z}}(c') e^{\imath q_{\rm c} c'} \right] \tag{8.11}$$

where, assuming that $\mathcal{C}_{i-s}$ is an open curve, the first term into brackets is the Fourier transform of $f_{j,j',k_{\rm z},k'_{\rm z}}$, and the second term is the complex conjugate of its Fourier transform. Therefore:

$$\langle \left| M_{j,j'}(k_{\rm z},k'_{\rm z}) \right|^2 \rangle = \frac{1}{2\pi L} \int dq_{\rm c} C(q_{\rm c}, q^f_{\rm z}) \left| F_{j,j',k_{\rm z},k'_{\rm z},}(q_{\rm c}) \right|^2 \tag{8.12}$$

which is the final expression for the SR matrix element due to a transition between states $(k_{\rm z}, j)$ and $(k'_{\rm z}, j')$.

8.2.2 Derivation for closed cross-sections

When $\mathcal{C}_{\rm i\text{-}s}$ is a closed curve (for example in a NW FET), some variations must be introduced in the determination of $\langle \left| M_{j,j'}(k_{\rm z},k'_{\rm z}) \right|^2 \rangle$. First, $\Delta(\mathbf{r}) = \Delta(c,z)$ is a periodic function in c, and therefore its spectrum in the $q_{\rm c}$ direction is a summation of δ functions

at multiples of $q_{\mathrm{c},0} = \frac{2\pi}{P}$, where P is the length of $\mathcal{C}_{\text{i-s}}$ [239]. Thus, we can write:

$$C(\mathbf{r}) = \frac{1}{4\pi^2}\int dq_{\mathrm{z}}\int dq_{\mathrm{c}} \sum_m C(q_{\mathrm{z}}, mq_{\mathrm{c},0})\frac{2\pi}{P}\delta(q_{\mathrm{c}} - mq_{\mathrm{c},0})e^{\imath q_{\mathrm{c}}(c'-c)}e^{\imath q_{\mathrm{z}}(z'-z)} \tag{8.13}$$

where the $\frac{2\pi}{P}$ inside the integrals relates the continuous spectrum corresponding to the non-periodic signal with the δ series Fourier components of the periodic signal. Then, $\langle \left| M_{j,j'}(k_{\mathrm{z}}, k'_{\mathrm{z}}) \right|^2 \rangle$ can be written as:

$$\begin{aligned}\langle \left| M_{j,j'}(k_{\mathrm{z}}, k'_{\mathrm{z}}) \right|^2 \rangle = \frac{1}{2\pi L^2 P}\int_{\mathcal{C}_{\text{i-s}}} dc \int_{\mathcal{C}_{\text{i-s}}} dc' \int_0^L dz \int_0^L dz' \int dq_{\mathrm{z}} \int dq_{\mathrm{c}} f_{j,j',k_{\mathrm{z}},k'_{\mathrm{z}}}(c) f^*_{j,j',k_{\mathrm{z}},k'_{\mathrm{z}}}(c') \\ \sum_m C(q_{\mathrm{z}}, mq_{\mathrm{c},0})\delta(q_{\mathrm{c}} - mq_{\mathrm{c},0}) e^{-\imath q_{\mathrm{c}}(c-c')} e^{\imath(k_{\mathrm{z}} - k'_{\mathrm{z}} + q_{\mathrm{z}})(z'-z)}\end{aligned} \tag{8.14}$$

Solving the integrals in z, z' and q_{z} as previously, we get:

$$\begin{aligned}\langle \left| M_{j,j'}(k_{\mathrm{z}}, k'_{\mathrm{z}}) \right|^2 \rangle = \frac{1}{LP}\int_{\mathcal{C}_{\text{i-s}}} dc \int_{\mathcal{C}_{\text{i-s}}} dc' \int dq_{\mathrm{c}} f_{j,j',k_{\mathrm{z}},k'_{\mathrm{z}}}(c) f^*_{j,j',k_{\mathrm{z}},k'_{\mathrm{z}}}(c') \\ e^{-\imath q_{\mathrm{c}}(c-c')} \sum_m C(q^f_{\mathrm{z}}, mq_{\mathrm{c},0})\delta(q - mq_{\mathrm{c},0})\end{aligned} \tag{8.15}$$

being again $q^f_{\mathrm{z}} = k'_{\mathrm{z}} - k_{\mathrm{z}}$. The q_{c} integral can be solved using the δ function property, leading to:

$$\begin{aligned}\langle \left| M_{j,j'}(k_{\mathrm{z}}, k'_{\mathrm{z}}) \right|^2 \rangle = \frac{1}{LP}\sum_m C(q^f_{\mathrm{z}}, mq_{\mathrm{c},0}) \left[\int_{\mathcal{C}_{\text{i-s}}} f_{j,j',k_{\mathrm{z}},k'_{\mathrm{z}}}(c) e^{-\imath m q_{\mathrm{c},0} s} dc\right] \\ \left[\int_{\mathcal{C}_{\text{i-s}}} f^*_{j,j',k_{\mathrm{z}},k'_{\mathrm{z}}}(c') e^{\imath m q_{\mathrm{c},0} s'} dc'\right]\end{aligned} \tag{8.16}$$

The integrals into brackets can be readily related to the m-th coefficient of the Fourier series of $f_{j,j',k_{\mathrm{z}},k'_{\mathrm{z}}}$ and its complex conjugate, given that f is a periodic function with period the curve perimeter, $P = 2\pi/q_{\mathrm{c},0}$. This last condition can be straightforwardly checked taking into account that ξ are single-valued functions. Therefore, the matrix element can be calculated as:

$$\langle \left| M_{j,j'}(k_{\mathrm{z}}, k'_{\mathrm{z}}) \right|^2 \rangle = \frac{P}{L}\sum_m C(q^f_{\mathrm{z}}, mq_{\mathrm{c},0}) \left| f_m \right|^2 \tag{8.17}$$

where:

$$f_m = \frac{1}{P}\int_{\mathcal{C}_{\text{i-s}}} f_{j,j',k_z,k'_z}(c) e^{-\imath\frac{2\pi m s}{P}} dc \tag{8.18}$$

which is the same expression proposed by Jin *et al.* [238] except for the different definition of the normalization factor P, included as a part of f_m coefficients here. The advantage of this definition is that f_m in Eq. (8.18) can be calculated employing FFT algorithms, as proposed by Stanojevic and Kosina, thus accelerating their calculation.

8.2.3 SR power spectrum

The power spectrum of the SR is well known for planar structures [228], [240]. We will assume here that the same expression of $C(\mathbf{q})$ can be used in non-planar structures [95], which is a valid assumption when $P \gg \Lambda_{\text{SR}}$. Thus, for an exponential autocorrelation function, the following expression is achieved for the power spectrum [95, 229, 233]:

$$C(\mathbf{q}) = \frac{\pi\Delta_{\text{SR}}^2\Lambda_{\text{SR}}^2}{\left(1+\frac{\Lambda_{\text{SR}}^2|\mathbf{q}|^2}{2}\right)^{3/2}} \tag{8.19}$$

where Δ_{SR} and Λ_{SR} are the rms value and the correlation length of the roughness, and characterize the roughness in the direction perpendicular and parallel to the interface, respectively. Equation (8.19) is then introduced into Eqs. (8.12) and (8.17) to determine $\langle\left|M_{j,j'}(k_z,k'_z)\right|^2\rangle$ for open and closed cross-section interface curves respectively.

8.2.4 Form factor

The form factor definition introduced in Eq. (8.6) is not unique. According to Ref. [230] it should be modified if the effective mass discontinuity in the semiconductor-insulator interface is taken into consideration, as:

$$f_{j,j',k_z,k'_z}(c) = \xi^*_{j,k_z}(c)\xi_{j',k'_z}(c)\Delta\phi - \frac{\hbar^2}{2}\left(\nabla\xi^*_{j,k_z}(c)\frac{1}{m_{\text{ins}}}\nabla\xi^*_{j,k_z}(c) + \nabla\xi^*_{j,k_z}(c)W\nabla\xi^*_{j,k_z}(c)\right) \tag{8.20}$$

where m_{ins} is the insulator isotropic effective mass and W is the semiconductor effective mass tensor (see Section 3.6). A non isotropic insulator effective mass could also be considered introducing the appropriate tensor in Eq. (8.20) in the stead of $1/m_{\text{ins}}$.

Alternatively, if no wavefunction penetration into the insulator is considered, the

form factor can be approximated by [230]:

$$f_{j,j',k_z,k'_z}(c) = \frac{\hbar^2}{2} m_{\text{ins}} \left[\mathbf{n} \cdot W \nabla \xi^*_{j,k_z}(c)\right] \left[\mathbf{n} \cdot W \nabla \xi^*_{j,k_z}(c)\right] \tag{8.21}$$

or according to Ref. [238] as:

$$f_{j,j',k_z,k'_z}(c) = \frac{\hbar^2}{2} \left[\mathbf{n} \cdot \nabla \xi^*_{j,k_z}(c)\right] W \left[\mathbf{n} \cdot \nabla \xi^*_{j,k_z}(c)\right] \tag{8.22}$$

which are equivalent expressions except for a factor $m_{\text{ins}}W$ which may be non-negligible. Otherwise stated we have opted for using Eq. (8.20) in the mobility results presented in the forthcoming Chapter.

8.3 Coulomb dispersion

Nearby the semiconductor-insulator interface of a MIS heterostructure there are several kind of charges, mainly resulting from the fabrication process, which adversely affect to the displacement of the carriers along the transport direction. The effects of some of these charges (concretely those due to interface traps) on some electrostatic quantities (such as V_{T} or SS) have been already analyzed in Chapter 4. Nevertheless there are other kinds of charges which deserve mention here: interface fixed charges, insulator charges, charge due to mobile ions, and ionized impurities [140, 175]. All these charges, induce a perturbing potential which is the responsible of the so-called as coulomb dispersion, CO. A comprehensive introduction to the aforementioned charges and an extensive discussion on coulomb dispersion for 2D electron gases was accomplished by Gámiz *et al.* in Ref. [241]. Several works have dealt with the modeling of the coulomb perturbing potential in 1D-confined devices [209, 232, 242**?** –244]. For such devices, Green functions can be analytically found and most of these works rely on them. Screening has been proven to have an impact in the coulomb limited mobility, and therefore it has been included in the models either using the long-wavelength approximations based on work by Stern and Howard [245] or using the Lindhard theory [95, 233]. Most of these works assume uncorrelated charges within the confinement direction, but correlation on the transport direction has been treated in [241] following the approach by Ning *et al.*[246].

The works dealing with coulomb scattering mechanism in NWs, such as Ref. [95, 215] assume specific geometries where the Green functions can again be calculated

analytically. Moreover, a non-uniform distribution of the charge within the confinement plane does not seem to be considered, leading to very high Columb limited mobilities.

In this work we follow an approach similar to that implemented in Ref.[241], including the correlation along the transport direction, but maintaining the charge uncorrelated among the different regions of the cross section. This allows us to simulate any situation, from a totally correlated charge in the confinement plane to a totally uncorrelated one, by just adjusting the size of each region.

As for screening, we deal in this manuscript with the tensorial dielectric screening based on the work by Jin *et al.* [95] (see Section 8.7) and therefore in our derivation of the perturbing potential, the charge due to screening, needed to introduce the long-wavelength approach, is not considered.

We focus here on the determination of the matrix element due to a 1D electron gas. The perturbing potential, $\tilde{\psi}^{\mathrm{CO}}$, associated to the coulomb scattering can be obtained by solving the Poisson equation for a given distribution of ionized impurities, $-\rho^{\mathrm{CO}}(\mathbf{r})$.

$$\nabla\epsilon(\mathbf{r})\nabla\tilde{\psi}^{\mathrm{CO}}(\mathbf{r}) = -\rho^{\mathrm{CO}}(\mathbf{r}) \tag{8.23}$$

As it happens with $\Delta^{\mathrm{SR}}(\mathbf{r})$ in SR scattering, $\rho^{\mathrm{CO}}(\mathbf{r})$ is actually a random variable. The approach used in SR, based on the determination of the expected value of the autocorrelation function, is not applicable to coulomb dispersion as it makes Eq. (8.23), to the best of our knowledge, irresolvable. An alternative approach consist on solving Eq. (8.23) for a known uncorrelated distribution of punctual charges in the confinement plane with a random distribution in the transport direction. Thus, we can write [241]:

$$\rho^{\mathrm{CO}}(\mathbf{r}) = q\sum_{m}\sigma_m(z)\delta(\mathbf{s}-\mathbf{s}_m) \tag{8.24}$$

where, as in SR, we have decomposed the position vector $\mathbf{r}$ into a confinement plane variable s and a transport variable z. Introducing Eq. (8.24) into Eq. (8.23) and writing ∇ as sum of its components in the confinement plane and transport direction we get:

$$[\nabla_{\mathrm{s}}\epsilon(\mathbf{r})\nabla_{\mathrm{s}} + \nabla_{\mathrm{z}}\epsilon(\mathbf{r})\nabla_{\mathrm{z}}]\,\tilde{\psi}^{\mathrm{CO}}(s,z) = -q\sum_{m}\sigma_m(z)\delta(\mathbf{s}-\mathbf{s}_m) \tag{8.25}$$

Following the approach by Gámiz *et al.* in Ref. [241], Eq. (8.25) is multiplied by $e^{-\imath q_{\mathrm{z}} z}$

and integrated over z, to take the Fourier transform on the longitudinal direction:

$$\left[\nabla_{\mathrm{s}}\varepsilon(\mathbf{r})\nabla_{\mathrm{s}} + \varepsilon(\mathbf{r})q_{\mathrm{z}}^2\right]\tilde{\psi}^{\mathrm{CO}}(s,q_{\mathrm{z}}) = -q\sum_m \sigma_m(q_{\mathrm{z}})\delta(\mathbf{s}-\mathbf{s}_m) \tag{8.26}$$

where the derivative ∇_{z} in the real space is transformed into a factor, q_{z}, in the wavenumber space. Using the superposition principle we can write the perturbing potential as:

$$\tilde{\psi}^{\mathrm{CO}}(\mathbf{s},q_{\mathrm{z}}) = \sum_m G_{q_{\mathrm{z}}}(\mathbf{s},\mathbf{s}_m)\sigma_m(q_{\mathrm{z}}) \tag{8.27}$$

where Eq. (8.26) can be separately solved for each contribution to the potential:

$$\left[\nabla_{\mathrm{s}}\epsilon(\mathbf{r})\nabla_{\mathrm{s}} + \epsilon(\mathbf{r})q_{\mathrm{z}}^2\right]G_{q_{\mathrm{z}}}(\mathbf{s},\mathbf{s}_m) = -q\delta(\mathbf{s}-\mathbf{s}_m) \tag{8.28}$$

being $G_{q_{\mathrm{z}}}(\mathbf{s},\mathbf{s}_m)$ in Eq. (8.28) the impulse response of the differential equation; in other words its Green function.

The matrix element for a transition between states (k_{z},j) and (k'_{z},j') was introduced in Eq. (7.17):

$$M_{j,j'}(k_{\mathrm{z}},k'_{\mathrm{z}}) = \int_{\mathcal{V}} dV\ \xi_{j,k_{\mathrm{z}}}(x,y)\frac{e^{-\imath k_{\mathrm{z}}z}}{\sqrt{L}}\tilde{\psi}^{\mathrm{CO}}(s,z)\xi^*_{j',k'_{\mathrm{z}}}(x,y)\frac{e^{\imath k'_{\mathrm{z}}z}}{\sqrt{L}} \tag{8.29}$$

Decomposing the integral in the confinement plane and transport direction we have:

$$M_{j,j'}(k_{\mathrm{z}},k'_{\mathrm{z}}) = \frac{1}{L}\int_{\mathcal{A}} d\mathbf{s}\ \xi_{j,k_{\mathrm{z}}}(x,y)\xi^*_{j',k'_{\mathrm{z}}}(x,y)\int dz e^{-\imath(k_{\mathrm{z}}-k'_{\mathrm{z}})z}\tilde{\psi}^{\mathrm{CO}}(\mathbf{s},z) \tag{8.30}$$

Then, the expected value of the squared matrix element can be written as:

$$\begin{aligned}\langle|M_{j,j'}(k_{\mathrm{z}},k'_{\mathrm{z}})|^2\rangle = \frac{1}{L^2}\int_{\mathcal{A}} d\mathbf{s}\int_{\mathcal{A}} d\mathbf{s}'\ f_{j,j',k_{\mathrm{z}},k'_{\mathrm{z}}}(\mathbf{s})f^*_{j,j',k_{\mathrm{z}},k'_{\mathrm{z}}}(\mathbf{s}')\\ \int dz\int dz' e^{-\imath(k_{\mathrm{z}}-k'_{\mathrm{z}})(z-z')}\langle\tilde{\psi}^{\mathrm{CO}}(\mathbf{s},z)\tilde{\psi}^{\mathrm{CO}}(\mathbf{s}',z')\rangle\end{aligned} \tag{8.31}$$

where equivalently to what was done for SR, we have defined:

$$f_{j,j',k_{\mathrm{z}},k'_{\mathrm{z}}}(\mathbf{s}) = \xi_{j,k_{\mathrm{z}}}(x,y)\xi^*_{j',k'_{\mathrm{z}}}(x,y) \tag{8.32}$$

being, $\mathbf{s}=(x,y)$.

The Fourier transform of the autocorrelation function, $\langle\tilde{\psi}^{\mathrm{CO}}(s,z)\tilde{\psi}^{\mathrm{CO}}(s',z')\rangle$, gives

us:

$$C(\mathbf{s},q_{\mathrm{z}})=\langle\tilde{\psi}^{\mathrm{CO}}(\mathbf{s},q_{\mathrm{z}})\tilde{\psi}^{\mathrm{CO}}(\mathbf{s}',q_{\mathrm{z}})\rangle=\sum_{m}\sum_{i}G^{*}_{q_{\mathrm{z}}}(\mathbf{s}',\mathbf{s}'_{i})G_{q_{\mathrm{z}}}(\mathbf{s},\mathbf{s}_{m})\langle\sigma_{m}(q_{\mathrm{z}})\sigma^{*}_{i}(q_{\mathrm{z}})\rangle \quad (8.33)$$

We assume that the charge is uncorrelated for different regions in the confinement plane, so that the previous sum is null for $m\neq i$. Then we can define the autocorrelation of the perturbing potential as:

$$\langle\tilde{\psi}^{\mathrm{CO}}(\mathbf{s},z)\tilde{\psi}^{\mathrm{CO}}(\mathbf{s}',z')\rangle=C(\mathbf{s},z)=\frac{1}{2\pi}\int C(\mathbf{s},q_{\mathrm{z}})e^{-\imath q_{\mathrm{z}}(z'-z)}dq_{\mathrm{z}} \quad (8.34)$$

Thus, Eq. (8.31) can be rewritten as:

$$\langle|M_{j,j'}(k_{\mathrm{z}},k'_{\mathrm{z}})|^{2}\rangle=\frac{1}{2\pi L^{2}}\int_{\mathcal{A}}d\mathbf{s}\int_{\mathcal{A}}d\mathbf{s}'\ f_{j,j',k_{\mathrm{z}},k'_{\mathrm{z}}}(\mathbf{s})f^{*}_{j,j',k_{\mathrm{z}},k'_{\mathrm{z}}}(\mathbf{s}')$$
$$\int dz\int dz'\int dq_{\mathrm{z}}e^{-\imath(k_{\mathrm{z}}-k'_{\mathrm{z}}-q_{\mathrm{z}})(z-z')}\sum_{m}G^{*}_{q_{\mathrm{z}}}(\mathbf{s}',\mathbf{s}'_{m})G_{q_{\mathrm{z}}}(\mathbf{s},\mathbf{s}_{m})\langle\sigma_{m}(q_{\mathrm{z}})\sigma^{*}_{m}(q_{\mathrm{z}})\rangle \quad (8.35)$$

The integration along q_{z}, z, and z' can be simplified as in Appendix E for SR. Thus:

$$\langle|M_{j,j'}(k_{\mathrm{z}},k'_{\mathrm{z}})|^{2}\rangle=\frac{1}{L}\int_{\mathcal{A}}d\mathbf{s}\int_{\mathcal{A}}d\mathbf{s}'f_{j,j',k_{\mathrm{z}},k'_{\mathrm{z}}}(\mathbf{s})f^{*}_{j,j',k_{\mathrm{z}},k'_{\mathrm{z}}}(\mathbf{s}')\sum_{m}$$
$$G^{*}_{q^{f}_{\mathrm{z}}}(\mathbf{s}',\mathbf{s}'_{m})G_{q^{f}_{\mathrm{z}}}(\mathbf{s},\mathbf{s}_{m})\langle\sigma_{m}(q^{f}_{\mathrm{z}})\sigma^{*}_{m}(q^{f}_{\mathrm{z}})\rangle \quad (8.36)$$

where $q^{f}_{\mathrm{z}}=k_{\mathrm{z}}-k_{\mathrm{z}'}$. $\langle\sigma_{m}(q^{f}_{\mathrm{z}})\sigma^{*}_{i}(q^{f}_{\mathrm{z}})\rangle$ is the power spectrum of the random distribution of charges along the axial direction which can be determined under the hard-sphere model, as proposed for a 2D electron gas by Ning *et al.* in Ref. [246] and also studied by Gámiz *et al.* in Ref. [241]. In Appendix E we detail the calculus of the hard-sphere model for a 1D electron gas. The resulting power spectrum is:

$$\langle\sigma_{m}(q^{f}_{\mathrm{z}})\sigma^{*}_{m}(q^{f}_{\mathrm{z}})\rangle=N_{\mathrm{avg}}\left(1-C\,\mathrm{sinc}(q_{\mathrm{z}}R_{\mathrm{t}})\right) \quad (8.37)$$

where, as explained in Appendix E, N_{avg} is the average ionized impurities per unit length and R_{t} is the radius of the hard sphere which determines the minimum distance between ionized impurities. $C=R_{\mathrm{t}}N_{\mathrm{avg}}$ is a measure of the degree of correlation in the transport direction: $C=0$ correspond to a completely uncorrelated random distribution while $C=1$ is a uniform fully correlated distribution. In Eq. (8.37) we have assumed that the axial distribution of charges corresponding to different confinement

plane positions are completely uncorrelated. Therefore Eq. (8.36) can be reformulated as:

$$\langle |M_{j,j'}(k_z, k'_z)|^2 \rangle = \frac{N_{\text{avg}}}{L} \int_{\mathcal{A}} d\mathbf{s} \int_{\mathcal{A}} d\mathbf{s}' f_{j,j',k_z,k'_z}(\mathbf{s}) f^*_{j,j',k_z,k'_z}(\mathbf{s}') \sum_m G_{q_z^f}(\mathbf{s}, \mathbf{s}_m) G^*_{q_z^f}(\mathbf{s}', \mathbf{s}_m) \left(1 - C\,\text{sinc}(q_z^f R_t)\right) \tag{8.38}$$

Eq. (8.38) is the final expression for the coulomb dispersion matrix element due to a transition between states (k_z, j) and (k'_z, j').

8.4 Bulk non-polar phonons

For a non-null temperature the atoms in the semiconductor lattice vibrate, oscillating around their equilibrium positions. Phonons (PH) are the result of a quantum mechanical analysis of these semiconductor lattice vibrations. The mathematical derivation of the phonon-electron interaction can be found in several textbooks [247], [88]. We briefly summarize here the main ideas to understand the perturbation potential due to phonons. In this manuscript, we neglect the confinement effects that may influence the behavior of phonons in small devices [236, 248, 249].

The vibrations can be modeled as a set of harmonic oscillators. For a crystal with a diatomic unit cell, there are six allowed modes of oscillation: two for each direction in real space. In the first of these two modes, the two atoms of the unit cell oscillate in phase while for the second one atoms vibrate in opposite phase. The two modes are known as acoustic, A, (due to its similarities with the propagation of an acoustic wave on air) and optic, O, (because in some ionic crystal they are excited by electromagnetic radiation), respectively [247]. Regarding the direction of vibration of the modes they are called transverse, T, when the atoms vibrate perpendicularly to the phonon wavevector, $\mathbf{q}$ direction (there are two transverse modes) and longitudinal, L, when the atoms vibrate aligned with $\mathbf{q}$ (there is one longitudinal mode).

The modes of oscillation for Si obtained from Refs. [88, 250, 251] are shown in Fig. 8.1 where the phonon energy is plotted as a function of the phonon wavevector magnitude $|\mathbf{q}|$. Transversal modes (TA, TO) are degenerated. For low $|\mathbf{q}|$ values, acoustic phonons modes (LA and TA), show a linear $E(|\mathbf{q}|) - |\mathbf{q}|$ dependence and the energy is commonly modeled by a term $E_{\text{PH}} = \hbar v_s |\mathbf{q}|$, where v_s is the slope of the ω-$|\mathbf{q}|$

curve. For optic phonons, LO and TO, keep a constant energy $E_{\mathrm{PH}}(|\mathbf{q}|) = \hbar\omega_{\mathrm{OPH}}$,

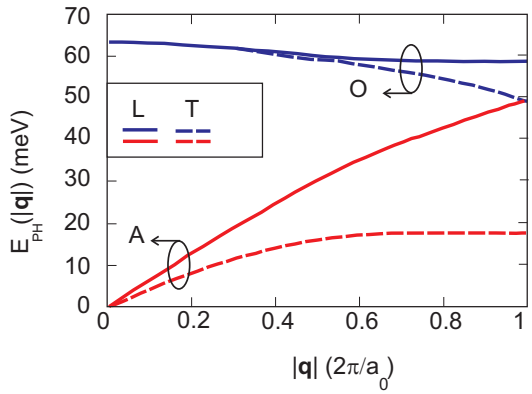

Figure 8.1: Phonon energy, E_{PH}, as a function of the phonon wavevector magnitude $|\mathbf{q}|$ for different modes of vibration of Si oriented in [100] crystallographic direction. Transversal and longitudinal modes are plotted as dashed and solid lines respectively. Acoustic and optic modes are marked as A and O, respectively. Adapted from Ref. [88] after Refs. [250], [251].

The vibrations of the crystal induce a strain in the lattice which modifies the band edges of the semiconductor resulting in a deformation potential whose expression is given by[247][1]:

$$\tilde{\psi}^{\mathrm{PH}}(\mathbf{r}) = D(\mathbf{q})u^{\mathrm{PH}}(\mathbf{r},\mathbf{q},t) = D(\mathbf{q})\sqrt{\frac{\hbar}{2\varrho_{\mathrm{s}}\omega_{\mathrm{PH}}(\mathbf{q})L}}A(\mathbf{q})e^{\pm\imath(\mathbf{q}\mathbf{r}-\omega_{\mathrm{PH}}(\mathbf{q})t)} \tag{8.39}$$

where $D(\mathbf{q})$ is a deformation potential, $u^{\mathrm{PH}}(\mathbf{r},\mathbf{q},t)$ is the phonon wave, ϱ_{s} is the semiconductor density, $\omega_{\mathrm{PH}} = E_{\mathrm{PH}}/\hbar$ is the phonon frequency and $A(\mathbf{q})$ is the wave magnitude which is related to the number of phonons, $n_{\mathrm{PH}}(\mathbf{q})$, as $A(\mathbf{q}) = \sqrt{n_{\mathrm{PH}}(\mathbf{q}) + \frac{1}{2} \pm \frac{1}{2}}$. [2] $n_{\mathrm{PH}}(\mathbf{q})$, is given by the Bose-Einstein distribution

$$n_{\mathrm{PH}}(\mathbf{q}) = \frac{1}{e^{\frac{E_{\mathrm{PH}}}{k_{\mathrm{B}}T}} - 1} \tag{8.40}$$

To include the effect of phonons scattering in the transport calculations we have

[1] The ± sign in the exponential correspond to phonon emission and absorption processes respectively. This result stems from a quantum treatment of the electron-phonon interaction.

[2] Again the ± sign correspond to phonon emission and absorption processes, respectively.

assumed that only small $|\mathbf{q}|$ phonons play a relevant role in the scattering process.

8.4.1 Acoustic phonons

As seen in Fig. 8.1, for acoustic phonons a small value of $|\mathbf{q}|$ implies a small value of energy, E_{PH}, which in most of cases is negligible compared with the electron energy, $E_i(k_{\text{z}})$, and can therefore be obliterated in the calculus. As a consequence, acoustic phonon mechanism is assumed to be elastic [3]. Two implication derive from this assumption [206]:

(a) The term ωt in the exponential of Eq. (8.39), which as explained in Section 7.3 determines the energy transfer due to the scattering process, is removed.

(b) The Bose-Einstein function in Eq. (8.40) is simplified to $k_{\text{B}}T/E_{\text{PH}}$ and $n_{\text{PH}}(|\mathbf{q}|) = k_{\text{B}}T/E_{\text{PH}} = k_{\text{B}}T/\hbar v_{\text{s}}|\mathbf{q}|$

Moreover, the deformation potential for acoustic phonons is proportional to the wavenumber: $D(\mathbf{q}) = D_{\text{APH}}\mathbf{q}$. Thus, for acoustic phonons Eq. (8.39) is simplified to:

$$\tilde{\psi}^{\text{APH}}(\mathbf{r}) = D_{\text{APH}}\sqrt{\frac{k_BT}{2AL\varrho_{\text{s}}}}\frac{1}{v_{\text{s}}}e^{\pm\imath\mathbf{qr}} \tag{8.41}$$

where we have used $\Omega = AL$. The matrix element due to a transition between states (k_{z}, j) and (k'_{z}, j') is:

$$M_{j,j'}(k_{\text{z}}, k'_{\text{z}}) = \int_0^L dz \int_{\mathcal{A}} dA\ \xi_{j,k_{\text{z}}}(x,y)\frac{e^{-\imath k_{\text{z}}z}}{\sqrt{L}}\left(D_{\text{APH}}\sqrt{\frac{k_BT}{2\varrho_{\text{s}}AL}}\frac{1}{v_{\text{s}}}e^{\pm\imath\mathbf{qr}}\right)\xi^*_{j',k'_{\text{z}}}(x,y)\frac{e^{\imath k'_{\text{z}}z}}{\sqrt{L}} \tag{8.42}$$

which can be written as[4]:

$$M_{j,j'}(k_{\text{z}}, k'_{\text{z}}) = \frac{D_{\text{APH}}}{L}\sqrt{\frac{k_BT}{2\varrho_{\text{s}}AL}}\frac{1}{v_{\text{s}}}\int_0^L dz \int_{\mathcal{A}} dA\ \xi_{j,k_{\text{z}}}(x,y)e^{-\imath(q_{\text{x}}x+q_{\text{y}}y)}\xi^*_{j',k'_{\text{z}}}(x,y)e^{-\imath(k_{\text{z}}-k'_{\text{z}}+q_{\text{z}})z} \tag{8.43}$$

[3] This approximation is not valid for low temperatures and highly confined structures [249].

[4] For the sake of simplicity just the minus branch was considered. Equivalent derivation can be found for the positive branch.

The squared matrix element can then be calculated as:

$$|M_{j,j'}(k_z,k'_z)|^2 = \frac{D^2_{\text{APH}}}{L^2}\frac{k_BT}{2\varrho_s AL}\frac{1}{v_s^2}\int_{\mathcal{A}}d\mathbf{s}\int_{\mathcal{A}}d\mathbf{s}'\int_0^L dz\int_0^L dz'\; f_{j,j',k_z,k'_z}(x,y)e^{-\imath(q_x x+q_y y)} f^*_{j,j',k_z,k'_z}(x',y')e^{\imath(q_x x'+q_y y')}e^{-\imath(k_z-k'_z-q_z)(z'-z)} \tag{8.44}$$

where $f_{j,j',k_z,k'_z}(x,y)$ was defined in Eq. (8.32). The mathematical details of the integration procedure are given in Appendix E. The resulting expression is:

$$|M_{j,j'}(k_z,k'_z)|^2 = \frac{D^2_{\text{APH}}}{L}\frac{k_BT}{2\varrho_s}\frac{1}{v_s^2}\int_{\mathcal{A}}dA\; f_{j,j',k_z,k'_z}(x,y)f^*_{j,j',k_z,k'_z}(x,y) \tag{8.45}$$

which is the same expression proposed in Refs. [95, 227]. It is important to highlight that the matrix element does not depend on q_z and, therefore, it is isotropic.

8.4.2 Optical phonons

For optical phonons a small q_z does not imply a small energy, E_{PH}, and therefore neither of the previous approximations for acoustic phonons can be made. Instead, $\omega_{\text{PH}}(|\mathbf{q}|)$ weakly depends on $|\mathbf{q}|$ and can be assumed as constant $\omega_{\text{PH}}(|\mathbf{q}|) = \omega_{\text{OPH}}$, see Fig. 8.1. Consequently the energy, E_{PH}, and the number of phonons $n_{\text{PH}}(q_z) = n_{\text{PH}}$ are also constant. In addition, for optical phonons the deformation potential is assumed to be constant $D(q_z) = D_{\text{OPH}}$. Thus, the perturbing potential can be written as:

$$\tilde{\psi}^{\text{OPH}}(z) = D_{\text{OPH}}\sqrt{\frac{\hbar}{2AL\varrho_s\omega_{\text{OPH}}}}\sqrt{n_{\text{PH}}+\frac{1}{2}\pm\frac{1}{2}}e^{\pm\imath(|\mathbf{qr}|-\omega_{\text{OPH}}t)} \tag{8.46}$$

One main difference between the perturbing potential presented in Eq. (8.46) and those obtained for other scattering mechanisms such as surface roughness, coulomb dispersion and acoustic phonons in Eqs. (8.1), (8.27), and (8.41) respectively, is the factor $e^{\imath\omega_{\text{OPH}}t}$. As explained in Section 7.3, this factor implies a change in the energy between the initial and final states E and E' of states (k_z, j) and (k'_z, j') such that $E' = E \pm \hbar\omega_{\text{PH}}$.

The matrix element due to a transition between states (k_z, j) and (k'_z, j') is given

by:

$$M_{j,j'}(k_{\mathrm{z}},k'_{\mathrm{z}}) = \int_0^L dz \int_{\mathcal{A}} dA\; f_{j,j',k_{\mathrm{z}},k'_{\mathrm{z}}}(\mathbf{s}) \frac{e^{-\imath k_{\mathrm{z}} z}}{\sqrt{L}} \left(D_{\mathrm{OPH}} \sqrt{\frac{\hbar}{2AL\varrho_{\mathrm{s}}\omega_{\mathrm{OPH}}}} \sqrt{n_{\mathrm{PH}} + \frac{1}{2} \pm \frac{1}{2}} e^{\pm \imath q_{\mathrm{s}} s \pm \imath q_{\mathrm{z}} z} \right) \frac{e^{\imath k'_{\mathrm{z}} z}}{\sqrt{L}} \tag{8.47}$$

The square matrix element can then be written after the appropriate integration for q_{x}, q_{y}, q_{z}, z, z' equivalent to the carried ot for acoustic phonons in Appendix E as:

$$|M_{j,j'}(k_{\mathrm{z}},k'_{\mathrm{z}})|^2 = \frac{D^2_{\mathrm{OPH}}}{L} \frac{\hbar}{2\varrho_{\mathrm{s}}\omega_{\mathrm{OPH}}} \left(n_{\mathrm{PH}} + \frac{1}{2} \pm \frac{1}{2} \right) \int_{\mathcal{A}} dA\; f_{j,j',k_{\mathrm{z}},k'_{\mathrm{z}}}(\mathbf{s}) f^*_{j,j',k_{\mathrm{z}},k'_{\mathrm{z}}}(\mathbf{s}) \tag{8.48}$$

which also coincides with the expression proposed in Refs. [95, 227] As in acoustic phonons the matrix element is not dependent on q_{z}, being therefore modeled as an inelastic isotropic mechanism.

8.5 Polar Optical Phonons

Similarly to non-polar bulk phonons, polar optical phonons (POP) result from vibrations of the crystal lattice. The main difference is related to the ionic nature of POP. In polar crystals, such as III-V compound semiconductors, there is a net electronic charge transfer between atoms of both compounds. This charge transfer leads to an effective dipole which results into a contribution to the dielectric function and modifies the potential induced by the lattice vibrations. The term optical comes from the high frequency and weakly wavevector dependent nature of these phonons. The mathematical derivation of the perturbing potential due to POP can be found elsewhere [252] leading to the so-called Fröhlich potential given by [217, 253, 254]:

$$\tilde{\psi}^{\mathrm{POP}}(\mathbf{r}) = -\imath \sqrt{\frac{q^2\hbar\omega_{\mathrm{POP}}}{2AL} \left(\frac{1}{\epsilon_\infty} - \frac{1}{\epsilon_0} \right)} \frac{1}{|\mathbf{q}|} \sqrt{n_{\mathrm{PH}} + \frac{1}{2} \pm \frac{1}{2}} e^{\pm \imath \mathbf{q}\mathbf{r} - \omega_{\mathrm{POP}} t} \tag{8.49}$$

being ω_{POP} the phonon frequency, $\epsilon(\infty)$ the high-frequency dielectric constant and $\epsilon(0)$ the static dielectric constant. The rest of the terms keep the meaning used in Section 8.4. We have assumed that ω_{POP} does not depend on $|\mathbf{q}|$ and consequently neither does n_{PH}. As proposed in Section 7.3 and previously discussed in Section 8.4 for optical phonons, the factor $e^{-\imath\omega_{\mathrm{POP}} t}$ implies a change of energy in the scattering process. The

derivation of the matrix element for 2D-confined devices has been addressed in Ref. [217, 253, 254]. We reproduce it here for the sake of completeness. The matrix element can then be calculated as:

$$M_{j,j'}(k_{\rm z},k'_{\rm z}) = \frac{1}{\sqrt{AL}}\int_0^L dz \int_{\mathcal{A}} dA\ \xi_{j,k_{\rm z}}(x,y)\frac{e^{-\imath k_{\rm z} z}}{\sqrt{L}}\left(\frac{C_{\rm POP}}{|\mathbf{q}|}e^{\imath \mathbf{qr}}\right)\xi^*_{j',k'_{\rm z}}(x,y)\frac{e^{\imath k'_{\rm z} z}}{\sqrt{L}} \quad (8.50)$$

where we have defined the constant:

$$C_{\rm POP} = -\imath\sqrt{\frac{q^2\hbar\omega_{\rm POP}}{2}\left(\frac{1}{\epsilon_\infty}-\frac{1}{\epsilon_0}\right)\left(n_{\rm PH}+\frac{1}{2}\pm\frac{1}{2}\right)} \quad (8.51)$$

The square matrix element is then given by:

$$\left|M_{j,j'}(k_{\rm z},k'_{\rm z})\right|^2 = \frac{C^2_{\rm POP}}{L^2}\frac{1}{AL}\int_0^L dz\int_0^L dz'\int_{\mathcal{A}} dA\int_{\mathcal{A}'} dA'\ \ f_{j,j',k_{\rm z},k'_{\rm z}}(\mathbf{s})f_{j,j',k_{\rm z},k'_{\rm z}}(\mathbf{s}') \frac{e^{\mp\imath q_{\rm x}(x-x')\mp i q_{\rm y}(y-y')}}{q_{\rm x}^2+q_{\rm y}^2+q_{\rm z}^2}e^{\imath(k_{\rm z}-k'_{\rm z}-q_{\rm z})z} \quad (8.52)$$

where have used the $f_{j,j',k_{\rm z},k'_{\rm z}}(\mathbf{s})$ definition of Eq. (8.32). If we account for all the possible $q_{\rm x}$, $q_{\rm y}$ and $q_{\rm z}$ contributions, and transforming the $q_{\rm x}$, $q_{\rm y}$ and $q_{\rm z}$ sums in integrals as in Eqs. (E.23), we obtain:

$$\left|M_{j,j'}(k_{\rm z},k'_{\rm z})\right|^2 = \frac{C^2_{\rm POP}}{L^2}\frac{1}{8\pi^3}\int dq_{\rm z}\int_0^L dz\int_0^L dz'\int_{\mathcal{A}} dA\int_{\mathcal{A}'} dA'\ \ f_{j,j',k_{\rm z},k'_{\rm z}}(\mathbf{s})f_{j,j',k_{\rm z},k'_{\rm z}}(\mathbf{s}') \int\int dq_{\rm x}dq_{\rm y}\frac{e^{\mp\imath q_{\rm x}(x-x')\mp i q_{\rm y}(y-y')}}{q_{\rm x}^2+q_{\rm y}^2+q_{\rm z}^2}e^{\imath(k_{\rm z}-k'_{\rm z}-q_{\rm z})z} \quad (8.53)$$

The axial and $q_{\rm z}$ integration of Eq. (8.53) leads to:

$$\left|M_{j,j'}(k_{\rm z},k'_{\rm z})\right|^2 = \frac{C^2_{\rm POP}}{L}\frac{1}{4\pi^2}\int_{\mathcal{A}} dA\int_{\mathcal{A}'} dA'\ \ f_{j,j',k_{\rm z},k'_{\rm z}}(\mathbf{s})f_{j,j',k_{\rm z},k'_{\rm z}}(\mathbf{s}') \int\int dq_{\rm x}dq_{\rm y}\frac{e^{\mp\imath q_{\rm x}(x-x')\mp i q_{\rm y}(y-y')}}{q_{\rm x}^2+q_{\rm y}^2+q_{\rm z}^{2f}} \quad (8.54)$$

where $q_{\rm z}^f = k_{\rm z}-k'_{\rm z}$ and we have substituted $\mathbf{q}$ by its components. The inner integral in Eq. (8.54) is analytically solved in Appendix E. Substituting the result into Eq. (8.53)

we get:

$$\left|M_{j,j'}(k_z,k'_z)\right|^2 = \frac{C^2_{\text{POP}}}{2\pi L}\int_{\mathcal{A}} dA \int_{\mathcal{A}'} dA' f_{j,j',k_z,k_{z'}}(\mathbf{s}) f_{j,j',k_z,k_{z'}}(\mathbf{s}') K_0\left(q^f_z\left|s-s'\right|\right) \quad (8.55)$$

where K_0 is the modified Bessel function of the second kind and order zero. This is the final expression for the POP matrix element due to a transition between states (k_z, j) and (k'_z, j'), which coincides with the expression achieved by Wang *et al.* in Ref. [253].

8.6 Alloy Disorder

In alloy semiconductors, there is some randomness in the distribution of atoms in the positions of the zinc-blende structure. Commonly one the semiconductors occupy one fcc lattice while the other two semiconductors distribute themselves randomly in the second fcc lattice [255]. As a consequence, the crystal potential is not periodic. The most common treatment of the problem consists on assuming that the alloy is actually ordered and the resulting virtual periodic crystal potential can be calculated as an average of those corresponding to the different semiconductor involved. The actual non-periodic potential influence is then modeled by a scattering mechanism called alloy disorder (AD). The expected value of the squared perturbing potential due to AD can be determined from a statistical analysis of the differences between actual and virtual potentials [234, 255], resulting into:

$$\langle|\psi^{\text{AD}}|^2\rangle = \frac{a_0^3 x(1-x)}{L}|V_{\text{a}} - V_{\text{b}}|^2 \quad (8.56)$$

where x is the alloy molar fraction, $|V_{\text{a}}-V_{\text{b}}|$ is the potential variation due to the presence of the alloys atoms and a_0 is the lattice constant (therefore a_0^3 is the integration volume of the perturbation potential). According to Harrison *et al.* [256], although $|V_{\text{a}} - V_{\text{b}}|$ could be taken as the difference in energy band gaps for the two components of the alloy, a more reasonable assumption is to take the vacuum level as the reference energy level. This last option is also chosen by Bastard [255]. The matrix element between states (k_z, j) and (k'_z, j') is:

$$M_{j,j'}(k_z,k'_z) = \int_0^L dz \int_{\mathcal{A}} d\mathbf{s}\ \xi_{j,k_z}(x,y)\frac{e^{-\imath k_z z}}{\sqrt{L}}\tilde{\psi}^{\text{AD}}\xi^*_{j',k'_z}(x,y)\frac{e^{\imath k'_z z}}{\sqrt{L}} \quad (8.57)$$

Then, the expected value of the squared matrix element is:

$$\langle |M_{j,j'}(k_z, k'_z)|^2 \rangle = \frac{a_0^3 x(1-x)}{4L} |V_a - V_b|^2 \int_{\mathcal{A}} d\mathbf{s}\ f_{j,j',k_z,k'_z}(\mathbf{s}) f^*_{j,j',k_z,k'_z}(\mathbf{s}) \tag{8.58}$$

where $f^*_{j,j',k_z,k'_z}(\mathbf{s})$ was defined in Eq. (8.32).

8.7 Dielectric Screening

Dielectric screening of the surface roughness, coulomb dispersion and alloy disorder scattering potentials needs to be included in order to get the correct dependence of the electron mobility on the effective field [95]. Moreover as it was pointed out in Ref. [257], a tensorial dielectric screening approach is needed for an accurate model.

In this Section, we introduce screening following Lindhard theory for 2D confined devices as in Ref. [95], but extending their approach to deal with arbitrary geometries and with scattering mechanisms for which the unscreened matrix element, $M_{j,j'}(k_z, k'_z)$, cannot be calculated directly, and only their mean quadratic value, $\langle |M_{j,j'}(k_z, k'_z)| \rangle$ can be attained. This is the case for AD and for SR when calculated as proposed in this manuscript following Refs. [238, 258**? ?**]. The influence of screening on the phonon-electron interaction is neglected [95, 229, 233, 257]. The effective screened perturbing potential, ψ^s, for a given value of q_z is written as [95]:

$$\psi^s_{q_z}(\mathbf{s}) = \psi^{us}_{q_z}(\mathbf{s}) + \int d\mathbf{s} G_{q_z}(\mathbf{s}, \mathbf{s}') \frac{\rho^{ind}_{q_z}(\mathbf{s})}{\epsilon_s} \tag{8.59}$$

where ψ^{us} is the unscreened perturbing potential and ρ_{ind} is the charge induced by the perturbing potential and can be calculated as:

$$\rho^{ind}_{q_z}(\mathbf{s}) = -\sum_{j,j'} \Pi_{q_z,j,j'} \psi^s_{q_z,j,j'} \xi(\mathbf{s}) \xi_{j'}(\mathbf{s}) \tag{8.60}$$

with

$$\Pi_{q_z,j,j'} = e^2 \frac{2g_v}{L} \sum_k \frac{f_{j,k+q} - f_{j',k}}{E_{j',k} - E_{j,k+q}} \tag{8.61}$$

where e is the electron charge, $E_{j,k} = E_j(k)$ corresponds to the sum of potential and kinetic energy of a state of subband j with wave number k, and $f_{j,k}$ is the occupation of such state, namely the Fermi-Dirac function evaluated at $E_{j,k}$. The $2g_v$ term accounts

for spin and valley degeneracy. Finally, $\psi^{\mathrm{s}}_{q_{\mathrm{z}},j,j'}$ is calculated as:

$$\psi^{\mathrm{s}}_{q_{\mathrm{z}},j,j'} = \int_{\mathcal{A}} d\mathbf{s}\xi_j(\mathbf{s})\psi^{\mathrm{s}}_{q_{\mathrm{z}}}(\mathbf{s})\xi^*_{j'}(\mathbf{s}) \tag{8.62}$$

Equation (8.62) can be readily identified with the definition of the matrix element proposed in Eq. (**??**).

$$\psi^{\mathrm{s}}_{q_{\mathrm{z}},j,j'} = M^{\mathrm{s}}_{j,j'}(k_{\mathrm{z}},k'_{\mathrm{z}})\big|_{q_{\mathrm{z}}=k_{\mathrm{z}}-k_{\mathrm{z}},} \tag{8.63}$$

Multiplying Eq. (8.59) by $\xi_i(\mathbf{s})\xi_{i'}(\mathbf{s})$ and integrating in the confinement plane we can write:

$$\psi^{\mathrm{s}}_{q_{\mathrm{z}},i,i'} = \psi^{\mathrm{us}}_{q_{\mathrm{z}},i,i'} + \int d\mathbf{s}\xi_i(\mathbf{s})\xi_{i'}(\mathbf{s}) \int d\mathbf{r}' G_{q_{\mathrm{z}}}(\mathbf{s},\mathbf{s}') \sum_{j,j'} \Pi_{q_{\mathrm{z}},j,j'}\psi^{\mathrm{s}}_{q_{\mathrm{z}},j,j'}\xi(\mathbf{s}')\xi_{j'}(\mathbf{s}') \tag{8.64}$$

which can be rewritten as:

$$\psi^{\mathrm{s}}_{q_{\mathrm{z}},i,i'} = \psi^{\mathrm{us}}_{q_{\mathrm{z}},i,i'} + \sum_{j,j'} \Pi_{q_{\mathrm{z}},j,j'}\psi^{\mathrm{s}}_{q_{\mathrm{z}},j,j'}\nu_{q_{\mathrm{z}},i,i',j,j'} \tag{8.65}$$

where $\nu_{q_{\mathrm{z}},i,i',j,j'}$ is defined as:

$$\nu_{q_{\mathrm{z}},i,i',j,j'} = \int d\mathbf{s}\xi_i(\mathbf{s})\xi_{i'}(\mathbf{s}) \int d\mathbf{s}' G_q(\mathbf{s},\mathbf{s}')\xi_j(\mathbf{s}')\xi_{j'}(\mathbf{s}') \tag{8.66}$$

Therefore, to achieve the screened matrix elements, the following equation system has to be solved

$$\psi^{\mathrm{us}}_{q_{\mathrm{z}},i,i'} = \sum_{j,j'} \left(\delta_{ij,i'j'} - \Pi_{q_{\mathrm{z}},j,j'}\nu_{q_{\mathrm{z}},i,i',j,j'}\right)\psi^{\mathrm{s}}_{q_{\mathrm{z}},j,j'} = \varepsilon_{q_{\mathrm{z}},i,i',j,j'}\psi^{\mathrm{s}}_{q_{\mathrm{z}},j,j'} \tag{8.67}$$

where $\varepsilon_{q_{\mathrm{z}},i,i',j,j'}$ is the dielectric tensor. Thus, the screened matrix elements are given by:

$$\psi^{\mathrm{s}}_{q_{\mathrm{z}},j,j'} = \sum_{i,i'} \varepsilon^{-1}_{q_{\mathrm{z}},i,i',j,j'}\psi^{\mathrm{us}}_{q_{\mathrm{z}},i,i'} \tag{8.68}$$

The calculation of $G_{q_{\mathrm{z}}}(\mathbf{s},\mathbf{s}')$ for cylindrical devices was addressed by Jin *et al.* in [95] and later extended for cylindrical structures with several insulator layers by Dura *et al.* [215]. Nevertheless, their work deals with a isotropic effective mass, where the angular wave number of the calculated wave functions is known *a priori* when solving the Schrödinger equation. However, when the effective mass tensor is anisotropic (as,

for example, at X and L valleys of III-V semiconductors), it is necessary to expand the wave functions into a series of cylindrical functions in order to use those G_{q_z} functions even for cylindrical geometries. Moreover, these Green function are not appropriate for any other geometry. In our simulator we have chosen to numerically solve Eq. (8.59) for a discrete set of q_z values, interpolating between them when needed. This makes possible to work with arbitrary geometries, at the cost of a higher computational burden.

8.7.1 Screening formulation

In this subsection we shed light on the introduction of screening in the matrix elements of surface roughness, coulomb dispersion and alloy disorder. The process is equivalent for all of them and therefore we will detail it in a general formulation similar to that proposed in Ref. [259] for AD. Let us start with the unscreened expression of the matrix element given by Eq. (8.68): Attending to the equivalence between Eqs. (8.62) and (8.63, the screened, $M^{\mathrm{s}}_{j,j'}(k_z, k_{z'})$, and unscreened, $M^{us}_{i,i'}(k_z, k_{z'})$, matrix elements are related by:

$$M^{\mathrm{s}}_{j,j'}(k_z, k_{z'}) = \sum_{j,j'} \varepsilon^{-1}_{q_z,i,i',j,j'} M^{\mathrm{us}}_{i,i'}(k_z, k_{z'}) \tag{8.69}$$

being as previously proposed $q_z = k'_z - k_z$. Thus, if the matrix element can be calculated, the screening can be directly applied using Eq. (8.69). When this is not possible, from the definition of the matrix element in Eq. (8.62) we have:

$$M^{\mathrm{s}}_{i,i'}(k_z, k_{z'}) = \frac{1}{L} \int_{\mathcal{A}} d\mathbf{s} \tilde{\psi}^{\mathrm{us}}_{q_z}(\mathbf{s}) \sum_{j,j'} \varepsilon^{-1}_{q_z,i,i',j,j'} f_{j,j',k_z,k'_z}(\mathbf{s}) e^{\imath(k'_z - k_z)z} \tag{8.70}$$

with $f_{j,j',k_z,k'_z}(\mathbf{s})$ as in Eq. (8.32). We can define the screened function form factor as:

$$f^{\mathrm{s}}_{i,i',k_z,k'_z}(\mathbf{s}) = \sum_{j,j'} \varepsilon^{-1}_{q_z,i,i',j,j'} f_{j,j',k_z,k'_z}(\mathbf{s}) \tag{8.71}$$

and rewrite (8.70) as:

$$M^{\mathrm{s}}_{i,i'}(k_z, k_{z'}) = \frac{1}{L} \int_{\mathcal{A}} d\mathbf{s} \tilde{\psi}^{\mathrm{us}}_{q_z}(\mathbf{s}) f^{\mathrm{s}}_{i,i',k_z,k'_z}(\mathbf{s}) \tag{8.72}$$

The former equation proves that the screened matrix element can be calculated using the same expressions developed in the previous Sections but with a screened form factor,

defined in (8.71).

8.8 Conclusions

In this Chapter, the main scattering mechanisms for III-V and Silicon nanowires have been modeled for 2D confined devices. Novel models of surface roughness, coulomb, bulk phonons, polar optical phonons and alloy disorder scattering mechanisms have been developed. Moreover, tensorial dielectric screening has been considered and implemented. It should be highlighted that our simulator is useful for any device geometry and for both Silicon and III-V semiconductor materials, therefore constituting a state-of-the-art nanowire mobility simulator.

Chapter 9

Transport studies of MuG devices

9.1 Introduction

The previous two Chapters were devoted to the theoretical frame in which the electron mobility of MuG devices can be calculated under the MRT approximation. In this Chapter we study the electron mobility of Si and III-V Trigates and NWs. Specifically we 1) discuss the electron mobility of InAs NWs, analyzing its dependence on the NW diameter, carrier density and population of the Γ, L and X valleys; 2) compare the mobility behavior of Si and InGaAs Trigate's architectures of different widths; and 3) analyze the influence of the back gate bias on the transport properties of SOI Trigates.

9.2 Electron mobility in InAs nanowires

During the last few years, numerous studies on the behavior of III-V NWs have been carried out [260–265]. In particular, InAs NWs have received a lot of attention due to their high electron mobility and ease of near-ohmic metal contact formation [262]. Different experiments have analyzed their transport properties as a function of parameters such as the temperature or the NW diameter [100**?**]. However, in spite of this interest there is a lack of knowledge about the detailed role played by each one of the scattering mechanisms that influence on the electron mobility. So that, the main goal of this Section is to carry out a comprehensive analysis of the electron mobility in InAs

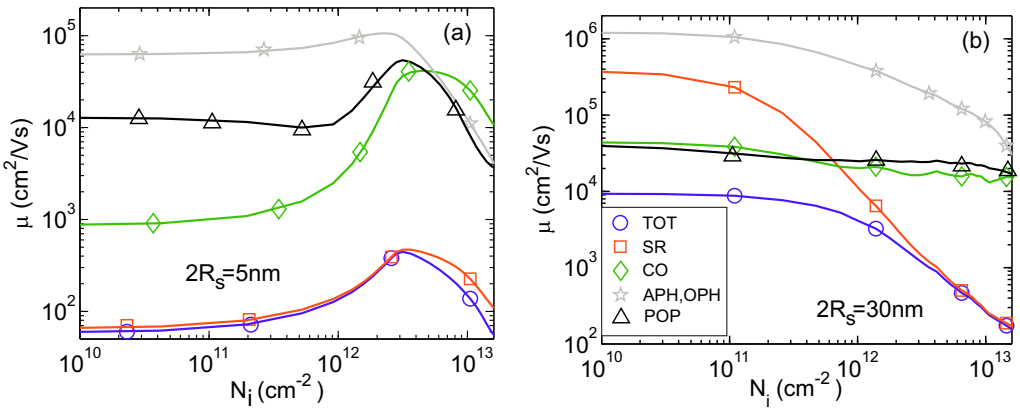

Figure 9.1: Electron mobility (μ) as a function of N_i for the different mechanisms: TOT (circles), SR (squares), CO (diamonds), OPH and APH (stars), and POP (triangles) for two InAs NW diamaters: (a) $2R_\mathrm{s}$=5nm, and (b) $2R_\mathrm{s}$=30nm.

NWs making use of the Kubo-Greenwood formalism. The implicit approach in the calculation of the MRT, explained in Chapter 9, is used. The most influencing scattering mechanisms: non-polar optical and acoustic phonons, polar optical phonons , surface roughness and coulomb dispersion, presented in Chapter 8, are analyzed. Screening has a non-negligible effect and is considered in the calculation of the surface roughness and coulomb dispersion scattering rates. Finally, in this Section, we also ponder on the contribution of the different valleys on the total electron mobility providing a thorough understanding of the transport phenomena that may occur in these devices.

In this study, device diameters ranging from 5nm to 30nm are considered. Al_2O_3 is employed as gate insulator, with $T_\mathrm{ins} = 1.5$nm, which corresponds to an EOT of 0.6nm [200], in good correspondence with previous works [201]. The transport axis of the NWs is oriented along the [001] direction. The material parameters for phonons are presented in Appendix F. A high density of interface traps ($5 \cdot 10^{12}\mathrm{cm}^{-2}$) is assumed as traditionally the quality of interfaces between III-V materials and insulators is far from being perfect [141, 145]. As for the interface roughness an exponential autocorrelation function is considered, see Eq. (8.19), with $\Delta_\mathrm{SR} = 0.5$nm and $\Lambda_\mathrm{SR} = 1.5$nm. A metal gate work function of $\Phi_\mathrm{m} = 5.05$eV is used, and the doping density is $N_a = 10^{14}\mathrm{cm}^{-3}$.

We begin analyzing the mobility dependencies with the electron density, N_i, and the nanowire diameter, $2R_\mathrm{s}$. Fig. 9.1 shows the contribution of each scattering mechanism to the total mobility as a function of the inversion charge for two NW diameters:

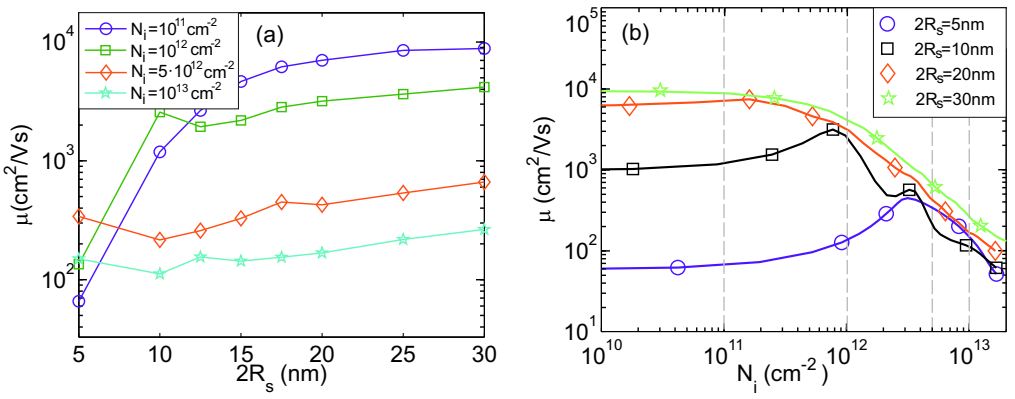

Figure 9.2: (a) μ_{T} as a function of $2R_{\mathrm{s}}$ for different values of N_{i}: $10^{11}\mathrm{cm}^{-2}$ (circles), $10^{12}\mathrm{cm}^{-2}$ (squares), $5\cdot10^{12}\mathrm{cm}^{-2}$ (diamonds) and $10^{13}\mathrm{cm}^{-2}$ (stars). (b) μ as a function of N_{i} for different values of $2R_{\mathrm{s}}$: 5nm (circles), 10nm (squares), 20nm (diamonds) and 30nm (stars).

5nm and 30nm. Total (TOT), surface roughness (SR), coulomb dispersion (CO), bulk acoustic and optical phonons (APH-OPH), and polar optical phonons (POP) limited mobilities are plotted as circles, squares, diamonds, stars, and triangles, respectively. The scattering mechanism's parameters are those collected in Appendix F. As may be seen, SR is the more limiting factor to the total mobility. For the smallest device ($2R_{\mathrm{s}} = 5$nm), its control extends from low to high N_{i}. For low inversion charge, CO slightly reduces the total mobility with respect to the value given by SR, while for $N_{\mathrm{i}} > 4\cdot10^{12}\mathrm{cm}^{-2}$ the influence of phonons actually affects the total mobility, reducing its value to half of the SR-limited mobility. For larger devices, SR is still the dominant scattering mechanism for intermediate and high N_{i}, as the inversion charge moves towards the semiconductor insulator interface. For small electric fields, however, μ_{CO} and μ_{POP} fall below μ_{SR}, affecting the final value of the total mobility.

To better appreciate the dependence of the mobility with the diameter of the NW, Fig. 9.2(a) shows the total mobility as a function of $2R_{\mathrm{s}}$ for different values of inversion charge: $10^{11}\mathrm{cm}^{-2}$ (circles), $10^{12}\mathrm{cm}^{-2}$ (squares), $5\cdot10^{12}\mathrm{cm}^{-2}$ (diamonds) and $10^{13}\mathrm{cm}^{-2}$ (stars). To help us to interpret the results from Fig. 9.2(a), Fig. 9.2(b) shows the mobility as a function of the inversion charge for different NW sizes. The N_{i} values considered in Fig. 9.2(a) are plotted in Fig 9.2(b) as vertical dashed lines. Studying these figures, some conclusions can be extracted:

1. For small NWs, $2R_{\mathrm{s}} < 20$nm, μ decreases as the NW size is reduced. This trend

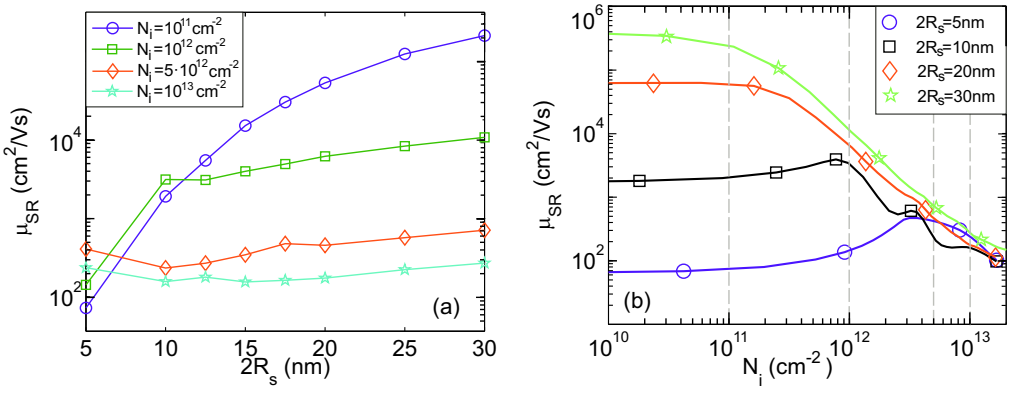

Figure 9.3: (a) μ_{SR} as a function of $2R_s$ for different values of N_i: 10^{11}cm^{-2} (circles), 10^{12}cm^{-2} (squares), $5 \cdot 10^{12}$cm^{-2} (diamonds) and 10^{13}cm^{-2} (stars). (b) μ_{SR} as a function of N_i for different NW diameters: 5nm (circles), 10nm (squares), 20nm (diamonds) and 30nm (stars).

is not so clear for high N_i around $2R_s = 10$nm due to the oscillations associated to the finite density of states that can also be appreciated in Fig. 9.2(b) [1].

2. For diameters larger than 20nm, and for each N_i value, the mobility tends to saturate with the size (see Fig. 9.2(a)).

Once the total mobility dependence with $2R_s$ has been analyzed, it is interesting to have a more detailed look at the most limiting scattering mechanism. So that, SR-limited mobility (μ_{SR}) behavior as a function of the NW diameter and N_i have been depicted in Figs. 9.3(a) and 9.3(b), respectively. The same color and symbol code previously used in Figs. 9.2(a) and 9.2(b) is kept now. According to these figures, we can highlight some conclusions about the μ_{SR} behavior in InAs NWs:

1. For low N_i values, there is a continuous growth of μ_{SR} with the NW diameter. As the electric field is low, the semiconductor charge is mainly located in the center of the NW, minimizing the effect of SR for large devices. Therefore, the geometrical confinement is the main reason of the reduction of μ_{SR} for small devices.

2. For large N_i values, SR scattering is the dominant mechanism, and therefore the curves corresponding to $N_i = 5 \cdot 10^{12}$cm^{-2} and $N_i = 10^{13}$cm^{-2} in Fig. 9.3(a) do

[1] These oscillations are similar to those experimentally demonstrated for Si devices at low temperature in Ref. [266].

not show big differences with the corresponding ones for the total mobility shown in Fig. 9.2(a).

3. For large NWs, μ_{SR} decreases monotonically with N_i, mainly due to the higher electrical confinement, which increases the influence of the SR. It should be noticed, however, that this trend is not maintained for small devices, where the low density of states is responsible for the fluctuations observed for the 5nm and 10nm curves in Fig. 9.3(b).

Now, we analyze the influence of the different valleys (Γ, L and X) on the mobility behavior. We have first estimated the relative population of each valley for two NW diameters, $2R_s = 5$nm and $2R_s = 20$nm, in a wide N_i range. Our results indicate that the population of the X valley is negligible in any case and it will not be considered in the following discussion.

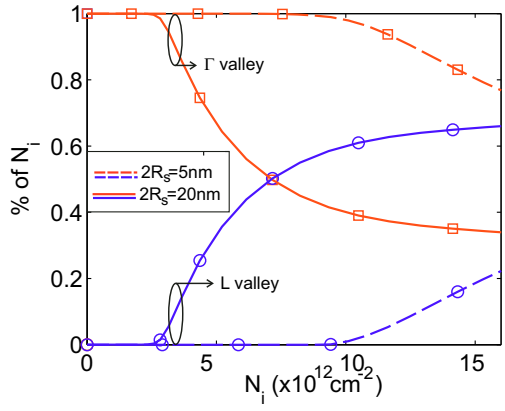

Figure 9.4: Relative population of the Γ-valley (squares) and the L-valley (circles) for the $2R_s = 5$nm (dashed) and the $2R_s = 20$nm (solid) NWs as a function of the electron density.

The Γ valley collects all the electrons at very low inversion densities, regardless of the NW diameter, as it could be expected due to its lower energy. However, as the applied gate bias increases, more electrons populate the L valleys. Moreover, the NW size plays an important role in the relative contribution of each valley, as shown in Fig. 9.4. Thus, the reduction of the diameter increases the relative population of the L valley (as explained in Section 4.3), making it more important than the Γ one in the case of the $2R_s = 5$nm NW for N_i values around $N_i = 7 \cdot 10^{12}\text{cm}^{-2}$.

For the transport orientation considered for these devices, the four L valleys have the same, high transport effective mass ($0.64m_0$) compared to the Γ valley ($0.026m_0$). Therefore, it could be expected that the L valley contribution would actually spoil the mobility behavior as the NW diameter is reduced, since its relative weight steadily increases. To shed light on the potential degrading effect of the L valley, we have to evaluate first the contribution of a single subband to the total mobility. To do so, we calculate $\mu_j n_j/N_\mathrm{i}$, where μ_j is the mobility of the *j-th* subband, n_j is its population and N_i is the total one. Then, the contribution to the total mobility of a certain valley v can be computed as

$$\mu_v = \sum_{j\in v} \mu_j \frac{n_j}{N_\mathrm{i}} \tag{9.1}$$

being the total mobility $\mu = \sum_v \mu_v$.

Making use of Eq. (9.1), we have calculated the contribution to the total mobility of the Γ and L valleys for the same two diameters considered in Fig. 9.4, $2R_\mathrm{s} = 5$nm and $2R_\mathrm{s} = 20$nm. The results are depicted in Fig. 9.5. As shown, the contribution to the electron mobility corresponding to the L valley is much lower than the corresponding to the Γ valley except for very large values ($N_\mathrm{i} > 10^{13}\mathrm{cm}^{-2}$). We wish to draw the reader's attention to the logarithmic scale in the mobility axis. As the total mobility is achieved adding up the contributions of each valley, the total mobility essentially coincides with the contribution of the Γ valley in the range up to $N_\mathrm{i} > 10^{13}\mathrm{cm}^{-2}$. Taking into account the non-negligible population of the L valley shown in Fig. 9.4, its low contribution to the total mobility can be read as an effective degradation of the transport properties, in particular for high values of N_i and small diameters. Thus, Fig. 9.5 provides a clear evidence of the importance of considering the L valley when studying the transport properties of InAs NWs.

Let us go on with the study of mobility results. As the oscillations due to the density of states usually shadow the mobility dependence with the NW size for a given N_i, it is interesting to consider the peak mobility in its stead. Fig. 9.6 presents the peak mobility as a function of $2R_\mathrm{s}$ for SR (squares) and POP (diamonds) and for the total mobility (circles).

It can be observed that the total peak mobility reaches a constant value for large NW sizes. This behavior is coherent with what was observed in Fig. 9.2(a). The peak mobility in SR describes a continuous increase with size. This result is very similar to that presented for low N_i in Fig. 9.3(a). It actually makes sense, as the SR mobility is maximum at low N_i where the charge is far from the semiconductor-insulator interface.

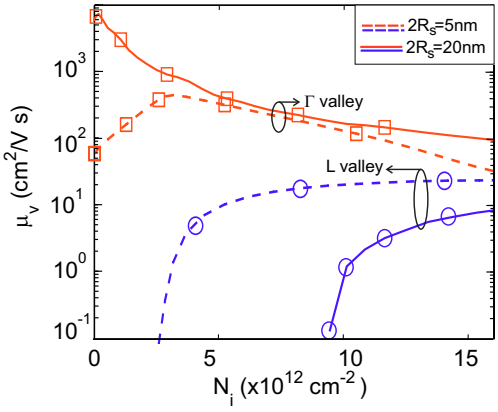

Figure 9.5: Mobility contribution of the Γ-valley (squares) and the L-valleys (scircles) in a $2R_s$=5nm (dashed lines) and a $2R_s$=20nm (solid lines) InAs NW as a function of the electron density.

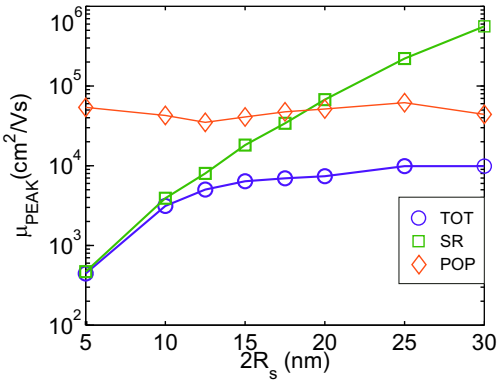

Figure 9.6: Total (circles), SR (squares), and POP (diamonds) peak mobility, μ_{PEAK} as a function of $2R_s$.

On the other hand, the reduction of the SR peak mobility for small devices is directly related to the trend observed for the total mobility, showing again that, even at low inversion densities, SR is the most limiting scattering mechanism for small devices. As for POP, roughly a constant value for the peak mobility is found. It is clear, however, that the peak mobility for large devices is strongly influenced by POP and therefore this mechanism should not be neglected when studying the mobility behavior of large III-V NWs

9.3 Comparison of Si and InGaAs mobility in Trigate FETs

In this Section, we complicate the scenario introducing more complex geometries: Trigate FET; and an alternative III-V material: InGaAs. The Trigate FET introduces the fewest changes to conventional planar transistor processing, while allowing a very good control of the channel [67, 151]. InGaAs adds to the well known advantages of III-V materials could offer an improved semiconductor-insulator interface [61].

Thus, we complete the electrostatic study performed in Section 4.4 comparing the behavior of Si and InGaAs Trigate's architectures. The same geometries and material properties presented in the aforementioned Section are considered, keeping SiO_2 and $TaSiO_x$ as insulators with and EOT 1.1nm. The material parameters of $TaSiO_x$ were calculated by a linear interpolation between those corresponding to SiO_2 and Ta_2O_5. In this work, [110]-oriented devices fabricated on (001) wafers are considered, thus confining electrons within two different directions: [001] (top and bottom surfaces) and $[1\overline{1}0]$ (left and right surfaces). As for the scattering mechanisms, those presented in Chapter 8 are used here, adding to the previous Section the Alloy AD disorder characteristic of this ternary material. The material and transport parameters are summed up in Appendix F.

Regarding the interface quality, the density of ionized impurities is set to $N_{\mathrm{CO}} = 5 \cdot 10^{11} \mathrm{cm}^{-2}$, while a surface roughness correlation length $\Lambda_{\mathrm{SR}} = 1.5\mathrm{nm}$ is used. Distinct rms surface roughness values are considered for the top and lateral interfaces of the Trigate: $\Delta_{\mathrm{SR,TOP}} = 0.4\mathrm{nm}$ and $\Delta_{\mathrm{SR,LAT}} = 0.5\mathrm{nm}$, after Ref. [238].

First, let us contrast the total electron mobility, μ, of Si and InGaAs Trigates assuming equal quality semiconductor-insulator interfaces for both cases. Fig. 9.7 shows μ as a function of N_{i} for 30nm height Si (solid lines) and InGaAs (dashed lines) Trigates of three different widths: 5nm (diamonds), 10nm (squares) and 20nm (circles).

In both materials, there is not a significant difference in the mobility tendency between the two largest widths ($W_{\mathrm{s}} = 10\mathrm{nm}$ and $W_{\mathrm{s}} = 20\mathrm{nm}$). Moreover, the InGaAs mobility is for these two sizes larger than the Si mobility in the whole depicted range of inversion charge. The InGaAs-Si mobility ratio, for a given size, reaches its maximum at low N_{i} values where the InGaAs mobility is around one order of magnitude higher than that of Si. This mobility ratio is reduced as we move toward higher N_{i} falling to a factor of ~ 2. That change in the mobility ratio of InGaAs and Si widest Trigates

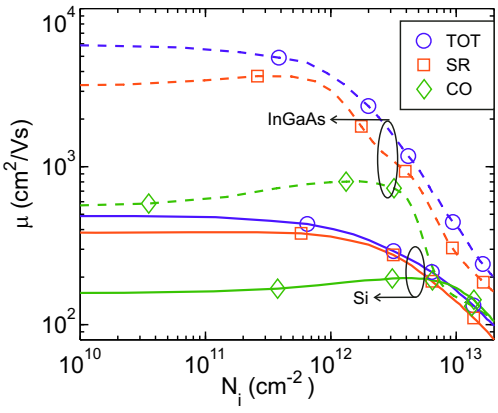

Figure 9.7: Electron mobility as a function of N_i for 30nm height Si (solid lines) and InGaAs (dashed lines) Trigates with three different widths: 5nm (diamonds), 10nm (squares) and 30nm (circles).

can be better analyzed attending to the different scattering mechanism contributions to the mobility.

Fig. 9.8 shows the contribution to the total mobility (circles) of the different scattering mechanism: SR (squares), AD (asterisks), POP (triangles), CO (diamonds) and APH-OPH (stars) as a function of N_i for $W_s = 20$nm, $H_s = 30$nm (a) InGaAs and (b) Si Trigates. Meaningful differences are observed in the mechanisms' contributions to the total mobility for both materials. While bulk non-polar phonons play a negligible role in InGaAs, they mostly control the mobility at low N_i in Si. For the InGaAs Trigates, two mechanisms not present in Si, as AD and POP, are the most limiting in that range of N_i. This change in the mechanisms controlling the mobility explain the large discrepancies, around one order of magnitude, observed (for that width) between both materials in Fig. 9.7 at low N_i. However, when high electric fields are considered SR becomes dominant for InGaAs while for Si its contribution is of the same order of magnitude than bulk phonons. While SR limited mobility behaves distinctly in both materials at low inversion charges, mainly due to the higher spatial confinement of InGaAs (as a consequence of its lower effective mass), it is pretty similar for high N_i (when the charge distribution is close to the interface in both cases). The factor ~ 2 observed in the InGaAs-Si mobility ratio for high N_i can be attributed to the role of bulk phonons in Si.

Up to this point, we have intentionally omitted the thinnest ($W_s = 5$nm) Trigates in our analysis. The mobility behavior for them shows some dissimilarities with respect

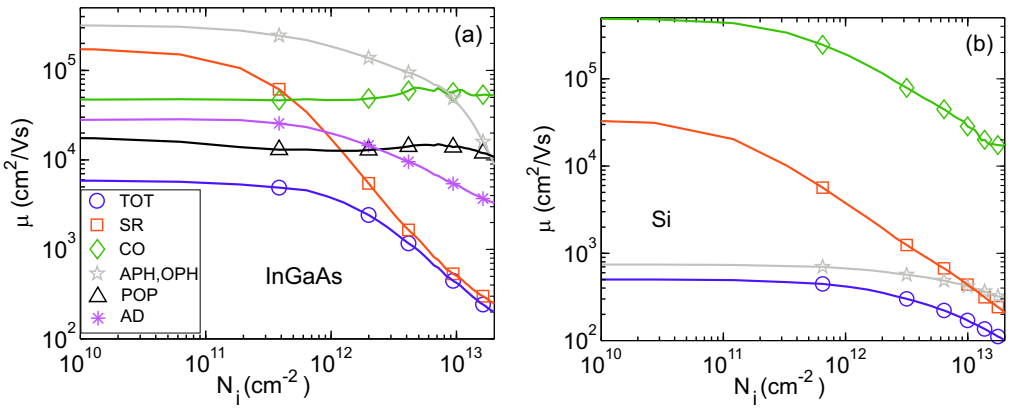

Figure 9.8: Contributions to the total mobility (circles) of SR (squares), AD (asterisks), POP (triangles), CO (diamonds) and APH-OPH (stars) as a function of $N_{\rm i}$ for a $W_{\rm s}$ = 20nm, $H_{\rm s}$ = 30nm (a) InGaAs and (b) Si Trigates.

to the wider sizes as it was shown in Fig. **??**. First, the density of states bottleneck in the InGaAs Trigate results in a pronounced oscillation in the total mobility. Second, for $N_{\rm i} \simeq .7 \cdot 10^{13}{\rm cm}^{-2}$ the mobility of InGaAs is degraded below that of Si. To better understand this performance, we depict the different contributions to the mobility in Fig. 9.9. The symbols code from the Fig. 9.8 is kept.

As can be seen, at low $N_{\rm i}$ values SR gains importance (with respect to wider devices) in both InGaAs and Si. It is worth to note that (due to the stronger spatial confinement) the separation from the charge centroid to the semiconductor-insulator interface (at low electric fields) is reduced with the semiconductor width; augmenting the relevance of SR. The distinct behavior observed between Si and InGaAs can again be ascribed to the relevance of bulk-phonons in Si, which degrades the total mobility to ~ 0.25 the value given by SR. For InGaAs, AD, POP, and CO are also relevant at low $N_{\rm i}$, reducing the total mobility to ~ 0.7 the SR mobility value. For high $N_{\rm i}$ there is an important reduction in the total mobility of InGaAs (around a factor 2 that of SR) due to AD.

Since it was not commented in the previous Section, we focus now on the AD mechanism. Fig. 9.10 shows the AD limited mobility as a function of $N_{\rm i}$ for 30nm height InGaAs Trigates with three different widths: 5nm (diamonds), 10nm (squares) and 20nm (circles). As can be observed, there is a monotonic decrease in AD limited mobility with size for the whole range of depicted $N_{\rm i}$. As explained in Chapter 8 the matrix element of AD is controlled by the overlapping of the wavefunctions correspond-

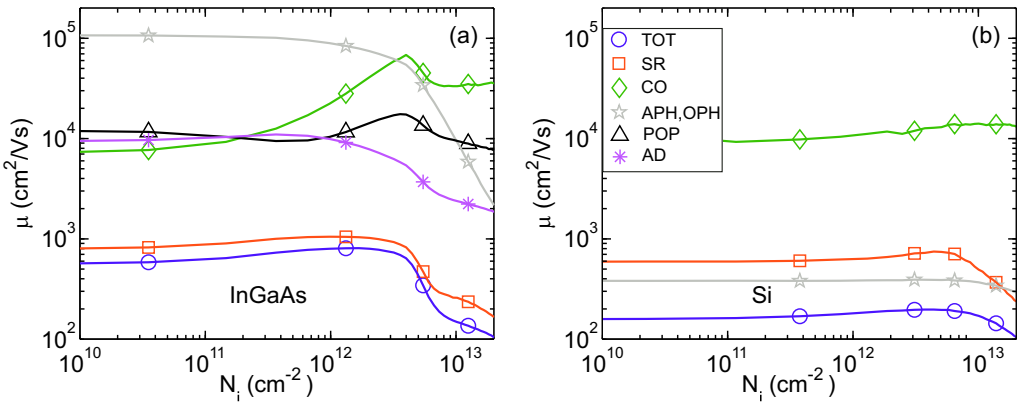

Figure 9.9: Contributions to the total mobility (circles) of SR (squares), AD (asterisk), POP (triangle), CO (diamonds) and APH-OPH (stars) as a function of N_i for a $W_s = 5$nm (a) InGaAs and (b) Si Trigates.

ing to the subbands involved in the electron transitions. As the device size is reduced, the spatial confinement tends to increase the overlapping, and therefore augments the matrix elements and reduces the mobility. The behavior with N_i can also be easily explained: the higher N_i, the larger the number of occupied subbands and available transitions for AD, and therefore, the lower the mobility.

One last question, regarding AD limited mobility, deserves to be commented: this mechanism is extremely sensitive to the value chosen for of the alloy scattering potential, $|V_a - V_b|$ in Eq. (8.58). In this Section we have set $|V_a - V_b|$ to the difference between the conduction band levels of InAs and GaAs, 0.52V according to Ref. [115]. However, it should be pointed out that other works in the literature choose a different value for this parameter (see for example Ref. [267], where of $|V_a - V_b| = 1.6$V). As the matrix elements depend on $|V_a - V_b|^2$ that difference in the value of the alloy scattering potentials is translated into a factor $(1.6/0.5)^2 \sim 10$ in the matrix elements and, consequently, $\sim 1/10$ in the AD limited mobility. Therefore, we highlight here the need of a proper selection of the alloy potential for a reasonable study of the AD influence on the mobility.

We focus now on the mobility degradation due to the L-valley population. As explained in Section 4.4, the relative population of L-valleys in the InGaAs Trigates tends to increase when reducing the semiconductor width. Thus we can expect a spoil in the mobility due to their large effective mass. For the device orientation considered

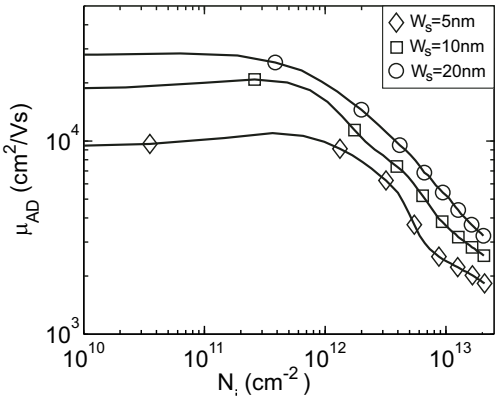

Figure 9.10: AD limited mobility as a function of N_{i} for 30nm height InGaAs Trigates with three different widths: 5nm (diamonds), 10nm (squares) and 20nm (circles).

here, two L valleys have a transport effective mass $m^* = 1.1461m_0$ and the other two have $m^* = 0.1154m_0$. Therefore, significant differences are expected between them. Figs. 9.11 and 9.12 show the relative population and the contribution to the total mobility, calculated using Eq. (9.1), of the Γ-valley (squares) and the two groups of L-valleys ($m^* = 1.1461m_0$ plotted as circles, $m^* = 0.1154m_0$ plotted as diamonds) in a $W_{\mathrm{s}} = 5$nm (dashed lines) and a $W_{\mathrm{s}} = 20$nm (solid lines) InGaAs Trigate. As expected, the contribution to the electron mobility of the L valleys is lower than the one of the Γ-valley, resulting (as explained in the previous Section) in an effective degradation of the mobility. The contribution of the two kinds of L valleys was plotted separately, highlighting the relevance that the orientation can have on the L-valley degradation of the mobility for thinner devices.

Up to this point, we have compared InGaAs and Si Trigates with the same interface characteristics. However, technological difficulties result in poorer interfaces in up-to-date III-V insulator interfaces [268, 269]. Thus, it is interesting to analyze the relative contributions of SR and CO when a poorer semiconductor-insulator interface is present. Fig. 9.13 compares the InGaAs total mobility (circles), as well as SR (squares) and CO (diamonds) limited mobilities for the previous interface ($N_{\mathrm{CO}} = 5 \cdot 10^{11}\mathrm{cm}^{-2}$, $\Delta_{\mathrm{SR,TOP}} = 0.4$nm, $\Delta_{\mathrm{SR,LAT}} = 0.5$nm and $\Lambda_{\mathrm{SR}} = 1.5$nm), plotted as solid lines and a degraded interface ($N_{\mathrm{CO}} = 5 \cdot 10^{12}\mathrm{cm}^{-2}$, $\Delta_{\mathrm{SR,TOP}} = 0.8$nm, $\Delta_{\mathrm{SR,LAT}} = 1$nm and $\Lambda_{\mathrm{SR}} = 1.5$nm) plotted as dashed lines, for 30nm height InGaAs Trigates with two different widths: (a) 5nm and (b) 20nm

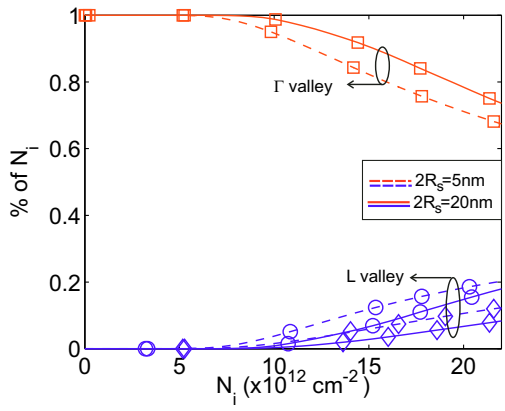

Figure 9.11: Relative population of the Γ-valley (squares) and the two groups of L-valleys ($m^* = 1.1461m_0$ circles, $m^* = 0.1154m_0$ diamonds) in a $W_s = 5$nm (dashed lines) and a $W_s = 20$nm (solid lines) InGaAs Trigate as a function of the electron density.

The rest of the scattering mechanism are not shown since they would not be modified as the interface is changed. The degradation in the mobility due to the degraded quality of the interface is obvious in both sizes. The CO limited mobility is reduced proportionally to N_{CO}, namely in a factor 10. The SR mobility dependence on Δ_{SR} goes down with Δ_{SR}^2. Thus, for the widest device the SR limited mobility is reduced around a factor 4.

For the widest device, μ_{CO} is the most limiting contribution to the mobility for low inversion charges when the poorest interface is considered. For the better interface, CO affects more than SR (at low $N_{\mathrm{i}} < 10^{12}\mathrm{cm}^{-2}$), but as already shown in Fig. 9.8(a) there are other mechanisms, such as POP and AD, which degrade further the mobility. When higher electric fields are considered the charges moves towards the interface and the SR becomes more relevant. In the thinner device, SR is the dominant mechanism in the whole depicted range of N_{i} and the total mobility is degraded in the poor interface in a similar amount than it is the SR limited mobility. Therefore, improving the quality of the interface is shown to have a direct impact in the total electron mobility and should be one of the main technological purposes to consider III-V materials as potential substitutes of Si in MuG architectures.

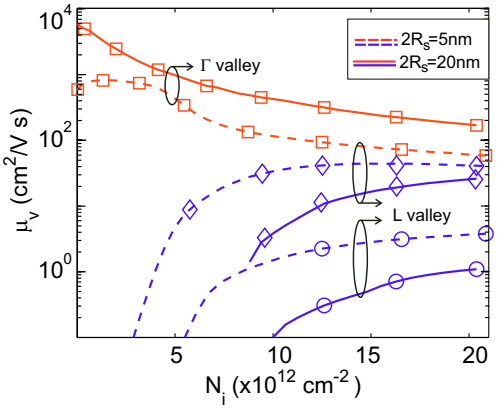

Figure 9.12: Mobility contribution of the Γ-valley (squares) and the two groups of L-valleys ($m^* = 1.1461m_0$ circles, $m^* = 0.1154m_0$ diamonds) in a $W_s = 5$nm (dashed lines) and a $W_s = 20$nm (solid lines) InGaAs Trigate as a function of the electron density.

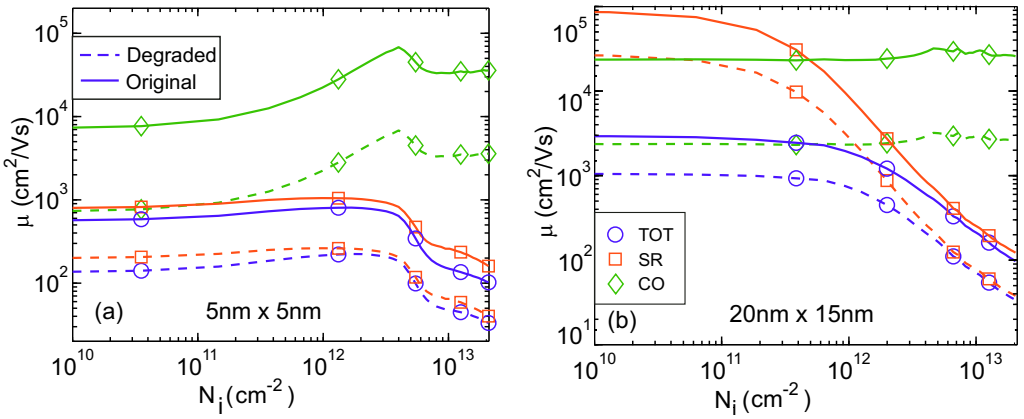

Figure 9.13: Total mobility (circles), as well as SR (squares) and CO (diamonds) limited mobilities for the original interface ($N_{\mathrm{CO}} = 5 \cdot 10^{11}\mathrm{cm}^{-2}$, $\Delta_{\mathrm{SR,TOP}} = 0.4$nm, $\Delta_{\mathrm{SR,LAT}} = 0.5$nm and $\Lambda_{\mathrm{SR}} = 1.5$nm), plotted as solid lines and a degraded interface ($N_{\mathrm{CO}} = 5 \cdot 10^{12}\mathrm{cm}^{-2}$, $\Delta_{\mathrm{SR,TOP}} = 0.8$nm, $\Delta_{\mathrm{SR,LAT}} = 1$nm and $\Lambda_{\mathrm{SR}} = 1.5$nm) plotted as dashed, for 30nm height InGaAs Trigates with two different widths: (a) 5nm and (b) 20nm

9.4 Influence of back gate bias on the electron mobility of Si Trigates

Let us finally study the influence of the back gate bias on the transport behavior of Si Trigate devices completing the electrostatic study of Section 4.6. To the best of our knowledge, there is not such a study in the literature for MuG devices, although the results for ultrathin SOI devices have pointed out that the influence of $V_{\rm bg}$ may be non-negligible [163], [270].

As in Section 4.6 SOI Trigate structures have been studied here [165, 166]. A midgap metal gate ($\Phi_{\rm m}$=4.61eV) is considered, and the gate and buried oxide (SiO_2) thicknesses are $t_{\rm ins}$ = 1.2nm and $t_{\rm box}$ = 10nm, respectively. The channel is oriented along the [011] crystallographic direction, being the top and bottom Si-insulator interfaces [100]-oriented, and the lateral ones [011]-oriented. Back-gate bias ($V_{\rm bg}$) is applied beneath the buried oxide. A rectangular silicon channel is simulated, being $W_{\rm s}$ and $H_{\rm s}$ the silicon width and height respectively.

Bulk optical (OPH) and acoustic (APH) phonons, surface-roughness (SR) and Coulomb (CO) scattering mechanisms are included in the simulations. Again, both SR and CO scattering mechanisms are implemented taking into account the tensorial dielectric screening [95], while the phonon interactions remain unscreened. The scattering mechanisms are introduced as in Chapter 8. The phonons parameters are summed up in Appendix F. The surface characteristics are: $\Delta_{\rm sr}$ = 0.5nm, $L_{\rm sr}$ = 1.5nm and $N_{\rm CO} = 5 \times 10^{11}$ cm^{-2})

In this study, we have chosen two devices with sizes: $W_{\rm sc} \times H_{\rm s}$ = 20nm×15nm, and $W_{\rm sc} \times H_{\rm s}$ = 5nm×5nm. Both of them have similar, relatively high values of the body factor, $\gamma \simeq 0.05$, see Fig. 4.25, and square-like cross sections. $V_{\rm bg}$ values ranging from −2V to 2V are considered. Fig. 9.14 depicts the electron mobility as a function of the inversion charge for constant values of $V_{\rm bg}$, for both device sizes. As shown, higher $V_{\rm bg}$ values increase the electron mobility for the largest device, and also for the smaller one at high inversion charges. However, there is a non-monotonic behavior as a function of the back-gate voltage at low $N_{\rm i}$ values, which can be better seen in Fig. 9.15, where μ has been depicted as a function of $V_{\rm bg}$ for constant $N_{\rm i}$ values.

The behavior of these curves can be explained by studying the role of the different scattering mechanisms. Let us first compare, in Figs. 9.16, the behavior of phonon-limited mobility, $\mu_{\rm PH}$ (circles), phonon and SR-limited mobility, $\mu_{\rm PH+SR}$ (diamonds),

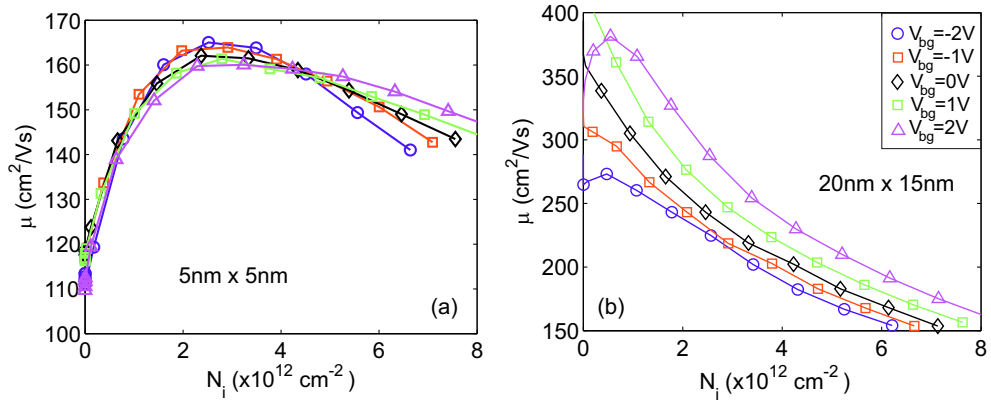

Figure 9.14: Electron mobility as a function inversion charge for (a) a 5nm×5nm and (b) a 20nm× 15nm Trigates. $V_{\rm bg}$ varies from −2V to 2V.

and phonon, SR and coulomb-limited mobility , $\mu_{\rm PH+SR+CO}$ (stars) as a function of the inversion charge for $V_{\rm bg} = \pm 2V$.

As can be seen, the influence of PH, SR and CO is similar in the smallest device for both $V_{\rm bg} = \pm$2V. The reason may be found in the strong geometrical confinement. However, for the biggest device, where the charge position can be modulated using the back-gate bias, the mobility reduction due to SR and CO is stronger at negative values of $V_{\rm bg}$.

The non-monotonic behavior of $\mu_{\rm SR}$ for $V_{\rm bg} = 2$V observed in Fig. 9.16(b) is related to the charge redistribution that occurs when $N_{\rm i}$ increases, as shown in Fig. 4.26. For small $N_{\rm i}$ values, the charge is located close to the Si/BOX interface and the SR scattering due to this surface is not negligible. However, as $V_{\rm fg}$ is increased and $N_{\rm i}$ grows, the charge is shifted from the Si/BOX towards the center of the fin, as shown in Figs. 4.26 and 4.27, and therefore the influence of the SR scattering is reduced. As a consequence, the achieved mobility is larger than in the $V_{\rm bg} = -2$V case, where the charge get closed to the top interface.

Taking into account that the Si/BOX interface is expected to have a better quality than the lateral and top ones [271], we have simulated the behavior of the mobility curves when, only in this interface, $\Delta_{\rm SR}$ is reduced to 0.2nm and $N_{\rm CO}$ to $10^{11}{\rm cm}^{-2}$. Fig. 9.17 presents the total mobility curves as a function of $N_{\rm i}$ for both, the original device (solid lines) and the one with improved Si/BOX interface quality (dashed lines), for $V_{\rm bg} = \pm$2V.

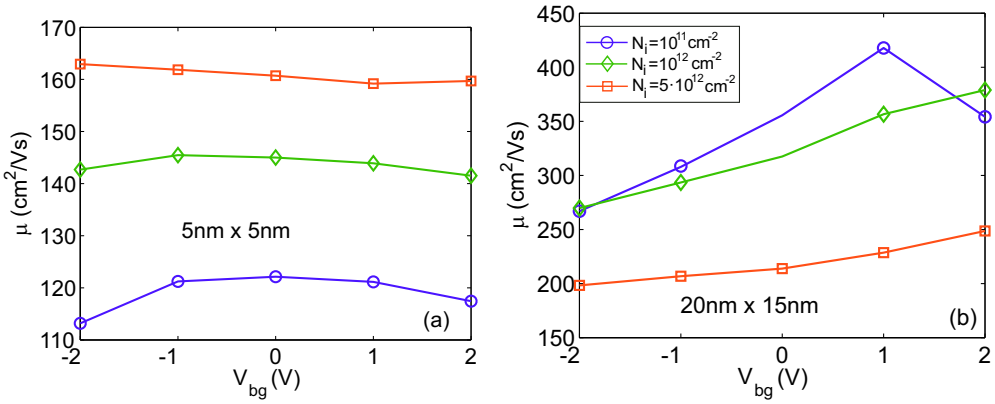

Figure 9.15: Electron mobility as a function of $V_{\rm bg}$ for inversion charge values $N_{\rm i} = 10^{11}$ cm^{-2} (circles), $N_{\rm i} = 10^{12}$ cm^{-2} (diamonds) and 5×10^{13} cm^{-2} (squares) for: (a) 5nm $\times$ 5nm and (b) 20nm $\times$ 15nm Trigates.

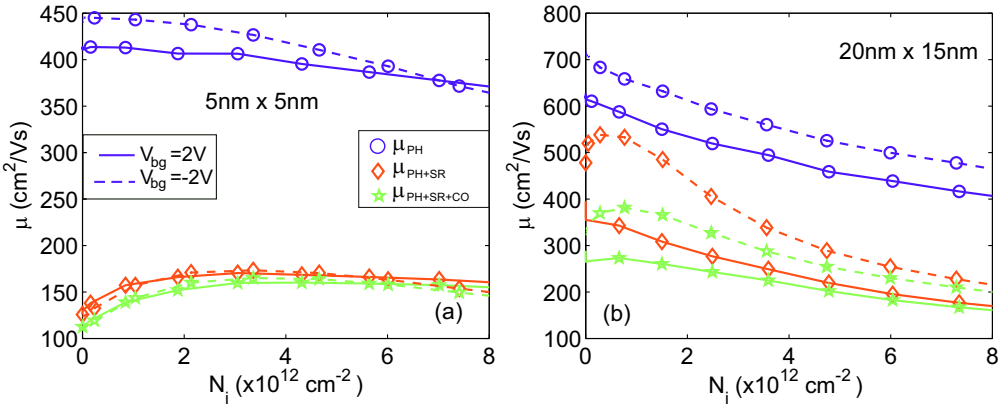

Figure 9.16: $\mu_{\rm PH}$ (circles), $\mu_{\rm PH+SR}$ (diamonds) and $\mu_{\rm PH+SR+CO}$ (stars) as a function of the inversion charge for the two $V_{\rm bg}$ values: 2V (solid) and -2V, for (a) 5nm $\times$ 5nm and (b) 20nm $\times$ 15nm Trigates.

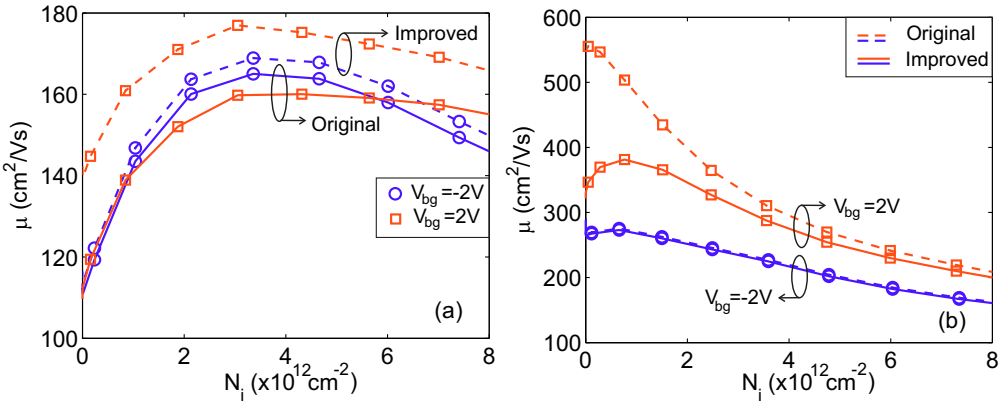

(a) (b)

Figure 9.17: Total mobility as a function of N_i for both, the original device (solid lines) and the one with improved Si/BOX interface quality (dashed lines), for $V_{bg} = \pm 2$V for 30nm height InGaAs Trigates with two different widths: (a) 5nm and (b) 20nm

In the small device, the improvement of one of the interfaces reduces the matrix elements due to SR and CO scattering mechanisms regardless the back-gate voltage, due to the strong geometrical confinement. Therefore, an improvement of the total mobility is found for both $V_{bg} = \pm 2$V, although this improvement is higher in the $V_{bg} = 2$V, where the charge is closer to the Si/BOX interface.

In the larger device, there is almost no influence of the Si/BOX interface improvement at $V_{bg} = -2$V, as the charge is quite far from this interface even at low inversion charges (see Fig. 4.26). However, for small N_i and positive back-gate bias, a strong increase of the mobility is found, due to the proximity of the inversion charge to the Si/BOX interface.

As can be seen, in the larger device, the mobility achieved for positive V_{bg} values doubles that achieved for negative V_{bg} values in a large range of N_i values. Therefore, the impact of V_{bg} on the electron mobility should not be neglected when studying the back gate influence on the device performance.

9.5 Conclusion

In this Chapter, we have accomplished three transport studies using the implicit solution from the MRT approximation of the Boltzmann transport equation.

First, we have analyzed the electron mobility behavior for InAs NWs as a function of their diameter and inversion charge. We have demonstrated that surface roughness is the most limiting mechanism as the device size is shrunk. However, polar optical phonons and Coulomb interactions should also be considered in order to explain the trend observed for the total mobility as a function of the device size and the electron density. We have also demonstrated the importance of including the L valley in the calculations as its increasing population when the diameter is reduced strongly degrades the mobility. Therefore, neglecting the contribution of the L valley would lead to wrong conclusions.

Second, we have compared the mobility performance of InGaAs and Si Trigates. The mechanism contributions to the mobility have been studied for different Trigate widths, observing relevant differences in the InGaAs-Si ratio with size.

We have analyzed the influence of the back-gate bias on the electron mobility of Trigate silicon devices. It has been confirmed the strong impact of the back-gate bias on the electron mobility. Positive back-gate bias pushes the charge further from the top and lateral Si/insulator interfaces, reducing the influence of SR and Coulomb scattering mechanisms and therefore increasing the carrier mobility. On the contrary, the carrier mobility is degraded for negative back-gate bias.

Part IV

Conclusions

Chapter 10

Conclusions

As explained in the Objectives section, the main objective of this PhD Thesis was the study of MuG architectures and III-V compounds semiconductors. In this context, the main contributions of this work are listed next:

1. A self-consistent Schrödinger-Poisson solver was developed, which is able to deal with arbitrary geometries, materials and orientations to achieve the charge and potential distribution in the cross-section of a MuG structure. A non-parabolic effective mass approach was employed for the Schrödinger equation, and the contribution of Γ, X (Δ for Silicon) and L valleys was included. In addition, the developed simulator allows the inclusion of an arbitrary profile of interface states.

2. Using this self-consistent Schrödinger-Poisson solver, Trigates and NWs made of Si and III-V semiconductors were analyzed. It was demonstrated that the low density of states has a strong influence on the charge density and gate capacitance behavior of III-V NWs. Moreover, the population of higher energy valleys (in particular, of L valleys) can strongly modify the small conduction effective mass associated to III-V semiconductors. Additionally, we studied the behavior of InGaAs, and SOI Trigate FETs, as a function of the channel width, showing that the semiconductor width has a strong impact on InGaAs Trigates: both the threshold voltage and the gate voltage at which the L valleys begin to be populated depend on the width. Besides, it was demonstrated the importance of considering the two-dimensional confinement for III-V materials to accurately reproduce the electron distribution near the corners. This effect produces a noticeable impact on the conduction effective mass as a result of the different population

of each valley. The control the threshold voltage and the charge distribution of Trigate SOI devices by modifying the back-gate bias was studied, confirming the possibility of achieving body factors higher than γ=0.1 as long as the channel width over height ratio is increased as much as possible. Finally, the influence of the interfacial states, D_{it}, on the performance of Si MuG FET and, specifically, on the subthreshold swing and the threshold voltage was analyzed observing relevant variations with the temperature and the oxide thickness. It was concluded that the higher the number of gates the lower the degradation due to the interface states, caused by the higher electrostatic control of the semiconductor-insulator interface.

3. A fully analytical model for the charge and potential distributions in cylindrical III-V nanowires was developed. This model presented analytical expressions for the calculation of the subband energies and their corresponding wavefunctions, taking into account their penetration into the gate insulator and the effective mass discontinuity in the semiconductor-oxide interface, Fermi-Dirac statistics, two-dimensional confinement of the carriers and non-parabolic effects. It also allowed the inclusion of arbitrary analytical profiles of interfacial states. We demonstrated that our analytical solution fits very well the numerical simulations in all operating regimes for a wide range of NW sizes and gate voltages. The model was extended to calculate the current in a long-channel nanowire including the interface charge.

4. Using the results from the charge and potential models, we proposed physically based analytical models for the gate capacitance and the threshold voltage in III-V NWs. Regarding the gate capacitance model, it was demonstrated that the model fits very well the numerical results for different NW sizes and materials, without considering any fitting parameters. The different contributions to the total gate capacitance were identified and modeled, showing their relation with the finite density of states and the charge distribution in the NWs. The capacitance behavior of III-V NWs were compared with that of their Si counterparts. Significant differences were found for the dominant contribution to the inversion capacitance, as well as for the semiconductor potential dependence on the gate voltage. Furthermore, we showed the limited impact of the EOT reduction in the gate capacitance of III-V NWs, in contrast to the behavior observed in Si devices. The role of the wavefunction penetration into the gate insulator was

also analyzed, evidencing its relevance for an accurate description of the gate capacitance. Concerning the threshold voltage model, after some reasonable approximations, we came up with a simple expression of V_{T} that will be useful for the development of compact models for III-V cylindrical NWs. We demonstrated that the threshold voltage expression accurately reproduces the numerical results for different III-V semiconductor materials, NW sizes, and oxide thicknesses. The influence of the wavefunction penetration into the gate insulator was discussed, illustrating its relevance for an accurate modeling of V_{T}. The V_{T} variations due to the changes in the semiconductor effective mass were evaluated. We gave insight into the different contributions to the threshold voltage finding interesting differences among materials. Furthermore, we studied the V_{T} dependence on the insulator thickness, showing no relevant changes in a wide range of t_{ins}, contrary to what is observed in Si devices.

5. We have developed a model to calculate the electron mobility of a 1D electron gas based on the linearization of the Boltzmann Transport Equation using the momentum relaxation time approximation (MRT). Besides the explicit approach for the calculation of the MRT, which has been extensively used in the literature, we implemented an implicit approach resolution. The formulation of the implicit equation system was exemplified, considering the nested interdependency of the transitions, and the truncation of the discretized wavenumber space with a Neumann boundary condition. We have to highlight that this implicit solution of the MRT, taking into account several scattering mechanisms is, to the best of our knowledge, unique in the literature for 2D confined devices.

6. The main scattering mechanisms for III-V and Silicon nanowires have been modeled for 2D confined devices. Novel models for surface roughness, Coulomb, bulk phonons, polar optical phonons and alloy disorder scattering mechanisms have been developed. Moreover, tensorial dielectric screening has been considered and implemented. It should be stressed that our simulator is useful for any device geometry and for both Silicon and III-V semiconductor materials, therefore constituting a state-of-the-art nanowire mobility simulator.

7. Finally, the mobility behavior of III-V and Silicon nanowires has been addressed. In our studies, which include InAs nanowires and InGaAs trigate devices, we have shown that the surface quality has to be improved in order to fulfil the high electron mobility expected for III-V nanowires. In particular, surface roughness

seems to be the most critical scattering mechanism, and for very small sizes it limits the mobility of III-V nanowires to that of Si nanowires, therefore canceling the potential improvement on the device performance given by the low conduction effective mass. We observed that polar optical phonons and Coulomb interactions should also be considered in order to explain the trend for the total mobility as a function of the device size and the electron density. We have also demonstrated the importance of including the L valley in the calculations as its increasing population when the diameter is reduced strongly degrades the mobility. Therefore, neglecting the contribution of the L valley would lead to wrong conclusions. We analyzed the influence of the back-gate bias on the electron mobility of Trigate SOI devices confirming its strong impact. Positive back-gate bias pushes the charge further from the top and lateral Si/insulator interfaces, reducing the influence of surface roughnes and Coulomb scattering mechanisms and therefore increasing the carrier mobility. On the contrary, the carrier mobility was degraded for negative back-gate bias.

Part V

Appendixes

Appendix A

Numerical implementation of surface interface charge

In this Appendix we deal with the mathematical details regarding the relation between surface interface charge, $Q_{\text{it,sf}}$, and volumetric interface charge, $Q_{\text{it,vl}}$, discussed in Chapter 3. Specifically we: 1) detail the procedure to obtain a relation between $Q_{\text{it,vl}}$ and $\psi|_{\text{i-m}} - \psi|_{\text{i-s}}$ in both Cartesian and cylindrical coordinates; and 2) we determine the values of A_{cte}, A_{lin}, A_{exp}, and A_{gau} for a given value of $Q_{\text{it,sf}}$.

First, we determine the relation between $\psi|_{\text{i-m}} - \psi|_{\text{i-s}}$ and $Q_{\text{it,vl}}$ for regions with straight and curved segments. To do it, let us properly define both problems. Fig. A.1 shows a region, $\mathcal{R}_i$, corresponding to a curved segment (left) and another corresponding to a straight segment (right).

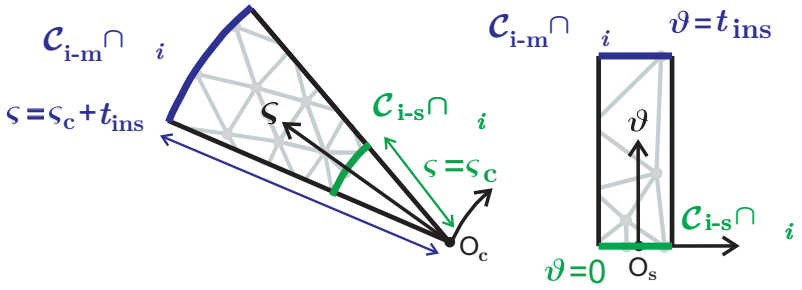

Figure A.1: Definition of system references to find a relation $\psi|_{\text{i-m}} - \psi|_{\text{i-s}}$ $Q_{\text{it,vl}}$ and $Q_{\text{it,sf}}$ for a curved segment (left) and a straight region (right).

It is straightforward to see that the reference system which easiest describe the

problem are cylindrical (for the curved segments) and Cartesian (for the straight segment) with the origins marked as O at Fig. A.1. Thus, $\mathcal{C}_{\text{i-s}} \cap \mathcal{R}_i$ can be easily defined as $\varsigma = \varsigma_{\text{c}}$ for the curved region and as $\vartheta = 0$ for the straight region. Other reference systems, with other origins could be selected, but the definition of $\mathcal{C}_{\text{i-s}} \cap \mathcal{R}_i$ will be not so simple. Then, we have $\psi|_{\text{i-s}} = \psi(\varsigma_{\text{c}})$ for the curved region and $\psi|_{\text{i-s}} = \psi(0)$ for the straight region.

Equivalently we obtain that $\varsigma_{\text{c}} + t_{\text{ins}}$ and t_{ins} are the values of the variables ς and ϑ which describe $\mathcal{C}_{\text{i-m}} \cap \mathcal{R}_i$ for the curved and the straight regions. As a consequence, $\psi|_{\text{i-m}} = \psi(\varsigma_{\text{c}} + t_{\text{ins}})$ for the curved region and $\psi|_{\text{i-m}} = \psi(t_{\text{ins}})$ for the straight region.

We have noted the coordinate system variables as ς and ϑ to differentiate them from typical Cartesian and cylindrical coordinates, as ϑ and ς are region dependent. Thus, ϑ can be x o y, as defined in Section 3.2, depending on the orientation of the region, and shifted by a certain quantity O_{s}; while ς would be $r = \sqrt{x^2 + y^2}$ shifted by the position of O_{c} with respect to origin of the Cartesian coordinate defined in Section 3.8

Moreover, $Q_{\text{it,vl}}$ is defined as non-null in a region of thickness $t_{\text{o}} \leq t_{\text{ins}}$ and (as proposed in Section 3.8) only dependent on the coordinate perpendicular to $\mathcal{C}_{\text{i-s}}$.

Then, we can reformulate Eq. (3.35) for straight segments as:

$$\frac{d^2\psi(\vartheta)}{d\vartheta^2} = -\frac{Q_{\text{it,vl}}(\vartheta)}{\epsilon_{\text{ins}}} \tag{A.1}$$

And for curved segments, as:

$$\frac{1}{\varsigma}\frac{d}{d\varsigma}\varsigma\frac{d\psi(\varsigma)}{d\varsigma} = -\frac{Q_{\text{it,vl}}(\varsigma)}{\epsilon_{\text{ins}}} \tag{A.2}$$

A first integration between ϑ and t_{ins} for the straight region and between ς and $\varsigma_{\text{c}} + t_{\text{ins}}$ for the curved region gives

$$\left.\frac{d\psi(\vartheta')}{d\vartheta'}\right|_{\vartheta}^{t_{\text{ins}}} = -\int_{\vartheta}^{t_{\text{ins}}} \frac{Q_{\text{it,vl}}(\vartheta)}{\epsilon_{\text{ins}}} d\vartheta \tag{A.3}$$

$$\varsigma'\left.\frac{d\psi(\varsigma')}{d\varsigma'}\right|_{\varsigma}^{\varsigma_{\text{c}}+t_{\text{ins}}} = \int_{\varsigma}^{\varsigma_{\text{c}}+t_{\text{ins}}} \varsigma\frac{Q_{\text{it,vl}}(\varsigma)}{\epsilon_{\text{ins}}} d\varsigma \tag{A.4}$$

But due to the charge neutrality of the whole structure, no electric field is expected at $\mathcal{C}_{\text{i-m}}$, and, therefore: $\frac{d\psi(\vartheta')}{d\vartheta'}|_{\vartheta'=t_{\text{ins}}} = 0$, for straight regions, and $\frac{d\psi(\varsigma')}{d\varsigma'}|_{\varsigma'=\varsigma_{\text{c}}+t_{\text{ins}}} = 0$ for curved regions. So:

$$\frac{d\psi(\vartheta)}{d\vartheta} = -\int_{\vartheta}^{t_{\text{ins}}} \frac{Q_{\text{it,vl}}(\vartheta)}{\epsilon_{\text{ins}}} d\vartheta \tag{A.5}$$

$$\varsigma \frac{d\psi(\varsigma)}{d\varsigma} = \int_{\varsigma}^{\varsigma_{\text{c}}+t_{\text{ins}}} \varsigma \frac{Q_{\text{it,vl}}(\varsigma)}{\epsilon_{\text{ins}}} d\varsigma \tag{A.6}$$

A second integration between 0 and t_{ins} for straight region and between ς_{c} and $\varsigma_{\text{c}} + t_{\text{ins}}$ for curved region gives:

$$\psi|_{\text{i-m}} - \psi|_{\text{i-s}} = \frac{1}{\epsilon_{\text{ins}}} \int_{0}^{t_{\text{ins}}} d\vartheta \int_{\vartheta}^{t_{\text{ins}}} Q_{\text{it,vl}}(\hat{\vartheta}) d\hat{\vartheta} \tag{A.7}$$

for straight segments and

$$\psi|_{\text{i-m}} - \psi|_{\text{i-s}} = \frac{1}{\epsilon_{\text{ins}}} \int_{\varsigma_{\text{c}}}^{\varsigma_{\text{c}}+t_{\text{ins}}} \frac{1}{\varsigma} d\varsigma \int_{\varsigma}^{\varsigma_{\text{c}}+t_{\text{ins}}} \hat{\varsigma} Q_{\text{it,vl}}(\hat{\varsigma}) d\hat{\varsigma} \tag{A.8}$$

for curved segments.

Now, we determine A_{cte}, A_{lin}, A_{exp}, and A_{gau} for a given value of $Q_{\text{it,sf}}$. Let us recall Eqs. (3.38) and (3.39):

$$Q_{\text{it,sf}}\, t_{\text{ins}} = \int_{0}^{t_{\text{ins}}} d\vartheta \int_{\vartheta}^{t_{\text{ins}}} Q_{\text{it,vl}}(\hat{\vartheta}) d\hat{\vartheta} \tag{A.9}$$

and:

$$Q_{\text{it,sf}}\, \varsigma_{\text{c}} \ln(1 + t_{\text{ins}}/\varsigma_{\text{c}}) = \int_{\varsigma_{\text{c}}}^{\varsigma_{\text{c}}+t_{\text{ins}}} \frac{1}{\varsigma} d\varsigma \int_{\varsigma}^{\varsigma_{\text{c}}+t_{\text{ins}}} \hat{\varsigma} Q_{\text{it,vl}}(\hat{\varsigma}) d\hat{\varsigma} \tag{A.10}$$

To determine A_{cte}, A_{lin}, A_{exp}, and A_{gau} we substitute the expressions for $Q_{\text{it,vl}}$ given in Tab. 3.1 into Eqs. (3.38) and (3.39) and we solve for A.

To keep this manuscript (to the best of our possibilities) clear and legible, we have omitted the integration procedure for each profile in Table (3.1). They mostly consist

on integrals of polynomial and exponentials functions. The results are summarized in Tables A.1 and A.2 for straight and curved regions. In Tables. A.1 and A.2, erf and e_{i} refers to the error complementary function and the exponential integral function, respectively.

$A_{\mathrm{cte}} = 2\dfrac{t_{\mathrm{ins}}}{t_{\mathrm{o}}^2}\, Q_{\mathrm{it,sf}}$
$A_{\mathrm{lin}} = 4\dfrac{t_{\mathrm{ins}}}{t_{\mathrm{o}}^2}\, Q_{\mathrm{it,sf}}$
$A_{\mathrm{exp}} = \dfrac{t_{\mathrm{ins}}}{\sigma_{\mathrm{e}}\left(1-(t_{\mathrm{o}}+\sigma_{\mathrm{e}})e^{-\frac{t_{\mathrm{o}}}{\sigma_{\mathrm{e}}}}\right)}\, Q_{\mathrm{it,sf}}$
$A_{\mathrm{gau}} = \left(\dfrac{t_{\mathrm{ins}}}{\sigma_{\mathrm{g}}}\dfrac{1}{t_{\mathrm{o}}\sqrt{\pi/2}}\mathrm{erf}\left(\dfrac{t_{\mathrm{o}}}{\sqrt{2}\sigma_{\mathrm{g}}}\right) + t_{\mathrm{ins}}(e^{-\frac{t_{\mathrm{o}}}{2\sigma_{\mathrm{g}}^2}}-1)\right)\, Q_{\mathrm{it,sf}}$

Table A.1: A_{cte}, A_{lin}, A_{exp}, and A_{gau} as a function of $Q_{\mathrm{it,sf}}$ for different profiles in straight segment regions.

$A_{\mathrm{cte}} = \dfrac{\varsigma_{\mathrm{c}} \ln(1+\frac{t_{\mathrm{ins}}}{\varsigma_{\mathrm{c}}})}{\frac{(\varsigma_{\mathrm{c}}+t_{\mathrm{o}})^2}{2}[\ln(1+\frac{t_{\mathrm{o}}}{\varsigma_{\mathrm{c}}})-\frac{1}{2}]+\frac{\varsigma_{\mathrm{c}}^2}{4}}\, Q_{\mathrm{it,sf}}$
$A_{\mathrm{lin}} = \dfrac{\varsigma_{\mathrm{c}} \ln(1+\frac{t_{\mathrm{ins}}}{\varsigma_{\mathrm{c}}})\, Q_{\mathrm{it,sf}}}{[\frac{(\varsigma_{\mathrm{c}}+t_{\mathrm{o}})^2}{2}[\ln(1+\frac{t_{\mathrm{o}}}{\varsigma_{\mathrm{c}}})-\frac{1}{2}]+\frac{\varsigma_{\mathrm{c}}^2}{4}](1+\frac{t_{\mathrm{o}}}{\varsigma_{\mathrm{c}}})-[\frac{(\varsigma_{\mathrm{c}}+t_{\mathrm{o}})^3}{3}[\ln(1+\frac{t_{\mathrm{o}}}{\varsigma_{\mathrm{c}}})-\frac{1}{3}]+\frac{\varsigma_{\mathrm{c}}^3}{9}]}$
$A_{\mathrm{exp}} = \dfrac{-\frac{\varsigma_{\mathrm{c}}}{\sigma_{\mathrm{e}}} \ln(1+\frac{t_{\mathrm{ins}}}{\varsigma_{\mathrm{c}}}) e^{-\frac{\varsigma_{\mathrm{c}}}{\sigma_{\mathrm{e}}}}\, Q_{\mathrm{it,sf}}}{(\varsigma_{\mathrm{c}}+t_{\mathrm{o}}+\sigma_{\mathrm{e}}) e^{-\frac{\varsigma_{\mathrm{c}}+t_{\mathrm{o}}}{\sigma_{\mathrm{e}}}} \ln(1+\frac{t_{\mathrm{o}}}{\varsigma_{\mathrm{c}}}) + \sigma_{\mathrm{e}}(e^{-\frac{\varsigma_{\mathrm{c}}+t_{\mathrm{o}}}{\sigma_{\mathrm{e}}}} - e^{-\frac{\varsigma_{\mathrm{c}}}{\sigma_{\mathrm{e}}}} + e_{\mathrm{i}}(\frac{\varsigma_{\mathrm{c}}+t_{\mathrm{o}}}{\sigma_{\mathrm{e}}}) - e_{\mathrm{i}}(\frac{\varsigma_{\mathrm{c}}}{\sigma_{\mathrm{e}}}))}$
$A_{\mathrm{gau}} = \dfrac{-\frac{\varsigma_{\mathrm{c}}}{\sigma_{\mathrm{g}}^2} \ln(1+\frac{t_{\mathrm{ins}}}{\varsigma_{\mathrm{c}}})\, Q_{\mathrm{it,sf}}}{-[e^{-\frac{t_{\mathrm{o}}^2}{2\sigma_{\mathrm{g}}^2}} - \frac{\sqrt{\pi}\varsigma_{\mathrm{c}}}{\sqrt{2}\sigma_{\mathrm{g}}} \mathrm{erf}(-\frac{t_{\mathrm{o}}}{\sqrt{2}\sigma_{\mathrm{g}}})] \ln(1+\frac{t_{\mathrm{o}}}{\varsigma_{\mathrm{c}}}) + \int_{\varsigma_{\mathrm{c}}}^{\varsigma_{\mathrm{c}}+t_{\mathrm{o}}} \frac{e^{-\frac{(\varsigma-\varsigma_{\mathrm{c}})^2}{2\sigma_{\mathrm{g}}^2}}}{\varsigma} d\varsigma + \frac{\sqrt{\pi}\varsigma_{\mathrm{c}}}{\sqrt{2}\sigma_{\mathrm{g}}} \int_{\varsigma_{\mathrm{c}}}^{\varsigma_{\mathrm{c}}+t_{\mathrm{o}}} \frac{\mathrm{erf}(\frac{\varsigma_{\mathrm{c}}-\varsigma}{\sqrt{2}\sigma_{\mathrm{g}}})}{\varsigma} d\varsigma}$

Table A.2: A_{cte}, A_{lin}, A_{exp}, and A_{gau} as a function of $Q_{\mathrm{it,sf}}$ for different profiles in curved segment regions.

Appendix B

Charge, potential and drain current models related calculi

In this appendix we sum up some calculi related to the charge and potential and drain current analytical models.

B.1 Normalization of the wavefunctions

In this Section we determine the wavefunction normalization constants A and C obtained in the resolution of the Schrödinger equation in Chapter 5. We recall here Eq. (5.20):

$$A_j^2 \int_0^{R_s} r J_l^2(\gamma_j r)\, dr + C_j^2 \int_{R_s}^{R_s+t_{ins}} r\, K_l^2(\alpha_j r)\, dr = 1 \tag{B.1}$$

Using Eq. (5.13) we have:

$$A_j^2 \int_0^{R_s} r J_l^2(\gamma_j r)\, dr + A_j^2 \left(\frac{J_l(\gamma_j R_s)}{K_l(\alpha_j R_s)}\right)^2 \int_{R_s}^{R_s+t_{ins}} r\, K_l^2(\alpha_j r)\, dr = 1 \tag{B.2}$$

Therefore:

$$A_j^2 = \left(\int_0^{R_s} r J_l^2(\gamma_j r)\, dr + \frac{J_l^2(\gamma_j R_s)}{K_l^2(\alpha_j R_s)} \int_{R_s}^{R_s+t_{ins}} r\, K_l^2(\alpha_j r)\, dr \right)^{-1} \tag{B.3}$$

Both integrals in Eq. (B.3) are known [221]:

$$\int r J_l^2(\gamma_j r)\, dr = \frac{r^2}{2}\left(J_l^2(\gamma_j r) - J_{l-1}(\gamma_j r) J_{l+1}(\gamma_j r)\right) \tag{B.4}$$

$$\begin{aligned}\int r K_l^2(\alpha_j r) dr = (-1)^{l+1}\frac{\pi^2}{4}\int r[H_l^{(1)}(i\alpha_j r)]^2 dr = \\ (-1)^{l+1}\frac{\pi^2}{4}\frac{r^2}{2}\left([H_l^{(1)}(\imath\alpha_j r)]^2 - H_{l-1}^{(1)}(\imath\alpha_j r) H_{l+1}^{(1)}(\imath\alpha_j r)\right) = \\ \frac{r^2}{2}\left(K_l^2(\alpha_j r) - K_{l-1}(\alpha_j r) K_{l+1}(\alpha_j r)\right)\end{aligned} \tag{B.5}$$

where we have used the connection formula between K_v, and the Hankel function of the first kind, $H_v^{(1)}$:

$$K_v(x) = \imath^{v+1}\frac{\pi}{2} H_v^{(1)}(\imath x) \tag{B.6}$$

being $\imath$ the imaginary unit. Then, evaluating the integrals in their limits we find:

$$\begin{aligned}A_j = \Bigg(\frac{R_{\rm s}^2}{2}\left[2J_l^2(\gamma_j R_{\rm s}) - J_{l-1}(\gamma_j R_{\rm s}) J_{l+1}(\gamma_j R_{\rm s}) - J_l^2(\gamma_j R_{\rm s})\frac{K_{l-1}(\alpha_j R_{\rm s}) K_{l+1}(\alpha_j R_{\rm s})}{K_l^2(\alpha_j R_{\rm s})}\right] \\ -\frac{J_l^2(\gamma_j R_{\rm s})}{K_l^2(\alpha_j R_{\rm s})}\frac{(R_{\rm s}+t_{\rm ins})^2}{2}\left[K_l^2(\alpha_j(R_{\rm s}+t_{\rm ins})) - K_{l-1}(\alpha_j(R_{\rm s}+t_{\rm ins}) K_{l+1}(\alpha_j(R_{\rm s}+t_{\rm tox}))\right]\Bigg)^{-1/2}\end{aligned} \tag{B.7}$$

and using Eq. (5.13):

$$\begin{aligned}C_j = \Bigg(\frac{R_{\rm s}^2}{2}\left[2K_l^2(\alpha_j R_{\rm s}) - K_l^2(\alpha_j R_{\rm s})\frac{J_{l-1}(\gamma_j R_{\rm s}) J_{l+1}(\gamma_j R_{\rm s})}{J_l^2(\gamma R_{\rm s})} - K_{l-1}(\alpha_j R_{\rm s}) K_{l+1}(\alpha_j R_{\rm s})\right] \\ -\frac{(R_{\rm s}+t_{\rm ins})^2}{2}\left[K_l^2(\alpha_j(R_{\rm s}+t_{\rm ins})) - K_{l-1}(\alpha_j(R_{\rm s}+t_{\rm ins}) K_{l+1}(\alpha_j(R_{\rm s}+t_{\rm tox}))\right]\Bigg)^{-1/2}\end{aligned} \tag{B.8}$$

B.2 Resolution of the Poisson equation

In this Section we deal with the resolution of the Poisson equation for a III-V cylindrical NW. Specifically we detail the mathematical procedure followed to obtain φ_j, that is the spatial distribution of the contribution of the subband j to the potential ψ. We

recall here Eq. (5.40):

$$\varphi_j(r) = \begin{cases} A_j^2 \iint r\, J_l^2\left(\gamma_j r\right) dr \frac{1}{\hat{r}} d\hat{r} & i = a \\ C_j^2 \iint r K_l^2\left(\alpha_j r\right) dr \frac{1}{\hat{r}} d\hat{r} = (-1)^{l+1}\, \frac{\pi^2}{4} C_j^2 \iint r[H_l^{(1)}\left(\imath\alpha_j r\right)]^2 dr \frac{1}{\hat{r}} d\hat{r} & i = b \end{cases} \tag{B.9}$$

where K_l was rewritten in terms of $H_l^{(1)}$ using the definition of Eq. (B.6). Expressing $\varphi_j(r)$ in this way allows us to give a unified treatment to the integral. This is because $H_l^{(1)}$ (also called Bessel function of the third kind) shares with J_l many recurrence relations and connection formulas. Thus, we use the notation $M(\nu x)$ to refer to both functions, $J_l\left(\gamma_j r\right)$ and $H_l^{(1)}\left(\imath\alpha_j r\right)$, in the forthcoming integration. The inner integral in Eq. (B.9) is known:

$$\int x M_v^2(ax) dx = \frac{x^2}{2}\left[M_v^2(ax) - M_{v-1}(ax) M_{v+1}(ax)\right] \tag{B.10}$$

being the equality valid for both J_v and $H_v^{(1)}$ as proposed in Eqs. (B.4) and (B.5). Therefore:

$$\int \int r'\, M_l^2(\nu_j r') dr' \frac{1}{r} dr = \frac{1}{2} \int r M_l^2(\nu_j r) dr - \frac{1}{2} \int r M_{1-1}(\nu_j r) M_{l+1}(\nu_j r) dr \tag{B.11}$$

The first integral in the right-hand side of Eq. (B.11) can again be solved using Eq. (B.10). The second one can be written as:

$$\int r M_{l-1}(\nu_j r) M_{l+1}(\nu_j r) dr = \int r M_{l-1}(\nu_j r) M_{l-1}(\nu_j r) dr - \frac{2}{\nu_j} \int r M_{l-1}(\nu_j r) \frac{dM_l(\nu_j r)}{dr} dr \tag{B.12}$$

where we have used the recurrence relation:

$$M_{v+1}(ax) = M_{v-1}(ax) - \frac{2}{a} \frac{dM_v(ax)}{dx} \tag{B.13}$$

which is valid for both J_v and $H_v^{(1)}$. Again the first integral in the right-hand side can be solved using Eq. (B.10). The second integral can be integrated by parts as:

$$\int r M_{l-1}(\nu_j r) \frac{dM_l(\nu_j r)}{dr} dr = r M_{l-1}(r) M_l(r) - \int M_l(\nu_j r)\left[l M_{l-1}(\nu_j r) - r\nu_j M_l(\nu_j r)\right] dr \tag{B.14}$$

where:

$$u = rM_{l-1}(\nu_j r) \longrightarrow du = l\, M_{l-1}(\nu_j r) - \nu_j r M_l(\nu_j r) \tag{B.15}$$

$$dv = \frac{dM_l(\nu_j r)}{dr} \longrightarrow v = M_l(\nu_j r) \tag{B.16}$$

and where the recurrence relation:

$$\frac{dM_v(ax)}{dx} = a\left[\frac{v}{ax}M_v(ax) - M_{v+1}(ax)\right] \tag{B.17}$$

holds for both J_v and $H_v^{(1)}$. Then, the integral in the right-hand side of Eq. (B.14):

$$\int M_l(\nu_j r)\left[lM_{l-1}(\nu_j r) - \nu_j r M_l(\nu_j r)\right] dr = l\int M_l(\nu_j r)M_{l-1}(\nu_j r)dr - \nu_j \int r M_l^2(\nu_j r)dr \tag{B.18}$$

where the second integral in the right-hand side of Eq. (B.18) can be calculated using Eq. (B.10). Applying Eq. (B.13) to $M_l(\nu_j r)$ with $l = v + 1$ in the first integral we obtain:

$$l\int M_l(\nu_j r)M_{l-1}(\nu_j r)dr = l\int M_{l-2}(\nu_j r)M_{l-1}(\nu_j r)dr - \frac{2l}{\nu_j}\int \frac{dM_{l-1}(\nu_j r)}{dr}M_{l-1}(\nu_j r)dr \tag{B.19}$$

where the first integral is direct:

$$\frac{2l}{\nu_j}\int M_{l-1}(\nu_j r)\frac{dM_{l-1}(\nu_j r)}{dr}dr = \frac{l}{\nu_j}M_{l-1}^2(\nu_j r) \tag{B.20}$$

and:

$$l\int M_l(\nu_j r)M_{l-1}(\nu_j r)dr = l\int M_{l-1}(\nu_j r)M_{l-2}(\nu_j r)dr - \frac{l}{\nu_j}M_{l-1}^2(\nu_j r) \tag{B.21}$$

but it is easy to see that the first integral in the right-hand side of Eq. (B.21) is just the integral in the left-hand side of Eq. (B.18) with a reduction of 1 in the order of M functions. We can apply this rule recursively until we reach,

$$\int M_1(\nu_j r)M_0(\nu_j r)dr = -\frac{M_0^2(\nu_j r)}{2\nu_j} \tag{B.22}$$

which is satisfied for both J_v and $H_v^{(1)}$. Then, the complete integral is:

$$\int\int_0^r r'\,|M_l(\nu_j r')|^2 dr' \frac{1}{r} dr = \frac{1}{2}\frac{r^2}{2} M_l^2(\nu_j r) - \frac{1}{2}\frac{r^2}{2} M_{l-1}(\nu_j r) M_{l+1}(\nu_j r) -$$
$$\frac{1}{2}\frac{r^2}{2} M_{l-1}^2(\nu_j r) + \frac{1}{2}\frac{r^2}{2} M_{l-2}(\nu_j r) M_l(\nu_j r) + \frac{1}{2}\frac{2}{\nu_j} r M_{l-1}(\nu_j r) M_l(\nu_j r) + \frac{1}{2}\frac{2}{\nu_j}\nu_j \frac{r^2}{2} M_l^2(\nu_j r)$$
$$- \frac{1}{2}\frac{2}{\nu_j}\nu_j \frac{r^2}{2} M_{l-1}(\nu_j r) M_{l+1}(\nu_j r) + \frac{1}{2}\frac{2}{\nu_j}\frac{l}{\nu_j} M_{l-1}^2(\nu_j r) - \frac{1}{2}\frac{2}{\nu_j} l \int M_{l-1}(\nu_j r) M_{l-2}(\nu_j r) dr \tag{B.23}$$

Rearranging terms we have:

$$\frac{3}{4} r^2 M_l^2(\nu_j r) - \frac{3}{4} r^2 M_{l-1}(\nu_j r) M_{l+1}(\nu_j r) - \frac{r^2}{4} M_{l-1}^2(\nu_j r) + \frac{r^2}{4} M_{l-2}(\nu_j r) M_l(\nu_j r) +$$
$$+ \frac{r}{\nu_j} M_{l-1}(\nu_j r) M_l(\nu_j r) + \frac{l}{\nu_j^2} M_{l-1}^2(\nu_j r) - \frac{l}{\nu_j} \int M_{l-1}(\nu_j r) M_{l-2}(\nu_j r) \tag{B.24}$$

We can use the recurrence relation:

$$M_{v+1}(ax) + M_{v-1}(ax) = \frac{2v}{ax} M_v(ax) \tag{B.25}$$

valid for J_v as well as for $H_v^{(1)}$ to rewrite M_{l-2} as:

$$M_{l-2}(\nu_j r) = \frac{2(l-1)}{\nu_j r} M_{l-1}(\nu_j r) - M_l(\nu_j r) \tag{B.26}$$

Using it in Eq. (B.24) and simplifying we get:

$$\frac{1}{2} r^2 M_l^2(\nu_j r) - \frac{3}{4} r^2 M_{l-1}(\nu_j r) M_{l+1}(\nu_j r) - \frac{r^2}{4} M_{l-1}^2(\nu_j r) + (\frac{l+1}{2}) \frac{r}{\nu_j} M_{l-1}(\nu_j r) M_l(\nu_j r) +$$
$$+ \frac{l}{\nu_j^2} M_{l-1}^2(\nu_j r) + \frac{l}{\nu_j} \int M_{l-1}(\nu_j r) M_{l-2}(\nu_j r) dr \tag{B.27}$$

Now we use again Eq. (B.25) for $M_{l+1}(\nu_j r)$ and we obtain:

$$\frac{1}{2} r^2 M_l^2(\nu_j r) + \frac{1}{2} r^2 M_{l-1}^2(\nu_j r) + (-l + \frac{1}{2}) \frac{r}{\nu_j} M_{l-1}(\nu_j r) M_l(\nu_j r) + \frac{l}{\nu_j^2} M_{l-1}^2(\nu_j r) -$$
$$- \frac{l}{\nu_j} \int M_{l-1}(\nu_j r) M_{l-2}(\nu_j r) dr \tag{B.28}$$

Or applying the recursive integral in Eq. (B.21) and the result from Eq. (B.22) we get:

$$\frac{1}{2}r^2M_l^2(\nu_j r)+\frac{1}{2}r^2M_{l-1}^2(\nu_j r)+(-l+\frac{1}{2})\frac{r}{\nu_j}M_{l-1}(\nu_j r)M_l(\nu_j r)+\frac{l}{\nu_j^2}\sum_{m=1}^{l}M_{m-1}^2(\nu_j r)$$
$$-\frac{l}{2\nu_j^2}M_0^2(\nu_j r) \tag{B.29}$$

Now, we can undo the change of notation to establish the contribution of the subband j to the potential in the semiconductor:

$$\varphi_j^a(r)=A_j^2\left(\frac{r^2}{2}J_l^2(\gamma_j r)+\frac{r^2}{2}J_{l-1}^2(\gamma_j r)+(-l+\frac{1}{2})\frac{r}{\gamma_j}J_{l-1}(\gamma_j r)J_l(\gamma_j r)+\right.$$
$$\left.+\frac{l}{\gamma_j^2}\sum_{m=1}^{l}J_{m-1}^2(\gamma_j r)-\frac{l}{2\gamma_j^2}J_0^2(\gamma_j r)\right) \tag{B.30}$$

Equivalently, using Eq. (B.6), with $\nu_j=i\alpha_j$

$$\varphi_j^b(r)=C_j^2\left(\frac{(-1)^{(l+1)}}{(-1)^{(l+1)}}\frac{1}{2}r^2K_l^2(\alpha_j r)+\frac{(-1)^{(l+1)}}{(-1)^l}\frac{1}{2}r^2K_{l-1}^2(\alpha_j r)+\right.$$
$$\frac{(-1)^{(l+1)}}{\imath^{l+1}\imath^l}(-\frac{l}{2}+1)\frac{r}{\imath\alpha_j}K_{l-1}(\alpha_j r)K_l(\alpha_j r)+\frac{l}{\imath^2\alpha_j^2}\sum_{m=1}^{l}\frac{(-1)^{l+1}}{(-1)^m}K_{m-1}^2(\alpha_j r)-$$
$$\left.-\frac{(-1)^{l+1}}{(-1)}\frac{l}{2\imath^2\alpha_j^2}K_0^2(\alpha_j r)\right) \tag{B.31}$$

and simplifying the powers of $\imath$, the contribution of the subband j to the potential in the insulator is:

$$\varphi_j^b(r)=C_j^2\left(\frac{rR^2}{2}K_l^2(\alpha_j r)-\frac{r^2}{2}K_{l-1}^2(\alpha_j r)+(-l+\frac{1}{2})\frac{r}{\alpha_j}K_{l-1}(\alpha_j r)K_l(\alpha_j r)+\right.$$
$$\left.+\frac{l}{\alpha_j^2}\sum_{m=1}^{l}(-1)^{l-m}K_{m-1}^2(\alpha_j r)-(-1)^{l-1}\frac{l}{2\alpha_j^2}K_0^2(\alpha_j r)\right) \tag{B.32}$$

B.3 Determination of C_i and D_i from Poisson boundary conditions

In this Section we apply the boundary conditions of Eqs. (5.42)-(5.45) to the solution of the Poisson equation obtained in Chapter 5 to determine the constants of integration C_a, D_a, C_b and D_b. Two of these boundary conditions, given by Eqs. (5.42) and (5.44), involve the derivatives of the potential in both media. For the sake of clarity, let us first calculate expressions for these derivatives. Thus, we recall the expression for the potential in the media i:

$$\psi^i(r) = \frac{q}{2\pi\epsilon_i}\sum_{j=0}^{N} g(\hat{E}_j)\varphi_j^i(r) + \frac{q}{\epsilon_i}\frac{r^2}{4}N_a\delta_{i,a} + C_i\ln(r) + D_i \tag{B.33}$$

Then its derivative is:

$$\psi'^i(r) = \frac{d\psi^i(r)}{dr} = \frac{q}{2\pi\epsilon_i}\sum_{j=0}^{N} g(\hat{E}_j)\varphi_j'^i(r) + \frac{q}{\epsilon_i}\frac{r}{4}N_a\delta_{i,a} + \frac{C_i}{r} \tag{B.34}$$

where $\varphi_j'^i(r) = d\varphi_j^i(r)/dr$ can be written, using Eqs. (B.29), (B.30) and (B.32) as:

$$\varphi_j'^i(r) = (B_j^i)^2\frac{d}{dr}\left(\frac{1}{2}r^2M_l^2(\nu_j r) + \frac{1}{2}r^2M_{l-1}^2(\nu_j r) + (-l+\frac{1}{2})\frac{r}{\nu_j}M_{l-1}(\nu_j r)M_l(\nu_j r) + \right.$$
$$\left. + \frac{l}{\nu_j^2}\sum_{m=1}^{l}M_{m-1}^2(\nu_j r) - \frac{l}{2\nu_j^2}M_0^2(\nu_j r)\right) \tag{B.35}$$

being B_j^i equal to A_j ($\imath^{l+1}\pi C_j/2$) for the media a (b). This way of expressing the potential allows (as in Appendix B.2) a unique treatment of J_v and K_v (trough $H_v^{(1)}$) simplifying the forthcoming calculus. Thus, applying the derivative relation:

$$\frac{dM_v(ax)}{dx} = \frac{1}{2}a\left(M_{l-1}(ax) - M_{l+1}(ax)\right) \tag{B.36}$$

which is valid for both J_v and $H_v^{(1)}$, we have:

$$\varphi_j'^i(r) = (B_j^i)^2 \left(rM_l^2(\nu_j r) + \frac{\nu_j r^2}{2} M_l(\nu_j r) \left[M_{l-1}(\nu_j r) - M_{l+1}(\nu_j r) \right] + \right.$$
$$+ rM_{l-1}^2(\nu_j r) + \frac{\nu_j r^2}{2} M_{l-1}(\nu_j r) \left[M_{l-2}(\nu_j r) - M_l(\nu_j r) \right] + (-l + \frac{1}{2}) \frac{1}{\nu_j} M_{l-1}(\nu_j r) M_l(\nu_j r)$$
$$(-l + \frac{1}{2}) \frac{r}{2} \left[M_{l-2}(\nu_j r) M_l(\nu_j r) - M_l^2(\nu_j r) + M_{l-1}^2(\nu_j r) - M_{l-1}(\nu_j r) M_{l+1}(\nu_j r) \right]$$
$$\left. + \frac{l}{\nu_j} \sum_{m=1}^{l} M_{m-1}(\nu_j r) \left[M_{m-2}(\nu_j r) - M_m(\nu_j r) \right] + \frac{l}{\nu_j} M_0(\nu_j r) M_1(\nu_j r) \right) \tag{B.37}$$

which rearranging terms can be expressed as:

$$\varphi_j'^i(r) = (B_j^i)^2 \left((-\frac{l}{2} + \frac{3}{4}) r M_l^2(\nu_j r) + \frac{\nu_j r^2}{2} M_l(\nu_j r) M_{l+1}(\nu_j r) + (-\frac{l}{2} + \frac{5}{4}) r M_{l-1}^2(\nu_j r) + \right.$$
$$+ \frac{\nu_j r^2}{2} M_{l-1}(\nu_j r) M_{l-2}(\nu_j r) +$$
$$+ (-l + \frac{1}{2}) \frac{1}{\nu_j} M_{l-1}(\nu_j r) M_l(\nu_j r) + (-l + \frac{1}{2}) \frac{r}{2} \left[M_{l-2}(\nu_j r) M_l(\nu_j r) - M_{l-1}(\nu_j r) M_{l+1}(\nu_j r) \right]$$
$$\left. + \frac{l}{\nu_j} \sum_{m=1}^{l} M_{m-1}(\nu_j r) \left[M_{m-2}(\nu_j r) - M_m(\nu_j r) \right] + \frac{l}{\nu_j} M_0(\nu_j r) M_1(\nu_j r) \right) \tag{B.38}$$

Then, using Eq. (B.26) for the first appearance of M_{l-2} in Eq. (B.38), we get:

$$\varphi_j'^i(r) = (B_j^i)^2 \left([-\frac{l}{2} + \frac{3}{4}] r M_l^2(\nu_j r) + [\frac{l}{2} + \frac{1}{4}] r M_{l-1}^2(\nu_j r) + \right.$$
$$+ (-l + \frac{1}{2}) \frac{1}{\nu_j} M_{l-1}(\nu_j r) M_l(\nu_j r) + (-l + \frac{1}{2}) \frac{r}{2} \left[M_{l-2}(\nu_j r) M_l(\nu_j r) - M_{l-1}(\nu_j r) M_{l+1}(\nu_j r) \right]$$
$$\left. + \frac{l}{\nu_j} \sum_{m=1}^{l} M_{m-1}(\nu_j r) \left[M_{m-2}(\nu_j r) - M_m(\nu_j r) \right] + \frac{l}{\nu_j} M_0(\nu_j r) M_1(\nu_j r) \right) \tag{B.39}$$

In addition, we can write:

$$(-l + \frac{1}{2}) \frac{r}{2} \left[M_{l-2}(\nu_j r) M_l(\nu_j r) - M_{l-1}(\nu_j r) M_{l+1}(\nu_j r) \right] = \tag{B.40}$$
$$(-l + \frac{1}{2}) \left[\frac{l-1}{\nu_j} M_{l-1}(\nu_j r) M_l(\nu_j r) - \frac{r}{2} M_l^2(\nu_j r) - \frac{l}{\nu_j} M_l(\nu_j r) M_{l-1}(\nu_j r) + \frac{r}{2} M_{l-1}^2(\nu_j r) \right]$$

where we have used the recurrence relation in Eq. (B.25) with $v-1=l-2$ for M_{l-2} and with $v+1=l+1$ for M_{l+1}. Thus, substituting Eq. (B.40) into Eq. (B.39) gives:

$$\varphi_j'^i(r)=(B_j^i)^2\left(\frac{r}{2}M_l^2(\nu_j r)+\frac{r}{2}M_{l-1}^2(\nu_j r)+\frac{l}{\nu_j}\sum_{m=1}^{l}M_{m-1}(\nu_j r)\left[M_{m-2}(\nu_j r)-M_m(\nu_j r)\right]\right.$$
$$\left.+\frac{l}{\nu_j}M_0(\nu_j r)M_1(\nu_j r)\right) \tag{B.41}$$

This expression can be particularized for each media giving:

$$\varphi_j'^a(r)=A_j^2\left(\frac{r}{2}J_l^2(\gamma_j r)+\frac{r}{2}J_{l-1}^2(\gamma_j r)+\frac{l}{\gamma_j}\sum_{m=1}^{l}J_{m-1}(\gamma_j r)\left[J_{m-2}(\gamma_j r)-J_m(\gamma_j r)\right]\right.$$
$$\left.+\frac{l}{\gamma_j}J_0(\nu_j r)J_1(\gamma_j r)\right) \tag{B.42}$$

$$\varphi_j'^b(r)=C_j^2\left(\frac{r}{2}K_l^2(\alpha_j r)-\frac{r}{2}K_{l-1}^2(\alpha_j r)-\right. \tag{B.43}$$
$$\left.\frac{l}{\alpha_j}\sum_{m=1}^{l}(-1)^{l-m}K_{m-1}(\alpha_j r)\left[K_{m-2}(\alpha_j r)+K_m(\alpha_j r)\right]+\frac{l}{\gamma_j}(-1)^{l-1}K_0(\alpha_j r)K_1(\alpha_j r)\right)$$

where we have used Eq. (B.6) with $\nu_j=\imath\alpha$ as it was done in Appendix B.2 to express Eq. (B.41) in terms of $K_v(\alpha_j r)$. Eqs. (B.34), (B.42) and (B.43) completely determine ψ'^i.

Now we can go on with the determination of the integration constants. The first boundary condition is:

$$\left.\frac{d\psi^a(r)}{dr}\right|_{r=0}=0. \tag{B.44}$$

Then

$$\left.\frac{q}{2\pi\epsilon_a}\sum_{j=0}^{N}g(\hat{E}_j)\varphi_j'^b(0)+\frac{C_a}{r}\right|_{r=0}=0. \tag{B.45}$$

Since $J_v(0)=0$ for $v\neq 0$, then it is easy to check that $\varphi_j'^a(0)=0$ and, consequently,

$$C_a=0 \tag{B.46}$$

From the second boundary condition we get:

$$\epsilon_a \left.\frac{d\psi^a(r)}{dr}\right|_{r=R_\mathrm{s}} = \epsilon_b \left.\frac{d\psi^b(r)}{dr}\right|_{r=R_\mathrm{s}} \tag{B.47}$$

Therefore:

$$\frac{q}{2\pi}\sum_{j=0}^{N} g(\hat{E}_j)\varphi_j'^b(R_\mathrm{s}) + \frac{q}{2}N_a R_\mathrm{s} = \frac{q}{2\pi}\sum_{j=0}^{N} g(\hat{E}_j)\varphi_j'^b(R_\mathrm{s}) + C_b\frac{\epsilon_b}{R_\mathrm{s}} \tag{B.48}$$

So,

$$C_b = \frac{R_\mathrm{s}}{\epsilon_b}\left(\frac{q}{2\pi}\sum_{j=0}^{N} g(\hat{E}_j)\varphi_j'^a(R_\mathrm{s}) + \frac{q}{2}N_a R_\mathrm{s} - \frac{q}{2\pi}\sum_{j=0}^{N} g(\hat{E}_j)\varphi_j'^b(R_\mathrm{s})\right) \tag{B.49}$$

where $\varphi_j'^b$ and $\varphi_j'^b$ are given by Eqs. (B.42) and (B.43). The third boundary condition imposes:

$$\psi^b(R_\mathrm{s} + t_\mathrm{ins}) = V_\mathrm{G} - \Phi_\mathrm{ms} \tag{B.50}$$

Then:

$$\frac{q}{2\pi\epsilon_b}\sum_{j=0}^{N} g(\hat{E}_j)\varphi_j^b(R_\mathrm{s} + t_\mathrm{ins}) + C_b\ln(R_\mathrm{s} + t_\mathrm{ins}) + D_b = V_\mathrm{G} - \Phi_\mathrm{ms} \tag{B.51}$$

and:

$$D_b = V_\mathrm{G} - \Phi_\mathrm{ms} - \frac{q}{2\pi\epsilon_i}\sum_{j=0}^{N} g(\hat{E}_j)\varphi_j^b(R_\mathrm{s} + t_\mathrm{ins}) + C_b\ln(R_\mathrm{s} + t_\mathrm{ins}) \tag{B.52}$$

where φ_j^b is given by Eq. (B.32) and C_b was obtained in Eq. (B.49). Finally the last boundary condition is:

$$\psi^a(R_\mathrm{s}) = \psi^b(R_\mathrm{s}) \tag{B.53}$$

So:

$$\frac{q}{2\pi\epsilon_a}\sum_{j=0}^{N} g(\hat{E}_j)\varphi_j^a(R_\mathrm{s}) + \frac{q}{\epsilon_a}\frac{R_\mathrm{s}^2}{4}N_a + D_a = \frac{q}{2\pi\epsilon_b}\sum_{j=0}^{N} g(\hat{E}_j)\varphi_j^b(R_\mathrm{s}) + C_b\ln(R_\mathrm{s}) + D_b \tag{B.54}$$

Thus:

$$D_a = \frac{q}{2\pi\epsilon_a}\sum_{j=0}^{N} g(\hat{E}_j)\varphi_j^a(R_\mathrm{s}) + \frac{q}{\epsilon_a}\frac{R_\mathrm{s}^2}{4}N_a + -\frac{q}{2\pi\epsilon_b}\sum_{j=0}^{N} g(\hat{E}_j)\varphi_j^b(R_\mathrm{s}) - C_b\ln(R_\mathrm{s}) - D_b \tag{B.55}$$

where φ_j^a and φ_j^b are given by Eqs.(B.30) and (B.32), and C_b and D_b were calculated in Eqs. (B.49) and (B.52)

B.4 Drain current analytical model related calculi

In this Section we accomplish the integration of Eq. (5.69) to obtain I_ds. First, we recall Eq. (5.69):

$$I_\mathrm{ds} = \frac{2\pi R_\mathrm{s}\mu}{L}\int_{V_\mathrm{s}}^{V_\mathrm{d}} Q_\mathrm{i}(V)dV \tag{B.56}$$

For the sake of simplicity, we use the following notation in the forthcoming procedure:

$$x = V, \quad f(x) = Q_\mathrm{it}, \quad \kappa_j = -\frac{\hat{E}_j + \Delta\hat{E}_j}{k_\mathrm{B}T}, \quad Q_\mathrm{i} = -\frac{qN_\mathrm{c}}{2\pi R_\mathrm{s}}\sum_{j=0}^{N}\mathcal{F}_{-\frac{1}{2}}(\kappa_j + y) \tag{B.57}$$

$$y = \frac{q\psi_\mathrm{s}}{k_\mathrm{B}T} - \frac{qx}{k_\mathrm{B}T} = \frac{q}{k_\mathrm{B}T}\left(V_\mathrm{G} - (\Phi_\mathrm{m} - \chi_\mathrm{s}) - \frac{f(x)}{C_\mathrm{ins}} - \frac{-\frac{qN_\mathrm{c}}{2\pi R_\mathrm{s}}\sum_{j=0}^{N}\mathcal{F}_{-\frac{1}{2}}(\kappa_j + y)}{C_\mathrm{ins}} - x\right) \tag{B.58}$$

where we have used Eq. (5.71) for the definition of y_s. Then, the integral in Eq. (B.56) can be written as:

$$-qN_\mathrm{c}\int\sum_{j=0}^{N}\mathcal{F}_{-\frac{1}{2}}(\kappa_j + y)dx = -qN_\mathrm{c}\int\sum_{j=0}^{N}\mathcal{F}_{-\frac{1}{2}}(\kappa_j + y)\frac{dx}{d(\kappa_j + y)}d(\kappa_j + y) \tag{B.59}$$

being

$$\frac{d(\kappa_j + y)}{dx} = \frac{d\kappa_j}{dx} + \frac{dy}{dx} \tag{B.60}$$

On the one hand, we can write

$$\frac{dy}{dx} = -\frac{q}{k_{\mathrm{B}}T}\frac{1}{C_{\mathrm{ins}}}\frac{df(x)}{dx} - \frac{q}{k_{\mathrm{B}}T}\frac{-qN_{\mathrm{c}}}{C_{\mathrm{ins}}}\frac{d\sum_{i=0}^{N}\mathcal{F}_{-\frac{1}{2}}(\kappa_i + y)}{d(\kappa_j + y)}\frac{d(\kappa_j + y)}{dx} - \frac{q}{k_{\mathrm{B}}T} \tag{B.61}$$

being the index j independent of the sum index i. On the other hand, using the definition for $\Delta\hat{E}_j$ proposed in Eq. 5.24:

$$\frac{d\kappa_j}{dx} = -\frac{q}{k_{\mathrm{B}}T}\frac{d\Delta\hat{E}_j}{dx} = -\frac{q}{k_{\mathrm{B}}T}\int R_j(r)\frac{d\hat{\psi}(r)}{dx}R_j^*(r)rdr \tag{B.62}$$

where $\hat{\psi}(r) = \psi(r) - \psi(R_{\mathrm{s}})$. Then we can write:

$$\frac{d\kappa_j}{dx} = -\frac{q}{k_{\mathrm{B}}T}\left(-qN_{\mathrm{c}}\sum_{i=0}^{N}\frac{d}{dx}\mathcal{F}_{-\frac{1}{2}}(\kappa_i + y)\Upsilon_{ij}\right) \tag{B.63}$$

being

$$\Upsilon_{ij} = \int R_j(r)\hat{\varphi}_i R_j^*(r)rdr \tag{B.64}$$

$\hat{\varphi}_i$ is given by Eq. (5.41). Using Eq. (**??**) directly into Eq. (B.62) would highly complicate the subsequent calculus. We consider here the following substitution:

$$\Upsilon_j = \frac{\sum_{i=0}^{N}\mathcal{F}_{-\frac{1}{2}}(\kappa_i + y)\Upsilon_{ij}}{\sum_{i=0}^{N}\mathcal{F}_{-\frac{1}{2}}(\kappa_i + y)} \tag{B.65}$$

Contrary to Υ_{ij}, Υ_j would depend on V as it does $\mathcal{F}_{-\frac{1}{2}}(\kappa_i + y)$. Actually, the Υ_j dependence on V is determined by the relative population of the subbands. But we can expect a reduced variation in the relative occupation of the subbands for medium and strong inversion (small V). In weak inversion (large V) some variations are observed as new subbands start to be populated. Nevertheless, the weak inversion scenario corresponds to a saturated drain, and as it is well known the drain charge contribution to the saturation current is not relevant. As a consequence, we assume Υ_j as a constant, determined by the subband populations at the source: $V = V_{\mathrm{s}}$. Then, after some algebr,

we get:

$$\frac{d(\kappa_j+y)}{dx} = -\frac{q}{k_{\mathrm{B}}T}\frac{1}{C_{\mathrm{ins}}}\frac{df(x)}{dx} - \frac{q}{k_{\mathrm{B}}T}\left(\frac{1}{C_{\mathrm{ins}}}+\Upsilon_j\right)(-qN_{\mathrm{c}})\frac{d\sum_{i=0}^{N}\mathcal{F}_{-\frac{1}{2}}(\kappa_i+y)}{d(\kappa_j+y)}\frac{d(\kappa_j+y)}{dx} - \frac{q}{k_{\mathrm{B}}T} \tag{B.66}$$

Using it into Eq. (B.56) we get:

$$I_{\mathrm{ds}} = -qN_{\mathrm{c}}\frac{\mu}{L}\int\sum_{j=0}^{N}\mathcal{F}_{-\frac{1}{2}}(\kappa_j+y)\frac{\frac{k_{\mathrm{B}}T}{q}+\left(\frac{1}{C_{\mathrm{ins}}}+\Upsilon_j\right)(-qN_{\mathrm{c}})\frac{d\sum_{i=0}^{N}\mathcal{F}_{-\frac{1}{2}}(\kappa_i+y)}{d(\kappa_j+y)}}{1+\frac{1}{C_{\mathrm{ins}}}\frac{df(x)}{dx}}d(\kappa_j+y) \tag{B.67}$$

Eq. (B.67) is not a straightforward expression to integrate analytically. Nevertheless, it can be integrated in some particular cases:

1. If no interface traps are considered, then $f(x) = 0$

2. If a constant profile of $D_{\mathrm{it}}(E)$ is considered, and the Fermi function is approximated by a step function, then $df(x)/dx = qD_{\mathrm{it}}$

B.4.1 Drain current if no D_{it} is considered

If no interface traps are considered, Eq. (B.67) is simplified to:

$$I_{\mathrm{ds}} = \frac{\mu}{L}(-qN_{\mathrm{c}})\int\sum_{j=0}^{N}\mathcal{F}_{-\frac{1}{2}}(\kappa_j+y)\left(\frac{k_{\mathrm{B}}T}{q}+\left(\frac{1}{C_{\mathrm{ins}}}+\Upsilon_j\right)(-qN_{\mathrm{c}})\frac{d\sum_{i=0}^{N}\mathcal{F}_{-\frac{1}{2}}(\kappa_i+y)}{d(\kappa_j+y)}\right)d(\kappa_j+y) \tag{B.68}$$

Therefore:

$$I_{\mathrm{ds}} = \frac{\mu}{L}(-qN_{\mathrm{c}})\frac{k_{\mathrm{B}}T}{q}\int\sum_{j=0}^{N}\mathcal{F}_{-\frac{1}{2}}(\kappa_j+y)d(\kappa_j+y)+ \tag{B.69}$$

$$+\frac{\mu}{L}(-qN_{\mathrm{c}})\int\sum_{j=0}^{N}\mathcal{F}_{-\frac{1}{2}}(\kappa_j+y)\left(\frac{1}{C_{\mathrm{ins}}}+\Upsilon_j\right)(-qN_{\mathrm{c}})d\sum_{i=0}^{N}\mathcal{F}_{-\frac{1}{2}}(\kappa_i+y) \tag{B.70}$$

The first integral in the right-hand side of Eq. (B.70) is easy to solve,

$$\int\sum_{j=0}^{N}\mathcal{F}_{-\frac{1}{2}}(\kappa_j+y)d(\kappa_j+y)=\sum_{j=0}^{N}\mathcal{F}_{\frac{1}{2}}(\kappa_j+y) \tag{B.71}$$

where we have used the Fermi-Dirac recurrence relation $\mathcal{F}_{j+1}(x)=\int\mathcal{F}_j(x)dx$. The second integral is not straightforward to solve as far as the integrand is a sum of terms scaled by a factor Υ_j which is not present in the differential. Similarly to the approximation made in Eq. (B.65) we can define:

$$\Upsilon=\frac{\sum_{j=0}^{N}\mathcal{F}_{-\frac{1}{2}}(\kappa_i+y)\Upsilon_j}{\sum_{j=0}^{N}\mathcal{F}_{-\frac{1}{2}}(\kappa_i+y)} \tag{B.72}$$

which allows us to write the second integral as:

$$\int\left(\frac{1}{C_{\mathrm{ins}}}+\Upsilon\right)\sum_{j=0}^{N}\mathcal{F}_{-\frac{1}{2}}(\kappa_j+y)d\left(\sum_{i=0}^{N}\mathcal{F}_{-\frac{1}{2}}(\kappa_i+y)\right)=$$

$$\left(\frac{1}{C_{\mathrm{ins}}}+\Upsilon\right)\frac{\left(\sum_{j=0}^{N}\mathcal{F}_{-\frac{1}{2}}(\kappa_j+y)\right)^2}{2} \tag{B.73}$$

The approximation made in Eq. (B.72) is equivalent to that used in Eq. (B.65). Therefore, the discussion about its validity referred previously can also be assumed

here. Finally, substituting Eqs. (B.71) and (B.73) into (B.70) we get:

$$I_{\rm ds} = \frac{\mu}{L}\left[(-qN_{\rm c})\sum_{j=0}^{N}\mathcal{F}_{\frac{1}{2}}(\kappa_j+y) + \frac{1}{C_{\rm ds}}(-qN_{\rm c})\frac{\left(\sum_{j=0}^{N}\mathcal{F}_{-\frac{1}{2}}(\kappa_j+y)\right)^2}{2}\right]_{V_{\rm s}}^{V_{\rm d}} \tag{B.74}$$

where C_Υ was defined as:

$$\frac{1}{C_\Upsilon} = \left(\frac{1}{C_{\rm ins}} + \Upsilon\right) \tag{B.75}$$

For the sake of clarity we can define the functions:

$$f_1(V) = -qN_{\rm c}\frac{k_{\rm B}T}{q}\sum_{j=0}^{N}\mathcal{F}_{\frac{1}{2}}\left(-\frac{\hat{E}_j + \Delta\hat{E}_j - q\psi_{\rm s} + qV}{k_{\rm B}T}\right) \tag{B.76}$$

$$f_2(V) = -qN_{\rm c}\frac{1}{C_{\rm ds}}\left[\sum_{j=0}^{N}\mathcal{F}_{-\frac{1}{2}}\left(-\frac{\hat{E}_j + \Delta\hat{E}_j - q\psi_{\rm s} + qV}{k_{\rm B}T}\right)\right]^2 \tag{B.77}$$

being the resulting drain current in absence of $D_{\rm it}$:

$$I_{\rm ds} = \frac{\mu}{L}\left(f_1(V_{\rm d}) + f_2(V_{\rm d}) - f_1(V_{\rm s}) - f_2(V_{\rm s})\right) \tag{B.78}$$

where $\psi_{\rm ss}$ ($\psi_{\rm sd}$) and $\Delta\hat{E}_j^{\rm s}$ ($\Delta\hat{E}_j^{\rm d}$) are the surface potential and correction to the energy level at the source (drain) respectively; and can be obtained solving the charge model for $V = V_{\rm s}$ ($V = V_{\rm d}$).

B.4.2 Drain current for a constant $D_{\rm it}$

Now, we extend the drain current model assuming a constant $D_{\rm it}$ profile in the gap. To do it we approximate the Fermi function by a step function. Furthermore, for the sake of simplicity, let us consider just acceptors traps. The extension to a profile with both kind of traps is straightforward. We can define $D_{\rm it}(E)$ as

$$D_{\rm it}(E) = D_{\rm it} \times \left[U(E - E_{\rm i}(R_{\rm s})) - U(E - E_{\rm c}(R_{\rm s}))\right] \tag{B.79}$$

that is a constant $D_{\rm it}$ in a certain range of energies between the conduction band at the interface, $E_{\rm c}(R_{\rm s})$, and the intrinsic Fermi level at the interface, $E_{\rm i}(R_{\rm s})$, being U the

step function. Introducing Eq. (B.79) into the expression for $Q_{\rm it}$, given by Eq. (5.64), we get

$$Q_{\rm it} = -qD_{\rm it}\int \frac{U(E-E_{\rm i}) - U(E-E_{\rm c})}{1+e^{\frac{E+qV}{k_{\rm B}T}}}dE = \tag{B.80}$$

where we have substituted $E_{\rm F}$ by the pseudo Fermi level. Using the references for energies proposed in Section 5.2, we can write $E_{\rm c}(r) = -q\psi(r)$. Then $E_{\rm c}(R_{\rm s}) = -q\psi(R_{\rm s}) = -q\psi_{\rm s}$. Thus, Eq. (5.64) can be rewritten in terms of $\psi_{\rm s}$ as:

$$Q_{\rm it} = -qD_{\rm it}\int \frac{U(E+q\psi_{\rm s}+E_{\rm g}/2) - U(E+q\psi_{\rm s})}{1+e^{\frac{E+qV}{k_{\rm B}T}}}dE \tag{B.81}$$

Assuming that the Fermi function can be approximated by a step function, its derivative is a Dirac delta function. Then, we can write:

$$\frac{dQ_{\rm it}}{dV} = -qD_{\rm it}\times[U(-qV+q\psi_{\rm s}+E_{\rm g}/2) - U(-qV+q\psi_{\rm s})] \tag{B.82}$$

which using the definition in Eq. (B.58) can be reformulated as:

$$\frac{f(x)}{x} = -qD_{\rm it}\left[U(y+E_{\rm g}/2) - U(y)\right] \tag{B.83}$$

Now we can substitute it in Eq. (B.67) resulting:

$$I_{\rm ds} = --qN_{\rm c}\int \sum_{j=0}^{N}\mathcal{F}_{-\frac{1}{2}}(\kappa_j+y)\frac{\dfrac{k_{\rm B}T}{q} + \left(\dfrac{1}{C_{\rm ins}}+\Upsilon_j\right)(-qN_{\rm c})\dfrac{d\sum\limits_{i=0}^{N}\mathcal{F}_{-\frac{1}{2}}(\kappa_i+y)}{d(\kappa_j+y)}}{1-\dfrac{q\,D_{\rm it}}{C_{\rm ins}}\left[U(y+E_{\rm g}/2)-U(y)\right]}d(\kappa_j+y) \tag{B.84}$$

Using the properties of the step function, we can split the previous integrals into three integrals:

$$I_{\rm ds} = -q^2 N_{\rm c}^2 \int_{y_{\rm s}}^{y_{\rm c}} \sum_{j=0}^{N} \mathcal{F}_{-\frac{1}{2}}(\kappa_j + y) \left(\frac{k_{\rm B}T}{q^2 N_{\rm c}} - \left(\frac{1}{C_{\rm ins}} + \Upsilon_j \right) \frac{d \sum_{i=0}^{N} \mathcal{F}_{-\frac{1}{2}}(\kappa_i + y)}{d(\kappa_j + y)} \right) d(\kappa_j + y)$$
$$- \frac{-q^2 N_{\rm c}^2}{1 - \dfrac{qD_{\rm it}}{C_{\rm ins}}} \int_{y_{\rm c}}^{y_{\rm i}} \sum_{j=0}^{N} \mathcal{F}_{-\frac{1}{2}}(\kappa_j + y) \left(\frac{k_{\rm B}T}{q^2 N_{\rm c}} - \left(\frac{1}{C_{\rm ins}} + \Upsilon_j \right) \frac{d \sum_{i=0}^{N} \mathcal{F}_{-\frac{1}{2}}(\kappa_i + y)}{d(\kappa_j + y)} \right) d(\kappa_j + y)$$
$$- q^2 N_{\rm c^2} \int_{y_{\rm i}}^{y_{\rm d}} \sum_{j=0}^{N} \mathcal{F}_{-\frac{1}{2}}(\kappa_j + y) \left(\frac{k_{\rm B}T}{q^2 N_{\rm c}} - \left(\frac{1}{C_{\rm ins}} + \Upsilon_j \right) \frac{d \sum_{i=0}^{N} \mathcal{F}_{-\frac{1}{2}}(\kappa_i + y)}{d(\kappa_j + y)} \right) d(\kappa_j + y) \tag{B.85}$$

where the integral limits $y_{\rm s}$, $y_{\rm d}$ are the y-values corresponding to $V = V_{\rm s}$ and $V = V_{\rm d}$; and $y_{\rm c} = 0$ and $y_{\rm i} = -E_{\rm g}/2$ correspond to V-values $V_{\rm c}$ and $V_{\rm i}$ such as $\psi_{\rm s} - V_{\rm c} = 0$ (that is $E_{\rm F}(z) = E_{\rm c}$) and $\psi_{\rm s} - V_{\rm i} = E_{\rm g}/2$ (that is $E_{\rm F}(z) = E_{\rm i}$). The three integrals in Eq. (B.85) are the same than that solved in Eq. (B.70). Then, following the afore explained procedure and using the definitions for f_1 and f_2 in Eqs. (B.76) and (B.77) we get:

$$\begin{aligned} I_{\rm ds} =& \frac{\mu}{L} \left[f_1(V_{\rm c}) + f_2(V_{\rm c}) - f_1(V_{\rm s}) - f_2(V_{\rm s}) + \right. \\ &+ \frac{f_1(V_{\rm i}) + f_2(V_{\rm i}) - f_1(V_{\rm c}) - f_2(V_{\rm c})}{1 + \dfrac{qD_{\rm it}}{C_{\rm ins}}} + f_1(V_{\rm d}) + f_2(V_{\rm d}) - f_1(V_{\rm i}) - f_2(V_{\rm i}) \left. \right] \end{aligned} \tag{B.86}$$

which can be simplified to:

$$I_{\rm ds} = \frac{\mu}{L} \left[f_1(V_{\rm d}) + f_2(V_{\rm d}) - f_1(V_{\rm s}) - f_2(V_{\rm s}) + \frac{f_1(V_{\rm c}) + f_2(V_{\rm c}) - f_1(V_{\rm i}) - f_2(V_{\rm i})}{1 + \dfrac{qD_{\rm it}}{C_{\rm ins}}} \right] \tag{B.87}$$

It should be noted that this $I_{\rm ds}$ expression requires solving the model for four Fermi

pseudo-potentials: V_s and V_d as it was in Eq. (B.68) and V_1 and V_2 which correspond to the cross of E_F trough $E_\mathrm{c}(R_\mathrm{s}) = -q\psi_\mathrm{s}$ and $E_\mathrm{i} = -q\psi_\mathrm{s} - E_\mathrm{g}/2$. As it was in Eq. (B.68), the values of $\hat{E}_j$ are constant and independent of V but not $\Delta\hat{E}_j$ and ψ_s which need to be calculated for each case.

In the linear region, $V_\mathrm{ds} < V_\mathrm{gs} - V_\mathrm{T}$, just the first two integrals of Eq. (B.86) make sense. V_d is not high enough as to move the pseudo Fermi potential below the intrinsic level. Then, the third integral in Eq. (B.85) can be removed and the upper limit in the second one is changed from y_i to y_c.

Appendix C

Capacitance and threshold voltage models related calculi

In this Appendix we sum up some calculi related to the capacitance and threshold voltage analytical models.

C.1 Determination of the centroid capacitance

In this Section we obtain an expression for the centroid capacitance of an arbitrary subband j, solving the integral proposed in Chapter 6. We recall here Eq. (6.12):

$$C_{Cj} = \frac{2\pi\epsilon_s}{\int_0^{R_0} r\ln\left(\frac{R_0}{r}\right)|A_j J_l(\gamma_j r)|^2 dr} \tag{C.1}$$

The integral in the denominator of Eq. (C.1) can be reformulated as:

$$\int_0^{R_0} r\ln\left(\frac{R_0}{r}\right)|A_j J_l(\gamma_j r)|^2 dr = \ln(R_0)\int_0^{R_0} r\,|A_j J_l(\gamma_j r)|^2 dr - \int_0^{R_0} r\ln(r)|A_j J_l(\gamma_j r)|^2 dr \tag{C.2}$$

where the second term can be integrated by parts:

$$\int_0^{R_0} r\,\ln(r)|A_j J_l(\gamma_j r)|^2 dr = \left[\ln(r)\int r\,|A_j J_l(\gamma_j r)|^2 dr\right]_0^{R_0} - \int_0^{R_0}\left(\int r\,|A_j J_l(\gamma_j r)|^2 dr\right)\frac{1}{r}dr \tag{C.3}$$

but the first term in the right-hand side of Eq. (C.3) is canceled out with the first term in the right-hand side of Eq. (C.2). Then:

$$\int_0^{R_0} r\ln\left(\frac{R_0}{r}\right)|A_j J_l(\gamma_j r)|^2 dr = \int_0^{R_0}\int r\,|A_j J_l(\gamma_j r)|^2 dr\frac{1}{\hat{r}}d\hat{r} \tag{C.4}$$

where we have used the symbol $\hat{}$ to distinguish between the two integrations. This integral is the same than the one solved in Appendix B.2 when dealing with the Poisson equation in the semiconductor. We recall here Eq. (B.30)

$$A_j^2\int\int r\,J_l^2(\gamma_j r)dr\frac{1}{\hat{r}}d\hat{r} = A_j^2\left(\frac{r^2}{2}J_l^2(\gamma_j r) + \frac{r^2}{2}J_{l-1}^2(\gamma_j r) + \right.$$
$$\left. +(-l+\frac{1}{2})\frac{r}{\gamma_j}J_{l-1}(\gamma_j r)J_l(\gamma_j r) + \frac{l}{\gamma_j^2}\sum_{m=1}^{l}J_{m-1}^2(\gamma_j r) - \frac{l}{2\gamma_j^2}J_0^2(\gamma_j r)\right) \tag{C.5}$$

So, evaluating Eq. (C.5) in their limits, $r = R_0$ and $r = 0$, we have::

$$\int_0^{R_0}\int r\,|A_j J_l(\gamma_j r)|^2 dr\frac{1}{\hat{r}}d\hat{r} = A_j^2\left(\frac{R_0^2}{2}J_l^2(\gamma_j R_0) + \frac{R_0^2}{2}J_{l-1}^2(\gamma_j R_0) + \right. \tag{C.6}$$
$$\left.(-l+\frac{1}{2})\frac{R_0}{\gamma_j}J_{l-1}(\gamma_j R_0)J_l(\gamma_j R_0) + \frac{l}{\gamma_j^2}\sum_{m=1}^{l}J_{m-1}^2(\gamma_j R_0) - \frac{l}{2\gamma_j^2}J_0^2(\gamma_j R_0) - \frac{l}{2\gamma_j^2}J_0^2(0)\right)$$

where we have used $J_v(0) = 0$ for $v \neq 0$. Therefore, using Eq. (C.6), $C_{\mathrm{C}j}$ can be written as:

$$C_{\mathrm{C}j} = \frac{2\pi\epsilon_{\mathrm{s}}}{A_j^2}\left(\frac{R_0^2}{2}J_l^2(\gamma_j R_0) + \frac{R_0^2}{2}J_{l-1}^2(\gamma_j R_0) + (-l+\frac{1}{2})\frac{R_0}{\gamma_j}J_{l-1}(\gamma_j R_0)J_l(\gamma_j R_0) + \right.$$
$$\left. +\frac{l}{\gamma_j^2}\sum_{m=1}^{l}J_{m-1}^2(\gamma_j R_0) - \frac{l}{2\gamma_j^2}J_0^2(\gamma_j R_0) - \frac{l}{2\gamma_j^2}J_0^2(0)\right)^{-1} \tag{C.7}$$

Furthermore, looking at the similarities between the resolution proposed here for the centroid capacitance and the one carried out in Appendix B.2 for φ_j it is easy to conclude that:

$$C_{\mathrm{C}j} = \frac{2\pi\epsilon_{\mathrm{s}}}{\varphi_j(R_0) - \varphi_j(0)} \tag{C.8}$$

Therefore, from φ_j properties (see Section 5.3), we can assume that degenerate energy levels have equal centroid capacitances.

To conclude this Appendix we give the particular centroid capacitance expressions for the first five subbands: $j = 0$, $l = 0$; $j = 1, 2$, $l = \pm 1$; and $j = 3, 4$, $l = \pm 2$. They are used later in Section 6.3. For $j = 0$, $l = 0$;

$$C_{\mathrm{C}0} = \frac{2\pi\epsilon_{\mathrm{s}}}{A_j^2}\frac{2}{R_0^2}\left(J_0^2(\gamma_0 R_0) + J_1^2(\gamma_0 R_0) - \frac{1}{\gamma_0 R_0}J_1(\gamma_0 R_0)J_0(\gamma_0 R_0)\right)^{-1} \tag{C.9}$$

For $j = 1, 2$, $l = \pm 1$;

$$C_{\mathrm{C}1,2} = \frac{2\pi\epsilon_{\mathrm{s}}}{A_1^2}\frac{2}{R_0^2}\left(J_1^2(\gamma_1 R_0) + J_0^2(\gamma_1 R_0) - \frac{1}{\gamma_1 R_0}J_0(\gamma_1 R_0)J_1(\gamma_1 R_0) + \frac{J_0^2(\gamma_1 R_0) - J_0^2(0)}{\gamma_1^2 R_0^2}\right)^{-1} \tag{C.10}$$

For $j = 3, 4$, $l = \pm 2$;

$$C_{\mathrm{C}3,4} = \frac{2\pi\epsilon_{\mathrm{s}}}{A_3^2}\frac{2}{R_0^2}\left(J_2^2(\gamma_3 R_0) + J_1^2(\gamma_3 R_0) - \frac{3}{\gamma_3 R_0}J_1(\gamma_3 R_0)J_2(\gamma_3 R_0) + \frac{4}{\gamma_3^2 R_0^2}J_1^2(\gamma_3 R_0) + 2\frac{J_0^2(\gamma_3 R_0) - J_0^2(0)}{\gamma_3^2 R_0^2}\right)^{-1} \tag{C.11}$$

where in all cases $J_0^2(0) = 1$

C.2 Validity of the approximations for the $C_{\mathbf{g}}$ and $V_{\mathbf{T}}$ models

In this Section we check the validity of the approximations made in Chapter 6, specifically in Eqs. (6.1) and (6.49), for the capacitance and threshold voltage models.

First, we deal with the approximation in Eq. (6.1). We recall it here:

$$C_{\mathrm{G}} = \frac{\partial Q_{\mathrm{G}}}{\partial V_{\mathrm{G}}} = -\frac{\partial Q_{\mathrm{s}} + Q_{\mathrm{ins}}}{\partial V_{\mathrm{G}}} \simeq -\frac{\partial Q_{\mathrm{s}}}{\partial V_{\mathrm{G}}} \tag{C.12}$$

Here, we supposed that Q_{ins} was negligible compared to Q_{s}. In the model, Q_{ins} (assuming no D_{it}) is determined by the wavefunction penetration into the insulator. For a subband j, the ratio between the electron charge in the semiconductor (neglecting N_a) and the electron charge in the insulator is proved to be:

$$\vartheta_{\mathrm{C}} = \frac{\int_{R_0}^{R_0+t_{\mathrm{ins}}} C_j^2 K_l(\alpha_j r) r dr}{\int_0^{R_0} A_j^2 J_l(\gamma_j r) r dr} = \frac{1}{\int_0^{R_0} A_j^2 J_l(\gamma_j r) r dr} - 1 \tag{C.13}$$

where we have applied Eq. (B.1). From, ϑ we can get an estimation of the relative error committed in Eq. (C.12). The exact value of the error depends on the relative occupations of the different subbands and the corresponding errors associated to each subband. Fig. shows ϑ as a function of the NW size for several materials InGaAs (solid lines), InAs (dashed lines) and GaAs (dash-dotted lines) and subbands: $j = 0$, $l = 0$ (blue), $j = 1, 2$, $l = \pm 1$ (green) and $j = 3, 4$, $l = \pm 2$.

InAs shows the maximum error as it has the lower confinement effective mass and consequently higher wavefunction penetration (see Fig 5.12 in Chapter 5). The behavior of the error is non-monotonic as the penetration of the wavefunction into the insulator is a not simple result which depends of several factors: the potential barrier height, the size of the NW or the effective mass in the insulator and the semiconductor among others. Nevertheless the maximum error achieved is around 5% (corresponding to $j = 3, 4$, $l = \pm 2$ subband in InAs for $2R_0 = 5$nm), but this subband for this size is nearly empty for a reasonable range of gate voltage (see Fig. 5.13 in Chapter 5), so its contribution to the error in Eq. (6.1) is negligible. From Fig. C.1 we can conclude that the approximation in Eq. (6.1) is appropriate.

In second place, we discuss the approximation in Eq. (6.49). It is a well known approximation for K_0 when the argument is high [204]. We define the relative error

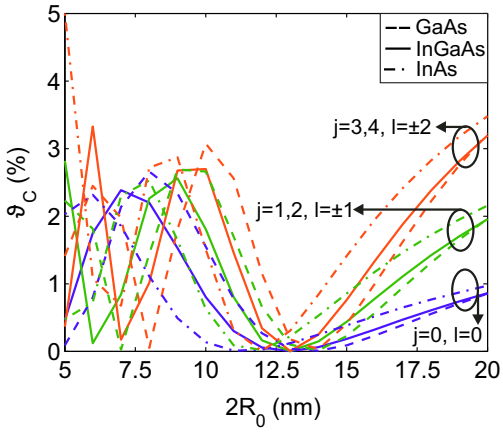

Figure C.1: ϑ as a function of the NW size for several materials: InGaAs (solid lines), InAs (dashed lines) and GaAs (dash-dotted lines) and subbands: $j = 0$, $l = 0$ (blue), $j = 1, 2$, $l = \pm 1$ (green) and $j = 3, 4$, $l = \pm 2$.

due to this approximation as:

$$\vartheta_{\mathrm{T}} = \frac{\int_{R_0}^{R_0+t_{\mathrm{ins}}} K_0(\alpha_0 r) - \sqrt{\frac{\pi}{2\alpha_0 r}} e^{-\alpha_0 r} r dr}{\int_{R_0}^{R_0+t_{\mathrm{ins}}} K_0(\alpha_0 r) r dr} \tag{C.14}$$

To validate the applicability of this expression in our threshold voltage model, Fig. C.2 shows the relative error between the analytical integral solution in Eq. (5.58) and the approximate solution in Eq. 6.50 for several III-V materials: InGaAs (blue), GaAs (green) and InAs (red), as a function of the semiconductor diameter when $t_{\mathrm{ins}} = 1.5$nm was considered. As can be seen the relative error is lower than 3% for the devices considered in this work.

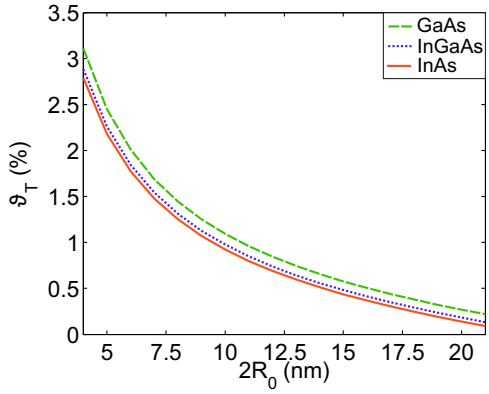

Figure C.2: Relative error (ϑ_T) between the analytical integral solution of Eq. (5.58) and the approximate solution of Eq. (6.50) as a function of the NW size, for several III-V materials: InGaAs (plotted as blue), GaAs (plotted as green) and InAs (plotted as red).

Appendix D

Scattering elements

In this Appendix we briefly discuss the characteristic of the three kinds of scattering mechanisms distinguished in Section 7.4 and their implication in the formulation of the implicit problem given by Eq. (7.34).

D.1 Inelastic anisotropic mechanism

For an inelastic anisotropic mechanism the energy is not conserved and $S_{j,j'}$ is wavenumber dependent. This can be written in the general formulation given in Eq. (7.19) as:

$$S^{ia}_{j,j'}(k_z, k'_z) = \frac{2\pi}{\hbar} \left| M_{j,j'}(k_z, k'_z) \right|^2 \delta \left(E_{j'}(k'_z) - E_j(k_z) \pm \hbar\omega \right) \tag{D.1}$$

where the delta function restricts the non null elements of $S_{j,j'}$ to those with $E_{j'}(k'_z) = E_j(k_z) \pm \hbar\omega$. We assume that the scattering mechanism is not k_z dependent itself, and $\omega \neq \omega(k_z - k'_z)$. Using the equivalence [88]:

$$\sum_{k_z} = \frac{L}{2\pi} \int dk_z \tag{D.2}$$

we can write:

$$\frac{1}{\tau_j^{\mathrm{ia}}(k_\mathrm{z})} = \sum_{j',k'_\mathrm{z}} S^{\mathrm{ia}}_{j,j'}(k_\mathrm{z},k'_\mathrm{z}) \left(\frac{1-f_0(E')}{1-f_0(E)}\right)\left(1-\frac{\tau_{j'}(k'_\mathrm{z})v_{j'}(k'_\mathrm{z})}{\tau_j(k_\mathrm{z})v_j(k_\mathrm{z})}\right) =$$
$$\frac{L}{\hbar}\sum_{j'}\int \left|M_{j,j'}(k_\mathrm{z},k'_\mathrm{z})\right|^2 \delta\left[E_{j'}(k'_\mathrm{z}) - E_i(k_\mathrm{z}) \pm \hbar\omega\right] \left(\frac{1-f_0(E')}{1-f_0(E)}\right)\left(1-\frac{\tau_{j'}(k'_\mathrm{z})v_{j'}(k'_\mathrm{z})}{\tau_j(k_\mathrm{z})v_j(k_\mathrm{z})}\right) dk'_\mathrm{z} \tag{D.3}$$

For a 1D electron gas, with a monotonic dispersion relation (guaranteed under non-parabolic EMA), there are only two k'_z states in the subband j' with energy $E_{j'}(k'_\mathrm{z}) = E_j(k_\mathrm{z})+\hbar\omega$ and other two k'_z states with $E_{j'}(k'_\mathrm{z}) = E_j(k_\mathrm{z})-\hbar\omega$. We name them here $k^+_{\mathrm{z,b}}$ and $k^+_{\mathrm{z,f}}$ for the process augmenting the electron energy and $k^-_{\mathrm{z,b}}$ and $k^-_{\mathrm{z,f}}$ for the process reducing the electron energy. The subindex b (backward) and f (forward) denotes transitions to final states with negative and positive k_z respectively. Fig. D.1 presents a schematic depiction of subbands j and j' and the different k_z states involved in a transition due to an inelastic intersubband process. Inelastic anisotropic mechanisms can also be intrasubband (see Chapter 8) and the resulting k_z are plotted in Fig. D.1 as squares.

Using the δ function property:

$$\int dk'_\mathrm{z} F(k_\mathrm{z})\delta(g(k^\pm_\mathrm{z})) = \sum_n \frac{F(k^\pm_{\mathrm{z},n})}{|g'(k^\pm_{\mathrm{z},n})|} \tag{D.4}$$

where $k^\pm_{\mathrm{z},n}$ are the zeros of $g(k_\mathrm{z})$ and $g' = dg/dk_\mathrm{z}$, we can rewrite Eq. (D.3) as:

$$\frac{1}{\tau_j^{\mathrm{ia}}(k_\mathrm{z})} = \sum_{j'}\frac{L}{2\pi}\int\frac{2\pi}{\hbar}\left|M_{j,j'}(k_\mathrm{z},k'_\mathrm{z})\right|^2\delta\left[E'-E\pm\hbar\omega\right]\left(\frac{1-f_0(E')}{1-f_0(E)}\right)\left(1-\frac{\tau_{j'}(k'_\mathrm{z})v_{j'}(k'_\mathrm{z})}{\tau_j(k_\mathrm{z})v_j(k_\mathrm{z})}\right)dk_\mathrm{z} =$$
$$\frac{L}{\hbar}\left(\frac{1-f_0(E\pm\hbar\omega)}{1-f_0(E)}\right)\sum_{j'}\left[\frac{|M_{j,j'}(k_\mathrm{z},k'^\pm_{\mathrm{z,b}})|^2}{|\hbar v_{j'}(k'^\pm_{\mathrm{z,b}})|}\left(1-\frac{\tau_{j'}(k'^\pm_{\mathrm{z,b}})v_{j'}(k'^\pm_{\mathrm{z,b}})}{\tau_j(k_\mathrm{z})v_j(k_\mathrm{z})}\right)\right.$$
$$\left.+\frac{|M_{j,j'}(k_\mathrm{z},k'^\pm_{\mathrm{z,f}})|^2}{|\hbar v_{j'}(k'^\pm_{\mathrm{z,f}})|}\left(1-\frac{\tau_{j'}(k'^\pm_{\mathrm{z,f}})v_{j'}(k'^\pm_{\mathrm{z,f}})}{\tau_j(k_\mathrm{z})v_j(k_\mathrm{z})}\right)\right] \tag{D.5}$$

where

$$\frac{\partial(E_{j'}(k'_\mathrm{z}) - E_j(k_\mathrm{z}) \pm \hbar\omega)}{\partial k'_\mathrm{z}} = \hbar v_{j'}(k'_\mathrm{z}) \tag{D.6}$$

Using the symmetry property of the non-parabolic EMA dispersion relation, we get $v_{j'}(k'^{\pm}_{\mathrm{z,b}}) = -v_{j'}(k'^{\pm}_{\mathrm{z,f}})$ and $\tau_{j'}(k'^{\pm}_{\mathrm{z,b}}) = \tau_{j'}(k'^{\pm}_{\mathrm{z,f}})$. Then Eq. (D.5) can be written as:

$$\frac{1}{\tau_j^{\mathrm{ia}}(k_{\mathrm{z}})} = \frac{L}{\hbar}\left(\frac{1-f_0(E\pm\hbar\omega)}{1-f_0(E)}\right)\sum_{j'}\left[\frac{|M_{j,j'}(k_{\mathrm{z}},k'^{\pm}_{\mathrm{z,f}})|^2 - |M_{j,j'}(k_{\mathrm{z}},k'^{\pm}_{\mathrm{z,b}})|^2}{|\hbar v_{j'}(k'^{\pm}_{\mathrm{z,f}})|}\right.$$
$$\left.\left(1-\frac{\tau_{j'}(k'^{\pm}_{\mathrm{z,f}})v_{j'}(k'^{\pm}_{\mathrm{z,f}})}{\tau_j(k_{\mathrm{z}})v_j(k_{\mathrm{z}})}\right)\right] \qquad \text{(D.7)}$$

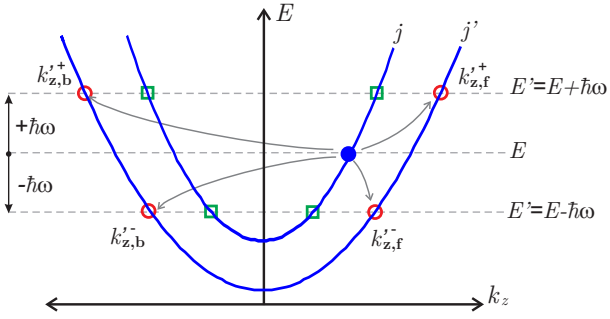

Figure D.1: Schematic view of the transitions between k-states in the subband j and the subband j' due to an inelastic mechanism. The initial state is plotted as a filled circle while the final states for a intersubband transitions are marked with arrows and plotted as unfilled circles. Final states resulting from a intrasubband transition are also plotted as squares.

D.2 Elastic anisotropic mechanism

For an elastic anisotropic mechanism, $S_{j,j'}$ depends on the wavenumber but there is energy conservation. Then, $S_{j,j'}$ can be written as:

$$S^{ea}_{j,j'}(k_{\mathrm{z}},k'_{\mathrm{z}}) = \frac{2\pi}{\hbar}\left|M_{j,j'}(k_{\mathrm{z}},k'_{\mathrm{z}})\right|^2\delta\left[E_{j'}(k'_{\mathrm{z}}) - E_j(k_{\mathrm{z}})\right] \qquad \text{(D.8)}$$

where the delta function restricts the non null elements of $S_{j,j'}$ to those with $E_{j'}(k'_{\rm z}) = E_j(k_{\rm z})$. Then, using (D.2) we can write:

$$\frac{1}{\tau_j^{ea}(k_{\rm z})} = \sum_{j',k'_{\rm z}} S^{ea}_{j,j'}(k_{\rm z},k'_{\rm z}) \left(\frac{1-f_0(E')}{1-f_0(E)}\right)\left(1-\frac{\tau_{j'}(k_{\rm z})' v_{j'}(k'_{\rm z})}{\tau_j(k_{\rm z})v_j(k_{\rm z})}\right) =$$
$$= \sum_{j'} \frac{L}{2\pi}\int \frac{2\pi}{\hbar}\left|M_{j,j'}(k_{\rm z},k'_{\rm z})\right|^2 \delta\left[E'-E\right]\left(\frac{1-f_0(E')}{1-f_0(E)}\right)\left(1-\frac{\tau_{j'}(k'_{\rm z})v_{j'}(k'_{\rm z})}{\tau_j(k_{\rm z})v_j(k_{\rm z})}\right) dk_{\rm z} \tag{D.9}$$

This expression is similar to (D.3) except for the term $[1-f_0(E')]\,/\,[1-f_0(E)] = 1$. For a transition between bands j and j' and non-parabolic EMA there are just two possible final states $k'_{\rm z,b}$ and $k'_{\rm z,f}$. Fig. D.2 presents a schematic depiction of subbands j and j' and the different k states involved in a transition due to an elastic process. Again just intersubband transitions were marked with arrows, denoting the final states with circles while the final states resulting from intrasubband transitions (also possible in elastic anisotropic mechanisms) are plotted as squares.

Following the same mathematical procedure and the symmetry of the dispersion relation under EMA discussed previously we reach to:

$$\frac{1}{\tau_j^{ea}(k_{\rm z})} = \frac{L}{\hbar}\sum_j \left[\left|\frac{M_{j,j'}(k_{\rm z},k'_{\rm z,f})|^2 - |M_{j,j'}(k_{\rm z},k'_{\rm z,b})|^2}{\hbar v_{j'}(k'_{\rm z,f})}\right|\left(1-\frac{\tau_{j'}(k'_{\rm z,f})v_{j'}(k'_{\rm z,f})}{\tau_j(k_{\rm z})v_j(k_{\rm z})}\right)\right] \tag{D.10}$$

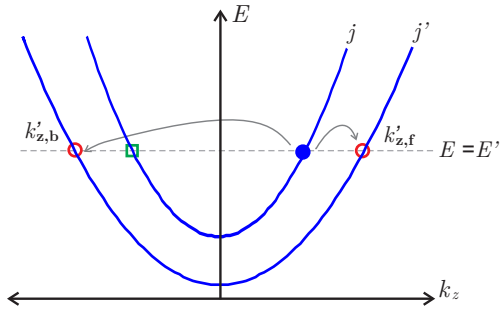

Figure D.2: Schematic view of the transition between k-states in the subband j and the subband j' due to an elastic process. The initial state is plotted as a filled circle, while final states for a intersubband transition are marked with arrows and plotted as unfilled circles. Final states resulting from an intrasubband transition are also plotted as squares.

D.3 Isotropic mechanism

For isotropic mechanisms (both elastic and inelastic), $S_{j,j'}$ does not depend on the wavenumber and there is not energy conservation. Thus, $S_{j,j'}$ can be written as:

$$S^{is}_{j,j'}(k_{\rm z},k'_{\rm z}) = S^{is}_{j,j'}(E) = \frac{2\pi}{\hbar}|M_{j,j'}|^2\delta[E_{j'}(k'_{\rm z}) - E_j(k_{\rm z}) \pm \hbar\omega)] \tag{D.11}$$

where the $M_{j,j'}$ dependence on $k_{\rm z}$ was annulled and we assumed inelastic process. The derivation for elastic processes is the same except for the factor $\pm\hbar\omega$. As in the inelastic anisotropic mechanisms, we assume that the scattering mechanism is not $k_{\rm z}$ dependent itself and $\omega \neq \omega(k_{\rm z} - k'_{\rm z})$. Then, the sum over all $k'_{\rm z}$ states which contribute to the inelastic isotropic τ_j would be:

$$\frac{1}{\tau^{is}_j(k_{\rm z})} = \sum_{j',k'_{\rm z}} S^{is}_{j,j'}\left(\frac{1-f_0(E')}{1-f_0(E)}\right)\left(1-\frac{\tau_{j'}(k'_{\rm z})v_{j'}(k'_{\rm z})}{\tau_j(k_{\rm z})v_j(k_{\rm z})}\right) = \frac{2\pi}{\hbar}\sum_{j'}|M_{j,j'}|^2\sum_{k'_{\rm z}}\delta[E'-E\pm\hbar\omega]\left(\frac{1-f_0(E')}{1-f_0(E)}\right) \tag{D.12}$$

Here the term $\left[1-\tau_{j'}(k'_{\rm z})v_{j'}(k'_{\rm z})/\tau_j(k_{\rm z})v_j(k_{\rm z})\right]$ drops in the sum. This is because for symmetric bands: $v_{j'}(k'^{\pm}_{\rm z,f}) = -v_{j'}(k'^{\pm}_{\rm z,b})$, being $k'^{\pm}_{\rm z,b}$ and $k'^{\pm}_{\rm z,f}$ the possible final sates (see Fig. D.1). Due to the isotropy: $\tau_{j'}(k'^{\pm}_{\rm z,f}) = \tau_{j'}(k'^{\pm}_{\rm z,b}) = \tau_{j'}(E')$.

Then using (D.2) we get:

$$\sum_j \frac{L}{2\pi}\left|M_{j,j'}\right|^2\int\frac{2\pi}{\hbar}\delta\left[E'-E\pm\hbar\omega\right]\left(\frac{1-f_0(E')}{1-f_0(E)}\right)dk'_{\rm z} \tag{D.13}$$

This expression is similar to (D.3) except for the term $\left[1-\tau_{j'}(k'_{\rm z})v_{j'}(k'_{\rm z})/\tau_j(k_{\rm z})v_j(k_{\rm z})\right]$. Following the same mathematical procedure and the approximations for a monotonic symmetric dispersion relation we reach:

$$\frac{1}{\tau^{is}_j(k_{\rm z})} = \frac{L}{\hbar}\left(\frac{1-f_0(E\pm\hbar\omega)}{1-f_0(E)}\right)\sum_{j'}\left[\frac{2M_{j,j'}}{|\hbar v_{j'}(k'^{\pm}_{\rm z,f})|}\right] \tag{D.14}$$

Unlike in anisotropic scattering mechanisms, the momentum relaxation time of an isotropic mechanism can be calculated independently of the rest of scattering mechanism as no implicit dependence on τ_j is present.

Appendix E

Scattering mechanisms related calculi

In this Appendix we sum up some of the necessary calculi for the determination of the matrix element of the different scattering mechanisms.

E.1 Surface Roughness: axial and q_z integrations

In this Section we detail the space and wavenumber axial integration of Eq. (8.9) paying attention to the normalization of the delta Dirac function. We recall space and wavenumber axial integration in Eq. (8.9) as:

$$\int dq_z \int_0^L dz \int_0^L dz' e^{\imath(k_z - k'_z + q_z)(z-z')} C(q_z, q_s) = \int dq_z C(q_z, q_s) \int_0^L dz e^{\imath(k_z - k'_z + q_z)z} \int_0^L dz' e^{-\imath(k_z - k'_z + q_z)z'} \tag{E.1}$$

Each of the previous space axial integrations can be solved, assuming $L \longrightarrow \infty$, taking into account that:

$$\int_{-\infty}^{\infty} e^{-\imath q z} dz = 2\pi\delta(q) \tag{E.2}$$

Then, we can rewrite Eq. (E.1) as:

$$2\pi \int dq_z C(q_z, q_s) \int_0^L dz e^{\imath(k_z - k'_z + q_z)z} \delta(k_z - k'_z + q_z) \tag{E.3}$$

Let us now define, for simplicity, $g(q_z) = \int_0^L dz e^{\imath(k_z - k'_z + q_z)z}$. Then the previous integral leads to:

$$2\pi C(q_z^f, q_s) g(q_z^f) \tag{E.4}$$

being $q_z^f = k'_z - k_z$. From the definition of $g(q_z)$, it is clear that $g(q_z^f) = \int_0^L dz = L$, and therefore Eq. (E.1):

$$2\pi L C(q_z^f, q_s) \tag{E.5}$$

E.2 Coulombian dispersion hard-sphere model

In this Section we apply the hard-spheres model proposed by Ning *et al.* [246] to a 1D electron gas. The aim is to determine a power spectrum $C_{m,i}^{\mathrm{CO}}(q_z)$ from the autocorrelation function of a random distribution of ionized impurities along the axial direction. The first approximation made here assumes that the distribution of charges along the axial direction for a given position $s = s_i$ in the confinement plane is completely independent of the axial distribution corresponding to another position $s = s_m$.[1]

Now we assume that for each position $\mathbf{s}_m$ in the confinement plane there is a random distribution of N punctual particles along the axial direction. As explained in [241], it is not the charge density, but its fluctuations, the responsible of the Coulomb scattering. Therefore, we will define:

$$\sigma_m(z) = \sum_{i=1}^{N} \delta(z - z_i) - N_{\mathrm{avg}} \tag{E.6}$$

where N_{avg} is the average charge density per unit length, and is related to N as, $N_{\mathrm{avg}} = N/L$.S Taking the Fourier transform we get:

$$\sigma_m(q_z) = \sum_{i=1}^{N} e^{-\imath q_z z_i} - N_{\mathrm{avg}} \delta(q_z) \tag{E.7}$$

[1] The approximation makes sense as far as the positions s_i and s_m are far from each other but can be criticizes otherwise. For the sake of simplicity we go on with it here.

The power spectrum $C^{\mathrm{CO}}_{m,m}(q_\mathrm{z})$ is given by:

$$C^{\mathrm{CO}}_{m,m}(q_\mathrm{z}) = \langle \sigma_m(q_\mathrm{z}) \sigma^*_m(q_\mathrm{z}) \rangle = \int \left(\sum_{i=1}^{N} e^{-\imath q_\mathrm{z} z_i} - N_\mathrm{avg} \delta(q_\mathrm{z}) \right) \left(\sum_{j=1}^{N} e^{\imath q_\mathrm{z} z_j} - N_\mathrm{avg} \delta(q_\mathrm{z}) \right) P(z_1, ..., z_N) dz_1 ... dz_N \tag{E.8}$$

where $P(z_1, ..., z_N)dz_1...dz_N$ is the probability of a set of particles $1...N$ to be placed near the set of positions $z_1...z_N$. We will call $W(z_i, z_j)dz_i dz_j$ the joint probability of particles i and j being at z_i and z_j regardless the positions of the rest of the particles:

$$W(z_i, z_j) = \int \frac{P(z_1 ... z_N) dz_1 ... dz_N}{dz_i dz_j} \tag{E.9}$$

After Ning *et al.* [246], Eq. (E.8) can be written as:

$$C^{\mathrm{CO}}_{m,m}(q_\mathrm{z}) = N_\mathrm{avg} + \sum_{i,j,i \neq j} \int W(z_i, z_j) e^{-\imath q_\mathrm{z}(z_i - z_j)} dz_i dz_j - N^2_\mathrm{avg} \delta\left(q_\mathrm{z}\right) \tag{E.10}$$

The hard sphere model assumes that two particles cannot be closer than R_t, and can be uniformly distributed otherwise. Thus, $W(z_i, z_j)$ is:

$$W(z_i, z_j) = \begin{cases} 0 & \text{if} |z_i - z_j| < R_\mathrm{t} \\ \frac{1}{(L - R_\mathrm{t})L} & \text{if} |z_i - z_j| > R_\mathrm{t} \end{cases} \tag{E.11}$$

where $1/L$ is the probability of a particle being at position z_i and $1/(L - R_\mathrm{t})$ is the probability of a particle being at a position z_j given that there is a particle at position z_i. $W(z_i, z_j)$ can be written in a more compact way as

$$W(z_i, z_j) = \frac{1}{(L - R_\mathrm{t})\, L} \left[1 - \mathrm{rect} \left(\frac{z_i - z_j}{R_\mathrm{t}} \right) \right] \tag{E.12}$$

The integral in Eq. (E.10) results into:

$$\int e^{\imath q_\mathrm{z} z_j} dz_j \int \left[1 - \mathrm{rect} \left(\frac{z_i - z_j}{R_\mathrm{t}} \right) \right] e^{-\imath q_\mathrm{z} z_i} dz_i \tag{E.13}$$

where the inner integral is the Fourier transform of $\left[1 - \text{rect}\left(\frac{z_j - z_i}{R_\text{t}}\right)\right]$. Thus: (E.13)

$$\int e^{\imath q_\text{z} z_j} \left[\delta(q_\text{z}) - R_\text{t} e^{-\imath q_\text{z} z_j} \text{sinc}(R_\text{t} q_\text{z})\right] dz_j \tag{E.14}$$

which results in:

$$\delta(q_\text{z})\delta(-q_\text{z}) - LR_\text{t}\text{sinc}(R_\text{t} q_\text{z}) \tag{E.15}$$

Then we can write Eq. (E.10) as:

$$C^\text{CO}_{m,m}(q_\text{z}) = N_\text{avg} + \frac{1}{L\left(L - R_\text{t}\right)} \sum_{i,j,i\neq j} \left[\delta(q_\text{z})\delta(-q_\text{z}) - LR_\text{t}\text{sinc}(R_\text{t} q_\text{z})\right] - N^2_\text{avg}\delta\left(q_\text{z}\right) \tag{E.16}$$

The terms accompanying $\delta\left(q_\text{z}\right)$ will only appear in the calculation when $q_\text{z} = 0$. But q_z does not affect in CO scattering mechanisms. Thus, they can be neglected:

$$C^\text{CO}_{m,m}(q_\text{z}) = N_\text{avg} - \frac{1}{L^2}(N)(N-1)LR_\text{t}\text{sinc}(R_\text{t} q_\text{z}) \tag{E.17}$$

which can be rewritten, taking into account the relation $L = N/N_\text{avg}$, and assuming $N \simeq N - 1$ and $L \simeq L - R_\text{t}$, as:

$$C^\text{CO}_{m,m}(q_\text{z}) = N_\text{avg}\left[1 - \frac{N}{L} R_\text{t}\text{sinc}(R_\text{t} q_\text{z})\right] \tag{E.18}$$

where $C = \frac{N}{L} R_\text{t} = N_\text{avg} R_\text{t}$ is defined as the autocorrelation coefficient: $C = 0$ correspond to a completely uncorrelated random distribution while $C = 1$ us a uniform fully correlated distribution.

E.3 Acoustic phonon: contributions over all q

In this Section, we sum up the mathematical details for the determination of the squared matrix element due to acoustic phonons. An equivalent procedure is followed in the determination of $|M_{j,j'}(k_\text{z}, k'_\text{z})|^2$ in Eq. (8.48) for optical phonons. First we recall the squared matrix element from Eq. (8.44):

$$|M_{j,j'}(k_\text{z}, k'_\text{z})|^2 = \frac{D^2_\text{APH}}{L^2}\frac{k_B T}{2\varrho_\text{s}}\frac{1}{v^2_\text{s}}\frac{1}{AL}\int_\mathcal{A} d\mathbf{s}\int_\mathcal{A} d\mathbf{s}'\int_0^L dz\int_0^L dz'\; f_{j,j',k_\text{z},k'_\text{z}}(\mathbf{s}) e^{-\imath(q_\text{x}x + q_\text{y}y)} f^*_{j,j',k_\text{z},k'_\text{z}}(\mathbf{s}') e^{\imath(q_\text{x}x' + q_\text{y}y')} e^{-\imath(k_\text{z} - k'_\text{z} - q_\text{z})(z'-z)} \tag{E.19}$$

We will focus in the term which is common to acoustic and optical phonon:

$$\frac{1}{AL}\int_{\mathcal{A}}d\mathbf{s}\int_{\mathcal{A}}d\mathbf{s}'dz\int_0^L dz'\ f_{j,j',k_z,k_z'}(\mathbf{s})e^{-\imath(q_x x+q_y y)} f^*_{j,j',k_z,k_z'}(\mathbf{s}')e^{\imath(q_x x'+q_y y')}e^{-\imath(k_z-k_z'-q_z)(z'-z)} \tag{E.20}$$

We can define the Fourier transform of $f_{j,j',k_z,k_z'}(x,y)$ as:

$$f_{j,j',k_z,k_z'}(q_{\mathbf{s}}) = \int_{\mathcal{A}}d\mathbf{s} f_{j,j',k_z,k_z'}(\mathbf{s})e^{-\imath q_{\mathbf{s}}\mathbf{s}} \tag{E.21}$$

where $q_{\mathbf{s}}\mathbf{s} = q_x x + q_y y$ Then:

$$\frac{1}{AL}\int_0^L dz\int_0^L dz'\ f_{j,j',k_z,k_z'}(q_{\mathbf{s}})f^*_{j,j',k_z,k_z'}(q_{\mathbf{s}})e^{-\imath(k_z-k_z'-q_z)(z'-z)} \tag{E.22}$$

Now we sum over all possible states q_x, q_y and q_z to take into consideration all the $\mathbf{q}$ contributions. We convert the summation into integrals taking into consideration that:

$$\sum_{q_x,q_y,q_z} = \frac{AL}{8\pi^4} \tag{E.23}$$

to rewrite Eq. (E.20) as:

$$\frac{1}{8\pi^3}\int_0^L dz\int_0^L dz'\int dq_z\int dq_x\int dq_y\ f_{j,j',k_z,k_z'}(q_{\mathbf{s}})f^*_{j,j',k_z,k_z'}(q_{\mathbf{s}})e^{-\imath(k_z-k_z'-q_z)(z'-z)} \tag{E.24}$$

Using the Parserval theorem:

$$\frac{1}{4\pi^2}\int dq_x\int dq_y\ f_{j,j',k_z,k_z'}(q_{\mathbf{s}})f^*_{j,j',k_z,k_z'}(q_{\mathbf{s}}) = \int_{\mathcal{A}}d\mathbf{s}\ f_{j,j',k_z,k_z'}(\mathbf{s})f^*_{j,j',k_z,k_z'}(\mathbf{s}) \tag{E.25}$$

Eq. (E.24) can be written as:

$$\frac{1}{2\pi}\int_0^L dz\int_0^L dz'\int_{\mathcal{A}}dA\ f_{j,j',k_z,k_z'}(\mathbf{s})f^*_{j,j',k_z,k_z'}(\mathbf{s}) e^{-\imath(k_z-k_z'-q_z)(z'-z)} \tag{E.26}$$

where the axial and q_z integration can be done as in Appendix **??** resulting into:

$$L\int_{\mathcal{A}}dA\ f_{j,j',k_z,k_z'}(\mathbf{s})f^*_{j,j',k_z,k_z'}(\mathbf{s}) \tag{E.27}$$

Then substituting into Eq. (E.19)

$$|M_{j,j'}(k_{\mathrm{z}},k'_{\mathrm{z}})|^2=\frac{D^2_{\mathrm{APH}}}{L}\frac{k_BT}{2\varrho_{\mathrm{s}}}\frac{1}{v^2_{\mathrm{s}}}\int_{\mathcal{A}}dA\ f_{j,j',k_{\mathrm{z}},k'_{\mathrm{z}}}(\mathbf{s})f^*_{j,j',k_{\mathrm{z}},k'_{\mathrm{z}}}(\mathbf{s}) \tag{E.28}$$

where the matrix element does not depend on q_{z} and therefore it is isotropic.

E.4 Non polar phonons: q_{x} and q_{y} contributions

In this Section we deal with the integration of all q_{x} and q_{y} contributions to the matrix element of polar optical phonons. Thus, we recall here the inner integral in Eq. (8.54).

$$\int\int dq_{\mathrm{x}}dq_{\mathrm{y}}\frac{e^{\mp\imath q_{\mathrm{x}}(x-x')\mp\imath q_{\mathrm{y}}(y-y')}}{q^2_{\mathrm{x}}+q^2_{\mathrm{y}}+q^2_{\mathrm{z}}} \tag{E.29}$$

I can be simplified to:

$$\int_{-\infty}^{\infty}dq_{\mathrm{y}}\frac{\pi}{\sqrt{q^2_y+q^2_z}}e^{\pm\imath q_{\mathrm{y}}(y-y')}e^{-\sqrt{q^2_{\mathrm{y}}+q^2_{\mathrm{z}}}|x-x'|} \tag{E.30}$$

To simplify the notation of the integral we rename:

$$\begin{aligned}y&=q_{\mathrm{y}}\\ a&=|x-x'|\\ c&=q_{\mathrm{z}}\\ b&=(y-y')\end{aligned} \tag{E.31}$$

Then, the integral to be solved is,

$$\int_{-\infty}^{\infty}\frac{e^{\pm\imath by}e^{-a\sqrt{y^2+c^2}}}{\sqrt{y^2+c^2}}dy \tag{E.32}$$

For the sake of clearness we will consider first just the minus sign in the exponential. We will analyze the plus sign of the exponential later. Now we can rearrange the square

root terms as:

$$\int_{-\infty}^{\infty} \frac{e^{-\imath by} e^{-a\sqrt{y^2+c^2}}}{\sqrt{y^2+c^2}} dy = \int_{-\infty}^{\infty} \frac{e^{-\imath by} e^{-a|c|\sqrt{(y/c)^2+1}}}{|c|\sqrt{(y/c)^2+1}} dy \tag{E.33}$$

where $\sqrt{c^2} = |c|$. We can use the change of variable:

$$y/c = \sinh(\varphi) \longrightarrow dy = c\cosh(\varphi) d\varphi \tag{E.34}$$

which keeps the integral limits: $y \to \infty \Rightarrow \varphi \to \infty$; $y \to -\infty \Rightarrow \varphi \to -\infty$ Here we have supposed $c > 0$. If not the integral limits are inverted: $\int_{\infty}^{-\infty} = -\int_{-\infty}^{\infty}$. But the minus sign of this integral would be cancelled with the minus sign of c in dy. So we can write $dy = |c|\ \cosh(\varphi) d\varphi$ regardless of the sign of c and keep the integral limits between $-\infty$ and ∞ . Then,

$$\int_{-\infty}^{\infty} \frac{e^{-\imath by} e^{-a|c|\sqrt{(y/c)^2+1}}}{|c|\sqrt{(y/c)^2+1}} dy = \int_{-\infty}^{\infty} \frac{e^{-\imath bc\sinh(\varphi)} e^{-a|c|\sqrt{\sinh^2(\varphi)+1}}}{|c|\sqrt{\sinh^2(\varphi)+1}} |c|\cosh(\varphi) d\varphi \tag{E.35}$$

Using the relation $\cosh^2(x) - \mathrm{senh}^2(x) = 1$ we get:

$$\int_{-\infty}^{\infty} \frac{e^{-\imath b|c|\sinh(\varphi)} e^{-a|c|\cosh(\varphi)}}{|c|\cosh(\varphi)} |c|\cosh(\varphi) d\varphi = \int_{-\infty}^{\infty} e^{-\imath bc\sinh(\varphi) - a|c|\cosh(\varphi)} d\varphi \tag{E.36}$$

This integral can be identified with the integral representations of the Hankel functions,

$$\left(\frac{z+\xi}{z-\xi}\right)^{\frac{1}{2}v} H_v^{(1)}\left((z^2-\xi^2)^{\frac{1}{2}}\right) = \frac{1}{\imath\pi} e^{-\frac{1}{2}v\pi\imath} \int_{-\infty}^{\infty} e^{\imath z\cosh(t) + \imath\xi\sinh(t) - vt} dt \quad \text{if } \mathrm{Im}(z \pm \xi) > 0 \tag{E.37}$$

$$\left(\frac{z+\xi}{z-\xi}\right)^{\frac{1}{2}v} H_v^{(2)}\left((z^2-\xi^2)^{\frac{1}{2}}\right) = -\frac{1}{\imath\pi} e^{\frac{1}{2}v\pi\imath} \int_{-\infty}^{\infty} e^{-\imath z\cosh(t) - \imath\xi\sinh(t) - vt} dt \quad \text{if } \mathrm{Im}(z \pm \xi) < 0 \tag{E.38}$$

which for $v = 0$ are particularized as:

$$H_0^{(1)}\left((z^2-\xi^2)^{\frac{1}{2}}\right) = \frac{1}{i\pi}\int_{-\infty}^{\infty} e^{\imath z\cosh(t)+\imath\xi\sinh(t)}dt \quad \text{if } \mathrm{Im}(z\pm\xi) > 0 \tag{E.39}$$

$$H_0^{(2)}\left((z^2-\xi^2)^{\frac{1}{2}}\right) = -\frac{1}{i\pi}\int_{-\infty}^{\infty} e^{-\imath z\cosh(t)-\imath\xi\sinh(t)}dt \quad \text{if } \mathrm{Im}(z\pm\xi) < 0 \tag{E.40}$$

Then, we can rearrange (E.36) as:

$$\int_{-\infty}^{\infty} e^{-\imath bc\sinh(\varphi)-a|c|\cosh(\varphi)}d\varphi = \int_{-\infty}^{\infty} e^{\imath a|c|\imath\cosh(\varphi)-\imath bc\sinh(\varphi)}d\varphi \tag{E.41}$$

It is easy to identify $z = a|c|\imath$ and $\xi = -bc$. Then $Im(a|c|\imath \pm -bc)$=$a|c|$, and, as a is always positive –see the definition in equation (E.31)–, $a|c|$ is always positive, and we use the first Hankel function

$$\int_{-\infty}^{\infty} e^{\imath a|c|\imath\cosh(\varphi)-ibc\sinh(\varphi)}d\varphi = i\pi H_0^{(1)}[\left((a|c|\imath)^2-(-bc)^2\right)^{\frac{1}{2}}] = \mathrm{sign(c)}\imath\pi H_0^{(1)}[\imath\left(c^2(a^2+b^2)\right)^{\frac{1}{2}}] \tag{E.42}$$

The first Hankel function is related to the modified Bessel function of the second kind,

$$K_v(x) = \frac{\pi}{2}\,\imath^{v+1}H_v^{(1)}(ix) \tag{E.43}$$

Then, we can write:

$$\int_{-\infty}^{\infty} e^{\imath ac\imath\cosh(\varphi)-\imath bc\sinh(\varphi)}d\varphi = 2K_0[\left(c^2(a^2+b^2)\right)^{\frac{1}{2}}] \tag{E.44}$$

Regarding the plus sign in the first exponential in equation (E.30), the procedure to solve the integral keeps. The only modification would be $\xi = bc$ instead of $\xi = -bc$ in the first Hankel function, but as ξ is squared, the solution will be:

$$\int_{-\infty}^{\infty} \frac{e^{\imath by}e^{-a\sqrt{y^2+c^2}}}{\sqrt{y^2+c^2}}dy = 2K_0[\left(c^2(a^2+b^2)\right)^{\frac{1}{2}}] \tag{E.45}$$

which is the same. Therefore we have:

$$\int_{-\infty}^{\infty} dq_{\mathrm{y}} \frac{\pi}{\sqrt{q_{\mathrm{y}}^2 + q_z^2}} e^{\pm \imath q_{\mathrm{y}}(y-y')} e^{-\sqrt{q_{\mathrm{y}}^2+q_{\mathrm{z}}^2}|x-x'|} = 2\pi K_0 \left(|q_{\mathrm{z}}| \sqrt{(x-x')^2 + (y-y')^2} \right) \tag{E.46}$$

Appendix F

Materials parameters

In this Appendix we collect the material parameters employed in the different electrostatic and transport studies carried out in this work. Table F.1 sums up the material parameters of several III-V compound semiconductors [89, 135, 272].

		InAs	GaAs	$In_{0.53}Ga_{0.47}As$
$E_{g,\Gamma}$	(eV)	0.416	1.518	0.829
$E_{g,X}$	(eV)	1.477	2.003	1.597
$E_{g,L}$	(eV)	1.14	1.812	1.185
m_Γ	(m_0)	0.026	0.082	0.052
m_{lX}	(m_0)	7.079	1.705	4.553
m_{tX}	(m_0)	0.232	0.236	0.233
m_{lL}	(m_0)	1.707	1.610	1.661
m_{tL}	(m_0)	0.106	0.126	0.115
β_Γ	(eV/eV)	1.4	0.61	1
β_X	(eV/eV)	0.5	0.204	0.5
β_L	(eV/eV)	0.5	0.461	0.5
χ_s	(eV)	4.9	4.15	4.6
ϵ_s	(ϵ_0)	15.15	12.9	14.17
$\epsilon_{s,\infty}$	(ϵ_0)	12.75	10.92	11.8
ρ_s	(g/cm^3)	5.67	5.36	5.06
$\phi_{CNL,s}$	(eV)	4.81	5.11	4.86

Table F.1: Material parameters of several III-V compound semiconductors. After [89, 135, 272]

Scattering mechanism parameters for III-V materials are collected in Table F.2,[273, 274]. The values for $In_{0.53}Ga_{0.47}As$ are obtained from linear interpolation of those

referenced for InAs and GaAs.

		InAs	GaAs	$In_{0.53}Ga_{0.47}As$
		APH		
D_{APH}	(eV)	5.8	5	5.42
v_{s}	(cm/s)	4.28	5.24	4.25
		OPH		
$\hbar\omega_{\mathrm{OPH},\Gamma\leftrightarrow X}$	(meV)	19.23	23.45	21.21
$\hbar\omega_{\mathrm{OPH},\Gamma\leftrightarrow L}$	(meV)	17.45	22.69	19.91
$\hbar\omega_{\mathrm{OPH},X\leftrightarrow X}$	(meV)	19.26	24.31	21.63
$\hbar\omega_{\mathrm{OPH},L\leftrightarrow L}$	(meV)	19.23	24.97	21.93
$\hbar\omega_{\mathrm{OPH},X\leftrightarrow L}$	(meV)	17.45	21.85	19.52
$D_{\mathrm{OPH},\Gamma\leftrightarrow X}$	(10^8ev/cm)	6.35	5.48	5.94
$D_{\mathrm{OPH},\Gamma\leftrightarrow L}$	(10^8ev/cm)	5.59	5.25	5.43
$D_{\mathrm{OPH},X\leftrightarrow X}$	(10^8ev/cm)	3.36	2.99	3.18
$D_{\mathrm{OPH},L\leftrightarrow L}$	(10^8ev/cm)	6.35	5.94	6.15
$D_{\mathrm{OPH},X\leftrightarrow L}$	(10^8ev/cm)	5.59	5.01	5.31
		POP		
$\hbar\omega_{\mathrm{POP},\Gamma\leftrightarrow\Gamma}$	(meV)	30	36	32.8
$\hbar\omega_{\mathrm{POP},X\leftrightarrow X}$	(meV)	30	36	32.8
$\hbar\omega_{\mathrm{POP},L\leftrightarrow L}$	(meV)	30	36	32.8
		AD		
$\lvert V_a - V_b\rvert$	(eV)	-	-	0.528
a_0	(10^{-8}m)	-	-	5.86

Table F.2: Scattering mechanism parameters for III-V compound semiconductors. After [273, 274]

Table F.3 sums up the material parameters of Si [92].

$E_{\mathrm{g},\Delta}$	(eV)	1.11
$m_{lX,\Delta}$	(m_0)	0.91
$m_{tX,\Delta}$	(m_0)	0.19
β_Δ	(eV/eV)	0.5
χ_s	(eV)	4.05
ϵ_s	(ϵ_0)	11.9
ρ_s	$(\mathrm{g/cm^3})$	2.33
$\phi_{\mathrm{CNL,s}}$	(eV)	4.96

Table F.3: Material parameters of Si. After [92]

Table F.4 summarizes the scattering mechanism parameters for Si [222, 275]:

	APH	
D_APH	(eV)	12
v_s	(cm/s)	9
	OPH	
$\hbar\omega_{\mathrm{OPH,g1}}$	(meV)	140
$\hbar\omega_{\mathrm{OPH,f1}}$	(meV)	210
$\hbar\omega_{\mathrm{OPH,g2}}$	(meV)	210
$\hbar\omega_{\mathrm{OPH,f2}}$	(meV)	570
$\hbar\omega_{\mathrm{OPH,g3}}$	(meV)	750
$\hbar\omega_{\mathrm{OPH,f3}}$	(meV)	700
$D_{\mathrm{OPH,g1},\Delta\leftrightarrow\Delta}$	$(10^8\mathrm{ev/cm})$	0.5
$D_{\mathrm{OPH,f1},\Delta\leftrightarrow\Delta}$	$(10^8\mathrm{ev/cm})$	0.3
$D_{\mathrm{OPH,g2},\Delta\leftrightarrow\Delta}$	$(10^8\mathrm{ev/cm})$	1.1
$D_{\mathrm{OPH,f2},\Delta\leftrightarrow\Delta}$	$(10^8\mathrm{ev/cm})$	1.34
$D_{\mathrm{OPH,g3},\Delta\leftrightarrow\Delta}$	$(10^8\mathrm{ev/cm})$	11
$D_{\mathrm{OPH,f3},\Delta\leftrightarrow\Delta}$	$(10^8\mathrm{ev/cm})$	4

Table F.4: Scattering mechanism parameters for Si. After [222, 275]

where six optical transitions has been considered: three for a low ω which as shown in Fig. 8.1 correspond to TA, LA and TO-LO; and three for a high ω which correspond to TA, LA-TO and LO respectively. The first three, with lower energy, are considered intravalley, and noted as g, while the last three, (with higher energy), are assumed intervalley and noted as f.

The materials parameters of several insulators are collected in Table [126, 134].

		SiO_2	Al_2O_3	Ta_2O_5
E_g	(eV)	9	8.8	4.4
m_{ins}	(m_0)	0.5	0.2	0.2
χ_{ins}	(eV)	0.9	1	3.3
ϵ_{ins}	(ϵ_0)	3.9	9	9
$\epsilon_{ins,\infty}$	(ϵ_0)	2.25	3.12	4.84
S		0.86	0.69	0.4
$\phi_{CNL,ins}$	(eV)	5.4	3.8	4.4

Table F.5: Material parameters of several insulators. After [126, 134]

Part VI

References

List of publications

Referenced papers

- **E. G. Marin**, F. G. Ruiz, I. M. Tienda-Luna, A. Godoy, P. Sáchez-Moreno, and F. Gámiz. Analytic potential and charge model for III-V Surrounding GateMOSFETs. Journal of Applied Physics, 112:084512, Oct 2012

- **E.G. Marin**, F.J.G. Ruiz, I.M. Tienda-Luna, A. Godoy, and F. Gámiz. Analytical gate capacitance modeling of III-V nanowire transistors. IEEE Transactions on Electron Devices, 60(5):1590, May 2013.

- **E.G. Marin**, F.G. Ruiz, I.M. Tienda-Luna, A. Godoy, and F. Gámiz. Analytical model for the threshold voltage of III-V nanowire transistors including quantum effects. Solid-State Electronics, 92:28, Feb 2014.

Conference Contributions

- **E. G. Marin**, and F. G. Ruiz, and A. Godoy, and I. M. Tienda-Luna, and F. Gámiz. Effect of interfacial states on the technological variability of Trigate MOSFETs. *Silicon Nanoelectronics Workshop (SNW), 2012 IEEE*. 2012.

- **E. G. Marin**, and F. G. Ruiz, and I. M. Tienda-Luna, and A. Godoy, and F. Gámiz. Study of the Gate Capacitance of GaAs, InAs and InGaAs Nanowires *36th Workshop on Compound Semiconductor Devices and Integrated Circuits 2012.* 2012.

- I. M. Tienda-Luna, and F. G. Ruiz, and A. Godoy, and **E. G. Marin**. and F. Gámiz. Dependence of the Phonon-Limited Mobility in Arbitrarily Oriented Si-Nanowires. *15th International Workshop on Computational Electronics (IWCE*

2012). 2012.

- F. G. Ruiz, and **E. G. Marin**, and I. M. Tienda-Luna, and A. Godoy, and C.Martinez-Blanque, and F. Gámiz Ruiz. Influence of the back-gate bias on the electron mobility of trigate MOSFETs. *Simulation of Semiconductor Processes and Devices (SISPAD), 2013. International Conference on*. 2013.

- F. G. Ruiz, and **E. G. Marin**, and I. M. Tienda-Luna, and A. Godoy, and C.Martinez-Blanque, and F. Gámiz Ruiz. Back-Gate Biasing Influence on the Electron Mobility and the Threshold Voltage of Ultra Thin Box Multigate MOSFET. *Silicon Nanoelectronics Workshop (SNW), 2013 IEEE*. 2013.

Bibliography

[1] D. Kahng. Silicon-silicon dioxide field induced surface devices. In *Technical memorandum issued by Bell Labs*, Jan 1961.

[2] H. Iwai. Evolution of Si CMOS technologies to sub-10 nm generation. Electron Devices Colloquium IMEC, Leuven, Belgium, Jan 2012.

[3] J. Bardeen and W. H. Brattain. The transistor, a semi-conductor triode. *Physical Review*, 74:230, Jul 1948.

[4] M. Riordan, L. Hoddeson, and C. Herring. The invention of the transistor. *Reviews of Modern Physics*, 71(2):S336, 1999.

[5] R. H. Dennard, F. H. Gaensslen, V. L. Rideout, E. Bassous, and A. R. LeBlanc. Design of ion-implanted MOSFET's with very small physical dimensions. *IEEE Journal of Solid-State Circuits*, 9(5):256, 1974.

[6] H. Iwai. Roadmap for 22 nm and beyond. *Microelectronic Engineering*, 86:1520, Sep 2009.

[7] W. Haensch, E. J. Nowak, R. H. Dennard, P. M. Solomon, A. Bryant, O. H. Dokumaci, A. Kumar, X. Wang, J. B. Johnson, and M. V. Fischetti. Silicon CMOS devices beyond scaling. *IBM Journal of Research and Development*, 50 (4.5):339, July 2006.

[8] B. Hoeneisen and C.A. Mead. Fundamental limitations in microelectronics-I. MOS technology. *Solid-State Electronics*, 15:819, 1972.

[9] J. T. Wallmark. Fundamental physical limitations in integrated electronic circuits. In *Institute of Physics Conference Series*, page 133, 1975.

[10] Chenming Hu. Gate oxide scaling limits and projection. In *Electron Devices Meeting (IEDM), 1996 IEEE International*, page 319, Dec 1996.

[11] J. H. Stathis and D. J. DiMaria. Reliability projection for ultra-thin oxides at low voltage. In *Electron Devices Meeting (IEDM), 1998 IEEE International*, page 167, Dec 1998.

[12] H. Iwai. CMOS downsizing toward sub-10 nm. *Solid-State Electronics*, 48(4):497, 2004.

[13] H. Iwai. Future of Nano-CMOS technology. CINVESTAV, Mexico City, Mexico, Apr 2014.

[14] G. E. Moore. Cramming more components onto integrated circuits, 1965.

[15] *International Technology Roadmap for Semiconductors*. Available online: http://www.itrs.net, 2013.

[16] H. Iwai. Si nanowire FET technology. ECS Tutorial, Montreal, Canada, May 2011.

[17] Y.-M. Lin, K. A. Jenkins, A. Valdes-Garcia, J. P. Small, D. B. Farmer, and P. Avouris. Operation of graphene transistors at Gigahertz frequencies. *Nano Letters*, 9(1):422–426, 2009.

[18] Y. Yoon, K. Ganapathi, and S. Salahuddin. How good can monolayer MoS2 transistors be? *Nano Letters*, 11(9):3768, 2011.

[19] S. J. Tans, A. R. Verschueren, and C. Dekker. Room-temperature transistor based on a single carbon nanotube. *Nature*, 393:49, 1998.

[20] J. M. Tour. Molecular electronics. synthesis and testing of components. *Accounts of Chemical Research*, 33:791, 2000.

[21] M. Fuechsle, J. A. Miwa, S. Mahapatra, H. Ryu, S. Lee, O. Warschkow, L. C. Hollenberg, G. Klimeck, and M. Y. Simmons. A single-atom transistor. *Nature Nanotechnology*, 7(4):242, 2012.

[22] Y. Taur, D. A. Buchanan, W. Chen, D. J. Frank, K. E. Ismail, S.-H. Lo, G. A. Sai-Halasz, R. G. Viswanathan, H.-J. C. Wann, S. J. Wind, and H.-S. Wong. CMOS scaling into the nanometer regime. *Proceedings of the IEEE*, 85:486, Apr 1997.

[23] A. P. Chandrakasan and R. W. Brodersen. Minimizing power consumption in digital CMOS circuits. *Proceedings of the IEEE*, 83(4):498, 1995.

[24] D. J. Frank. Power-constrained CMOS scaling limits. *IBM Journal of Research and Development*, 46:235, 2002.

[25] M. Horowitz, E. Alon, D. Patil, S. Naffziger, R. Kumar, and K. Bernstein. Scaling, power, and the future of CMOS. In *Electron Devices Meeting (IEDM), 2005 IEEE International*, page 7, 2005.

[26] N.C.-C. Lu and J. M. Sung. Reverse short-channel effects on threshold voltage in submicrometer salicide devices. *IEEE Electron Device Letters*, 10:446, 1989.

[27] A. Chaudhry and M. J. Kumar. Controlling short-channel effects in deep-submicron SOI MOSFETs for improved reliability: a review. *IEEE Transactions on Device and Materials Reliability*, 4:99, 2004.

[28] A. Asenov. Simulation of statistical variability in nano MOSFETs. In *VLSI Technology, 2007. Digest of Technical Papers. 2007 Symposium on*, page 86, 2007.

[29] A. Cathignol, B. Cheng, D. Chanemougame, A. R. Brown, K. Rochereau, G. Ghibaudo, and A. Asenov. Quantitative evaluation of statistical variability sources in a 45-nm technological node LP N-MOSFET. *IEEE Electron Device Letters*, 29(6):609, 2008.

[30] X. Wang, A. R. Brown, B. Cheng, and A. Asenov. Statistical variability and reliability in nanoscale FinFETs. In *Electron Devices Meeting (IEDM), 2011 IEEE International*, page 5, 2011.

[31] M. Ieong, B. Doris, J. Kedzierski, K. Rim, and M. Yang. Silicon device scaling to the sub-10-nm regime. *Science*, 306(5704):2057, 2004.

[32] J. P. Colinge, J. C. Alderman, W. Xiong, and C. R. Cleavelin. Quantum-mechanical effects in trigate SOI MOSFETs. *IEEE Transactions on Electron Devices*, 53(5):1131, 2006.

[33] C.-W. Lee, A. N. Nazarov, I. Ferain, N. D. Akhavan, R. Yan, P. Razavi, R. Yu, R. T. Doria, and J.-P. Colinge. Low subthreshold slope in junctionless multigate transistors. *Applied Physics Letters*, 96(10):102106, 2010.

[34] B. Doris, M. Ieong, T. Kanarsky, Z. Ying, R. A. Roy, O. Dokumaci, et al. Extreme scaling with ultra-thin Si channel MOSFETs. In *Electron Devices Meeting (IEDM), 2002 IEEE International*, page 267, Dec 2002.

[35] K. Uchida, H. Watanabe, A. Kinoshita, J. Koga, T. Numata, and S. Takagi. Experimental study on carrier transport mechanism in ultrathin-body SOI nand p-MOSFETs with SOI thickness less than 5 nm. In *Electron Devices Meeting, 2002. IEDM'02. International*, page 47, 2002.

[36] T. Skotnicki, J. A. Hutchby, T.-J. King, H.-S.P. Wong, and F. Boeuf. The end of CMOS scaling: toward the introduction of new materials and structural changes to improve MOSFET performance. *IEEE Circuits and Devices Magazine*, 21(1): 16, 2005.

[37] B. Yu, H. Wang, C. Riccobene, Q. Xiang, and M.-R. Lin. Limits of gate-oxide scaling in nano-transistors. In *VLSI Technology, 2000. Digest of Technical Papers. 2000 Symposium on*, page 90, 2000.

[38] T. Ghani, K. Mistry, P. Packan, S. Thompson, M. Stettler, S. Tyagi, and M. Bohr. Scaling challenges and device design requirements for high performance sub-50 nm gate length planar CMOS transistors. In *VLSI Technology, 2000. Digest of Technical Papers. 2000 Symposium on*, page 174, 2000.

[39] B. Wuand and A. Kumar. Extreme ultraviolet lithography: a review. *Journal of Vacuum Science & Technology B*, 25(6):1743, 2007.

[40] A. Asenov, S. Roy, R. A. Brown, G. Roy, C. Alexander, C. Riddet, et al. Advanced simulation of statistical variability and reliability in nano CMOS transistors. In *Electron Devices Meeting (IEDM), 2008 IEEE International*. IEEE, 2008.

[41] A. Asenov. Simulation of statistical variability in nanometer scale CMOS devices. In *SOI-3D-Subthreshold Microelectronics Technology Unified Conference (S3S), 2013 IEEE*, Oct 2013.

[42] A. V.-Y. Thean, Z.-H. Shi, L. Mathew, t. Stephens, H. Desjardin, et al. Performance and variability comparisons between multi-gate FETs and planar SOI transistors. In *Electron Devices Meeting (IEDM), 2006 IEEE International*, 2006.

[43] A. Asenov, G. Slavcheva, A. R. Brown, J. H. Davies, and S. Saini. Increase in the random dopant induced threshold fluctuations and lowering in sub-100

nm MOSFETs due to quantum effects: a 3-D density-gradient simulation study. *IEEE Transactions on Electron Devices*, 48(4):722, 2001.

[44] H.-S. P. Wong. Beyond the conventional transistor. *IBM Journal of Research and Development*, 46:133, Mar 2002.

[45] S. Thompson, N. Anand, M. Armstrong, C. Auth, B. Arcot, M. Alavi, et al. A 90 nm logic technology featuring 50 nm strained silicon channel transistors, 7 layers of Cu interconnects, low k ILD, and 1 /spl mu/m/sup 2/ SRAM cell. In *Electron Devices Meeting (IEDM), 2002 IEEE International*, Dec 2002.

[46] J. L. Hoyt, H. M. Nayfeh, S. Eguchi, I. Aberg, G. Xia, T. Drake, E. A. Fitzgerald, and D. A. Antoniadis. Strained silicon MOSFET technology. In *Electron Devices Meeting (IEDM), 2002 IEEE International*, page 23, 2002.

[47] D. A. Antoniadis, I. Aberg, C. Ni Chleirigh, O. M. Nayfeh, A. Khakifirooz, and J. L. Hoyt. Continuous MOSFET performance increase with device scaling: The role of strain and channel material innovations. *IBM Journal of Research and Development*, 50:363, 2006.

[48] E. Ungersbock. *Advanced Modeling of Strained CMOS Technology*. PhD thesis, Vienna University of Technology, Vienna, Austria, 2007.

[49] M. M. Frank. High-k/metal gate innovations enabling continued CMOS scaling. In *Proceedings of the ESSCIRC 2011*, page 50, 2011.

[50] G. C. F. Yeap, S. Krishnan, and M.-R. Lin. Fringing-induced barrier lowering (FIBL) in sub-100 nm MOSFETs with high-k gate dielectrics. *Electronics Letters*, 34:1150, 1998.

[51] K. Mistry, C. Allen, C. Auth, B. Beattie, D. Bergstrom, M. Bost, M. Brazier, et al. A 45nm logic technology with high-k+metal gate transistors, strained silicon, 9 Cu interconnect layers, 193nm dry patterning, and 100% Pb-free packaging. In *Electron Devices Meeting (IEDM), 2007 IEEE International*, page 247, Dec 2007.

[52] P. Packan, S. Akbar, M. Armstrong, D. Bergstrom, M. Brazier, H. Deshpande, et al. High performance 32nm logic technology featuring 2nd generation high-k + metal gate transistors. In *Electron Devices Meeting (IEDM), 2007 IEEE International*, Dec 2009.

[53] T. Koyanagi, K. Tachi, K. Okamoto, K. Kakushima, P. Ahmet, K. Tsutsui, N. Sugii, T. Hattori, and H. Iwai. Electrical characterization of La2O3-gated metal oxide semiconductor field effect transistor with Mg incorporation. *Japanese Journal of Applied Physics*, 48:05DC02, 2009.

[54] S. Cristoloveanu, D. Munteanu, and M. S. T. Liu. A review of the pseudo-MOS transistor in SOI wafers: operation, parameter extraction, and applications. *IEEE Transactions on Electron Devices*, 47(5):1018, 2000.

[55] G. K. Celler and S. Cristoloveanu. Frontiers of silicon-on-insulator. *Journal of Applied Physics*, 93:4955, 2003.

[56] G. G. Shahidi. SOI technology for the GHz era. *IBM journal of Research and Development*, 46:121, 2002.

[57] K. Oshima, S. Cristoloveanu, B. Guillaumot, H. Iwai, and S. Deleonibus. Advanced SOI MOSFETs with buried alumina and ground plane: self-heating and short-channel effects. *Solid-State Electronics*, 48(6):907, 2004.

[58] E. Pop, R. Dutton, and K. Goodson. Thermal analysis of ultra-thin body device scaling SOI and FinFet devices. In *Electron Devices Meeting (IEDM), 2005 IEEE International*, page 36, 2003.

[59] Soitec: revolutionary semiconductor materials for energy and electronics. Online. URL `http://www.soitec.com/en/index.php`. Accessed: 2014-07-05.

[60] M. Bohr. The evolution of scaling from the homogeneous era to the heterogeneous era. In *Electron Devices Meeting (IEDM), 2011 IEEE International*, Dec 2011.

[61] J.A. del Álamo. Nanometre-scale electronics with III-V compound semiconductors. *Nature*, 479:317, Nov 2011.

[62] S. Takagi and A. Toriumi. Quantitative understanding of inversion-layer capacitance in Si MOSFETs. *IEEE Transactions on Electron Devices*, 42:2125, 1995.

[63] T. Irisawa, T. Numata, K. Usuda, N. Sugiyama, and S.-I. Takagi. Device design and electron transport properties of uniaxially strained-SOI tri-gate n-MOSFETs. *IEEE Transactions on Electronic Devices*, 55(2):649, 2008.

[64] M. S. Lundstrom. On the mobility versus drain current relation for a nanoscale MOSFET. *IEEE Electron Device Letters*, 22:293, 2001.

[65] M. Lundstrom and Z. Ren. Essential physics of carrier transport in nanoscale MOSFETs. *IEEE Transactions on Electron Devices*, 49:133, 2002.

[66] M. V. Fischetti, L. Wang, B. Yu, C. Sachs, P.M. Asbeck, Y. Taur, and M. Rodwell. Simulation of electron transport in high-mobility MOSFETs: Density of states bottleneck and source starvation. In *Electron Devices Meeting (IEDM), 2007 IEEE International*, page 109, Dec 2007.

[67] K. Tachi, T. Ernst, C. Dupré, A. Hubert, S. Bécu, H. Iwai, S. Cristoloveanu, and O. Faynot. Transport optimization with width dependence of 3D-stacked GAA silicon nanowire FET with high-κ/Metal gate stack, 2009.

[68] S. Bangsaruntip, G.M. Cohen, A. Majumdar, Y. Zhang, S.U. Engelmann, N.C.M. Fuller, et al. High performance and highly uniform gate-all-around silicon nanowire MOSFETs with wire size dependent scaling. In *Electron Devices Meeting (IEDM), 2009 IEEE International*, 2009.

[69] D. Hisamoto, T. Kaga, Y. Kawamoto, and E. Takeda. A fully depleted lean-channel transistor (DELTA)-a novel vertical ultra thin SOI MOSFET. In *Electron Devices Meeting (IEDM), 1989 IEEE International*, page 833, Dec 1989.

[70] C. C. Lo, A. Persaud, S. Dhuey, D. Olynick, F. Borondics, M. C. Martin, et al. Device fabrication and transport measurements of FinFETs built with 28Si SOI wafers toward donor qubits in silicon. *Semiconductor Science and Technology*, 24:105022, 2009.

[71] X. Zhao, J. Lin, C. Heidelberger, E. A. Fitzgerald, and J. A. del Alamo. Vertical nanowire InGaAs MOSFETs fabricated by a top-down approach. In *Electron Devices Meeting (IEDM), 2013 IEEE International*, Dec 2013.

[72] D. Sacchetto, M. H. Ben-Jamaa, G. De Micheli, and Y. Leblebici. Fabrication and characterization of vertically stacked gate-all-around Si nanowire FET arrays. In *Solid State Device Research Conference, 2009. ESSDERC'09. Proceedings of the European*, page 245, 2009.

[73] S. Bangsaruntip, A. Majumdar, G. M. Cohen, S. U. Engelmann, Y. Zhang, M. Guillorn, et al. Gate-all-around silicon nanowire 25-stage CMOS ring oscillators with diameter down to 3 nm. In *VLSI Technology, 2010. Digest of Technical Papers. 2010 Symposium on*, page 21. IEEE, 2010.

[74] TSMC 2013 Symposium: Progress in 20nm, 16nm FinFET, and 3D-IC Technologies. Online. URL http://www.cadence.com/Community/blogs/ii/archive/2013/04/14/tsmc-2013-symposium-progress-in-20nm-16nm-finfet-and-3d-ic-technologies.aspx. Accessed: 2014-07-04.

[75] N. Collaert, A. Dixit, M. Goodwin, K. G. Anil, R. Rooyackers, B. Degroote, et al. A functional 41-stage ring oscillator using scaled FinFET devices with 25-nm gate lengths and 10-nm fin widths applicable for the 45-nm CMOS node. *Electron Device Letters, IEEE*, 25(8):568, 2004.

[76] M. J. H. Van Dal, N. Collaert, G. Doornbos, G. Vellianitis, G. Curatola, B. J. Pawlak, et al. Highly manufacturable FinFETs with sub-10nm fin width and high aspect ratio fabricated with immersion lithography. In *VLSI Technology, 2007. Digest of Technical Papers. 2007 Symposium on*, page 110, 2007.

[77] B. Doyle, B. Boyanov, S. Datta, M. Doczy, S. Hareland, B. Jin, J. Kavalieros, T. Linton, R. Rios, and R. Chau. Tri-gate fully-depleted CMOS transistors: Fabrication, design and layout. In *VLSI Technology, 2003. Digest of Technical Papers. 2003 Symposium on*, page 133, 2003.

[78] B. Lu, E. Matioli, and T. Palacios. Tri-gate normally-off GaN power MISFET. *Electron Device Letters, IEEE*, 33(3):360, 2012.

[79] V. Schmidt, H. Riel, S. Senz, S. Karg, W. Riess, and U. Gösele. Realization of a silicon nanowire vertical surround-gate field-effect transistor. *Small*, 2:85, 2006.

[80] S. D. Suk, K. H. Yeo, K. H. Cho, M. Li, Y. Y. Yeoh, S.-Y. Lee, et al. High-performance twin silicon nanowire MOSFET (TSNWFET) on bulk Si wafer. *IEEE Transactions on Nanotechnology*, 7(2):181, 2008.

[81] F.-L. Yang, H.-Y. Chen, F.-C. Chen, C.-C. Huang, C.-Y. Chang, H.-K. Chiu, et al. 25 nm CMOS Omega FETs. In *Electron Devices Meeting (IEDM), 2002 IEEE International*, page 255, 2002.

[82] J.-T. Park, J. P. Colinge, and C. H. Diaz. Pi-gate SOI MOSFET. *IEEE Electron Device Letters*, 22:405, 2001.

[83] S. Cristoloveanu, T. Ernst, D. Munteanu, and T. Ouisse. Ultimate MOSFETs on SOI: Ultra thin, single gate, double gate, or ground plane. *International journal of high speed electronics and systems*, 10(01):217, 2000.

[84] T. Ernst, S. Cristoloveanu, G. Ghibaudo, T. Ouisse, S. Horiguchi, Y. Ono, Y. Takahashi, and K. Murase. Ultimately thin double-gate SOI MOSFETs. *IEEE Transactions on Electron Devices*, 50(3):830, 2003.

[85] J. P. Colinge. Multiple-gate SOI MOSFETs. *Solid-State Electronics*, 48:897, Jun 2004.

[86] S. Datta. *Quantum phenomena*. Addison-Wesley Longman, Incorporated, 1989. ISBN 9780201079562.

[87] C. Hamaguchi. *Basic Semiconductor Physics*. Springer, 2001. ISBN 9783540416395.

[88] D. Esseni, P. Palestri, and L. Selmi. *Nanoscale MOS Transistors: Semi-classical Transport And Applications*. Cambridge University Press, New York. USA, 2011. ISBN 9780521516846.

[89] J. Kim and M.V. Fischetti. Electronic band structure calculations for biaxially strained Si, Ge, and III-V semiconductors. *Journal of Applied Physics*, 108: 013710, Jul 2010.

[90] I. Vurgaftman, J. R. Meyeer, and L. R. Ram-Mohan. Band parameters for III-V compound semiconductors and their alloys. *Journal of Applied Physics*, 89(11): 5815, 2001.

[91] J. R. Chelikowsky and M. L. Cohen. Nonlocal pseudopotential calculations for the electronic structure of eleven diamond and zinc-blende semiconductors. *Physical Review B*, 14:556, Jul 1976.

[92] *Landolt-Börnstein. Numerical Data and Functional Relationships in Science and Technology.Semiconductor Quantum Structures*. Springer, Berlin. Germany, 1st edition, 2001. ISBN 3540617418.

[93] V. Ariel Altschul, A. Fraenkel, and E. Finkman. Effects of band nonparabolicity on two-dimensional electron gas. *Journal of Applied Physics*, 71(9):4382, Jan 1992.

[94] A. Godoy, Z. Yang, U. Ravaioli, and F. Gámiz. Effects of nonparabolic bands in quantum wires. *Journal of Applied Physics*, 98, 2005.

[95] S. Jin, M. V. Fischetti, and T. Tang. Modeling of electron mobility in gated silicon nanowires at room temperature: Surface roughness scattering, dielectric screening, and band nonparabolicity. *Journal of Applied Physics*, 102:083715, Oct 2006.

[96] S. Mudanai, A. Roy, R. Kotlyar, T. Rakshit, and M. Stettler. Capacitance compact model for ultrathin low-electron-effective-mass materials. *IEEE Transactions on Electron Devices*, 58:4202, Dec 2011.

[97] Y. Yuan, B. Yu, J. Song, and Y Taur. An analytic model for threshold voltage shift due to quantum confinement in surrounding gate MOSFETs with anisotropic effective mass. *Solid State Electronics*, 53:140, 2009.

[98] E. G. Marin, F. G. Ruiz, I. M. Tienda-Luna, A. Godoy, P. Sánchez-Moreno, and F. Gámiz. Analytic potential and charge model for III-V Surrounding Gate MOSFETs. *Journal of Applied Physics*, 112:084512, Oct 2012.

[99] M. Radosavljevic, G. Dewey, J. M. Fastenau, J. Kavalieros, R. Kotlyar, B. Chu-Kung, et al. Non-planar, multi-gate InGaAs quantum well field effect transistors with high-k gate dielectric and ultra-scaled gate-to-drain/gate-to-source separation for low power logic applications. In *Electron Devices Meeting (IEDM), 2010 IEEE International*, page 126, Dec 2010.

[100] A. C. Ford, S. B. Kumar, R. Kapadia, J. Guo, and A. Javey. Observation of degenerate one-dimensional sub-bands in cylindrical InAs nanowires. *Nano Letters*, 12:1340, Jan 2012.

[101] M. Radosavljevic, G. Dewey, D. Basu, J. Boardman, B. Chu-Kung, J. M. Fastenau, et al. Electrostatics improvement in 3-D tri-gate over ultra-thin body planar InGaAs quantum well field effect transistors with high-κ gate dielectric and scaled gate-to-drain/gate-to-source separation. In *Electron Devices Meeting (IEDM), 2011 IEEE International*, 2011.

[102] S. Sato, W. Li, K. Kakushima, K. Ohmori, K. Natori, K. Yamada, and H. Iwai. Extraction of additional interfacial states of silicon nanowire field-effect transistors. *Applied Physics Letters*, 98:233506, Jun 2011.

[103] M. Cassé, K. Tachi, S. Thiele, and T. Ernst. Spectroscopic charge pumping in Si nanowire transistors with a high-κ metal gate. *Applied Physics Letters*, 96: 123506, Mar 2010.

[104] E. Dornel, T. Ernst, J. C. Barbe, J. M. Hartmann, V. Delaye, F. Aussenac, C. Vizioz, S. Borel, V. Maffini-Alvaro, C. Isheden, and J. Foucher. Hydrogen annealing of arrays of planar and vertically stacked Si nanowires. *Applied Physics Letters*, 91(23):233502, 2007.

[105] K. Ohmori, T. Matsuki, D. Ishikawa, T. Morooka, T. Aminaka, Y. Sugita, et al. Impact of additional factors in threshold voltage variability of metal/high-k gate stacks and its reduction by controlling crystalline structure and grain size in the metal gates. In *Electron Devices Meeting (IEDM), 2008 IEEE International*, 2008.

[106] S.E. Laux and M.V. Fischetti. Monte-carlo simulation of submicrometer Si n-MOSFETs at 77 and 300 k. *Electron Device Letters, IEEE*, 9:467, Sept 1988.

[107] T. Kerkhoven, A. T. Galick, U. Ravaioli, J. H. Arends, and Y. Saad. Efficient numerical simulation of electron states in quantum wires. *Journal of Applied Physics*, 68:3461, Jun 1990.

[108] Sentaurus Device. Online.

[109] Atlas Device Simulation Framework. Online.

[110] VSP - Global TCAD Solutions. Online. URL `http://www.globaltcad.com/en/products/vsp.html`. Accessed: 2014-24-03.

[111] Gold Standard Simulations. Online. URL `http://www.goldstandardsimulations.com`. Accessed: 2014-24-03.

[112] Athena Process Simulation Framework. Online. URL `http://www.silvaco.com/products/tcad/process_simulation/athena/athena.html`. Accessed: 2014-03-14.

[113] B. Laikhtman. Boundary conditions for envelope functions in heterostructures. *Phyical Review B*, 46:4769, Aug 1992.

[114] A. V. Rodina, A. Yu. Alekseev, Al. L. Efros, M. Rosen, and B. K. Meyer. General boundary conditions for the envelope function in the multiband kp model. *Phyical Review B*, 65:125302, Feb 2002.

[115] P. Harrison. *Quantum Wells, Wires and Dots*. John Willey & Sons, Chichester. UK, 2000.

[116] MATLAB. The Language of Technical Computing. Online. URL `http://www.mathworks.com/products/matlab/`. Accessed: 2014-02-28.

[117] Partial Differential Equation Toolbox™. Online. URL `http://www.mathworks.es/products/pde/`. Accessed: 2014-02-28.

[118] G. Smith. *Numerical Solution of Partial Differential Equations: Finite Diference Methods*. Oxford University Press, New York. USA, 3rd edition, 1985. ISBN 0198596502.

[119] O. Zienkiewicz and R. Taylor. *The Finite Element Method. Volume 1: The Basis*. Butterworth and Heinemann, Oxford. UK, 5th edition, 2000. ISBN 0750650494.

[120] J. Peiró and S. Sherwin. Finite Difference, Finite Element and Finite. Methods for partial differential equations. In Y. Sip, editor, *Handbook of Materials Modeling. Volume I: Methods and Models*. Springer, Dordrecht. The Netherlands, 1st edition, 2005. ISBN 1402032870.

[121] The MathWorks, Inc. *Partial Differential Equation Toolbox™ User's Guide*. The MathWorks, Inc.

[122] W. Schottky. Halbleitertheorie der sperrschicht. *Naturwissenschaften*, 26:843, 1938.

[123] J. Bardeen. Surface states and rectification at metal-semiconductor contact. *Physical Review*, 71:717, 1947.

[124] V. Heine. Theory of surface states. *Physical Review*, 138:A1689, 1965.

[125] J. Tersoff. Schottky barrier height and the continuum of gap states. *Physical Review Letters*, 52:465, 1984.

[126] J. Robertson. Band offsets of wide-band-gap oxides and implications for future electronic devices. *Journal of Vacuum Science Technology*, 18:1785, 2000.

[127] A. M. Cowley and S.M. Sze. Surface states and barrier height of metal semiconductor system. *Journal of Applied Physics*, 36:3212, 1965.

[128] J. Robertson. Model of interface states at III-V oxide interfaces. *Journal of Applied Physics*, 94:152104, 2009.

[129] L. Lin, H. Li, and J. Robertson. Control of schottky barrier heights by inserting thin dielectric layers. *Applied Physics Letters*, 101:172907, 2012.

[130] J. Tersoff. Theory of semiconductors heterojunctions: The role of quantum dipoles. *Physical Review B*, 30:4874, 1984.

[131] J. Tersoff. Schottky barriers and semiconductors band structures. *Physical Review B*, 32:6968, 1985.

[132] J. Tersoff and W. Harrison. Transition-metal impurities in semiconductors: Their connection with band lineups and schottky barriers. *Physical Review Letters*, 58: 2367, 1987.

[133] W. Mönch. Role of virtual gap states and defects in metal-semiconductor contacts. *Journal of Applied Physics*, 58:1260, 1987.

[134] J. Robertson. Band offsets of high dielectric constant gate oxides on silicon. *Journal of Non-Crystalline Solids*, 303:94, 2002.

[135] J. Robertson and B. Falabretti. Band offsets of high-κ gate oxides on III-V semiconductors. *Journal of Applied Physics*, 100:014111, Jul 2006.

[136] J. Robertson and L. Lin. Fermi level pinning in Si, Ge and GaAs systems – migs or defects? In *Electron Devices Meeting (IEDM), 2009 IEEE International*, page 119, Jun 2009.

[137] V. Pott, K.E. Moselund, D. Bouvet, L. De Michielis, and A.M. Ionescu. Fabrication and characterization of gate-all-around silicon nanowires on bulk silicon. *Nanotechnology, IEEE Transactions on*, 7(6):733, Nov 2008.

[138] TA. Rahman, M. Lundstrom, and A. Ghosh. Generalize effective mass approach for n-type semiconductor field-effect transistors on arbitrarily oriented wafers. *Journal of Applied Physics*, 97:053702–1–12, 2005.

[139] M. Bescond, N. Cavassilas, and M. Lannoo. Effective-mass approach for n-type semiconductor nanowire MOSFETs arbitrarily oriented. *Nanotechnology*, 18:255201, 2007.

[140] S. M. Sze. *Physics of semiconductor devices*. New York. USA, 2nd edition, 1981. ISBN 0471056618.

[141] G. Brammertz, H. C. Lin, K. Martens, D. Mercier, S. Sioncke, A. Delabie, W.-E. Wang, M. Caymax, M. Meuris, and M. Heyns. Capacitance-voltage characterization of GaAs-Al_2O_3 interfaces. *Applied Physics Letters*, 93:183504, Nov 2008.

[142] Y.C. Chang, C. Merckling, J. Penaud, C. Y. Lu, G. Brammertz, W. E Wang, M. Hong, J. Kwo, J. Dekoster, M. Caymax, M. Meuris, and M. Heyns. Great reduction of interfacial traps in Al_2O_3/GaAs (100) starting with Ga-rich surface and through systematic thermal annealing. In *Device Research Conference (DRC), 2010*, pages 51–52, Jun 2010.

[143] X. Sun, S. Cui, A. Alian, G. Brammertz, C. Merckling, D. Lin, and T-P Ma. AC transconductance dispersion (ACGD): A method to profile oxide traps in MOSFETs without body contact. *Electron Device Letters, IEEE*, 33:438, Mar 2012.

[144] X. Sun, O. I. Saadat, K. S. Chang-Liao, T. Palacios, S. Cui, and T. P. Ma. Study of gate oxide traps in HfO2/AlGaN/GaN metal-oxide-semiconductor high-electron-mobility transistors by use of ac transconductance method. *Applied Physics Letters*, 102:103504, 2013.

[145] G. Brammertz, H. C. Lin, M. Caymax, M. Meuris, M. Heyns, and M. Passlack. On the interface state density at $In_{0.53}Ga_{0.47}As$/oxide interfaces. *Applied Physics Letters*, 95(20):202109, Nov 2009.

[146] T. Kerkhoven, M. W. Raschke, and U. Ravaioli. Self-consistent simulation of quantum wires in periodic heterojunction structures. *Journal of Applied Physics*, 74:1119, Jul 1993.

[147] A. Trellakis, A.T. Galick, A. Pacelli, and U. Ravaioli. Iteration scheme for the solution of the two-dimensional schrödinger-poisson equations in quantum structures. *Journal of Applied Physics*, 81(12):7880, Mar 1997.

[148] A. Trellakis and U. Ravaioli. Computational issues in the simulation of semiconductor quantum wires. *Computer Methods in Applied Mechanics and Engineering*, 181:437–449, 2000.

[149] R.B. Dingle. The fermi-dirac integrals $\mathcal{F}_p(\eta) = (p!)^{-1} \int_0^\infty \varepsilon^p (e^{\varepsilon-\eta}+1)^{-1} d\varepsilon$. *Applied Scientific Research, Section B*, 6:225, 1957.

[150] J.S. Blakemore. Approximations for fermi-dirac integrals, especially the function $F_{-1/2}(\eta)$ used to describe electron density in a semiconductor. *Solid-State Electronics*, 25:1067 – 1076, 1982.

[151] J. Kavalieros, B. Doyle, S. Datta, G. Dewey, M. Doczy, B. Jin, D. Lionberger, M. Metz, W. Rachmady, M. Radosavljevic, U. Shah, N. Zelick, and R. Chau. Tri-gate transistor architecture with high-κ gate dielectrics,metal gates and strain engineering. In *VLSI Technology, 2006. Digest of Technical Papers. 2006 Symposium on*, page 50, Jun .

[152] C. Martinez-Blanque, F.G. Ruiz, L. Donneti, I.M. Tienda Luna, A. Godoy, and F. Gámiz. Two-band $k{\cdot}p$ solver for arbitrarily oriented Si-nanowires. In *Workshop on Silicon on Insulator Technology, Devices and Circuits, EUROSOI 2012,*, Sep 2012.

[153] J. Wang, A. Rahman, A. Ghosh, G. Klimeck, and M. Lundstrom. On the validity of the parabolic effective-mass approximation for the I-V calculation of silicon nanowire transistors. *IEEE Transactions on Electron Devices*, 52:1589, Jul 2005.

[154] K. Jansson, E. Lind, and L.-E. Wernersson. Intrinsic performance of InAs nanowire capacitors. *IEEE Transactions on Electron Devices*, 61(2):452, Feb 2014.

[155] *Fundamentals of III-V Semiconductor MOSFETs*. Springer, New York. USA, 3rd edition, 2010. ISBN 144191546X.

[156] E.G. Marin, F.G. Ruiz, I.M. Tienda-Luna, A. Godoy, and F. Gámiz. Analytical model for the threshold voltage of III-V nanowire transistors including quantum effects. *Solid-State Electronics*, 92:28, Feb 2014.

[157] Z. Yuan, A. Nainani, A. Kumar, X. Guan, B. R. Bennett, J. B. Boos, M. G. Ancona, and K. C. Saraswat. InGaSb: Single channel solution for realizing III-V

CMOS. In *VLSI Technology, 2012. Digest of Technical Papers. 2012 Symposium on*, page 185, Jun 2012.

[158] T. P. O'Regan and P. K. Hurley. Calculation of the capacitance-voltage characteristic of GaAs, $In_{0.53}Ga_{0.47}As$ and InAs metal-oxide-semiconductor structures. *Applied Physic Letters*, 99:163502, 2011.

[159] Y. Lee, K. Kakushima, K. Natori, and H. Iwai. Gate capacitance modeling and diameter-dependent performance of nanowire MOSFETs. *IEEE Transactions on Electron Devices*, 59:1037, Apr 2012.

[160] L. Ge, F. Gámiz, and G.O. Workman. On the gate capacitance limits of nanoscale DG and FD SOI MOSFETs. *IEEE Transactions on Electron Devices*, 53:753, Mar 2006.

[161] T. Nagumo and T. Hiramoto. Design guideline of Multi-Gate MOSFETs with substrate-bias control. *IEEE Transactions on Electron Devices*, 53(12):3025, 2006.

[162] T. Ohtou, T. Saraya, and T. Hiramoto. Variable-body-factor SOI MOSFET with ultrathin buried oxide for adaptative threshold voltage and leakage control. *IEEE Transactions on Electron Devices*, 55:40, 2008.

[163] C. Tanaka K. Uchida M. Saitoh, K. Ota and T. Numata. 10nm-diameter tri-gate silicon nanowire MOSFETs with enhanced high-field transport and v_{th} tunability through thin BOX. In *VLSI Technology, 2012. Digest of Technical Papers. 2012 Symposium on*, page 11, Jun 2012.

[164] K. Ota, M. Saitoh, C. Tanaka, and T. Numata. Threshold voltage control by substrate bias in 10-nm-diameter tri-gate nanowire MOSFET on ultrathin BOX. *IEEE Electron Device Letters*, 34:187, 2013.

[165] F. G. Ruiz, E. G. Marin, I. M. Tienda-Luna, A. Godoy, C.Martinez-Blanque, and F. Gámiz Ruiz. Back-gate biasing influence on the electron mobility and the threshold voltage of ultra thin box Multigate MOSFET. In *Silicon Nanoelectronics Workshop (SNW), 2013 IEEE*, 2012.

[166] F. G. Ruiz, E. G. Marin, I. M. Tienda-Luna, A. Godoy, C.Martinez-Blanque, and F. Gámiz Ruiz. Influence of the back-gate bias on the electron mobility of trigate

mosfets. In *Simulation of Semiconductor Processes and Devices (SISPAD), 2013 International Conference on*, page 304, 2013.

[167] E. G. Marin, F. G. Ruiz, A. Godoy, I. M. Tienda-Luna, and F. Gámiz. Effect of interfacial states on the technological variability of Trigate MOSFETs. In *Silicon Nanoelectronics Workshop (SNW), 2012 IEEE*, 2012.

[168] P Mensch, KE Moselund, S Karg, E Lortscher, MT Bjork, H Schmid, and H Riel. Cv measurements of single vertical nanowire capacitors. In *Device Research Conference (DRC), 2011 69th Annual*, page 119, 2011.

[169] G. Kapila, B. Kaczer, A. Nackaerts, N. Collaert, and G.V. Groeseneken. Direct measurement of top and sidewall interface trap density in SOI finfets. *IEEE Electron Device Letters*, 28:232, Mar 2007.

[170] B. H Hong, N. Cho, S. J. Lee, Y. S. Yu, L. Choi, Y.C. Jung, K. H. Cho, K. H. Yeo, D.-W. Kim, G. Y. Jin, K. S. Oh, D. Park, Song S.-H, J.-S. Rieh, and S.W. Hwang. Subthreshold degradation of gate-all-around silicon nanowire field-effect transistors: Effect of interface trap charge. *IEEE Electron Device Letters*, 32: 1179, Sep 2011.

[171] B. Yu, L. Wang, Y. Yuan, P.M. Asbeck, and Y. Taur. Scaling of nanowire transistors. *IEEE Transactions on Electron Devices*, 55:2846, Oct 2008.

[172] B. H. Bransden and C.J. Joachain. *Quantum Mechanics*. Pearson, London. UK, 2000.

[173] H. Jeffreys and B. Jeffreys. *Methods of Mathematical Physics*. Cambridge University Press, 1999. ISBN 9780521664028.

[174] H. Jin, Z. Jian, Z. Lining, M. Chenyue, and C. Mansun. A surface potential-based non-charge-sheet core model for undoped surrounding-gate MOSFETs. *Journal of Semiconductors*, 30(2):024001, Feb 2009.

[175] J. R. Brews. A charge-sheet model of the MOSFET. *Solid State Electronics*, 21 (2):345–355, Feb 2978.

[176] D. Jiménez, B. Iñíguez, J. Suñe, L.F. Marsal, J. Pallarès, J. Roig, and D. Flores. Continuous analytic I-V model for surrounding-gate MOSFETs. *Electron Device Letters, IEEE*, 25(8):571–573, Aug 2004.

[177] B. Íniguez, D. Jiménez, J. Roig, H. A. Hamid, L. F. Marsal, and J. Pallarès. Explicit continuous model for long-channel undoped surrounding gate MOSFETs. *IEEE Transactions on Electron Devices*, 52:1868, Aug 2005.

[178] E. H. Poindexter, G. J. Gerardi, M. E. Rueckel, P. J. Caplan, N. M. Johnson, and D. K. Biegelsen. Electronic traps and Pb centers at the Si-SiO2 interface: Band-gap energy distribution. *Journal of Applied Physics*, 56(10):2844, 1984.

[179] T. Rudenko, V. Kilchytska, M.K.M Arshad, J.-P. Raskin, A. Nazarov, and D. Flandre. On the MOSFET threshold voltage extraction by transconductance and transconductance-to-current ratio change methods: Part II-effect of drain voltage. *IEEE Transactions on Electron Devices*, 58:4180, Dec 2011.

[180] S. Luryi. Quantum capacitance devices. *Applied Physics Letters*, 52:501, Nov 1987.

[181] J. Knoch, W. Riess, and J. Appenzeller. Outperforming the conventional scaling rules in the quantum-capacitance limit. *IEEE Electron Device Letters*, 29:372, Apr 2008.

[182] Khayer M. A and R. K. Lake. Diameter dependent performance of high-speed, low-power InAs nanowire field-effect transistors. *Journal of Applied Physics*, 107: 014502, Jan .

[183] H. A. Hamid, B. Iniguez, and J.Roig Guitart. Analytical model of the threshold voltage and subthreshold swing of undoped cylindrical gate-all-around-based MOSFETs. *IEEE Transactions on Electron Devices*, 54:572, Mar 2007.

[184] Q. Chen, E. M. Harrell, and J. D. Meindl. A physical short-channel threshold voltage model for undoped symmetric double-gate MOSFETs. *IEEE Transactions on Electron Devices*, 50:1631, Jul 2003.

[185] J. Lacord, J.L. Huguenin, T. Skotnicki, G. Ghibaudo, and F. Boeuf. Simple and efficient MASTAR threshold voltage and subthreshold slope models for low-doped double-gate MOSFET. *IEEE Transactions on Electron Devices*, 59:2534, Sep 2012.

[186] H. S. Wong, M. H. White, T. Krutsick, and R. V. Bocrr. Modeling of transconductance degradation and extraction of threshold voltage in this oxide MOSFETs. *Solid State Electronics*, 30:953, Feb 1987.

[187] M. Tsuno, M. Suga, K. Shibahara M. Tanaka, M. Miura-Mattausch, and M. Hirose. Physically-based threshold voltage determination for MOSFETs of all gate lengths. *IEEE Transactions on Electron Devices*, 46:1929, Jul 1999.

[188] G. Ghibaudo. New method for the extraction of MOSFET pameters. *Electronic Letters*, 24:545, Apr 1988.

[189] K. Terada and K. I. Hatanaka K. Nishiyama. New method for the extraction of MOSFET pameters. *Solid State Electronics*, 45:35, Jul 2000.

[190] A. Ortiz-Conde, F.J. García Sánchez, J.J. Liou, A. Cerdeira, M. Estrada, and Y. Yue. A review of recent MOSFET threshold voltage extraction methods. *Microelectronics Reliability*, 42:583, Dec 2002.

[191] K. Nehari, J.L. Autran, D. Munteanu, and M. Bescond. A compact model for the threshold voltage of silicon nanowire MOS transistors including 2D-quantum confinement effects. In *NSTI Nanotech 2005. NSTI Nanotechnology Conference and Trade Show. Technical Proceedings*, page 175, May 2005.

[192] A. S. Medury, K. N. Bhat, and N. Bhat. Threshold voltage modeling under size quantization for ultra-thin silicon double-gate metal-oxide-semiconductor field-effect transistor. *Journal of Applied Physics*, 112:024513, Jul 2010.

[193] P. R. Kumar and S. Mahapatra. Quantum threshold voltage modeling of short channel quad gate silicon nanowire transistor. *IEEE Transactions on Electron Devices*, 10:121, Sep 2011.

[194] Denis Flandre, Valeria Kilchytska, and Tamara Rudenko. g_m/i_d method for threshold voltage extraction applicable in advanced MOSFETs with nonlinear behavior above threshold. *IEEE Transactions on Electron Devices*, 31:930, Sep 2010.

[195] T. Rudenko, V. Kilchytska, M.K.M Arshad, J.-P. Raskin, A. Nazarov, and D. Flandre. On the MOSFET threshold voltage extraction by transconductance and transconductance-to-current ratio change methods: Part I-effect of gate-voltage-dependent mobility. *IEEE Transactions on Electron Devices*, 58:4172, Dec 2011.

[196] A. Kloes, M. Weidemann, D. Goebel, and B. T. Bosworth. Three-dimensional closed-form model for potential barrier in undoped finFETs resulting in analytical

equations for v_t and subthreshold slope. *IEEE Transactions on Electron Devices*, 55(12):3467, 2008.

[197] F. J. G. Ruiz, I. M. Tienda-Luna, A. Godoy, L. Donetti, and F. Gámiz. A model of the gate capacitance of surrounding gate transistors: Comparison with double-gate MOSFETs. *IEEE Transactions on Electron Devices*, 57:2477, Oct 2010.

[198] D. Jin, D. Kim, T. Kim, and J. A. del Alamo. Quantum capacitance in scaled down III-V FETs. In *Electron Devices Meeting (IEDM), 2007 IEEE International*, page 495, Dec 2009.

[199] H.S. Pal, K.D. Cantley, S.S. Ahmed, and M.S. Lundstrom. Influence of the bandstructure and channel structure on the inversion layer capacitance of silicon and GaAs MOSFETs. *IEEE Transactions on Electron Devices*, 55:904, Mar 2008.

[200] I.M. Tienda-Luna, F.J. García Ruiz, L. Donetti, A. Godoy, and F. Gámiz. Modeling the equivalent oxide thickness of surrounding gate SOI devices with high-κ insulators. *Solid-State Electronics*, 52:1854, Dec 2008.

[201] S. H. Park, Y. Liu, N. Kharche, M.S. Jelodar, G. Klimeck, M.S. Lundstrom, and M. Luisier. Performance comparisons of III-V and strained-Si in planar FETs and nonplanar FinFETs at ultrashort gate length (12 nm). *IEEE Transactions on Electron Devices*, 59:2107, Aug 2012.

[202] I. M. Tienda-Luna, F. J. G. Ruiz, A. Godoy, B. Biel, and F. Gámiz. Influence of orientation, geometry, and strain on electron distribution in silicon gate-all-around (GAA) MOSFETs. *IEEE Transactions on Electron Devices*, 58:3350, Dec 2011.

[203] F.J. García Ruiz, A. Godoy, F. Gámiz, C. Sampedro, and L. Donetti. A comprehensive study of the corner effects in Pi-gate MOSFETs including quantum effects. *IEEE Transactions on Electron Devices*, 54:3369, Dec 2007.

[204] M. Abramowitz and I. A. Stegun. *Handbook of mathematical functions: with formulas, graphs, and Mathematical tables*. Dover Publications, New York. USA, 1970. ISBN 0486612724.

[205] E.G. Marin, F.J.G. Ruiz, I.M. Tienda-Luna, A. Godoy, and F. Gamiz. Analytical gate capacitance modeling of III-V nanowire transistors. *IEEE Transactions on Electron Devices*, 60(5):1590, May 2013.

[206] M. Lundstrom. *Fundamentals of Carrier Transport*. Cambridge University Press, New York. USA, 2009. ISBN 9780521637244.

[207] Francisco Gámiz, Juan A López-Villanueva, Juan B Roldán, Juan E Carceller, and Pedro Cartujo. Monte carlo simulation of electron transport properties in extremely thin SOI MOSFET's. *IEEE Transactions on Electron Devices*, 45: 1122, 1998.

[208] F. Gamiz, J. B. Roldán, P. Cartujo-Cassinello, J. E. Carceller, J. A. López-Villanueva, and S. Rodriguez. Electron mobility in extremely thin single-gate silicon-on-insulator inversion layers. *Journal of applied physics*, 86:6269, 1999.

[209] F. Gámiz, F. Jiménez-Molinos, J. B. Roldán, and P. Cartujo-Cassinello. Coulomb scattering model for ultrathin silicon-on-insulator inversion layers. *Applied Physics Letters*, 80:3835, 2002.

[210] F. Gámiz, J. B. Roldán, A. Godoy, J. E. Carceller, and P. Cartujo. Double gate silicon on insulator transistors. a monte carlo study. *Solid-State Electronics*, 48: 937, 2004.

[211] C. Sampedro, F. Gámiz, A. Godoy, R. Valín, A. García-Loureiro, and F. J. G. Ruiz. Multi-subband Monte Carlo study of device orientation effects in ultra-short channel DGSOI. *Solid-State Electronics*, 54:131, 2010.

[212] M. Lenzi, P. Palestri, E. Gnani, S. Reggiani, A. Gnudi, D. Esseni, L. Selmi, and G. Baccarani. Investigation of the transport properties of silicon nanowires using deterministic and Monte Carlo approaches to the solution of the Boltzmann transport equation. *IEEE Transactions on Electron Devices*, 55(8):2086, Aug 2008.

[213] S. Jin, T.-W. Tang, and M. V. Fischetti. Simulation of silicon nanowire transistors using Boltzmann transport equation under relaxation time approximation. *IEEE Transactions on Electron Devices*, 55:727, 2008.

[214] N. Neophytou and H. Kosina. Atomistic simulations of low-field mobility in Si nanowires: Influence of confinement and orientation. *Physical Review B*, 84: 085313, 2011.

[215] J. Dura, F. Triozon, S. Barraud, D. Munteanu, S. Martinie, and J. L. Autran. Kubo-greenwood approach for the calculation of mobility in gate-all-around nanowire metal-oxide-semiconductor field-effect transistors including screened remote Coulomb scattering. Comparison with experiment. *Journal of Applied Physics*, 111:103710, 2012.

[216] S. Barraud, E. Sarrazin, and A. Bournel. Temperature and size dependences of electrostatics and mobility in gate-all-around MOSFET devices. *Semiconductor Science and Technology*, 26:025001, 2011.

[217] T. P. OŔegan, M. V. Fischetti, B. Sorée, S. Jin, W. Magnus, and M. Meuris. Calculation of the electron mobility in III-V inversion layers with high-κ dielectrics. *Journal of Applied Physics*, 108:103705, 2010.

[218] S. Harris. *An Introduction to the Theory of the Boltzmann Equation*. Dover Publications, New York. USA, 2004. ISBN 9780486438313.

[219] D.K. Ferry and C. Jacoboni. *Quantum Transport in Semiconductors*. Berlin. Germany, 1992. ISBN 9780306438530.

[220] S. Datta. *Quantum Transport: Atom to Transistor*. Cambridge University Press, New York. USA, 2013. ISBN 9781107632134.

[221] F. W. J. Olver, D. W. Lozier, R. F. Boisvert, and C. W. Clark, editors. *NIST Handbook of Mathematical Functions*. Cambridge University Press, New York. USA, 2010.

[222] R. Kotlyar, C. Weber, L. Shifren, S. Cea, M.D. Giles, and M. Stettler. Effect of band warping and wafer orientation on NMOS mobility under arbitrary applied stress. *Journal of Computational Electronics*, 7:95, 2008.

[223] D. Esseni and F. Driussi. A quantitative error analysis of the mobility extraction according to the Matthiessen rule in advanced MOS transistors. *IEEE Transactions on Electron Devices*, 58:2415, 2011.

[224] A. Paussa and D. Esseni. An exact solution of the linearized Boltzmann transport equation and its application to mobility calculations in graphene bilayers. *Journal of Applied Physics*, 113:093702, 2013.

[225] R. Kubo. Statistical-mechanical theory of irreversible processes. I. General theory and simple applications to magnetic and conduction problems. *Journal of the Physical Society of Japan*, 12(6):570, 1957.

[226] D.A. Greenwood. The Boltzman equation in the theory of electrical conduction in metals. *Proc. Phys. Soc.*, 71:585, 1958.

[227] R. Kotlyar, B. Obradovic, P. Matagne, M. Stettler, and M. D. Giles. Assessment of room-temperature phonon-limited mobility in gated silicon nanowires. *Applied Physics Letters*, 84:5270, 2004.

[228] S. M. Goodnick, D. K. Ferry, C. W. Wilmsen, Z. Liliental, D. Fathy, and O. L. Krivanek. Surface roughness at the Si(100)-SiO_2 interface. *Physical Review B*, 32(12):8171, 1985.

[229] F. Gamiz, J. B. Roldán, P. Cartujo-Cassinello, J. A. López-Villanueva, and P. Cartujo. Role of surface-roughness scattering in double gate silicon-on-insulator inversion layers. *Journal of Applied Physics*, 89:1764, 2001.

[230] Z. Stanojevic and H. Kosina. Surface-roughness-scattering in non-planar channels: The role of band anisotropy. In *Simulation of Semiconductor Processes and Devices (SISPAD), 2013 International Conference on*, page 352, Sept 2013.

[231] Y. Ando and A. Cappy. Ensemble Monte Carlo simulation for electron transport in quantum wire structures. *Journal of Applied Physics*, 74:3983, 1993.

[232] M. V. Fischetti and S. E. Laux. Long-range coulomb interactions in small Si devices. Part I: Performance and reliability. *Journal of Applied Physics*, 89:1205, 2001.

[233] D. Esseni, A. Abramo, L. Selmi, and E. Sangiorgi. Physically based modeling of low field electron mobility in ultrathin single-and double-gate SOI n-MOSFETs. *IEEE Transactions onElectron Devices*, 50:2445, 2003.

[234] A.-T. Pham, C. Jungemann, and B. Meinerzhagen. Physics-based modeling of hole inversion-layer mobility in strained-SiGe-on-insulator. *IEEE Transactions on Electron Devices*, 54:2174, 2007.

[235] I M Tienda-Luna, F G. Ruiz, A Godoy, B Biel, and F Gámiz. Surface roughness scattering model for arbitrarily oriented silicon nanowires. *Journal of Applied Physics*, 110:084514, 2011.

[236] E. B. Ramayya, D. Vasileska, S. M. Goodnick, and I. Knezevic. Electron transport in silicon nanowires: The role of acoustic phonon confinement and surface roughness scattering. *Journal of Applied Physics*, 104:063711, 2008.

[237] T. Ando, A. B. Fowler, and F. Stern. Electronic properties of two-dimensional systems. *Review Modern Physics*, 54(2):437, 1982.

[238] S. Jin, S.-M. Hong, W. Choi, K.-H. Lee, and Y. Park. Coupled drift-diffusion (DD) and multi-subband boltzmann transport equation (MSBTE) solver for 3D multi-gate transistors. In *Simulation of Semiconductor Processes and Devices (SISPAD), 2013 International Conference on*, page 348, Sept 2013.

[239] A. V. Oppenheim, R. W. Schafer, and J. R. Buck. *Discrete-time signal processing*, volume 2. Prentice-hall Englewood Cliffs, 1989.

[240] S. Yamakawa, H. Ueno, K. Taniguchi, C. Hamaguchi, K. Miyatsuji, K. Masaki, and U. Ravaioli. Study of interface roughness dependence of electron mobility in Si inversion layers using the Monte Carlo method. *Journal of Applied Physics*, 79:911, 1996.

[241] F. Gámiz, J. A. López-Villanueva, J. A. Jiménez-Tejada, I. Melchor, and A. Palma. A comprehensive model for coulomb scattering in inversion layers. *Journal of Applied Physics*, 75:924, 1994.

[242] F. Gamiz and M. V. Fischetti. Monte carlo simulation of double-gate silicon-on-insulator inversion layers: The role of volume inversion. *Journal of Applied Physics*, 89:5478, 2001.

[243] F. Jiménez-Molinos, J. B. Roldán, M. Balaguer, and F. Gámiz. An in-depth simulation study of coulomb mobility in ultra-thin-body SOI MOSFETs. *Semiconductor Science and Technology*, 25:055002, 2010.

[244] D. Casterman and M. M. De Souza. Evaluation of the Coulomb-limited mobility in high-κ dielectric metal oxide semiconductor field effect transistors. *Journal of Applied Physics*, 107:063706, 2010.

[245] F. Stern and W. E. Howard. Properties of semiconductor surface inversion layers in the electric quantum limit. *Physical Review*, 163(3):816, 1967.

[246] T. H. Ning and C. T. Sah. Theory of scattering of electrons in a nondegenerate-semiconductor-surface inversion layer by surface-oxide charges. *Physical Review B*, 6:4605, 1972.

[247] N.W. Ashcroft and N.D. Mermin. *Solid state physics*. Saunders College, 1976. ISBN 9780030493461.

[248] W. Zhang, C. Delerue, Y.-M. Niquet, G. Allan, and E. Wang. Atomistic modeling of electron-phonon coupling and transport properties in n-type [110] silicon nanowires. *Physical Review B*, 82:115319, 2010.

[249] I. M. Tienda-Luna, F. G. Ruiz, A. Godoy, L. Donetti, c. Martínez-Blanque, and F. Gámiz. Effect of confined acoustic phonons on the electron mobility of rectangular nanowires. *Applied Physics Letters*, 103:163107, 2013.

[250] D. Long. Scattering of conduction electrons by lattice vibrations in silicon. *Physical Review*, 120:2024, 1960.

[251] B. N. Brockhouse. Lattice vibrations in silicon and germanium. *Physical Review Letters*, 2:256, 1959.

[252] D. Vasileska. Polar optical phonon scattering, Jun 2011. URL `http://nanohub.org/resources/11522`.

[253] T. Wang and T.W. Chen T. H. Hsieh. Quantum confinement effects on low dimensional electron mobility. *Journal of Applied Physics*, 74:426, 1993.

[254] J. P. Leburton. Optic-phonon-limited transport and anomalous carrier cooling in quantum-wire structures. *Physical Review B*, 45:11022, 1992.

[255] G. Bastard. *Wave mechanics applied to semiconductor heterostructures*. Monographies de physique. Les Éditions de Physique, 1988. ISBN 9780470217085.

[256] J. W. Harrison and J. R. Hauser. Alloy scattering in ternary III-V compounds. *Physical Review B*, page 5347, 1976.

[257] P. Toniutti, D. Esseni, and P. Palestri. Failure of the scalar dielectric function approach for the screening modeling in double-gate SOI MOSFETs and in FinFETs. *IEEE Transactions on Electron Devices*, 57:3074, 2010.

[258] M. Tsetseri and G. P. Triberis. Mobility in V-shaped quantum wires due to interface roughness and alloy scattering. *Physical Review B*, 69:075313, 2004.

[259] T. Sahu. Intersubband-coupling and screening effects on the electron subband mobility in a GaAs/$In_xGa_1 - x$As delta-doped double quantum well system. *Journal of Applied Physics*, 96:5576, 2004.

[260] JWW Van Tilburg, RE Algra, WGG Immink, M Verheijen, EPAM Bakkers, and LP Kouwenhoven. Surface passivated InAs/InP core/shell nanowires. *Semiconductor science and technology*, 25:024011, 2010.

[261] G W Holloway, Y Song, C M Haapamaki, R R LaPierre, and J Baugh. Electron transport in InAs-InAlAs core-shell nanowires. *Applied Physics Letters*, 102: 043115, 2013.

[262] A C Ford, J C Ho, Y-L Chueh, Y-C Tseng, Z Fan, J Guo, et al. Diameter-dependent electron mobility of InAs nanowires. *Nano Letters*, 9(1):360, 2008.

[263] S A Dayeh, D PR Aplin, X Zhou, P KL Yu, E T Yu, and D Wang. High electron mobility InAs nanowire field-effect transistors. *Small*, 3:326, 2007.

[264] S Chuang, Q Gao, R Kapadia, A C Ford, J Guo, and A Javey. Ballistic InAs nanowire transistors. *Nano letters*, 13:555, 2013.

[265] F Wang, S Yip, N Han, K Fok, H Lin, J J Hou, et al. Surface roughness induced electron mobility degradation in InAs nanowires. *Nanotechnology*, 24(37):375202, 2013.

[266] H Yoshioka, N Morioka, J Suda, and T Kimoto. Mobility oscillation by one-dimensional quantum confinement in Si-nanowire metal-oxide-semiconductor field effect transistors. *Journal of Applied Physics*, 106:034312, 2009.

[267] M. Poljak, V. Jovanovic, D. Grgec, and T. Suligoj. Assessment of electron mobility in ultrathin-body InGaAs-on-insulator MOSFETs using physics-based modeling. *IEEE Transactions on Electron Devices*, 59:1636, June 2012.

[268] M Yokoyama, Y Asakura, H Yokoyama, M Takenaka, and S Takagi. Impact of Al_2O_3 ALD temperature on Al_2O_3/GaSb metal-oxide-semiconductor interface properties. In *Indium Phosphide and Related Materials (IPRM), 2013 International Conference on*, 2013.

[269] SH Kim, M Yokoyama, R Nakane, O Ichikawa, T Osada, M Hata, M Takenaka, and S Takagi. Strained extremely-thin body $In_{0.53}Ga_{0.47}As$-on-insulator MOSFETs on Si substrates. In *VLSI Technology, 2013. Digest of Technical Papers. 2013 Symposium on*, 2013.

[270] N. Xu, F. Andrieu, B. Ho, B.-Y. Nguyen, O. Weber, C. Mazuré, O. Faynot, T. Poiroux, and T.-J. K. Liu. Impact of back biasing on carrier transport in ultra-thin-body and BOX (UTBB) fully depleted SOI MOSFETs. In *VLSI Technology, 2012. Digest of Technical Papers. 2012 Symposium on*, page 113, Jun 2012.

[271] N Rodríguez, S Cristoloveanu, and F Gámiz. Revisited pseudo-MOSFET models for the characterization of ultrathin SOI wafers. *Electron Devices, IEEE Transactions on*, 56:1507, 2009.

[272] M. Sotoodeh, A. H. Khalid, and A. A. Rezazadeh. Empirical low-field mobility model for III-V compounds applicable in device simulation codes. *Journal of Applied Physics*, 87:2890, 2000.

[273] M. V. Fischetti. Monte carlo simulation of transport in technologically significant semiconductors of the diamond and zinc-blende structures. I. homogeneous transport. *IEEE Transactions on Electron Devices*, 38:634, 1991.

[274] M. V. Fischetti and S. E. Laux. Monte carlo simulation of transport in technologically significant semiconductors of the diamond and zinc-blende structures. II. submicrometer MOSFET's. *IEEE Transactions on Electron Devices*, 38:650, 1991.

[275] M. V. Fischetti and S.E. Laux. Monte carlo study of electron transport in silicon inversion layers. *Physical Review B*, 48:2244, Jul 1993.

[276] D. H Kim, J. A. del Alamo, J. H. Lee, and K. S. Seo. Performance evaluation of 50 nm $In_{0.7}Ga_{0.3}As$ HEMTs for beyond-CMOS logic applications. In *Electron Devices Meeting (IEDM), 2005 IEEE International*, page 767, Dec 2005.

[277] A. Nainani, B. R. Bennett, J. B. Boos, M. G. Ancona, and K. C. Saraswat. Enhancing hole mobility in III-V semiconductors. *Journal of Applied Physics*, 111:103706, May 2012.

[278] J. J. Gu, Wu, Y. Liu, A. T. Neal, R. G. Gordon, and P. D. Ye. Size-dependent-transport study of in $ga_0.53$ $as_0.47$ gate-all-around nanowire MOSFETs: Impact

of quantum confinement and volume inversion. *IEEE Electron Device Letters*, 33: 967, Jul 2012.

[279] Y. Yuan, B. Yu, J. Song, and Y. Taur. An analytic model for threshold voltage shift due to quantum confinement in surrounding gate MOSFETs with anisotropic effective mass. *Solid State Electronics*, 53:140, Jan 2009.

[280] T. Bryllert, L. E. Wernersson, L. E. Froberg, and L. Samuelson. Vertical high-mobility wrap-gated InAs nanowire transistor. *IEEE Electron Device Letters*, 27: 323, 2006.

[281] R. Granzner, S. Thiele, C. Schippel, and F. Schwierz. Quantum effects on the gate capacitance of trigate SOI MOSFETs. *IEEE Transactions on Electron Devices*, 57:3231, Dec 2010.

[282] A. Ali, H. Madan R. Misra, A. Agrawal, P. Schiffer, B.R. Bennett, and S. Datta. Experimental determination of quantum and centroid capacitance in arsenide-antimonide quantum-well MOSFETs incorporating nonparabolicity effect. *IEEE Transactions on Electron Devices*, 58:1397, May 2011.

[283]

[284] R. Chau, B. Doyle, S. Datta, J. Kavalieros, and K. Zhang. Integrated nanoelectronics for the future. *Nature Materials*, 6:810, Nov 2007.

[285] I. Ferain, C. A. Colinge, and J.P. Colinge. Multigate transistors as the future of classical metal-oxide-semiconductor field-effect transistors. *Nature*, 410:310, Nov 2010.

[286] R. Chau, S. Datta, M. Doczy, B. Doyle, B. Jin, J. Kavalieros, A. Majumdar, M. Metz, and M. Radosavljevic. Benchmarking nanotechnology for high-performance and low-power logic transistor applications. *IEEE Transactions on Nanotechnology*, 4:153, Mar 2005.

[287] H. Werner and G. Raymann. An approximation to the fermi integral $f_{1/2}(x)$. *Mathematical Computing*, 17:193, Mar 1963.

[288] K. Terada, K. Nishiyama, and K.-I. Hatanaka. Comparison of MOSFET-threshold-voltage extraction methods. *Solid-State Electronics*, 45:35, Jan 2001.

[289] G.N. Watson. *A treatise on the theory of Bessel functions*. Cambridge University Press, Cambridge. UK, 1966. ISBN 0521483913.

[290] J. P. Colinge, J.W. Park, and W. Xiong. Threshold voltage and subthreshold slope of multiple-gate SOI MOSFETs. *IEEE Electron Device Letters*, 24:515, Aug 2003.

[291] Y. Nishi, K. Tanaka, and A. Ohwada. Study of silicon-silicon dioxide structure by electron spin resonance. *Japanese Journal of Applied Physics*, 11:85, Jul 1972.

[292] Y. Tsividis and C. McAndrew. *Operation and Modeling of the MOS Transistor*. Oxford University Press, Oxford. UK, 2010. ISBN 0195170156.

[293] C. Dupré, A. Hubert, S. Becu, M. Jublot, V. Maffini-Alvaro, C. Vizioz, et al. 15nm-diameter 3D stacked nanowires with independent gates operation: ϕ FET. In *Electron Devices Meeting (IEDM), 2008 IEEE International*, Dec 2008.

[294] C. Dupré, T. Ernst, S. Borel, Y. Morand, S. Descombes, B. Guillaumot, et al. Impact of isotropic plasma etching on channel Si surface roughness measured with AFM and on NMOS inversion layer mobility. In *9th International Conference on Ultimate Integration of Silicon*, page 133, 2008.

[295] C. Dupré, T. Ernst, V. Maffini-Alvaro, V. Delaye, J.-M. Hartmann, S. Borel, et al. 3D nanowire gate-all-around transistors: Specific integration and electrical features. *Solid-State Electronics*, 52:519, 2008.

[296] T. Ernst, E. Bernard, C. Dupre, A. Hubert, S. Becu, B. Guillaumot, et al. 3D multichannels and stacked nanowires technologies for new design opportunities in nanoelectronics. In *Integrated Circuit Design and Technology and Tutorial, 2008. ICICDT 2008. IEEE International Conference on*, pages 265–268, Jun 2008.

[297] M.V. Fischetti, T.P. O'Regan, N. Sudarshan, C. Sachs, S. Jin, J. Kim, and Y. Zhang. Theoretical study of some physical aspects of electronic transport in nMOSFETs at the 10-nm gate-length. *IEEE Transactions on Electron Devices*, 54:2116, Sept 2007.

[298] J.M. Hinckley and J. Singh. Influence of substrate composition and crystallographic orientation on the band structure of pseudomorphic Si-Ge alloy films. *Physical Review B*, 42(6):3546, 1990.

[299] L. Lin and J. Robertson. Defect states at III-V semiconductor oxide interfaces. *App. Phys. Let.*, 98:082903, 2011.

[300] S. Takagi, A. Toriumi, M. Iwase, and H. Tango. On the universality of inversion layer mobility in Si MOSFETs: Part II - effects of surface orientation. *IEEE Transactions on Electronic Devices*, 41(12):2363, 1994.

[301] S. Takagi, J. Koga, and A. Toriumi. Subband structure engineering for performance enhancement of Si MOSFETs. In *Electron Devices Meeting (IEDM), 1997 IEEE International*, page 219, 1997.

[302] N. Takiguchi, S. Koba, H. Tsuchiya, and Matsuto Ogawa. Comparisons of performance potentials of Si and InAs nanowire MOSFETs under ballistic transport. *IEEE Transactions on Electron Devices*, 59:206, Jan 2012.

[303] Y. Sun, S.E. Thompson, and T. Nishida. Physics of strain effects in semiconductors and metal-oxide-semiconductor field-effect transistors. *Journal of Applied Physics*, 101:104503, 2007.

[304] I. M. Tienda-Luna, F. J. Garcia Ruiz, A. Godoy, and F. Gámiz. The influence of orientation and strain on the transport properties of SOI trigate nMOSFETs. In *Solid State Device Research Conference, 2009. ESSDERC'09. Proceedings of the European*, 2009.

[305] K. Uchida, T. Krishnamohan, K. C. Saraswat, and Y. Nishi. Physical mechanisms of electron mobility enhancement in uniaxial stressed MOSFETs and impact of uniaxial stress engineering in ballistic regime. In *Electron Devices Meeting (IEDM), 2005 IEEE International*, page 135, 2005.

[306] C. Auth, C. Allen, A. Blattner, D. Bergstrom, M. Brazier, M. Bost, et al. A 22nm high performance and low-power CMOS technology featuring fully-depleted tri-gate transistors, self-aligned contacts and high density mim capacitors. In *VLSI Technology, 2012. Digest of Technical Papers. 2012 Symposium on*, page 131, Jun 2012.

[307] R.V. Booth, M.H. White, H.-S. Wong, and T.J. Krutsick. The effect of channel implants on MOS transistor characterization. *IEEE Transactions on Electron Devices*, 34:2501, Dec 1987.

[308] O. Moldovan, D. Jiménez, J.R. Guitart, F.A. Chaves, and B. Íniguez. Explicit analytical charge and capacitance models of undoped double-gate MOSFETs. *IEEE Transactions on Electron Devices*, 54:1718, Jul 2007.

[309] M. K. Hudait, G. Dewey, S. Datta, J. M. Fastenau, J. Kavalieros, W. K. Liu, et al. As quantum well transistor on silicon substrate using thin ($< 2\mu$m) composite buffer architecture for high-speed and low-voltage (0.5V) logic applications. In *Electron Devices Meeting (IEDM), 2007 IEEE International*, page 625, Dec 2005.

[310] DLMF. NIST Digital Library of Mathematical Functions. http://dlmf.nist.gov/, Release 1.0.6 of 2013-05-06. URL `http://dlmf.nist.gov/`. Online companion to [221].

[311] W. Mönch. Metal-semiconductor contacts: Electronics properties. *Surface Science*, 300:928, 1994.

[312] C. Tejedor, F. Flores, and E. Louis. The metal-semiconductor interface: Si (111) and zincblende (110) junctions. *Journal of Physics C: Solid State Physics*, 10: 2163, 1977.

[313] T. V. Perevalov, V. A. Gritsenko, and V. V. Kaichev. Electronic structure of aluminum oxide: ab initio simulations of α and γ phases and comparison with experiment for amorphous films. *The European Physical Journal Applied Physics*, 52, Dec 2010.

[314] S. Meng, C. Basceri, B. W. Busch, G. Derderian, and G. Sandhu. Leakage mechanisms and dielectric properties of Al_2O_3/TiN-based metal-insulator-metal capacitors. *Applied Physics Letters*, 83:4429, Nov 2003.

[315] B.G. Stretman. *Solid State Electronic Devices*. Pearson Education, Limited, 1972. ISBN 9780138220235.

[316] Intels revolutionary 22 nm transistor technology. Online. URL `http://www.intel.com/content/www/us/en/energy/intel-22nm-3-d-tri-gate-transistor-technology.html`. Accessed: 2014-07-04.

[317] J. Bardeen and W. Shockley. Deformation potentials and mobilities in non-polar crystal. *Physical Review*, 80(1):72, 1950.

[318] E. Bernard, T. Ernst, B. Guillaumot, N. Vulliet, P. Coronel, T. Skotnicki, S. Deleonibus, and O. Faynot. Multi-Channel Field-Effect transistor (MCFET)-Part I: Electrical performance and current gain analysis. *IEEE Transactions on Electron Devices*, 56(6):1243–1251, 2009.

[319] J. Chen, T. Saraya, and T. Hiramoto. Experimental investigations of electron mobility in silicon nanowire nMOSFETs on (110) silicon-on-insulator. *IEEE Electron Device Letters*, 30(11):1203, 2009.

[320] J. Chen, T. Saraya, K. Miyaji, K. Shimizu, and T. Hiramoto. Experimental study of mobility in [110]- and [100]-directed multiple silicon nanowire GAA MOSFETs on (100) SOI. In *VLSI Technology, 2008. Digest of Technical Papers. 2008 Symposium on*, page 32, 2008.

[321] N. Collaert, A. De Keersgieter, A. Dixit, I. Ferain, L.-S. Lai, and D. Lenoble. Multi-gate devices for the 32nm technology node and beyonds. *Solid-State Electronics*, 52:1291, 2008.

[322] F. Gámiz, L. Donetti, and N. Rodríguez. Anisotropy of electron mobility in arbitrarily oriented FinFETs. In *Solid State Device Research Conference, 2007. ESSDERC'07. Proceedings of the European*, page 378, 2007.

[323] F. Jiménez-Molinos, F. Gámiz, and L. Donetti. Coulomb scattering in high-κ gate stack silicon-on-insulator metal-oxide-semiconductor field effect transistors. *Journal of Applied Physics*, 104:063704, 2008.

[324] S-Y. Lee, E-J. Yoon, D-S. Shin, S-M. Kim, S-D. Suk, M-S. Kim, D-W. Kim, D. park, K. Kim, and B. Ryu. Sub-25nm single-metal gate CMOS Multi-Bridge-Channel MOSFET (MBCFET) for high performance and low power application. In *VLSI Technology. Digest of Technical Papers. 2005 Symposium on"*, page 154, 2005.

[325] T. C. Lim, E. Bernard, O. Rozeau, T. Ernst, B. Guillaumot, N. Vulliet, C. B. Dufournet, M. Paccaud, S. Lepilliet, G. Dambrine, and F. Danneville. Analog/RF performance of multichannel SOI MOSFET. *IEEE Transactions on Electron Devices*, 56(7):1473, 2009.

[326] N. Rodríguez, S. Cristoloveanu, and F. Gámiz. Evidence for mobility enhancement in double-gate silicon-on insulator metal-oxide-semiconductor field-effect transistors. *Jorunal of Applied Physics*, 102:083712, 2007.

[327] M. Chu, Y. Sun, U. Aghoram, and S.E. Thompson. Strain: A solution for higher carrier mobility in nanoscale MOSFETs. *Annual Review of Material Research*, 39:203, 2009.

[328] K. Yokoyama and K. Hess. Monte carlo study of electronic transport in $Al_{1-x}Ga_xAs$/GaAs single-well heterostructures. *Physical Review B*, 33:5595, 1986.

[329] K. S. Sieh and P. V. Smith. A localized orbital description of Si using non-local potentials. *Physica Status Solidi (b)*, 129:259, May 1985.

[330] W.-J. Qi, R. Nieh, B. H. Lee, K. Onishi, L. Kang, et al. Performance of mosfets with ultra thin zro/sub 2/and zr silicate gate dielectrics. In *VLSI Technology, 2000. Digest of Technical Papers. Symposium on*, 2000.

[331] T. Yamashita, V.S. Basker, T. Standaert, C. C Yeh, T. Yamamoto, K. Maitra, et al. Sub-25nm FinFET with advanced fin formation and short channel effect engineering. In *VLSI Technology, 2011. Digest of Technical Papers. 2011 Symposium on*, June 2011.

[332] T. Unuma, M. Yoshita, T. Noda, H. Sakaki, and H. Akiyama. Intersubband absorption linewidth in GaAs quantum wells due to scattering by interface roughness, phonons, alloy disorder, and impurities. *Journal of Applied Physics*, 93: 1586, 2003.

[333] S. Poli, M. G. Pala, and T. Poiroux. Full quantum treatment of remote Coulomb scattering in silicon nanowire FETs. *IEEE Transactions on Electron Devices*, 56: 1191, 2009.

[334] R. Mickevičius and V. Mitin. Acoustic-phonon scattering in a rectangular quantum wire. *Physical Review B*, 48:17194, 1993.

[335] M. J. Gilbert and S. K. Banerjee. Ballistic to diffusive crossover in III-V nanowire transistors. *IEEE Transactions on Electron Devices*, 54:645, 2007.

[336] F. Gamiz, J. B. Roldan, J. A. Lopez-Villanueva, P. Cartujo-Cassinello, and J. E. Carceller. Surface roughness at the Si-SiO2 interfaces in fully depleted silicon-on-insulator inversion layers. *Journal of Applied Physics*, 86:6854, 1999.

[337] Y Wang, V Schmidt, S Senz, and U Gösele. Epitaxial growth of silicon nanowires using an aluminium catalyst. *Nature nanotechnology*, 1:186, 2006.

[338] S Takagi and M Takenaka. III-V/Ge CMOS technologies on Si platform. In *VLSI Technology, 2010. Digest of Technical Papers. 2013 Symposium on*, page 147, 2010.

[339] E. G. Marin, F. G. Ruiz, I. M. Tienda-Luna, A. Godoy, and F. Gámiz. Study of the gate capacitance of GaAs, InAs and InGaAs nanowires. In *36th Workshop on Compound Semiconductor Devices and Integrated Circuits 2012*, 2012.

[340] I. M. Tienda-Luna, F. G. Ruiz, A. Godoy, E. G. Marin., and F. Gámiz. Dependence of the phonon-limited mobility in arbitrarily oriented si-nanowires. In *15th International Workshop on Computational Electronics (IWCE 2012)*, 2012.